The Modal Multifield Approach in Multibody Dynamics

Von der Fakultät für Maschinenbau
der Universität Hannover
zur Erlangung des akademischen Grades
Doktor-Ingenieur
genehmigte

Dissertation

von

Dipl.-Ing. Andreas Heckmann
geb. am 7. Juni 1962 in Worms

2005

1. Referent: Prof. Dr.-Ing. habil. B. Heimann

2. Referent: Prof. Dr. rer. nat. habil. M. Arnold

Tag der Promotion: 13.04.2005

Preface

This thesis is the result of my scientific work at the German Aerospace Center, DLR, in Oberpfaffenhofen, which I began as a member of the Vehicle System Dynamics Department at the Institute of Aeroelasticity in 2000. At the beginning of the year 2004 the department was reintegrated into the Institute of Robotics and Mechatronics.

First of all, I would like to thank Professor Dr. Bodo Heimann from the University of Hannover for his kind support and interest in my work. I would also like to thank Professor Dr. Martin Arnold from the Martin-Luther-University in Halle-Wittenberg. Professor Arnold initiated the subject of this thesis when he was a senior member of the Vehicle System Dynamics Department. Although he accepted a professorship at the Institute of Numerical Mathematics in Halle in 2002, he substantially supported the accomplishment of this doctoral thesis over the whole period.

Unfortunately, the head of the Department of Vehicle System Dynamics and co-initiator, Professor Willi Kortüm, PhD, did not live to see the end of this work, but nevertheless I am deeply indebted to him.

Furthermore, I very much appreciate the kindness of Professor Dr. Hirzinger, head of the Institute of Robotics and Mechatronics and Dr. Bals, head of the Control Design Engineering Department, who gave me the opportunity to finish this thesis.

Moreover, I am grateful to Dr. Wolfgang Rulka, Dr. Stefan Dietz and Dr. Lutz Mauer from INTEC GmbH in Oberpfaffenhofen who gave helpful advice and support whenever it was asked for.

Last but not least, many thanks to my colleagues from the Vehicle System Dynamics group. In particular Dr. Ondřej Vaculín had an open mind for every discussion. Dr. Wolf Krüger, Dr. Klaus Schott and Mrs. Christine Traurig in addition to Dr. Vaculín gave a great deal of useful hints on the writing of the manuscript.

Oberpfaffenhofen, 15th April 2005

Andreas Heckmann

gewidmet meinen beiden Kindern
Helena und Hannelore

Contents

Notation

Specific terms and their corresponding symbols are explained when they appear for the first time.

Scalar Quantities

c	specific heat capacity
h_f	film coefficient, specifying boundary heat flux due to convection
j	imaginary unit
m	mass
t	time
A	cross section area of a beam
B	boundary area
E	Young's modulus
G	electric Gibbs potential
I	geometrical moment of inertia of a beam
Q_φ	applied electric charge
S	heat source density
V	volume
α	thermal expansion coefficient
η	entropy density
φ	electric potential
ϑ	temperature increment w.r.t. reference temperature Θ_0
ϱ	density
ν	Poisson's constant
Λ	thermal conductivity
Θ	absolute temperature

Vectorial Quantities

$\boldsymbol{a}$	translatory acceleration
$\boldsymbol{b}$	generalised acceleration vector of a flexible body
$\boldsymbol{c}$	Lagrange co-ordinate
$\boldsymbol{d}$	electric displacement vector
$\boldsymbol{e}$	electric field strength
$\boldsymbol{f}$	external force
$\boldsymbol{h}$	load term of discretised differential equations
$\boldsymbol{n}_B$	outer unit normal vector
$\boldsymbol{q}$	heat flux
$\boldsymbol{r}$	position vector
$\boldsymbol{u}$	displacement vector
$\boldsymbol{v}$	translatory velocity
$\boldsymbol{y}$	vector constituted by a minimum set of generalised co-ordinates
$\boldsymbol{z}$	generalised co-ordinates
$\boldsymbol{\alpha}$	angular acceleration
$\boldsymbol{\varepsilon}$	strain tensor in vector format
$\boldsymbol{\lambda}$	vector of Lagrange multiplier
$\boldsymbol{\omega}$	angular velocity
$\boldsymbol{\sigma}$	stress tensor in vector format
$\underline{u}$	input vector in state space description
$\underline{x}$	state vector in state space description
$\underline{y}$	output vector in state space description

Matrices

$\boldsymbol{A}_{IR}$	rotation matrix, which transforms vector quantities defined w.r.t. the reference frame (R) into the equivalent description w.r.t. the inertial co-ordinate system (I)
$\boldsymbol{B}$	matrix of the partial derivatives of the modal shape functions
$\boldsymbol{D}$	damping, heat capacity or coupling matrix, to be multiplied by first time derivatives of generalised co-ordinates
$\boldsymbol{H}$	material coefficient matrix based on the electric Gibbs potential
$\boldsymbol{H}_c$	elasticity tensor at constant electric field and temperature
$\boldsymbol{H}_e$	piezoelectric tensor at constant temperature
$\boldsymbol{H}_\lambda$	thermal moduli at constant electric field
$\boldsymbol{H}_\epsilon$	permittivity tensor at constant strain and temperature

$\boldsymbol{H}_p$	pyroelectric tensor at constant strain
$\boldsymbol{H}_a$	heat capacity coefficient at constant strain and electric field
$\boldsymbol{I}_i$	identity matrix with dimension i, $\boldsymbol{I}_i \in \mathbb{R}^{i,i}$
$\boldsymbol{J}$	Jacobian matrix
$\boldsymbol{K}$	stiffness, conductivity, electric capacity or coupling matrix, to be multiplied by generalised co-ordinates
$\boldsymbol{M}$	mass matrix
$\boldsymbol{\Lambda}$	thermal conductivity matrix
$\boldsymbol{\Phi}$	matrix of the modal shape functions
$\underline{A}$	system matrix in state space description
$\underline{B}$	input matrix in state space description
$\underline{C}$	output matrix in state space description
$\underline{D}$	feed-through matrix in state space description

Generally Used Indices

$(\ )_j$	assigns a quantity to a joint.
$(\ )_u$	specifies a quantity to be related to the displacement field, e.g. $\boldsymbol{z}_u$ denotes the generalised co-ordinate vector of the displacements.
$(\ )_B$	relates a quantity to the boundary surface, e.g. $\boldsymbol{f}_B$ denotes a surface load [N/m^2].
$(\ )_R$	indicates motion terms of the body's reference frame.
$(\ )_V$	specifies a physical quantity as defined per volume, e.g. $\boldsymbol{f}_V$ denotes a volume force [N/m^3].
$(\ )_\varphi$	specifies a quantity to be related to the electrical field, e.g. $\boldsymbol{z}_\varphi$ denotes the generalised co-ordinate vector of the electrical field.
$(\ )_\vartheta$	relates a term to the thermal field, e.g. $\boldsymbol{z}_\vartheta$ denotes the generalised co-ordinate vector of the thermal field.
${}_I(\ )$	indicates that a vector is defined w.r.t. the inertial co-ordinate system.

The left hand indices specify the reference frame w.r.t. which the quantity is defined. This specification is omitted for terms resolved w.r.t. the body's floating frame of reference (R).

Superscripts

$(\ )^{(i)}$	relates terms to the specific body (i), if the complete multibody system is under consideration.
$(\ )^{(p)}$	assigns terms to the predecessor of body (i).

$(\ )^{(s)}$	indicates terms to a successor of body (i).
${}^{\vartheta}(\ )$	specifies an isothermal material constant.

The left hand superscripts indicate the terms kept constant during differentiation or measurement and are omitted for material coefficients based on the electric Gibbs potential.

Operators and Accents

$\delta(\ )$	variation
$\mathfrak{d}(\ )$	Dirac delta function
$\dot{(\ )}$	time derivative
$(\ )'$	partial derivative w.r.t. a geometric quantity
$(\ )_{,x}$	partial derivative w.r.t. x
$\widetilde{(\ )}$	The tilde operator defines a vector-matrix-transformation used to replace the vector cross product by a matrix multiplication: $\boldsymbol{a} \times \boldsymbol{b} = \tilde{\boldsymbol{a}}\boldsymbol{b} = -\tilde{\boldsymbol{b}}\boldsymbol{a}$
$\nabla(\ )$	the gradient operator
$\tilde{\nabla}(\ )$	the curl operator
$\nabla^T(\ )$	the divergence operator
$\nabla_u(\ )$	differential displacement-strain operator
$\hat{(\ )}$	indicates quantities in specific finite element representation, if they might be mixed up with the corresponding multibody terms.

Abbreviations

CACE	Computer aided control engineering
CPU	Central processing unit
DAE	Differential algebraic equation
DoF	Degrees of freedom
FEM	Finite element method
LQR	Linear quadratic regulator
MBS	Multibody simulation
MEMS	Micro-electromechanical system
MIMO	Multi-input multi-output system
MMA	Modal multifield approach
ODE	Ordinary differential equation
PZT	Lead Zirconate Titanate: $\mathrm{Pb}\left(\mathrm{Zr_x Ti_{1-x}}\right)\mathrm{O_3}$
TCP	Tool center point
w.r.t.	with respect to

Kurzfassung

Schlüsselwörter: modaler Mehrfeldansatz, erweiterte Darstellung flexibler Körper, Piezoelektrizität, Adaptronik, Thermoelastizität, thermische Verschiebungen.

Die Verwendung globaler Ansatzfunktionen ist eine etablierte Methode zur effizienten Darstellung des Verschiebungsfeldes flexibler Körper in der Mehrkörperdynamik. Die kleinen, elastischen Deformationen werden dabei den großen, nichtlinearen Referenzbewegungen des Körpers überlagert. Die mathematische Beschreibung der räumlich verteilten Verformungen mit einer geringen Anzahl von Freiheitsgraden gelingt insbesondere dann, wenn vorhandene physikalische Zusatzinformationen über das zu beschreibende System bereits im Lösungsansatz berücksichtigt werden.

Durch steigende Anforderungen an die Modellierung technischer Systeme und durch neue, auf multiphysikalischen Wirkprinzipien beruhende Technologien stellt sich nun die Frage, ob und wie die Verwendung globaler Ansatzfunktionen auch die effiziente Behandlung von Mehrfeldproblemen ermöglicht. Konkret befasst sich die vorliegende Arbeit deshalb mit Anwendungen aus den Gebieten Piezoelektrizität und Thermoelastizität aus dem Blickwinkel der Systemdynamik.

So genannte adaptive oder intelligente Strukturen sollen einen Nachteil von Leichtbaustrukturen, ihre Anfälligkeit für Schwingungen, eliminieren. Mit Hilfe von piezokeramischen Bauteilen, die auf der Struktur verteilt als Aktoren und Sensoren angeordnet sind, wird so zum Beispiel eine Verbesserung des Fahrkomforts in der Fahrzeugtechnik angestrebt. Gleichzeitig wird eine Einsparung an Kosten und Resourcen durch Leichtbau erwartet. Zur Auslegung und Simulation eines solchen mechatronischen Konzepts muss jedoch die Wechselwirkung der piezoelektrischen Bauteile mit der elastischen Struktur modelliert werden.

Wird ein mechanischer Prozess von einer relevanten Wärmeerzeugung zum Beispiel durch Reibung begleitet, kann eine gekoppelte thermische und elastische Analyse wertvoll sein. Typische Anwendungen sind Stabilitätsprobleme wie thermisches Kippen oder Beulen, Reibungsbremsen, Werkzeugmaschinen und mikromechanische Bauteile, diese oft sogar in Verbindung mit elektrostatischen und elektrothermischen Effekten.

Vor diesem Hintergrund wird in der vorliegenden Arbeit eine Methodik zur Beschreibung flexibler Körper entwickelt, die zusätzlich zu den klassischen mechanischen Größen auch Einflüsse durch elektrostatische oder thermische Felder berücksichtigt. Die vorgestellte Mehrfeldbeschreibung lässt sich als Erweiterung des klassischen modalen Verschiebungsfeldansatzes auffassen, wodurch auch hier die außerordentliche numerische Effizienz des modalen Ansatzes nutzbar gemacht werden soll.

Nach einem kurzen Überblick über den Stand der Technik bezüglich flexibler Mehrkörpersysteme wird in der vorliegenden Arbeit ein konsistentes theoretisches Konzept vorgestellt, das eine lineare multiphysikalische Materialbeschreibung und die gekoppelten Feldgleichungen in schwacher Form beinhaltet.

Darauf aufbauend werden spezifische Modellierungsannahmen und abgestimmte Prozesse zur Aufbereitung von Finiten-Element-Daten erläutert, so dass die Daten zur modalen Mehrfeldbeschreibung eines Körpers innerhalb eines integrierten Entwurfsprozesses generiert werden können. Die Anwendung und Schlüssigkeit der Prozesse und Modellierungsannahmen wird an Hand von überschaubaren Verifikationsbeispielen ausführlich diskutiert.

Die Berechnung zweier komplexer Anwendungen, die aktive Schwingungsdämpfung eines Schienenwagenkastens und eine Werkzeugmaschine mit thermischen Verschiebungen, belegt, dass die vorgeschlagene Methodik auch für komplexe Simulationsaufgaben geeignet ist. Eine kurze Zusammenfassung und ein Ausblick schließen die vorliegende Arbeit ab.

Abstract

Keywords: modal multifield representation, extended flexible body description, piezoelectricity, smart structures, thermoelasticity, thermally induced displacements.

In multibody dynamics the use of global modes in order to describe the linear displacement field of flexible bodies that undergo large reference motion is a well established approach. This technique enables the low-dimensional formulation of spatially distributed deflections, since all available physical and technical information may be exploited to streamline the solution basis.

In present days new technologies emerge and the demands on the design of technical systems increase, which gives reason to extend the existing modelling capabilities of multibody dynamics towards multifield problems. That is why the phenomena piezoelectricity and thermoelasticity are addressed in this thesis.

The so-called smart or adaptive structures, which are inter alia supposed to overcome the susceptibility of light-weight structures to vibrations, are frequently associated with distributed piezo-ceramic devices. If it is intended to evaluate this mechatronic design concept e.g. in order to improve comfort in vehicle applications, the interaction of the electrostatic field of the piezo-ceramic actuators or sensors with the displacement field has to be considered in addition to the purely mechanical description.

Whenever a mechanical process is associated with a remarkable heat generation e.g. by friction, a combined thermal and elastic analysis may make sense in order to describe the thermoelastic coupling that could even include thermal buckling as important nonlinearity. Applications such as friction brakes, machine tools or micro-mechanical devices, which often involve electrostatics too, here come to mind.

With this background, a methodology is introduced in the present thesis. It makes it possible to describe the behaviour of flexible bodies which are influenced by electrostatic or thermal field quantities in addition to the classical mechanical terms. The multifield representation is prepared in such a way that the modal multifield approach may be interpreted as an extension of the classical modal approach and recovers its extraordinary numerical efficiency.

After a short review of the state-of-the-art in the dynamics of flexible multibody systems, a consistent theoretical framework is outlined that includes a linear multiphysical material constitution and the coupled field equations in weak form.

Furthermore, specific modelling assumptions are proposed and preprocessing schemes are introduced that enable the transfer of appropriate finite element data into their modal multifield representation. The reasonability and the use of these techniques is extensively discussed by means of moderately complex verification examples.

Two advanced applications, the active damping of a railway car body and a machine tool with thermally induced displacements, demonstrate that the proposed simulation environment copes with complex simulation tasks as well. A short summary and outlook concludes the presentation.

1 Introduction

The demand to simulate and analyse light-weight space structures is frequently claimed to be the initial motivation of flexible multibody research in the 1970's [Sha97]. Indeed, in addition to the problems encountered in the analysis of multi-rigid-body systems, the nonlinear interaction of large displacements and rotations with small, elastic deformations cannot be ignored in aerospace applications and still is of major concern in flexible multibody dynamics.

With the achievements in the 1980's, the methodology was introduced to deal with elastic bodies in multibody systems. At first the description was based on an analytical representation of deformations. The incorporation of the finite element method as preprocessing step in the early 1990's improved that approach essentially and enabled a very general treatment also capable for bodies with a complex geometrical shape. In the last ten years the technique of describing the spatially distributed mechanical quantities with global modes has become state-of-the-art even for industrial applications.

Although we now look back on 30 years of research and development, flexible multibody dynamics is still a lively and promising field of research to which this thesis is intended to contribute. In the following exposition an extension of the flexible body representation is proposed which not only allows the consideration of elastic properties, but also provides an efficient description of spatially distributed piezo-thermoelastic behaviour.

The problems and tasks which have given reason to think about such an advanced representation of flexible bodies are summarised in the next section. The second section of this introduction is dedicated to the publications and authors who prepared the ground on which the present work is built up. An overview on the objectives of this thesis and the structure of the presentation concludes the introduction.

1.1 Motivation

Multibody dynamics generally focuses on the global behaviour of mechanical systems. As a result the modelling task is simplified because only a moderately detailed modelling level is required compared to the finite element method. However, this attitude makes it necessary to handle all engineering disciplines and problems significantly influencing the technical system under evaluation.

In addition, the complexity of technical systems tends to increase, involving more and more technical domains. The design of sophisticated technical systems requires extensive simulation and experimental studies to ensure reliable functionality. Ambitious simulation and experimental environments support these endeavours substantially. Especially multibody dynamics, which has been conceived for system dynamical analysis, is challenged and exposed as a continuous work field. Supplementary modelling capabilities like a multifield delineation enrich its application field and meet the demands of increasing complexity.

Imagine, for instance, the design of high performance machine tools. Working tasks in this field combine high speed motion with high demands on the accuracy. But the unavoidable losses in power transmission and the heat generation due to the working task necessarily lead to thermal loads. Industrial experience shows that beyond a specific level additional quality improvements require a combined elastic and thermal description of the system.

Conceptual design studies which work on that issue rely on the capability to describe the thermoelastic behaviour of bodies. And looking one step further, a control set-up which accounts for thermal displacements requires a low-dimensional system representation. Hence, it may be concluded that an efficient modal multifield representation is a promising approach to provide these requirements.

A specific importance of a combined thermal and elastic analysis can be stated for problems with large membrane or normal stresses due to temperature distribution. As a consequence the natural frequencies of flexural vibrations and the related stiffness terms will decrease or even drop down to zero so that thermal buckling may occur. Although the thermal deflection itself is small, at least if compared to displacements caused by mechanical forces, the consideration of both temperature and displacement field has to be called mandatory in such a case.

Disc brakes are actually components which have been used for a long time in automotive, railway or aeronautical applications. And certainly brakes have played an essential role in vehicle dynamics every time. But modern control strategies like anti-lock brake system and electronic stability program gain more and more importance and demand the comprehension of the complete vehicle system to a much greater extent. Since friction braking is necessarily related to high thermal loads, a consistent methodology to describe the distributed phenomenon thermoelasticity would be a valuable additional capability.

So far a classical multifield subject of continuum mechanics, namely thermoelasticity, is mentioned. A rather new application field, which involves the presence of distributed quantities with a different physical background, deals with so-called smart or adaptive structures.

Light-weight design is highly demanded for new generations of ground, air and space vehicles because of economic and environmental reasons. However, its application is usually limited because of the susceptibility to vibrations. Besides other objectives the concept of smart structures was developed and adapted for vibration control to overcome this drawback. In vehicle applications it is aimed to achieve comfort improvements by the adaptive modification of the structure's response to various stimuli.

In short, an adaptive structure is configured with distributed actuators and sensors and directed by a controller. In particular thin piezo-ceramic patches integrated into the structure are promising transduction devices which provide both the actuation and the sensing functionality. From the physical point of view, their transduction mechanism is based on the piezoelectric effect, i.e. the bidirectional interaction of the electrostatic field of the distributed piezo-ceramic devices and the mechanical structure. The modelling and evaluation of this interaction constitutes the second main application field of this thesis.

Since smart structures are mechatronic devices, their design involves a number of engineering disciplines such as structural mechanics, electronics and control. The optimisation of such a complex system is a challenging task, far from being straightforward, and may be supported advantageously by multibody dynamics.

If, for instance, the potential of structural control for advanced applications such as railway or automotive car bodies shall be evaluated, existing multibody simulation tools already provide a highly developed environment, since they are tailored for these applications. Assuming that an appropriate extension of this environment makes the computational representation of vehicles with adaptive components available, these virtual prototypes may be tested under realistic and verified conditions. The comparison to conventionally designed vehicles may be performed on the same virtual platform.

Micro-electromechanical devices are often used in conjunction with large reference motion e.g. for sensor purposes. Since their blueprint frequently requires a multiphysical analysis, multibody simulations with micro-electromechanical devices are not yet widespread. An extended multibody methodology with multifield capabilities fulfils the qualifications concerning this point and opens a new field of applications in the near future.

1.2 Overview on Related Literature

Flexible Multibody Dynamics and Structural Dynamics

The first achievements in the dynamics of flexible multibody systems were based on a purely analytical description of deflections. For this purpose the deformation assumptions of the classical theory of elasticity, mostly dedicated to scientists such as D. BERNOULLI, L. EULER, G.R. KIRCHHOFF and S. TIMOSHENKO, have to be adapted to represent bodies that undergo large reference motion. BREMER and PFEIFFER published a summary of this crucial groundwork in [BP92]. Moreover, they give a survey of the structure of the equations of motion of the complete multibody system and its efficient, recursive work-off using an explicit formalism. Their presentation is concluded by quite a few advanced application examples.

The book by SCHWERTASSEK and WALLRAPP [SW99], released seven years later than the previous one, delineates newer developments like the incorporation of the finite element method more extensively. The authors go into detail, even proposing a specific file format which is capable of storing the preprocessed body data reflecting the distributed elastic properties. The choice of the deformation variables and the consequences for the geometric linearisation regarding the so called geometric stiffness terms are also discussed.

Compared to these books by German authors who mainly present their approach in much detail, the second edition of SHABANA'S textbook [Sha98] is more diversified in fundamental representation aspects. Absolute Cartesian co-ordinates, generalised co-ordinate partitioning, minimum set of co-ordinates are discussed. A new approach dealing with the large deformation problem, the absolute nodal co-ordinate formulation is presented.

The textbook by STEJSKAL and VALÁŠEK [SV96] also reports on conceptual issues but additionally establishes the relationship from theoretical approaches to implemented formalisms addressing computational and numerical matters.

The basics of vehicle system dynamics and the employment of methods from multibody dynamics have been presented by KORTÜM and LUGNER in [KL93]. An overview on recent developments, extensions and improvements of multibody dynamics in this important application field is given in a special issue of the journal *Vehicle System Dynamics* [AV04].

In flexible multibody dynamics it is a common approach to use modal reduction techniques to obtain low-dimensional representations of elastic bodies. The quality of modal reduction strongly relies on the selection of appropriate modes. For this purpose both volumes of GASCH and KNOTHE, [GK87] and [GK89], provide important instructions to establish an adequate substructure representation of bodies. DIETZ [Die99] extends these considerations proposing a modal reduction scheme capable of stress recovery in the dynamic strength analysis of multibody systems.

SACHAU applied perturbation techniques to justify the truncation of specific terms of highly oscillatory influence in the equations of motion in [Sac96]. His approach enables a significant reduction of computation time, since deformations related to high frequencies are considered only statically.

Complex multibody systems with rigid and flexible bodies may be subdivided into subsystems for model set-up and time integration in such a way that each subproblem is handled by the corresponding specialised software tool. Appropriate examples of this method called *co-simulation* or *simulator coupling* have been published by VEITL, who studied the interaction between pantograph and catenary regarding high speed railway trains in [Vei01] and by DIETZ et al. [DHS01], who analysed the interaction of vehicle and elastic bridge while crossing. KRÜGER et al. [KHS02] coupled multibody dynamics and fluid dynamics software tools to examine the fluid-structure coupling in aeroelastic applications.

A short but comprehensive overview on multibody dynamics is provided by two companion review articles by SCHIEHLEN [Sch97] and SHABANA [Sha97] published in the same issue of the *Multibody System Dynamics* journal. In particular their extensive list of references is a worthwhile starting point for literature surveys.

Finite Element Method

Since the finite element method (FEM) is widely accepted, mechanical engineers are familiar with it and frequently analyse the mechanical performance of components and structures using this approach. As a result a data representation of these components exists. For that reason the most obvious way to obtain data for flexible bodies to be used in multibody dynamics is to organise the access to the finite element data base.

This computer aided engineering process chain requires flexible multibody research to keep track of finite element techniques. Well suited as a reference in this field is the classical textbook by ZIENKIEWICZ and TAYLOR, [ZT00a] and [ZT00b]. Also the monograph by BATHE [Bat96] provides fundamental information on many branches of the FEM such as structural analysis, heat transfer analysis and eigenvalue problems. The textbook by LEWIS et al. [LMTS96] is specialised on the application of the FEM in heat transfer analysis.

KNOTHE and WESSELS [KW92] present the principle of virtual displacements taking the deformation theory of second order into consideration which leads to a useful formulation of geometric stiffening.

The direct application of finite element techniques for the analysis of multibody systems without decomposition of large reference motion and small deformation is proposed by GÉRADIN and CARDONA in [GC01]. The benefit hereby is mainly concerned with the capability to describe the geometrically and/or physically nonlinear deformation behaviour of bodies with high resolution.

Thermoelasticity

As a general reference for the classical multifield problem thermoelasticity three outstanding publications are to be mentioned here. The monograph by NOWACKI [Now86] is an almost encyclopedic collection of exact analytical solutions. The textbook by NOWINSKI [Now78b], on the other hand, presents less problems but more discussions and conclusions which help to understand the physical background and its implications. The third book [BW97] gives a very broad overview. It deals with the theoretical foundation of thermodynamics of solids, it presents exact analytical as well as weak approximative solutions of thermoelastic continuum problems and it contains chapters in which the thermoelastic theory is prepared in the strength-of-material notation for beams and plates, which engineers are very familiar with. That is why NOWINSKI stated, referring to the first edition of [BW97]: “In 1960 B.A. BOLEY and J.H. WEINER gave a profound and comprehensive exposition of various facets of the theory of thermoelasticity, now considered classic”.

One active field of research in which thermoelastic considerations attract attention is the development of micro-electromechanical systems (MEMS). The layout of ultra-fast, high precision actuators and sensors on micro-scale needs to account for effects which are frequently neglected in classical design tasks. Thus LIFSHITZ and ROUKES examine the general influence of thermoelastic damping on micro-scale structures adapting analytical models in [LR00], cp. with [KM92]. Because of its fundamental significance their exposition is discussed in detail in Section 3.2.1. The thermal buckling phenomenon of micro-scale beams under Joule heating is analysed analytically as well by CHIAO and LIN in [CL00].

If a specific component layout for a given micro-scale design task involving structural and thermal influences is aimed at, it is frequently referred to the finite element method, e.g. TASCHINI et al. propose a new finite element, a multi-layered plate, tailored to model the thermo-mechanical response of micro-system components [TMGE00]. PAINTER and SHKEL quantify the error due to temperature changes on the measurements of their MEMS angular gyroscope in [PS03].

However, thermal analysis in MEMS-design is not primarily carried out in order to account for the thermo-mechanical but for the electro-thermal coupling, see [dR02]. Today’s high power dissipation density in MEMS makes on-chip thermal management very important.

In this field modal reduction schemes of the heat transfer equations emerge recently as a new task. In [OG00] OSTERGAARD and GYIMESI propose a reduction approach on the basis of the

Guyan-methodology. However, according to BECHTOLD et al. and their benchmark evaluation in [BRK02], the Guyan-reduction is less suitable to represent in particular the transient behaviour of a structure, see also [KR03]. Concluding the discussion of publications in this field, the simultaneous simulation and optimisation of electrical and thermal properties of a MEMS on a global system level is a major scientific issue and discussed e.g. by SCHWARZ and SCHNEIDER in [SS01]

Another field of research with an important thermoelastic context is the simulation of friction brakes. WALLASCHEK et al. submitted an informative literature review in [WHSM99] which covers thermal and thermoelastic aspects among other problems in the modelling of friction brakes. They refer for instance to the PhD-thesis [Rin96] of RINSDORF who aimed to optimise the comfort properties of disc brakes by means of coupled thermal and mechanical finite element analysis. The experimental validated FEM appraisal by KAO et al. in [KRD98] also aims at comfort improvements but focuses on the so-called brake disc hot judder phenomenon in a frequency range below 100 Hz.

HOHMANN [Hoh99] evaluates temperatures and displacements in brake discs to characterise the friction mechanism and to predict wear on disc brake pads. A combination of two- and three-dimensional FEM analysis with analytical considerations is used to obtain more global information on the life cycle of brake pads.

Besides these authentic thermoelastic studies, a range of surveys also combine heat transfer and mechanical analysis but are not concerned with the intrinsic coupling of both fields. In [KL95] KNOTHE and LIEBELT determine the temperature at the wheel-rail contact point which has a considerable influence on the tribological behaviour. RUDOLPH, POPP and HOGENKAMP [RPH03] recently proposed an analytical method to evaluate the temperatures in the contact region between brake disc and pad in order to account for the temperature dependence of the friction coefficient. The work of the last two research groups goes back to a publication of JAEGER [Jae42], who introduced the application of Green's functions to evaluate the temperature field due to sliding contact.

Last but not least the standard textbook written by BURCKHARDT should be mentioned in this context as a basic reference covering all aspects concerning vehicle brakes such as conceptual design, material selection and dimensioning criteria that are without doubt related to mechanical and thermal issues [Bur91].

Piezoelectricity and Structural Control

The comprehensive monograph [Pre02] about active vibration control with discrete and distributed structural actuators and sensors is written by PREUMONT. In view of the broad presentation including modelling aspects of continuum mechanics and material constitution as well as control issues such as LQR design and stability, he succeeds in crossing the bridge between the structural dynamics and control communities. Although PREUMONT also presents high frequency applications such as a distributed sensor for frequencies up to 10 kHz, his main concern covers active control of mechanical vibrations, e.g. tendon control of cable structures in civil engineering.

FULLER et al. complement the latter monograph since they address wave propagation and noise reduction more extensively in [FEN96].

Supplementary information on modelling matters may be found in the PhD-thesis of PIEFORT [Pie01], who developed shell and beam elements with attached piezoelectric patches ready for implementation in an FEM-tool.

YE and TZOU additionally consider thermal excitations and formulate a three field finite element of shell-type in order to simulate in particular the so-called thermal shock load case [YT00].

Another publication mentioned here because of its modelling particularity is written by GABBERT et al. [GKK00]. They introduce a method to evaluate homogenised material tensors for composites with piezoelectric fibres. Those structures may then be simulated as finite elements with homogeneous piezoelectric material properties.

ROSE and SACHAU are the first authors who consider distributed piezo-ceramic sensors and actuators on the background of flexible multibody dynamics submitting a purely theoretical appraisal [RS01].

The textbook by TICHÝ and GAUTSCHI [TG80] actually deals with the design and handling of conventional, discrete piezoelectric sensors for force, pressure and acceleration measurements. However, their description of the fundamentals of solid state physics and thermodynamics of crystal lattices is of course also valid and useful for piezo-ceramics.

An interesting insight into the piezo-mechanical behaviour on the microscopic level is given by the paper [CH94] of CHAN and HAGOOD, who propose a physical nonlinear model that delineates the polarisation reversal in piezoelectric crystallites.

Another important issue in structural control consists of the determination of appropriate actuator and sensor locations. In [HL93] HAĆ and LIU review some approaches in literature and propose a methodology that is based on the eigenvalues of the controllability and observability Gramians. That way quantitative measures of degree of controllability and observability are provided and exploited in order to define a performance index which is balanced according to the energy contribution of each mode. In particular for structures with small structural damping and well separated eigenfrequencies the computational efforts are quite small since in these cases the Gramians are diagonal-dominated, i.e. their diagonal elements provide a sufficient approximation of the eigenvalues.

While the latter publication explicitly separates the determination of actuator and sensor locations from the control optimisation task, GABBERT et al. work the other way around and use the cost functional from optimal control in order to simultaneously optimise discrete actuator positions and continuous parameters of the control law [GSW97].

BALS introduces quantitative positioning measures in [Bal89] that are based on a dominance and pole sensitivity analysis. The aim is to choose those actuator and sensor locations which allow the highest influence on the placement of those eigenvalues that are easy to excite by disturbances. Concurrently, the poles with a sufficient stability margin shall be influenced as little as possible.

A strong correlation between the radiated sound power of a structure and its volume velocity can be proven. In other words: modes which do not contribute to the net volume velocity or displacement, such as antisymmetric modes for a symmetric plate, radiate noise poorly at least at low frequencies. That is why DE MAN et al. define a combined cost function that considers the modal volume displacement weighted with the modal amplitudes together with bonuses for good controllability of the modes within the bandwidth of the controller and penalties for those in the cross-over region [DFP01].

Most of the publications regarding structural vibration control with distributed devices consider moderately complex structures like beams and plates. This holds for theoretical expositions, for computer based simulations and for experimental studies as well. There is no doubt that essential knowledge and experience are gained examining these fundamental types of structures. On the other hand the set-up of models and experiments that use structures closer to realistic design extends the complexity of the modelling, optimisation and control task significantly. One outstanding example of a study that tackles this issue is submitted by HANSSON et al. In [HTTT03] piezoelectric elements are attached to a 1:5 scaled Shinkansen car body in order to reduce vertical flexural vibrations. Experimental results are compared to those obtained by computer simulations. The achievements encourage the authors to continue the study using an actual railway vehicle and carry out running tests.

1.3 Objectives and Structure of this Thesis

As outlined in Sec. 1.1, a whole range of applications such as machine tools with thermal loads, friction brakes, MEMS or structural control design for light-weight components may be mentioned in order to motivate the introduction of multifield capabilities in multibody dynamics. Hence the general goal, which is deduced from these applications, is to present a consistent description of solid bodies simultaneously influenced by mechanical, thermal and electrostatic fields.

The main emphasis is placed on an efficient, low-dimensional multifield representation with just a few global modes. It is intended to build up a ready-to-use methodology supposed to be implemented in a multibody system simulation environment. Thus the present work includes theoretical foundation, addresses practical considerations regarding data preprocessing and concludes with advanced application examples.

In detail, the presentation begins by recalling the state-of-the-art in flexible multibody dynamics and thermodynamical material description. After this preparation a coherent theoretical framework describing distributed multiphysical phenomena in multibody dynamics is proposed as a conclusion to the second chapter.

In the third chapter the physical description is revised and carried over in order to meet the demands of daily engineering practise. The chapter is divided into two sections which exclusively deal with the piezoelectric and the thermoelastic problem respectively.

The technical relevance of some physical effects is reviewed and appropriate assumptions for the practical modelling task are deduced. Analytical considerations as well as moderately complex, single body verification examples are therefore introduced and compared with corresponding finite element models.

Furthermore, appropriate finite element analysis scenarios and subsequent data preprocessing are explained which facilitates the provision of numerical data of a body's modal multifield representation.

Among other things the data preprocessing is mentioned once again in the fourth chapter where all software extensions of the multibody simulation environment are introduced in the first section. Two advanced multibody simulation examples are presented in the following two sections.

For the piezoelectric application, piezo-ceramic patches are attached to the car body of a bogie railway vehicle. The simulation is supposed to give an impression as to which extent the flexural vibrations of the car body could be reduced and the riding comfort might be improved using piezo-ceramic actuators and sensor as structural control elements.

The thermoelastic application consists of a model of a high-performance machine tool which is subjected to thermal loads. A feasibility study is defined to figure out what a multibody simulation environment may look like which is capable of developing new measurement and control strategies accounting for thermally induced displacements.

The fifth and last chapter gives a short summary, outlines the achievements, addresses the open problems and therefore concludes the present thesis.

2 Theoretical Framework

Multibody dynamics is a discipline of technical dynamics and deals with mechanical systems consisting of interconnected rigid and deformable bodies. These bodies interact dynamically and compose the multibody system.

An important characteristic of a multibody system is given by its topology, which is defined by the geometric configuration of the bodies. Three main types are here to distinguish, chain-structured systems, tree-structured systems and multibody systems with closed kinematic loops, see Fig. 2.1.

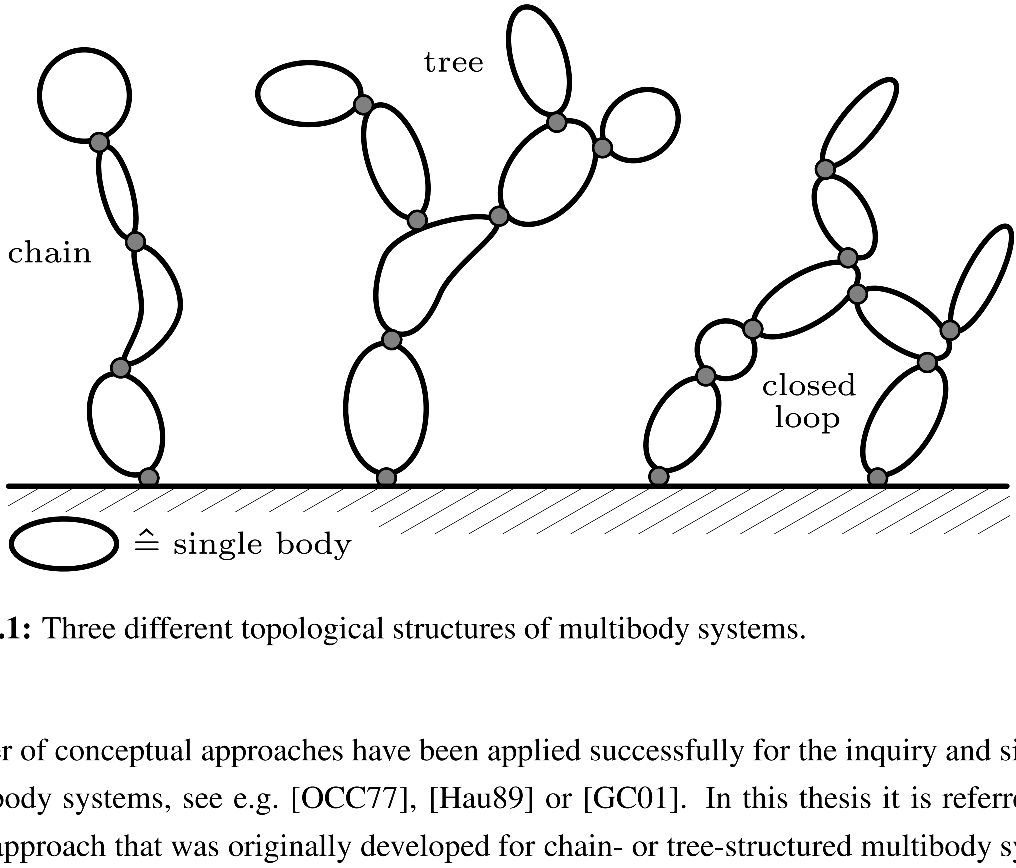

Figure 2.1: Three different topological structures of multibody systems.

A number of conceptual approaches have been applied successfully for the inquiry and simulation of multibody systems, see e.g. [OCC77], [Hau89] or [GC01]. In this thesis it is referred to one specific approach that was originally developed for chain- or tree-structured multibody systems in robotics [BJO86]. The corresponding algorithm by BRANDL et al. exploits the topology of the multibody system which enables an outstanding numerical efficiency. Their approach, which will be called analytical multibody dynamics in the following, is based on the principle of d'Alembert that says [Lan70, Ch. IV]: *Constraint forces do not work.*

This statement is exploited in such a way, that the equations of motion of each body are solved separately in a recursively organised evaluation process, see also [BP92, Sec. 4.3.3]. Since the concept of analytical multibody dynamics has been extended to multibody systems with closed kinematic loops as well, see [Rul98, Sec. 5.4.5] or [SW99, Sec. 6.5], it is well suited for the analysis of general articulated mechanical systems.

In the meantime analytical multibody dynamics is not only a well established field of research but has already been applied for many industrial engineering problems. Therefore a stable and proven ground for the development of new methods is given.

The first section of this chapter is devoted to the fundamental ideas of analytical multibody dynamics. The presentation mainly follows the textbooks of BREMER and PFEIFFER [BP92] and SCHERTASSEK and WALLRAPP [SW99], whereby in particular flexible multibody systems are emphasised.

Hence the bridge is built to the second important concept, which will be applied extensively in what follows. The low-dimensional semi-discretisation of the displacement field with just a few global modes is a well established approach in flexible multibody dynamics. Despite its limitations mainly due to linearity, the modal approach offers the capability to reproduce spatially distributed physical properties in a very efficient way. With this knowledge it is a natural step forward to think about a modal multifield approach, if it is aimed to reproduce not only the mechanical displacement field of a body but also other distributed physical quantities such as thermal or electrostatic fields. This idea, its theoretical foundation, its practical implementation and application is the actual novel contribution of this thesis.

The second section of this chapter, which is based on the monograph of TICHÝ and GAUTSCHI [TG80, Ch. 5, 6] and on the article of MINDLIN [Min74], briefly resumes the linear material constitution, which considers mechanical, thermal and electrostatic quantities in order to uniquely specify the thermodynamical state of a body particle.

The representation of the different physical fields and their interrelations is established in the third section. Moreover, the central issue of Sec. 2.3 is concerned with the construction of a coherent framework that combines analytical multibody dynamics, modal semi-discretisation approach, multiphysical material constitution and multifield description.

2.1 Analytical Multibody Dynamics

In this section, the line of presentation follows the structure of the laws of mechanics. Before tackling the dynamics, a kinematic description of the body motion and the semi-discretisation of the body's displacement field are required. The subsequent introduction and application of Hamilton's principle enables the formulation of the equations of motion of a single elastic body. Then the subsystem synthesis is explained which assembles the multibody system from its components. The section is rounded off by a brief summary of how time integration may be organised.

2.1.1 The Floating Frame of Reference

Consider a flexible body as shown in Fig. 2.2. In order to describe the motion of each particle of the body, two frames are introduced. The inertial co-ordinate system (I) serves as a reference for the whole multibody system. A floating reference frame (R) is assigned and fixed to every body of the multibody system.

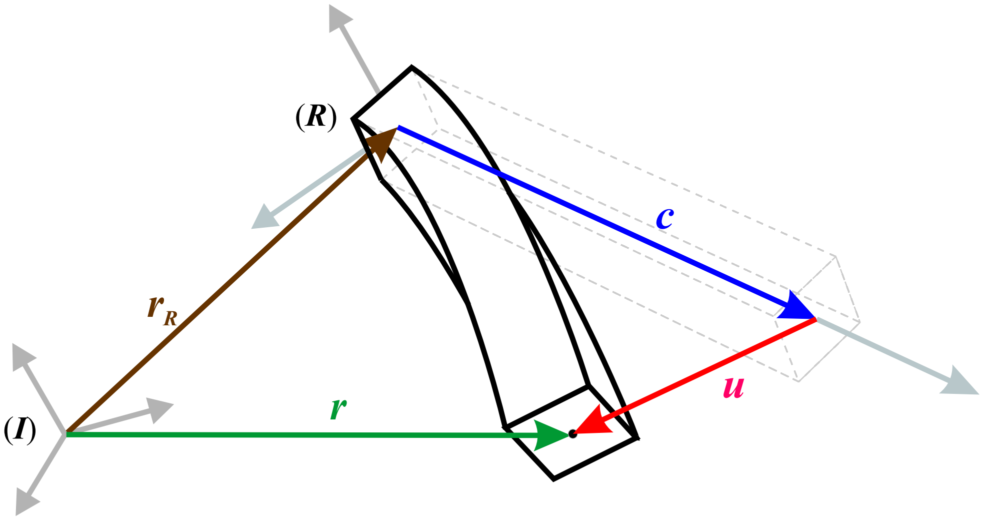

Figure 2.2: Kinematics of floating frame of reference.

In (2.1) the absolute position $\boldsymbol{r}(\boldsymbol{c},t)$ of a specific particle of a flexible body is subdivided into three parts: the position vector $\boldsymbol{r}_R(t)$ to the body's reference frame, the initial position of the body particle within the body's reference frame, i.e. the Lagrange co-ordinate $\boldsymbol{c} \neq \boldsymbol{c}(t)$, and the elastic displacement $\boldsymbol{u}(\boldsymbol{c},t)$:

$$\boldsymbol{r} = \boldsymbol{r}_R + \boldsymbol{c} + \boldsymbol{u} \; . \tag{2.1}$$

All terms in (2.1) are resolved w.r.t. the body's floating frame of reference (R). In general, left hand indices specify the reference frame w.r.t. which the quantity is resolved. This specification is only omitted for terms defined w.r.t. (R).

The vectors in (2.1) may be transformed into quantities w.r.t. the inertial frame (I) applying the rotation matrix $\boldsymbol{A}_{IR}$. Here, the information about the orientation of the body's reference frame w.r.t. the inertial system, e.g. using Cardan or Eulerian angles β_i is exploited [HGP98, Sec. 6.1]:

$$ {}_I\boldsymbol{r}_R = \boldsymbol{A}_{IR}\, \boldsymbol{r}_R\ , \qquad \boldsymbol{A}_{IR} = \boldsymbol{A}_{IR}(\beta_1, \beta_2, \beta_3)\ . \tag{2.2} $$

Since composed finite rotations are in general noncommutative, they cannot be interpreted as vector quantities. However, it can be proven that the infinitesimal rotation increment $\mathrm{d}\boldsymbol{\gamma}_R$ is a vector. Therefore, the angular velocity $\boldsymbol{\omega}_R$ of the body's reference frame may either be expressed as vectorial time derivative or may be related to the rotation matrix $\boldsymbol{A}_{IR}$. For this purpose the $\widetilde{(\ )}$-operator is defined in such a way that the identity $\boldsymbol{\omega} \times \boldsymbol{c} = \tilde{\boldsymbol{\omega}}\boldsymbol{c}$ holds:

$$ \boldsymbol{\omega}_R := \frac{\mathrm{d}\boldsymbol{\gamma}_R}{\mathrm{d}t} = \begin{pmatrix} \dot{\gamma}_1 \\ \dot{\gamma}_2 \\ \dot{\gamma}_3 \end{pmatrix} \quad \Longleftrightarrow \quad \tilde{\boldsymbol{\omega}}_R := \boldsymbol{A}_{IR}^T \dot{\boldsymbol{A}}_{IR} = \begin{pmatrix} 0 & -\dot{\gamma}_3 & \dot{\gamma}_2 \\ \dot{\gamma}_3 & 0 & -\dot{\gamma}_1 \\ -\dot{\gamma}_2 & \dot{\gamma}_1 & 0 \end{pmatrix} . \tag{2.3} $$

When deriving additional kinematic quantities, $\boldsymbol{\omega}_R$ and the angular acceleration $\boldsymbol{\alpha}_R$ of the body's reference frame have to be taken into account:

$$ \boldsymbol{v} = \tilde{\boldsymbol{\omega}}_R \boldsymbol{r} + \dot{\boldsymbol{r}} \ = \ \boldsymbol{v}_R + \tilde{\boldsymbol{\omega}}_R(\boldsymbol{c} + \boldsymbol{u}) + \dot{\boldsymbol{u}}\ , \tag{2.4} $$

$$ \boldsymbol{\alpha}_R := \dot{\boldsymbol{\omega}}_R\ , \tag{2.5} $$

$$ \boldsymbol{a} = \tilde{\boldsymbol{\omega}}_R \boldsymbol{v} + \dot{\boldsymbol{v}} \ = \ \boldsymbol{a}_R + (\tilde{\boldsymbol{\alpha}}_R + \tilde{\boldsymbol{\omega}}_R\tilde{\boldsymbol{\omega}}_R)(\boldsymbol{c} + \boldsymbol{u}) + 2\, \tilde{\boldsymbol{\omega}}_R\dot{\boldsymbol{u}} + \ddot{\boldsymbol{u}}\ . \tag{2.6} $$

The vectors $\boldsymbol{v}$ and $\boldsymbol{a}$ denote the absolute translatory velocity and acceleration of the body particle, while $\boldsymbol{v}_R$ and $\boldsymbol{a}_R$ represent the corresponding kinematic quantities for the body's reference frame.

The decomposition in (2.1) makes it possible to superimpose a large nonlinear overall motion with linearised, small elastic deformations. As long as the strains remain small, the linear description of the displacement field is consistent even if large rotations and large displacements are involved.

The advantages of the kinematic decomposition is underlined by the fact that a problem of this category requires a fully nonlinear analysis in the finite element formulation, even if the strains are small and linearly dependent on the stresses, see [Bat96, Table 6.1].

2.1.2 The Modal Approach for Displacements, Strains and Stresses

According to the Rayleigh-Ritz method, the displacement field $\boldsymbol{u}(\boldsymbol{c}, t)$ may be approximated by a finite dimensional linear combination of a priori known shape functions $\boldsymbol{\Phi}_u(\boldsymbol{c})$ and modal amplitudes $\boldsymbol{z}_u(t)$ that are functions of time [Sha98, Sec. 5.1]:

$$ \boldsymbol{u}(\boldsymbol{c}, t) = \boldsymbol{\Phi}_u(\boldsymbol{c})\ \boldsymbol{z}_u(t)\ , \qquad \boldsymbol{\Phi}_u \in \mathbb{R}^{3,n},\ \boldsymbol{z}_u \in \mathbb{R}^n\ . \tag{2.7} $$

In industrial multibody packages a range of modal data of an elastic body is provided by a finite element analysis. As a generic modelling issue qualified modes have to be selected that are capable to reflect the mechanical properties of the flexible body properly with respect to the given modelling task. That way, a set of n selected modes, i.e. n displacement fields, is obtained in discretised form as $\boldsymbol{\Phi}_u(\boldsymbol{c}_k)$ for every finite element node k, located at the position $\boldsymbol{c}_k$.

Once a representation of the displacement field $\boldsymbol{u}(\boldsymbol{c}, t)$ is given, the strain field $\boldsymbol{\varepsilon}(\boldsymbol{c}, t)$ follows from applying the differential displacement-strain operator ∇_u:

$$\boldsymbol{\varepsilon}(\boldsymbol{c}, t) = \nabla_u \boldsymbol{u}(\boldsymbol{c}, t) = \boldsymbol{B}_u(\boldsymbol{c})\ \boldsymbol{z}_u(t)\ , \qquad \boldsymbol{\varepsilon} \in \mathbb{R}^6, \tag{2.8a}$$

$$\text{with} \qquad \boldsymbol{B}_u(\boldsymbol{c}) := \nabla_u \boldsymbol{\Phi}_u\ , \qquad \boldsymbol{B}_u \in \mathbb{R}^{6,n},$$

$$\nabla_u := \begin{pmatrix} \frac{\partial}{\partial x_1} & 0 & 0 & \frac{\partial}{\partial x_2} & 0 & \frac{\partial}{\partial x_3} \\ 0 & \frac{\partial}{\partial x_2} & 0 & \frac{\partial}{\partial x_1} & \frac{\partial}{\partial x_3} & 0 \\ 0 & 0 & \frac{\partial}{\partial x_3} & 0 & \frac{\partial}{\partial x_2} & \frac{\partial}{\partial x_1} \end{pmatrix}^T . \tag{2.8b}$$

The six independent elements of the geometric quantity strain, actually a symmetric tensor of rank two, are here organised in vector form:

$$\boldsymbol{\varepsilon} = (\varepsilon_{11},\ \varepsilon_{22},\ \varepsilon_{33},\ 2\varepsilon_{12},\ 2\varepsilon_{23},\ 2\varepsilon_{13})^T\ .$$

Since linear relations between displacements and strains are assumed in (2.8a) to (2.8b), this evaluation is often referred to as geometric linearisation. The matrix $\boldsymbol{B}_u$ contains the modal shape functions used to approximate the strain field.

For reasons to expose in Sec. 2.1.3 below, the consideration of stress stiffening effects in the equations of motion requires a nonlinear analysis of the strain field. The additional, nonlinear strain $\bar{\boldsymbol{\varepsilon}}(\boldsymbol{c}, t)$ is obtained by the differential operation with $\bar{\nabla}_u$, see [Lov44, Ch. I App.]:

$$\bar{\boldsymbol{\varepsilon}}(\boldsymbol{c}, t) = \frac{1}{2}\bar{\nabla}_u(\boldsymbol{u}, t)\ \boldsymbol{u}(\boldsymbol{c}, t)\ , \tag{2.8c}$$

$$\bar{\nabla}_u(\boldsymbol{u}, t) := \begin{pmatrix} \frac{\partial u_1}{\partial x_1}\frac{\partial}{\partial x_1} & \frac{\partial u_2}{\partial x_1}\frac{\partial}{\partial x_1} & \frac{\partial u_3}{\partial x_1}\frac{\partial}{\partial x_1} \\ \frac{\partial u_1}{\partial x_2}\frac{\partial}{\partial x_2} & \frac{\partial u_2}{\partial x_2}\frac{\partial}{\partial x_2} & \frac{\partial u_3}{\partial x_2}\frac{\partial}{\partial x_2} \\ \frac{\partial u_1}{\partial x_3}\frac{\partial}{\partial x_3} & \frac{\partial u_2}{\partial x_3}\frac{\partial}{\partial x_3} & \frac{\partial u_3}{\partial x_3}\frac{\partial}{\partial x_3} \\ \frac{\partial u_1}{\partial x_1}\frac{\partial}{\partial x_2} + \frac{\partial u_1}{\partial x_2}\frac{\partial}{\partial x_1} & \frac{\partial u_2}{\partial x_1}\frac{\partial}{\partial x_2} + \frac{\partial u_2}{\partial x_2}\frac{\partial}{\partial x_1} & \frac{\partial u_3}{\partial x_1}\frac{\partial}{\partial x_2} + \frac{\partial u_3}{\partial x_2}\frac{\partial}{\partial x_1} \\ \frac{\partial u_1}{\partial x_2}\frac{\partial}{\partial x_3} + \frac{\partial u_1}{\partial x_3}\frac{\partial}{\partial x_2} & \frac{\partial u_2}{\partial x_2}\frac{\partial}{\partial x_3} + \frac{\partial u_2}{\partial x_3}\frac{\partial}{\partial x_2} & \frac{\partial u_3}{\partial x_2}\frac{\partial}{\partial x_3} + \frac{\partial u_3}{\partial x_3}\frac{\partial}{\partial x_2} \\ \frac{\partial u_1}{\partial x_3}\frac{\partial}{\partial x_1} + \frac{\partial u_1}{\partial x_1}\frac{\partial}{\partial x_3} & \frac{\partial u_2}{\partial x_3}\frac{\partial}{\partial x_1} + \frac{\partial u_2}{\partial x_1}\frac{\partial}{\partial x_3} & \frac{\partial u_3}{\partial x_3}\frac{\partial}{\partial x_1} + \frac{\partial u_3}{\partial x_1}\frac{\partial}{\partial x_3} \end{pmatrix} . \tag{2.8d}$$

Since the nonlinear strain is again a geometric quantity, stress stiffening is frequently addressed as geometric stiffening as well. The added up strains read:

$$\breve{\boldsymbol{\varepsilon}}(\boldsymbol{c}, t) = \boldsymbol{\varepsilon} + \bar{\boldsymbol{\varepsilon}} \tag{2.8e}$$

The generalisation of Hooke's law, which states the stress components to be linear functions of the strain elements, leads to the definition of the elasticity tensor $\boldsymbol{H}_c$, which will be discussed in detail in Sec. 2.2:

$$\begin{aligned}\breve{\boldsymbol{\sigma}}(\boldsymbol{c},t) &= \boldsymbol{\sigma}_0 + \boldsymbol{\sigma} + \bar{\boldsymbol{\sigma}} = \boldsymbol{\sigma}_0 + \boldsymbol{H}_c(\boldsymbol{\varepsilon} + \bar{\boldsymbol{\varepsilon}}) \ , \qquad \boldsymbol{H}_c \in \mathbb{R}^{6,6}, \\ &= \left(\breve{\sigma}_{11},\ \breve{\sigma}_{22},\ \breve{\sigma}_{33},\ \breve{\sigma}_{12},\ \breve{\sigma}_{23},\ \breve{\sigma}_{13}\right)^T \ .\end{aligned} \tag{2.9}$$

The term $\boldsymbol{\sigma}_0$ in (2.9) denotes large initial stresses, which are related to zero strains. That way, it is aimed to incorporate geometric stiffening (or softening) effects. A frequently studied example is a slender beam under large axial loads. Although the axial stretching itself is often out of interest, the dynamic bending characteristics are dramatically influenced by the axial loads [SW99, Sec. 4.3].

Eq. (2.7) applies for a general, three-dimensional continuum. In technical applications, however, it is best practice to refer to deformation hypotheses tailored for structures with a specific geometric shape. The Euler-Bernoulli beam may be considered as a typical example. Here, a cross-section initially normal to the beam axis is assumed to remain normal to the axis even in the deformed configuration. As a consequence the displacements only depend on one scalar Lagrange co-ordinate c_1, the position on the axis the cross-section is assigned to.

The beam deformation can then be described by the displacements of the beam's axis $\bar{\boldsymbol{u}} = (\bar{u}_1, \bar{u}_2, \bar{u}_3)^T$, their partial derivatives w.r.t. c_1, denoted by $(\ )'$ and the torsion angle β_1 [BP92, Sec. 2.1]:

$$\boldsymbol{u}(\boldsymbol{c},t) = \begin{pmatrix} \bar{u}_1(c_1,t) \\ \bar{u}_2(c_1,t) \\ \bar{u}_3(c_1,t) \end{pmatrix} + \tilde{\boldsymbol{\varphi}}(c_1,t) \begin{pmatrix} 0 \\ c_2 \\ c_3 \end{pmatrix} \quad \text{with} \quad \boldsymbol{\varphi}(c_1,t) = \begin{pmatrix} \beta_1(c_1,t) \\ -\bar{u}_3'(c_1,t) \\ \bar{u}_2'(c_1,t) \end{pmatrix} . \tag{2.10}$$

Eq. (2.10) reflects the classical beam theory combining four degrees of freedom: axial stretching, torsion and bending in two planes as visualised in Fig. 2.3. The rotations may be interpreted as vectorial quantities, since they are assumed to be small. This description is used in Sec. 3.1.2 in order to quantify the influence of piezo-ceramic devices on the mechanical field.

A Rayleigh-Ritz approximation of the Euler-Bernoulli beam has to consider both, the modal axis displacements $\boldsymbol{\Phi}_u(c_1)$, which may look like the example in Fig. 4.4, and the modal cross section rotations $\boldsymbol{\Psi}_u(c_1)$:

$$\boldsymbol{u}(\boldsymbol{c},t) = \left[\boldsymbol{\Phi}_u(c_1) - \widetilde{\begin{pmatrix} 0 \\ c_2 \\ c_3 \end{pmatrix}} \boldsymbol{\Psi}_u(c_1) \right] \boldsymbol{z}_u(t) \ , \quad \text{with} \ \left\{ \begin{array}{l} \bar{\boldsymbol{u}}(c_1,t) = \boldsymbol{\Phi}_u(c_1)\, \boldsymbol{z}_u(t) \ , \\ \boldsymbol{\varphi}(c_1,t) = \boldsymbol{\Psi}_u(c_1)\, \boldsymbol{z}_u(t) \ , \\ \boldsymbol{\Phi}_u, \boldsymbol{\Psi}_u \in \mathbb{R}^{3,n} \ , \ \boldsymbol{z}_u \in \mathbb{R}^n \ . \end{array} \right. \tag{2.11}$$

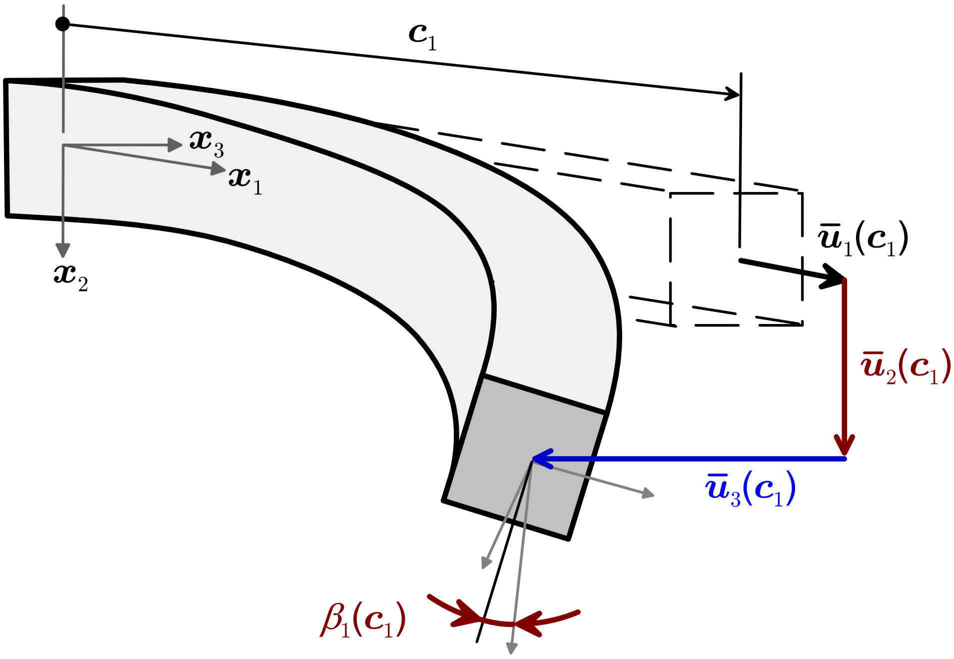

Figure 2.3: Sketch of a deflected beam cross section with four degrees of freedom.

The beam example is supposed to point out how internal deformation constraints can be formulated and implemented in an implicit way. Corresponding representations can be found for plates and shells according to the Kirchhoff or Reissner-Mindlin assumptions and are used in Sec. 3.1.3.

In fact, constraints can improve the numerical efficiency substantially, since degrees of freedom that only contribute a very small amount of deformation energy are neglected. Furthermore, ill-conditioned equations are avoided that may occur if large stiffnesses are used instead of deformation constraints.

2.1.3 Hamilton's Principle

Hamilton's principle states that an arbitrary mechanical system moves in such a way that the following definite integral becomes stationary for arbitrary consistent variations of the system configuration:

$$\delta \int_{t_1}^{t_2} (T - U + W)\,\mathrm{d}t = 0\,, \tag{2.12}$$

where T denotes the kinetic energy, U is the deformation energy and W represents the work of the external forces $\boldsymbol{f}$, acting on a volume or a surface element dV or dB:

$$T = \frac{1}{2}\int_m \boldsymbol{v}^T\boldsymbol{v}\,\mathrm{d}m\,, \qquad U = \int_V \left[\frac{1}{2}(\boldsymbol{\sigma}+\bar{\boldsymbol{\sigma}})^T\breve{\boldsymbol{\varepsilon}} + \boldsymbol{\sigma}_0^T\breve{\boldsymbol{\varepsilon}}\right]\,\mathrm{d}V$$

$$\text{and} \qquad W = \int_V \boldsymbol{f}_V^T\boldsymbol{r}\,\mathrm{d}V + \oint_B \boldsymbol{f}_B^T\boldsymbol{r}\,\mathrm{d}B\,.$$

Eq. (2.12) presumes that in particular the deformation energy and the virtual work of the external forces are of monogenic nature, i.e. can be derived out of a scalar function. They do not need to be conservative [Lan70, Ch. V].

If the external forces are not monogenic, Eq. (2.12) must be reformulated [RWW93, Sec. 4.2.3]:

$$\int_{t_1}^{t_2} (\delta T - \delta U + W_{virt})\,\mathrm{d}t = 0 \;, \tag{2.13a}$$

$$\text{with} \qquad W_{virt} = \int_V \boldsymbol{f}_V^T\,\delta\boldsymbol{r}\;\mathrm{d}V + \oint_B \boldsymbol{f}_B^T\,\delta\boldsymbol{r}\;\mathrm{d}B \;. \tag{2.13b}$$

Compared to (2.12), Eq. (2.13a) has lost its character as a variational principle, but the variational equation formulated in terms of the virtual position change $\delta\boldsymbol{r}$ still remains valid, see [Tay03, Ch. 2, 3] and [FLS64, Ch. 19] for further discussion.

The variation of the kinetic energy in (2.13) can be rewritten as a function of the virtual displacements recalling the facts that the variation vanishes at the limits t_1 and t_2 and the inner vector product is invariant regarding co-ordinate transformations:

$$\int\limits_{t_1}^{t_2} \delta T\;\mathrm{d}t = \int\limits_{t_1}^{t_2}\int_V \delta_I\dot{\boldsymbol{r}}^T{}_I\dot{\boldsymbol{r}}\;\varrho\mathrm{d}V\,\mathrm{d}t = \underbrace{\left[\int_V \delta_I\boldsymbol{r}^T{}_I\dot{\boldsymbol{r}}\;\varrho\mathrm{d}V\right]_{t_1}^{t_2}}_{0} - \int\limits_{t_1}^{t_2}\int_V \delta\boldsymbol{r}^T\boldsymbol{a}\;\varrho\mathrm{d}V\,\mathrm{d}t \;. \tag{2.13c}$$

Substituting the stresses according to (2.9) the variation of U gets the form:

$$\delta U = \int_V (\boldsymbol{\varepsilon}^T\boldsymbol{H}_c^T\,\delta\boldsymbol{\varepsilon} \;+\; \boldsymbol{\sigma}_0^T\,\delta\bar{\boldsymbol{\varepsilon}} \;+ 2\underbrace{\boldsymbol{\varepsilon}^T\boldsymbol{H}_c^T\,\delta\bar{\boldsymbol{\varepsilon}}}_{\mathcal{O}(||\boldsymbol{\varepsilon}||^3)} + \underbrace{\bar{\boldsymbol{\varepsilon}}^T\boldsymbol{H}_c^T\,\delta\bar{\boldsymbol{\varepsilon}}}_{\mathcal{O}(||\boldsymbol{\varepsilon}||^4)} + \underbrace{\boldsymbol{\sigma}_0^T\delta\boldsymbol{\varepsilon}}_{\equiv 0})\;\mathrm{d}V \;, \tag{2.13d}$$

$$\approx \int_V (\boldsymbol{\varepsilon}^T\boldsymbol{H}_c^T\,\delta\boldsymbol{\varepsilon} \;+\; \boldsymbol{\sigma}_0^T\,\delta\bar{\boldsymbol{\varepsilon}})\;\mathrm{d}V \;, \tag{2.13e}$$

where the terms of third and forth order, $\mathcal{O}(||\boldsymbol{\varepsilon}||^3$ and $\mathcal{O}(||\boldsymbol{\varepsilon}||^4)$, are neglected. The initial stress $\boldsymbol{\sigma}_0$ is presumed to be large, i.e. of order zero. Consequently, the product $\boldsymbol{\sigma}_0^T\boldsymbol{\varepsilon}$ is of first order. Since small displacements are related to large forces if specified by a first order potential, the assumed equilibrium of the large forces would be disturbed even by small displacements. This contradiction can only be resolved by the identity $\boldsymbol{\sigma}_0^T\delta\boldsymbol{\varepsilon} \equiv 0$, which is a physically motivated conclusion, see [BP92, Sec. 4.5.4.4.1], [Was82, Ch. 5] and [WS91].

It can be concluded that there are two terms contributing significantly to the deformation potential. The first order strains $\boldsymbol{\varepsilon}$ and stresses $\boldsymbol{\sigma}$ result from the classical linear approximation of the displacement field. The geometric stiffness terms, represented by the product $\boldsymbol{\sigma}_0^T\delta\bar{\boldsymbol{\varepsilon}}$, play a special but important role and have to be evaluated separately. KNOTHE and WESSELS [KW92, Ch. 10] for instance express them as linear functions of specific relevant loads such as the axial force concerning a beam structure.

Since the geometric stiffness terms are to be evaluated separately and independently, it is not necessary to consider them as distributed field quantities. In what follows only the linear strain field approximation (2.8a) and the related first order stresses will be used to describe distributed mechanical properties.

The substitution of the virtual terms in (2.13) and the application the Fundamental lemma of the variational approach yield the mechanical field equations in weak form:

$$\int_V \left[-\varrho \delta \boldsymbol{r}^T \boldsymbol{a} - \delta \boldsymbol{\varepsilon}^T \boldsymbol{\sigma} - \delta \bar{\boldsymbol{\varepsilon}}^T \boldsymbol{\sigma}_0 + \delta \boldsymbol{r}^T \boldsymbol{f}_V\right] \,\mathrm{d}V + \oint_B \delta \boldsymbol{r}^T \boldsymbol{f}_B \,\mathrm{d}B = 0\ . \tag{2.14}$$

2.1.4 The Equations of Motion of an Elastic Body

All virtual quantities in (2.14) are further evaluated according to the kinematic approach in Sec. 2.1.1 and Sec. 2.1.2. Concerning the virtual displacement $\delta \boldsymbol{r}$, the eqs. (2.1) and (2.7) are employed. However, the variation of the angular vector $\delta \boldsymbol{\gamma}_R$, which may be defined by means of (2.3) and describes the virtual, infinitesimal rotation of the floating frame of reference w.r.t. the inertial system has to be taken into account [Was82, (5.141)]:

$$\delta \boldsymbol{r} = \delta \boldsymbol{r}_R + \delta \tilde{\boldsymbol{\gamma}}_R\, \boldsymbol{r}_R + \delta \tilde{\boldsymbol{\gamma}}_R \left(\boldsymbol{c} + \boldsymbol{\Phi}_u\, \boldsymbol{z}_u\right) + \boldsymbol{\Phi}_u\, \delta \boldsymbol{z}_u\ . \tag{2.15}$$

Eq. (2.15) may be rearranged to

$$\delta \boldsymbol{r} = \left[\boldsymbol{I}_3 \vdots - \widetilde{(\boldsymbol{c} + \boldsymbol{\Phi}_u \boldsymbol{z}_u)} \vdots \boldsymbol{\Phi}_u\right] \begin{pmatrix} \delta \boldsymbol{r}_R + \delta \tilde{\boldsymbol{\gamma}}_R\, \boldsymbol{r}_R \\ \delta \boldsymbol{\gamma}_R \\ \delta \boldsymbol{z}_u \end{pmatrix} . \tag{2.16}$$

The acceleration in (2.6) is written in similar form:

$$\boldsymbol{a} = \left[\boldsymbol{I}_3 \vdots - \widetilde{(\boldsymbol{c} + \boldsymbol{\Phi}_u \boldsymbol{z}_u)} \vdots \boldsymbol{\Phi}_u\right] \boldsymbol{b} \ + \ \tilde{\boldsymbol{\omega}}_R \tilde{\boldsymbol{\omega}}_R (\boldsymbol{c} + \boldsymbol{\Phi}_u \boldsymbol{z}_u) + 2\, \tilde{\boldsymbol{\omega}}_r \boldsymbol{\Phi}_u \dot{\boldsymbol{z}}_u\ , \tag{2.17}$$

$$\boldsymbol{b} := \left(\boldsymbol{a}_R^T \ \boldsymbol{\alpha}_R^T \ \ddot{\boldsymbol{z}}_u^T\right)^T\ , \tag{2.18}$$

where $\boldsymbol{b}$ denotes the generalised acceleration vector of the flexible body.

The virtual deformation energy in (2.14) is expressed analogously. In doing so, the geometric stiffness terms are approximated as quadratic form depending on the large initial stresses:

$$\delta\boldsymbol{\varepsilon}^T\boldsymbol{\sigma} + \delta\bar{\boldsymbol{\varepsilon}}^T\boldsymbol{\sigma}_0 \approx \begin{pmatrix} \delta\boldsymbol{r}_R + \delta\tilde{\boldsymbol{\gamma}}_R\,\boldsymbol{r}_R \\ \delta\boldsymbol{\gamma}_R \\ \delta\boldsymbol{z}_u \end{pmatrix}^T \begin{pmatrix} \boldsymbol{0} \\ \boldsymbol{0} \\ \bar{\boldsymbol{K}}(\boldsymbol{\sigma}_0)\,\boldsymbol{z}_u + \boldsymbol{B}_u^T\boldsymbol{H}_c\boldsymbol{B}_u\,\boldsymbol{z}_u \end{pmatrix} . \tag{2.19}$$

With this background it is possible to reformulate (2.14) in order to evaluate the unknown generalised acceleration vector $\boldsymbol{b}$ from (2.18) in such a way, that the volume integration can be performed in a separate step in advance of the time integration. The abbreviations in Tab. 2.1 allow to give the equations of motion a convenient form as a system of nonlinear ordinary differential equations in time:

$$\boldsymbol{M}\begin{pmatrix} \boldsymbol{a}_R \\ \boldsymbol{\alpha}_R \\ \ddot{\boldsymbol{z}}_u \end{pmatrix} = \boldsymbol{h}_{gcc} + \boldsymbol{h}_f + \boldsymbol{h}_i\ . \tag{2.20}$$

The detailed definition of the volume integrals and the procedure how to generate them using available finite element data is given by SCHWERTASSEK and WALLRAPP in [SW99, Ch. 6]. An analytical derivation of the volume integrals for selected body models such as Rayleigh beam, Timoshenko beam and circular ring may be found in [BP92, Sec. 4.5].

Eq. (2.20) describes the motion of an unconstrained, single elastic body that undergoes large reference displacements. If, for the sake of demonstration, the body is assumed to be rigid, those rows and columns in (2.20) vanish that are associated with the generalised elastic acceleration $\ddot{\boldsymbol{z}}_u$. Since (2.20) is formulated in terms of the translatory and angular acceleration in $\boldsymbol{b}$, such reduction leads to the classical Newton-Euler equations of a rigid body. Therefore, SHABANA calls (2.20) the generalised Newton-Euler equations of an unconstrained deformable body in [Sha98, Sec. 5.5] and qualifies this formulation to be especially suited for the evaluation by a recursive multibody formalism.

2.1.5 Topology

The paradigm of multibody dynamics is founded on the idea that each component of a real mechanical system can be idealised by one of the following basic modelling elements:

Bodies: A body is the only modelling element to which inertia is assigned.

Joints: The kinematic interconnections of the bodies are provided by joints. A joint is uniquely assigned to a corresponding body and specifies the directions in which the body is free to move. Joints may be seen as the idealisation of real construction components like hinges or

$\boldsymbol{M}$
The mass matrix
$\boldsymbol{M} = \int\limits_V \begin{pmatrix} \boldsymbol{I}_3 & \vdots & -(\widetilde{\boldsymbol{c}+\boldsymbol{\Phi}_u\boldsymbol{z}_u}) & \vdots & \boldsymbol{\Phi}_u \\ & \vdots & (\widetilde{\boldsymbol{c}+\boldsymbol{\Phi}_u\boldsymbol{z}_u})^T(\widetilde{\boldsymbol{c}+\boldsymbol{\Phi}_u\boldsymbol{z}_u}) & \vdots & -(\widetilde{\boldsymbol{c}+\boldsymbol{\Phi}_u\boldsymbol{z}_u})^T\boldsymbol{\Phi}_u \\ \text{sym.} & \vdots & & \vdots & \boldsymbol{\Phi}_u^T\boldsymbol{\Phi}_u \end{pmatrix} \varrho \mathrm{d}V = \begin{pmatrix} \boldsymbol{M}_{aa} & \boldsymbol{M}_{a\alpha} & \boldsymbol{M}_{au} \\ & \boldsymbol{M}_{\alpha\alpha} & \boldsymbol{M}_{\alpha u} \\ \text{sym.} & & \boldsymbol{M}_{uu} \end{pmatrix}$
The sub-matrices specify the inertia coupling between acceleration terms due to translatory, angular and elastic motion, denoted by $(\ )_a$, $(\ )_\alpha$ and $(\ )_u$.

$\boldsymbol{h}_{gcc}$
The vector of gyroscopic, centripetal and Coriolis forces
$\boldsymbol{h}_{gcc} = \int_V \begin{pmatrix} 2\,\tilde{\boldsymbol{\omega}}_R\,\boldsymbol{\Phi}_u\dot{\boldsymbol{z}}_u & + & \tilde{\boldsymbol{\omega}}_R\tilde{\boldsymbol{\omega}}_R(\boldsymbol{c}+\boldsymbol{\Phi}_u\boldsymbol{z}_u) \\ -2\,(\widetilde{\boldsymbol{c}+\boldsymbol{\Phi}_u\boldsymbol{z}_u})^T\tilde{\boldsymbol{\omega}}_R\,\boldsymbol{\Phi}_u\dot{\boldsymbol{z}}_u & - & (\widetilde{\boldsymbol{c}+\boldsymbol{\Phi}_u\boldsymbol{z}_u})^T\,\tilde{\boldsymbol{\omega}}_R\tilde{\boldsymbol{\omega}}_R\,(\widetilde{\boldsymbol{c}+\boldsymbol{\Phi}_u\boldsymbol{z}_u}) \\ 2\,\boldsymbol{\Phi}_u^T\,\tilde{\boldsymbol{\omega}}_R\,\boldsymbol{\Phi}_u\dot{\boldsymbol{z}}_u & + & \boldsymbol{\Phi}_u^T\,\tilde{\boldsymbol{\omega}}_R\tilde{\boldsymbol{\omega}}_R\,(\boldsymbol{c}+\boldsymbol{\Phi}_u\boldsymbol{z}_u) \end{pmatrix} \varrho \mathrm{d}V$

$\boldsymbol{K}_{uu}$	$\boldsymbol{K}_\sigma$
The stiffness matrix	The geometric stiffness matrix
$\boldsymbol{K}_{uu} = \int_V \boldsymbol{B}_u^T\boldsymbol{H}_c\boldsymbol{B}_u\ \mathrm{d}V = \boldsymbol{K}_{uu}^T$	$\boldsymbol{K}_\sigma(\boldsymbol{\sigma}_0) = \int_V \bar{\boldsymbol{K}}(\boldsymbol{\sigma}_0)\ \mathrm{d}V = \boldsymbol{K}_\sigma^T$

$\boldsymbol{D}_{uu}$	$\boldsymbol{h}_i$
The damping matrix	The vector of the internal forces
$\boldsymbol{D}_{uu} := \gamma\boldsymbol{M}_{uu} + \beta\boldsymbol{K}_{uu}$ Damping effects are approximated according to Raleigh's approach with two parameters γ and β.	$\boldsymbol{h}_i = \begin{pmatrix} \boldsymbol{0} \\ \boldsymbol{0} \\ -\boldsymbol{D}_{uu}\dot{\boldsymbol{z}}_u - \boldsymbol{K}_{uu}\boldsymbol{z}_u - \boldsymbol{K}_\sigma\boldsymbol{z}_u \end{pmatrix}$

$\boldsymbol{h}_f$
The vector of the external forces
$\boldsymbol{h}_f := \int_V \begin{pmatrix} \boldsymbol{I}_3 \\ -(\widetilde{\boldsymbol{c}+\boldsymbol{\Phi}_u\boldsymbol{z}_u})^T \\ \boldsymbol{\Phi}_u^T \end{pmatrix} \boldsymbol{f}_V\ \mathrm{d}V + \int_B \begin{pmatrix} \boldsymbol{I}_3 \\ -(\widetilde{\boldsymbol{c}+\boldsymbol{\Phi}_u\boldsymbol{z}_u})^T \\ \boldsymbol{\Phi}_u^T \end{pmatrix} \boldsymbol{f}_B\ \mathrm{d}B$
Torques are represented by the equivalent couple for forces.

Table 2.1: Definition of abbreviations and volume integrals for terms of the equations of motion of an elastic body.

bearings. However, a joint with six degrees of freedom that has no material counterpart is also possible and stands for the fact that the body is free to move in any direction.

Force elements: All kinds of active forces are modelled as force elements. Here and in what follows, the term force is used in a general meaning that includes torques as well. Springs, dampers, any kind of actuators are represented by force elements which may have their own inner state variables to describe nonmechanical elements like electrical or hydraulic drives.

Constraints: A constraint represents passive forces, which are defined in such a way that additional kinematic conditions are maintained. The incorporation of constraint equations will be discussed at the end of this section, so that the preceding presentation is restricted to unconstrained multibody systems.

In analytical multibody dynamics it is assumed that each body, denoted by $(\ )^{(i)}$, has one unique predecessor $(\ )^{(p)}$, $p = p(i)$, but it may have an arbitrary number of successors $(\ )^{(s)}$, $s = s(i)$, see Fig. 2.4.

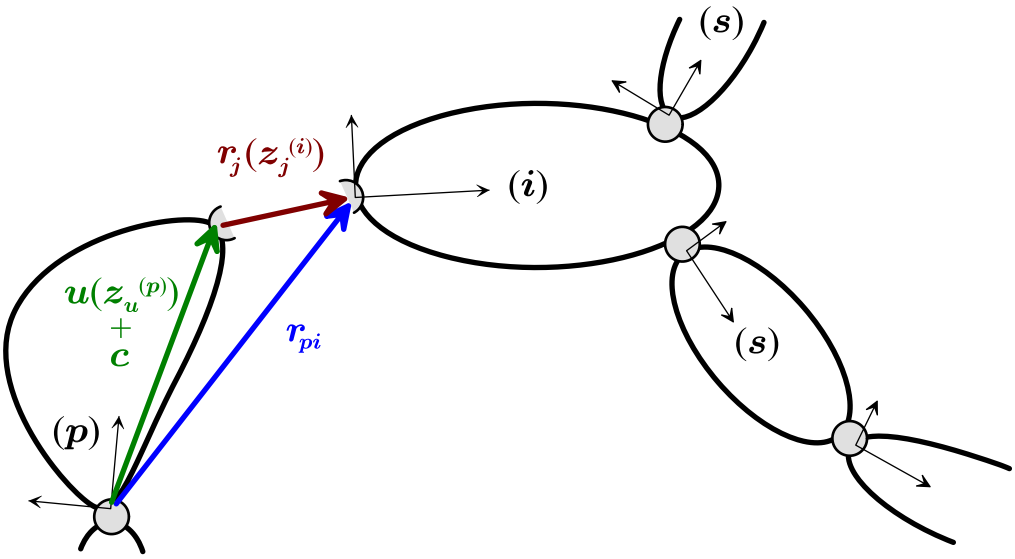

Figure 2.4: Body (i) with unique predecessor (p) and multiple successors (s)

The origin of the body's reference frame is defined by the point where the joint is attached to the corresponding body. The first joint connects the first body to the inertial frame of reference, or more generally to Body $(\ )^{(0)}$ with prescribed motion. Hence, a multibody system can be built up recursively depicting a chain- or a tree-structure.

Furthermore, a vector $\boldsymbol{y}$ is defined as a minimum set of generalised co-ordinates for the whole multibody system. It turns out to be advantageous to relate $\boldsymbol{y}$, and analogously its derivatives $\dot{\boldsymbol{y}}$ and $\ddot{\boldsymbol{y}}$, to the local degrees of freedom. More precisely, the motion of the origin of body $(\ )^{(i)}$ relative to the origin of body $(\ )^{(p)}$ w.r.t. reference frame p is addressed here and denoted by the indices ${}_p(\ )_{pi}$. This kinematics involve the relative degrees of freedom of joints $(\ )_j$ and elastic deformations $(\;)_u$:

$$\boldsymbol{y} = \begin{pmatrix} \vdots \\ \boldsymbol{z}^{(p)}_{\dots} \\ \boldsymbol{z}^{(i)}_j \\ \boldsymbol{z}^{(i)}_u \\ \boldsymbol{z}^{(s)}_{\dots} \\ \vdots \end{pmatrix} , \quad {}_p\boldsymbol{r}_{pi} \;=\; {}_p\boldsymbol{r}_{pi}(\boldsymbol{z}^{(i)}_j, \boldsymbol{z}^{(p)}_u) , \quad \boldsymbol{A}_{ip} \;=\; \boldsymbol{A}_{ip}(\boldsymbol{z}^{(i)}_j, \boldsymbol{z}^{(p)}_u) . \tag{2.21}$$

The formal representation of the equations of motion describing the complete multibody system is obtained by the following summation, where Eq. (2.20) is rewritten for every body $(\;)^{(i)}$ of the system and $\boldsymbol{J}^{(i)}$ denotes the global Jacobian of $(\;)^{(i)}$, see [Sch97]:

$$\sum_{(i)} \left[\boldsymbol{J}^{(i)}\right]^T \left[\boldsymbol{M}^{(i)}\boldsymbol{b}^{(i)} - \boldsymbol{h}^{(i)}_{gcc} - \boldsymbol{h}^{(i)}_i - \boldsymbol{h}^{(i)}_f\right] = \boldsymbol{0} \quad \text{with} \quad \boldsymbol{J}^{(i)} := \frac{\partial \boldsymbol{b}^{(i)}}{\partial \ddot{\boldsymbol{y}}} , \tag{2.22a}$$

$$\Longrightarrow \qquad \bar{\boldsymbol{M}}(\boldsymbol{y}, t)\, \ddot{\boldsymbol{y}} - \bar{\boldsymbol{h}}(\boldsymbol{y}, \dot{\boldsymbol{y}}, t) = \boldsymbol{0} \tag{2.22b}$$

$\bar{\boldsymbol{M}}(\boldsymbol{y}, t)$ represents the symmetric inertia matrix of the complete system. $\bar{\boldsymbol{h}}(\boldsymbol{y}, \dot{\boldsymbol{y}}, t)$ includes the generalised Coriolis forces as well as all generalised applied forces.

Since the equations of motion are highly nonlinear, the mostly preferred analysis method is numerical time integration. For stability reasons an implicit formulation of time integration is today's state-of-the-art. Therefore it may make sense to evaluate the mechanical system implicitly, too.

A numerical formalism which is organised accordingly was introduced by EICHBERGER in [Eic93] and is called the residual formalism. The equations of motion are not only analysed numerically w.r.t. a given state on the position and velocity level with the known vectors $\boldsymbol{y}$ and $\dot{\boldsymbol{y}}$, but also the second time derivative of the generalised co-ordinate vector $\ddot{\boldsymbol{y}}$ is employed within the evaluation. If the vector set $\boldsymbol{y}$, $\dot{\boldsymbol{y}}$ and $\ddot{\boldsymbol{y}}$ turns out to be consistent w.r.t. the equations of motion, the desired solution of (2.22b) has been found. If not, the vector set $\boldsymbol{y}$, $\dot{\boldsymbol{y}}$ and $\ddot{\boldsymbol{y}}$ is iteratively corrected until the equations of motion are satisfied.

However, the most important characteristic of this formalism consists of the generation of the equations of motion in a resolved form. The formalism does not assemble and solve (2.22b), but separately analyses (2.20) for each body$(\;)^{(i)}$ in a recursive evaluation process, which is organised in three steps:

Step 1: All kinematic quantities can be calculated step by step in a forward recursion loop beginning with Body $(\;)^{(0)}$. Eq. (2.23a) states the relations for the motion of body $(\;)^{(i)}$ w.r.t. its own reference frame, denoted by ${}_{i}(\;)_{oi}$ [BP92, Sec. 4.2]:

$$
\begin{aligned}
{}_{i}\boldsymbol{r}_{oi} &= \sum_{l=1}^{i} \boldsymbol{A}_{ip}\,{}_{p}\boldsymbol{r}_{pl}\,, \qquad p = p(l)\,, \qquad {}_{i}\boldsymbol{\omega}_{oi} = \sum_{l=1}^{i} \boldsymbol{A}_{il}\,{}_{l}\boldsymbol{\omega}_{pl}\,, \\
{}_{i}\boldsymbol{v}_{oi} &= \sum_{l=1}^{i} \boldsymbol{A}_{ip}\,\left({}_{p}\dot{\boldsymbol{r}}_{pl} + {}_{p}\tilde{\boldsymbol{\omega}}_{op}\,{}_{p}\boldsymbol{r}_{pl}\right), \qquad {}_{i}\boldsymbol{\alpha}_{oi} = \sum_{l=1}^{i} \boldsymbol{A}_{il}\big({}_{l}\dot{\boldsymbol{\omega}}_{pl} + {}_{l}\tilde{\boldsymbol{\omega}}_{ol}\,{}_{l}\boldsymbol{\omega}_{pl}\big)\,, \qquad (2.23a) \\
{}_{i}\boldsymbol{a}_{oi} &= \sum_{l=1}^{i} \boldsymbol{A}_{ip}\,\left[({}_{p}\ddot{\boldsymbol{r}}_{pl} + ({}_{p}\ddot{\tilde{\boldsymbol{\omega}}}_{op} + {}_{p}\tilde{\boldsymbol{\omega}}_{op}\;{}_{p}\tilde{\boldsymbol{\omega}}_{op})_{p}\boldsymbol{r}_{pl} + 2\,{}_{p}\tilde{\boldsymbol{\omega}}_{op}\,{}_{p}\dot{\boldsymbol{r}}_{pl}\right]\,.
\end{aligned}
$$

Step 2: The evaluation of the force elements.

Step 3: Then, the dynamic analysis is performed, which is also organised recursively but going backwards starting with the terminal body of the chain. The single body $(\;)^{(i)}$ is virtually cut off the system. All cuts are represented by the equivalent cutting forces, which are introduced into the vector $\boldsymbol{h}_{f}^{(i)}$ of (2.20), see Fig. 2.5.

In order to separate those forces (including torques) that are associated to the body's joint $\boldsymbol{h}_{fj}^{(i)}$, the force vector $\boldsymbol{h}_{f}^{(i)}$ is split in the following manner:

$$
\boldsymbol{h}_{f}^{(i)} = \boldsymbol{h}_{fe}^{(i)} + \boldsymbol{h}_{fj}^{(i)}\,. \qquad (2.23b)
$$

$\boldsymbol{h}_{fj}^{(i)}$ can be evaluated by means of (2.23c). Since the terminal body has no successor, the sum

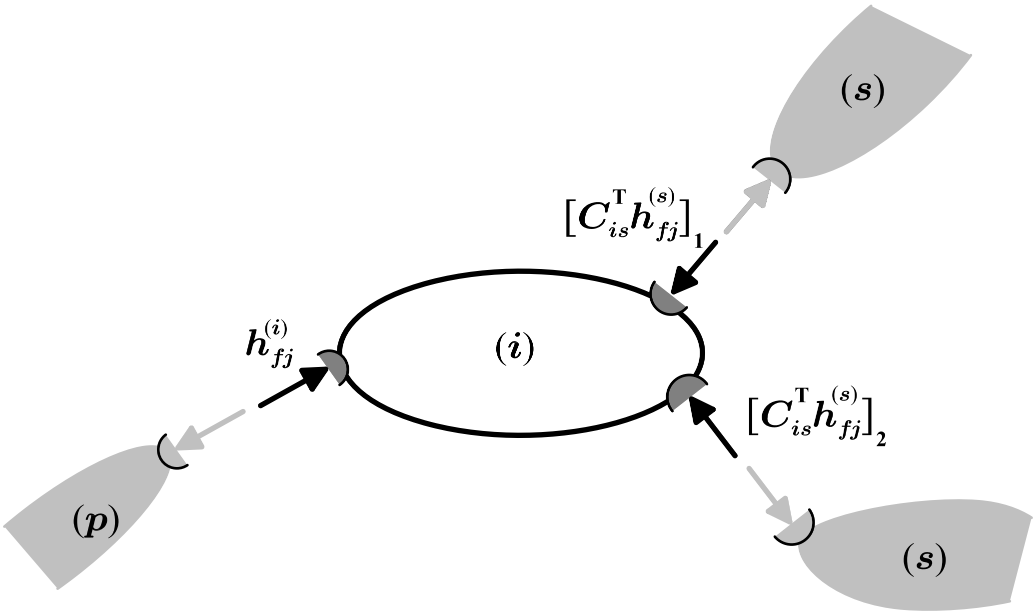

Figure 2.5: Cutting off quantities that are needed to analyse the equations of motion of body $(\;)^{(i)}$ separately.

of all successor joint forces $\boldsymbol{C}_{is}^T \boldsymbol{h}_{fj}^{(s)}$ according to (2.23e) vanishes for the terminal body:

$$\boldsymbol{M}^{(i)} \boldsymbol{b}^{(i)} - \boldsymbol{h}_{gcc}^{(i)} - \boldsymbol{h}_i^{(i)} - \boldsymbol{h}_{fe}^{(i)} + \sum \boldsymbol{C}_{is}^T \boldsymbol{h}_{fj}^{(s)} = \boldsymbol{h}_{fj}^{(i)} \tag{2.23c}$$

$\boldsymbol{h}_{fj}^{(i)}$ represents the passive forces of the joint, which act locally orthogonal to the direction of motion of the body. It follows that the multiplication of the transpose of the local Jacobian $\boldsymbol{J}_j^{(i)}$ yields a zero vector provided the equations of motion are satisfied, see [BP92, Sec. 4.3.3]. If not, a residual force $\Delta \boldsymbol{h}^{(i)}$ is obtained, which can be used to iteratively correct the vector set $\boldsymbol{y}$, $\dot{\boldsymbol{y}}$ and $\ddot{\boldsymbol{y}}$ w.r.t. the equations of motion.

$$\Delta \boldsymbol{h}^{(i)} = \left[\boldsymbol{J}_j^{(i)}\right]^T \boldsymbol{h}_{fj}^{(i)} \qquad \text{with} \qquad \boldsymbol{J}_j^{(i)} = \frac{\partial\, {}_i\boldsymbol{b}_j^{(i)}}{\partial \ddot{\boldsymbol{z}}_j^{(i)}} \tag{2.23d}$$

When the next body downwards, i.e. the predecessor body, is evaluated with (2.23c), the reactio of the just calculated passive joint force is interpreted as a specific boundary load $\boldsymbol{f}_B$ in Tab. 2.1 and is transformed into the system of the predecessor body by the matrix $\boldsymbol{C}_{is}^T$ [Rul98, Sec. 5.4]:

$$\boldsymbol{h}_{fj}^{(i)} \longrightarrow \boldsymbol{C}_{is}^T \boldsymbol{h}_{fj}^{(s)} \tag{2.23e}$$

The downwards recursion ends with Body $(\ )^{(0)}$ and yields residual forces for each body $\Delta \boldsymbol{h}^{(i)}$. These forces vanish identically for the analytical solution and remain in the size of the discretisation error as result of the iterative numerical evaluation.

If a tree-structured multibody system is considered, the recursion loops have to be organised in such a way that all $\boldsymbol{h}_{fj}^{(s)}$ in (2.23c) are available when needed.

Since the numerical effort in evaluating the mechanical system is linearly dependent on the number of degrees of freedom $N = \dim(\boldsymbol{y})$, the residual formalism is a so called $\mathcal{O}(N)$-formalism, which avoids the inversion of the mass matrix in (2.22b). $\mathcal{O}(N)$-formalisms that evaluate the accelerations explicitly have been proposed a few years earlier than this implicit scheme and are still widespread, see e.g. [BJO86]. If the efficiency of explicit and implicit $\mathcal{O}(N)$-formalisms is compared, the result will depend on the mechanical system under consideration.

The incorporation of the modelling element *constraints* enables the description of mechanical systems with closed loops, see Fig. 2.1. Closed loops result in the holonomic kinematic constraint equation

$$\boldsymbol{0} = \boldsymbol{g}(\boldsymbol{y}) \ , \qquad \boldsymbol{G}(\boldsymbol{y}) := \frac{\partial \boldsymbol{g}(\boldsymbol{y})}{\partial \boldsymbol{y}} \ , \tag{2.24a}$$

with the constraint matrix $\boldsymbol{G}(\boldsymbol{y})$ [Bre88, Sec. 3.1.1]. Following the approach of Lagrange, the constraints have to be introduced into (2.22b) by means of the corresponding passive forces $\boldsymbol{G}^T \boldsymbol{\lambda}$.

The columns of $\boldsymbol{G}^T$ define the generalised directions, i.e. the directions w.r.t. vector space of $\boldsymbol{y}$, in which the constraint forces act, and $\boldsymbol{\lambda}$ denotes the vector of the Lagrange multiplier:

$$\bar{\boldsymbol{M}}(\boldsymbol{y},t)\,\ddot{\boldsymbol{y}} = \bar{\boldsymbol{h}}(\boldsymbol{y},\dot{\boldsymbol{y}},t) - \boldsymbol{G}^T(\boldsymbol{y})\,\boldsymbol{\lambda} \tag{2.24b}$$

The ordinary differential equations (2.22) are extended by constraint forces in (2.24b) and the additional algebraic equations (2.24a). Therefore, Eqs. (2.24) describe a differential-algebraic system (DAE) in the so-called index-3 formulation [Sch97].

For numerical time integration, the DAE (2.24) is transformed into an equivalent first order system by introducing the velocities $\boldsymbol{w} := \dot{\boldsymbol{y}}$. Following an approach by GEAR, GUPTA and LEIMKUHLER, a formulation is obtained that guarantees stable time integration [HW96, Ch. VII (1.48)]:

$$\bar{\boldsymbol{M}}\,(\dot{\boldsymbol{y}} - \boldsymbol{w}) = -\,\boldsymbol{G}^T\boldsymbol{\eta} \tag{2.25a}$$

$$\bar{\boldsymbol{M}}\,\dot{\boldsymbol{w}} = \bar{\boldsymbol{h}} - \boldsymbol{G}^T\boldsymbol{\lambda} \tag{2.25b}$$

$$0 = \boldsymbol{g} \tag{2.25c}$$

$$0 = \frac{\mathrm{d}\boldsymbol{g}}{\mathrm{d}t} = \frac{\partial \boldsymbol{g}}{\partial \boldsymbol{y}}\,\dot{\boldsymbol{y}} = \boldsymbol{G}\,\boldsymbol{w} \tag{2.25d}$$

In (2.25d) this formulation makes explicit use of a relation that is obvious from the physical point of view: if the position vector is constrained by means of (2.25c), it is implicitly given that the related velocities are constrained as well. Analytically, the instantaneous incorporation of position and velocity constraints is redundant but avoids instabilities during the numerical evaluation. Furthermore, the kinematic equations $\dot{\boldsymbol{y}} = \boldsymbol{w}$ are extended by the correction term $\boldsymbol{G}^T\boldsymbol{\eta}$ with auxiliary variables $\boldsymbol{\eta}$ in (2.25a). These variables $\boldsymbol{\eta}$ vanish identically for the analytical solution and remain in the size of the discretisation error during time integration.

A frequently used implicit time integrator is the variable step size variable order BDF-(Backward Differentiation Formulae)-Code DASSL [BCP96].

2.2 Material Constitution

This thesis deals with three physical fields, each specified by a pair of field variable terms. The mechanical state of a material particle is quantified by its stress tensor $\boldsymbol{\sigma}$ and its strain tensor $\boldsymbol{\varepsilon}$, the electrical state by its electrical field strength $\boldsymbol{e}$ and the electrical displacement vector $\boldsymbol{d}$ and the thermal state by the scalar terms temperature Θ and entropy density η.

In order to describe the properties and the influence of the material, it is presumed that the thermodynamical state of the material only depends on the current values of the field variables but not on their histories. The constitutive relation between the six field terms is supposed to define the thermodynamical state of a material point uniquely, no matter which process, which change of state variables has led to the current configuration.

Consequently it makes sense to base the material constitution on a thermodynamical potential. This is the purpose of the present section.

2.2.1 The Electric Gibbs Potential

In principle, for three fields with two state terms each, $3^2 - 1 = 8$ different thermodynamical potentials could be formulated to fulfil the predescribed task. The decision, which potential to prefer, is identical with the selection of independent field variables.

In multibody dynamics and as well in finite element analysis the mechanical field is traditionally described in terms of displacements. Since the strain field follows from the displacement field just by mathematical differentiation with respect to the undeformed geometry, the strain tensor is the preferable independent variable concerning the mechanical field.

Contrary to the entropy density temperature is a generic intensive state variable and easy to measure. This fact gives the reason to select the temperature as independent thermal field variable.

Because of its scalar nature it is convenient to take the electric potential as the basic electrical field quantity. Assuming electrostatic conditions the electrical field strength may be defined as the associated gradient field to the electrical potential. Therefore the electrical field strength turns out to be well suited as independent variable to describe the electrical field.

The thermodynamical potential associated with these independent variables is called the electric Gibbs potential G:

$$\mathrm{d}G = \boldsymbol{\sigma}^T \mathrm{d}\boldsymbol{\varepsilon} - \boldsymbol{d}^T \mathrm{d}\boldsymbol{e} - \eta \mathrm{d}\Theta \ . \tag{2.26}$$

Furthermore, the introduction of a new variable ϑ, replacing the absolute temperature Θ by the increment w.r.t. the linearisation temperature Θ_0 proved to be advantageous:

$$\vartheta = \Theta - \Theta_0 \ . \tag{2.27}$$

To provide a linear material description, the electric Gibbs potential is expanded into a Taylor series around a working point, neglecting terms of higher than second order:

$$
\begin{aligned}
G(\boldsymbol{\varepsilon},\boldsymbol{e},\vartheta) = G(\mathbf{0},\mathbf{0},\Theta_o) &+ \left.\frac{\partial G}{\partial \boldsymbol{\varepsilon}}\right|_0 \boldsymbol{\varepsilon} + \left.\frac{\partial G}{\partial \boldsymbol{e}}\right|_0 \boldsymbol{e} + \left.\frac{\partial G}{\partial \Theta}\right|_0 \vartheta + \\
&+ \frac{1}{2}\Bigg[\boldsymbol{\varepsilon}^T \left.\frac{\partial^2 G}{\partial \boldsymbol{\varepsilon}^T \partial \boldsymbol{\varepsilon}}\right|_0 \boldsymbol{\varepsilon} + \boldsymbol{e}^T \left.\frac{\partial^2 G}{\partial \boldsymbol{e}^T \partial \boldsymbol{e}}\right|_0 \boldsymbol{e} + \vartheta \left.\frac{\partial^2 G}{\partial \Theta^2}\right|_0 \vartheta + \\
&\qquad + 2\boldsymbol{\varepsilon}^T \left.\frac{\partial^2 G}{\partial \boldsymbol{\varepsilon}^T \partial \boldsymbol{e}}\right|_0 \boldsymbol{e} + 2\boldsymbol{\varepsilon}^T \left.\frac{\partial^2 G}{\partial \boldsymbol{\varepsilon}^T \partial \Theta}\right|_0 \vartheta + 2\boldsymbol{e}^T \left.\frac{\partial^2 G}{\partial \boldsymbol{e}^T \partial \Theta}\right|_0 \vartheta\Bigg] \; . \qquad (2.28)
\end{aligned}
$$

The dependent thermodynamic state variables stress $\boldsymbol{\sigma}$, electrical displacement $\boldsymbol{d}$ and entropy density η may be specified using (2.26):

$$
\boldsymbol{\sigma} = \left(\frac{\partial G}{\partial \boldsymbol{\varepsilon}}\right)^T , \qquad \boldsymbol{d} = -\left(\frac{\partial G}{\partial \boldsymbol{e}}\right)^T , \qquad \eta = -\left(\frac{\partial G}{\partial \Theta}\right) . \qquad (2.29)
$$

The first derivatives in (2.28) allow the consideration of pre-loads like initial stresses:

$$
\left.\frac{\partial G}{\partial \boldsymbol{\varepsilon}}\right|_0 = \boldsymbol{\sigma}_0^T , \qquad \left.\frac{\partial G}{\partial \boldsymbol{e}}\right|_0 = \boldsymbol{d}_0^T , \qquad \left.\frac{\partial G}{\partial \Theta}\right|_0 = \eta_0 . \qquad (2.30)
$$

Here the existence of a natural state $\vartheta = 0$, $\boldsymbol{e} = \mathbf{0}$ and $\boldsymbol{\varepsilon} = \mathbf{0}$ is assumed at which $\boldsymbol{\sigma}$, $\boldsymbol{d}$ and η vanish. For this state the electric Gibbs potential is set to zero: $G(\mathbf{0},\mathbf{0},\Theta_0) = 0$.

The linear material constitution is obtained by the comparison of (2.29) and (2.28). The evaluation of the second order partial derivatives in (2.28) leads to the definition of material coefficients, assumed to be constant. The indices and superscripts of the following coefficient matrices are chosen analogously to the notation used by [Min74]. The superscripts indicate the terms kept constant during differentiation and will be skipped in the following for material coefficients based on the electric Gibbs potential:

- The elasticity tensor $\boldsymbol{H}_c = \boldsymbol{H}_c^T \in \mathbb{R}^{6,6}$, whereby the electric field and the temperature are kept constant during differentiation:

$$
{}^{e\vartheta}\boldsymbol{H}_c = \boldsymbol{H}_c = \left.\frac{\partial \boldsymbol{\sigma}}{\partial \boldsymbol{\varepsilon}}\right|_0 = \left.\frac{\partial^2 G}{\partial \boldsymbol{\varepsilon}^T \partial \boldsymbol{\varepsilon}}\right|_0 . \qquad (2.31a)
$$

- The piezoelectric tensor $\boldsymbol{H}_e \in \mathbb{R}^{3,6}$ with the temperature kept constant:

$$
{}^{\vartheta}\boldsymbol{H}_e = \boldsymbol{H}_e = \left.\frac{\partial \boldsymbol{d}}{\partial \boldsymbol{\varepsilon}}\right|_0 = -\left.\frac{\partial^2 G}{\partial \boldsymbol{e} \partial \boldsymbol{\varepsilon}}\right|_0 = \left[-\left.\frac{\partial^2 G}{\partial \boldsymbol{\varepsilon}^T \partial \boldsymbol{e}}\right|_0\right]^T = \left[-\left.\frac{\partial \boldsymbol{\sigma}}{\partial \boldsymbol{e}}\right|_0\right]^T . \qquad (2.31b)
$$

- The thermal moduli $\boldsymbol{H}_\lambda \in \mathbb{R}^{1,6}$ at constant electrical field:

$$
{}^{e}\boldsymbol{H}_\lambda = \boldsymbol{H}_\lambda = \left.\frac{\partial \eta}{\partial \boldsymbol{\varepsilon}}\right|_0 = -\left.\frac{\partial^2 G}{\partial \Theta \partial \boldsymbol{\varepsilon}}\right|_0 = \left[-\left.\frac{\partial^2 G}{\partial \boldsymbol{\varepsilon}^T \partial \Theta}\right|_0\right]^T = \left[-\left.\frac{\partial \boldsymbol{\sigma}}{\partial \Theta}\right|_0\right]^T . \qquad (2.31c)
$$

- The permittivity tensor $\boldsymbol{H}_\epsilon = \boldsymbol{H}_\epsilon^T \in \mathbb{R}^{3,3}$, which is obtained via differentiation with the temperature and strain and kept constant:

$$ {}^{\epsilon\vartheta}\boldsymbol{H}_\epsilon = \boldsymbol{H}_\epsilon = \left.\frac{\partial \boldsymbol{d}}{\partial \boldsymbol{e}}\right|_0 = -\left.\frac{\partial^2 G}{\partial \boldsymbol{e}^T \partial \boldsymbol{e}}\right|_0 . \tag{2.31d} $$

- The pyroelectric tensor $\boldsymbol{H}_p \in \mathbb{R}^{3,1}$ at constant strain:

$$ {}^{\epsilon}\boldsymbol{H}_p = \boldsymbol{H}_p = \left.\frac{\partial \boldsymbol{d}}{\partial \Theta}\right|_0 = -\left.\frac{\partial^2 G}{\partial \boldsymbol{e}^T \partial \Theta}\right|_0 = \left[-\left.\frac{\partial^2 G}{\partial \Theta \partial \boldsymbol{e}}\right|_0 \right]^T = \left[-\left.\frac{\partial \eta}{\partial \boldsymbol{d}}\right|_0 \right]^T . \tag{2.31e} $$

- The heat capacity coefficient $\boldsymbol{H}_a \in \mathbb{R}^{1,1}$ at constant strain and electric field involves the linearisation temperature Θ_0, the density ϱ and the specific heat capacity c:

$$ {}^{\epsilon e}\boldsymbol{H}_a = \boldsymbol{H}_a = \left.\frac{\partial \eta}{\partial \Theta}\right|_0 = -\left.\frac{\partial^2 G}{\partial \Theta^2}\right|_0 = \frac{\varrho\, c}{\Theta_o} . \tag{2.31f} $$

Presuming a general unsymmetric structure the material description above forms a system with 55 independent material coefficients. Whenever a material displays some kind of symmetry regarding its physical behaviour, it is possible to formulate relations between these variables and define a reduced set of independent material coefficients.

Tab. 2.2 gives an overview of frequently encountered symmetry configurations and the corresponding material coefficients. Orthotropic materials possess three mutually perpendicular planes of symmetry. Isotropic structures exhibit no preferred directions with regard to their physical behaviour. Piezo-ceramic materials such as Lead Zirconate Titanate (PZT) expose different properties in the polarisation direction (here assumed to coincide with the x_3-direction), than in all directions normal to the polarisation. They are therefore called transversely isotropic. This characteristic can be attributed to their crystalline structure, see Sec. 2.2.3.

With the definitions in (2.31a) to (2.31f) the constitutive equation can be formulated in matrix form:

$$ \begin{pmatrix} \boldsymbol{\sigma} \\ \boldsymbol{d} \\ \eta \end{pmatrix} = \begin{pmatrix} \boldsymbol{H}_c & -\boldsymbol{H}_e^T & -\boldsymbol{H}_\lambda^T \\ \boldsymbol{H}_e & \boldsymbol{H}_\epsilon & \boldsymbol{H}_p \\ \boldsymbol{H}_\lambda & \boldsymbol{H}_p^T & \boldsymbol{H}_a \end{pmatrix} \begin{pmatrix} \boldsymbol{\varepsilon} \\ \boldsymbol{e} \\ \vartheta \end{pmatrix} = \boldsymbol{H} \begin{pmatrix} \boldsymbol{\varepsilon} \\ \boldsymbol{e} \\ \vartheta \end{pmatrix} . \tag{2.31g} $$

In Fig. 2.6, which illustrates (2.31g), the independent field variables are arranged as corners of the outer triangle. Each arrow represents one of the coefficients defined in (2.31a) to (2.31f) and reflects the dependence of the field quantities at the corners of the inside triangle.[1]

Considering the uncoupled, isotropic thermoelastic problem the first row of (2.31g) may be rewritten to extract the widely used thermal strain $\boldsymbol{\varepsilon}_\vartheta$, which depends on the temperature and the thermal

---

[1] According to TICHÝ and GAUTSCHI this diagram was published for the first time in 1925 by the German physicist G. Heckmann.

<table>
<tr><th colspan="2">$\boldsymbol{H}_c$</th></tr>
<tr><td colspan="2">The elasticity tensor</td></tr>
<tr><td>orthotropic material:</td><td>transversely isotropic material:</td></tr>
<tr><td>$$\begin{pmatrix} c_{11} & c_{12} & c_{13} & 0 & 0 & 0 \\ & c_{22} & c_{23} & 0 & 0 & 0 \\ & & c_{33} & 0 & 0 & 0 \\ & & & c_{44} & 0 & 0 \\ & & & & c_{55} & 0 \\ \text{symm.} & & & & & c_{66} \end{pmatrix}$$</td><td>$c_{11} = c_{22}$, $c_{44} = c_{55}$
$c_{13} = c_{23}$, $c_{66} = (c_{11} - c_{12})/2$
isotropic material:
$c_{11} = c_{22} = c_{33} = \dfrac{E\,(1-\nu)}{(1+\nu)(1-2\nu)}$
$c_{12} = c_{13} = c_{23} = \dfrac{E\,\nu}{(1+\nu)(1-2\nu)}$
$c_{44} = c_{55} = c_{66} = \dfrac{E}{2(1+\nu)}$</td></tr>
<tr><th colspan="2">$\boldsymbol{H}_e$</th></tr>
<tr><td colspan="2">The piezoelectric tensor</td></tr>
<tr><td>orthotropic material:</td><td>transversely isotropic material:</td></tr>
<tr><td>$$\begin{pmatrix} 0 & 0 & 0 & 0 & e_{15} & 0 \\ 0 & 0 & 0 & e_{24} & 0 & 0 \\ e_{31} & e_{32} & e_{33} & 0 & 0 & 0 \end{pmatrix}$$</td><td>$e_{31} = e_{32}$
$e_{24} = e_{15}$</td></tr>
<tr><th colspan="2">$\boldsymbol{H}_\epsilon$</th></tr>
<tr><td colspan="2">The permittivity tensor</td></tr>
<tr><td>orthotropic material:</td><td>transversely isotropic material:</td></tr>
<tr><td>$$\begin{pmatrix} \epsilon_{11} & 0 & 0 \\ & \epsilon_{22} & 0 \\ \text{symm.} & & \epsilon_{33} \end{pmatrix}$$</td><td>$\epsilon_{11} = \epsilon_{22}$</td></tr>
<tr><th colspan="2">$\boldsymbol{H}_\lambda$</th></tr>
<tr><td colspan="2">The thermal moduli</td></tr>
<tr><td>orthotropic material:</td><td>isotropic material:</td></tr>
<tr><td>$(\ \lambda_1\ \lambda_2\ \lambda_3\ 0\ 0\ 0\ )$</td><td>$\lambda_1 = \lambda_2 = \lambda_3 = \dfrac{E}{1-2\nu}\ \alpha$</td></tr>
</table>

Table 2.2: Frequently encountered structures of material coefficient matrices, see [Now78b, Ch. 8] and [TG80, Ch. 6].

expansion coefficient α [ZT00a, (4.26)]:

$$\boldsymbol{\sigma} = \boldsymbol{H}_c(\boldsymbol{\varepsilon} - \boldsymbol{\varepsilon}_\vartheta) \qquad \text{with} \qquad \boldsymbol{\varepsilon}_\vartheta = \boldsymbol{H}_c^{-1}\boldsymbol{H}_\lambda^T\vartheta = (\alpha\ \alpha\ \alpha\ 0\ 0\ 0)^T\vartheta\ . \tag{2.32}$$

It should be noted, that the use of a thermodynamical potential in order to derive constitutive relations implies that no intrinsic dissipation is considered. It follows, that an adiabatic or isothermal evolution of the piezo-thermoelastic material is thermodynamically reversible [Sal01, Ch. 4].

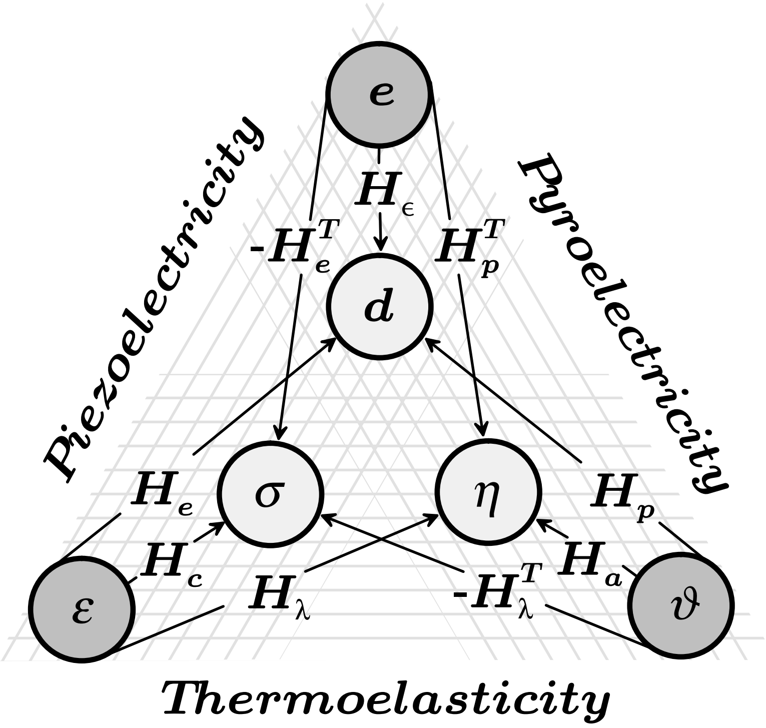

Figure 2.6: Thermodynamical variables and their interrelations, cp. [TG80, Fig. 5.1].

2.2.2 Alternative Material Constants

As mentioned above the formal shape of the constitutive equations depends primarily on the selected thermodynamical potential. This choice determines the material constants to be used. Tab. 2.3 gives an overview about the possible combinations of dependent and independent field variables which constitute the different potentials.

Each potential may be derived from any other potential by means of a Legendre-transformation. This indicates that each potential comprises the identical physical information. All potentials in Tab. 2.3 are equivalent.

These equivalent potentials may simplify the model set-up of a given simulation task substantially. Published material data is often measured under specific thermodynamical conditions, which may not align to the presumptions underlying (2.31). Therefore, relations that allow the transformation of a given set of constants into a corresponding set but referring to other measurement conditions are very helpful.

In order to prepare an example, the material constitution on base of the electric enthalpy $\bar{P}$ is

Name	Definition	independent
internal energy	$\mathrm{d}U = \boldsymbol{\sigma}^T \mathrm{d}\boldsymbol{\varepsilon} + \boldsymbol{e}^T \mathrm{d}\boldsymbol{d} + \Theta \mathrm{d}\eta$	$\boldsymbol{\varepsilon}\ , \boldsymbol{d}\ , \eta$
free energy	$\mathrm{d}F = \boldsymbol{\sigma}^T \mathrm{d}\boldsymbol{\varepsilon} + \boldsymbol{e}^T \mathrm{d}\boldsymbol{d} - \eta \mathrm{d}\Theta$	$\boldsymbol{\varepsilon}\ , \boldsymbol{d}\ , \Theta$
enthalpy	$\mathrm{d}P = -\boldsymbol{\varepsilon}^T \mathrm{d}\boldsymbol{\sigma} - \boldsymbol{d}^T \mathrm{d}\boldsymbol{e} + \Theta \mathrm{d}\eta$	$\boldsymbol{\sigma}\ , \boldsymbol{e}\ , \eta$
elastic enthalpy	$\mathrm{d}\bar{P} = -\boldsymbol{\varepsilon}^T \mathrm{d}\boldsymbol{\sigma} + \boldsymbol{e}^T \mathrm{d}\boldsymbol{d} + \Theta \mathrm{d}\eta$	$\boldsymbol{\sigma}\ , \boldsymbol{d}\ , \eta$
electric enthalpy	$\mathrm{d}\hat{P} = \boldsymbol{\sigma}^T \mathrm{d}\boldsymbol{\varepsilon} - \boldsymbol{d}^T \mathrm{d}\boldsymbol{e} + \Theta \mathrm{d}\eta$	$\boldsymbol{\varepsilon}\ , \boldsymbol{e}\ , \eta$
Gibbs potential	$\mathrm{d}\bar{G} = -\boldsymbol{\varepsilon}^T \mathrm{d}\boldsymbol{\sigma} - \boldsymbol{d}^T \mathrm{d}\boldsymbol{e} - \eta \mathrm{d}\Theta$	$\boldsymbol{\sigma}\ , \boldsymbol{e}\ , \Theta$
elastic Gibbs potential	$\mathrm{d}\hat{G} = -\boldsymbol{\varepsilon}^T \mathrm{d}\boldsymbol{\sigma} + \boldsymbol{e}^T \mathrm{d}\boldsymbol{d} - \eta \mathrm{d}\Theta$	$\boldsymbol{\sigma}\ , \boldsymbol{d}\ , \Theta$
electric Gibbs potential	$\mathrm{d}G = \boldsymbol{\sigma}^T \mathrm{d}\boldsymbol{\varepsilon} - \boldsymbol{d}^T \mathrm{d}\boldsymbol{e} - \eta \mathrm{d}\Theta$	$\boldsymbol{\varepsilon}\ , \boldsymbol{e}\ , \Theta$

Table 2.3: Thermodynamical potentials and independent variables [TG80, Table 5.1].

formulated:

$$\begin{pmatrix} \boldsymbol{\sigma} \\ \boldsymbol{d} \\ \vartheta \end{pmatrix} = \begin{pmatrix} {}^{\eta e}\boldsymbol{H}_c & -{}^{\eta}\boldsymbol{H}_e^T & {}^{e}\boldsymbol{H}_\gamma^T \\ {}^{\eta}\boldsymbol{H}_e & {}^{\eta\varepsilon}\boldsymbol{H}_\epsilon & {}^{\varepsilon}\boldsymbol{H}_\rho \\ {}^{e}\boldsymbol{H}_\gamma & -{}^{\varepsilon}\boldsymbol{H}_\rho^T & {}^{e\varepsilon}\boldsymbol{H}_b \end{pmatrix} \begin{pmatrix} \boldsymbol{\varepsilon} \\ \boldsymbol{e} \\ \eta \end{pmatrix} = \bar{\boldsymbol{H}} \begin{pmatrix} \boldsymbol{\varepsilon} \\ \boldsymbol{e} \\ \eta \end{pmatrix} . \tag{2.33}$$

Contrary to the point of view in (2.31), the material constants in $\bar{\boldsymbol{H}}$ are based on the linearisation at $\boldsymbol{\varepsilon} = \boldsymbol{0}$, $\boldsymbol{e} = \boldsymbol{0}$, $\eta = \eta_0$. The Eqs. (2.31) and (2.33) are connected by straightforward linear transformations that result, e.g., in:

$${}^{\eta e}\boldsymbol{H}_c = \boldsymbol{H}_c + \boldsymbol{H}_\lambda^T \boldsymbol{H}_a^{-1} \boldsymbol{H}_\lambda \, . \tag{2.34}$$

The elasticity tensor ${}^{\eta e}\boldsymbol{H}_c$ is defined under isentropic conditions on contrary to $\boldsymbol{H}_c$ in (2.31a), which bases on isothermal prerequisites. In Section 3.2.1 an example is given that demonstrates the physical implications of this difference.

The relation between the specific heat capacities, defined at constant strain in (2.31f) and at constant stress, may be obtained by virtue of the Gibbs potential $\bar{G}$:

$$c = {}^{\varepsilon}c = {}^{\sigma}c - \left(\frac{\Theta_0}{\varrho}\right) \boldsymbol{H}_\lambda \boldsymbol{H}_c^{-1} \boldsymbol{H}_\lambda^T \, . \tag{2.35}$$

In evaluations considering the thermodynamics of gases, the corresponding relation between the specific heat capacities at constant pressure and at constant volume is frequently applied. But compared to gases these values differ only slightly for solids, by 2% for instance for 1.5% carbon steel.

2.2.3 Physical Nonlinearities

Although it is not intended to apply physical nonlinearities in what follows, there are two specific reasons that may motivate a survey on nonlinear material description.

The response of piezoelectric materials on large electrical fields is of essential technical importance since the manufacturing of piezoelectric ceramics relies on this nonlinear dependence. Additionally the knowledge of the nonlinear characteristics provides an interesting insight into the working mechanism of the piezoelectric effect.

Moreover, it is well known that almost all real material coefficients depend on the temperature. Nevertheless the set-up of a linear thermoelastic analysis with large thermal loads and temperature increments may make sense, if appropriate values for the material coefficients, assumed to be constant within the evaluated temperature range, are adopted. And of course, the results of such a linear analysis have to be assessed against the background of the limitations of the physical linearisation.

These two facts give reason to outline the nonlinear dielectric properties and the temperature dependence of the mechanical and thermal properties in the following two paragraphs.

Dielectric Properties

Fig. 2.7 illustrates the crystal lattice of the frequently used piezo-ceramic material PZT [Vog97, Sec. 6.2.5]. The central Zircon or Titan atom and the Oxygen ions are slightly shifted compared to the cubic configuration of the Lead atoms. Although this unsymmetry constitutes a local dipole moment, the positive and negative charges are in equilibrium in the undeformed state of the lattice.

Supposed the crystal becomes mechanically extended, then the action of the positive charges at the upper face is stiffer than the action of the negative charges near the upper face. The charges at the lower face behave exactly the other way around. Here, the positive charges move less compared to the negative ones at the same time. As a result, the upper face becomes charged positively and the lower face negatively.

There is a companion characteristics to this direct piezoelectric effect called the converse effect consisting in the deformation of a piezoelectric crystal under the influence of an external electric field. Assuming linear behaviour the piezoelectric polarisation is directly proportional to the applied strain, and vice versa, the piezoelectric deformation is directly proportional to the applied electric field. The dashed line in Figure 2.8 visualises this linear material law.

Nowadays, no mono-crystalline structures but poly-crystalline ceramics are used in technical appli-

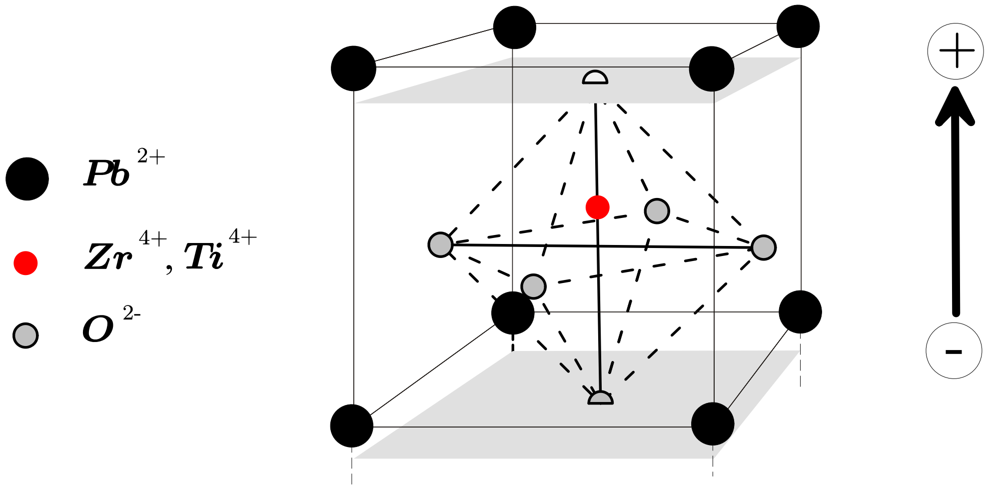

Figure 2.7: The unit cell of the Lead Zirconate Titanate (PZT) lattice of the Perovskite type and its dipole moment.

cations since there is no difficulty in manufacturing piezo-ceramic elements of almost any desired shape. The production process of the ceramics gives wafers with domains in which the dipole moment is uniformly oriented. State *A* in Fig. 2.8 shows schematically how the dipole orientation may be randomly distributed over the volume of a piezo-ceramic workpiece. As a result of this distribution there is no net polarisation and the workpiece behaves isotropically.

However, under the influence of a strong electric field, the dipoles of the domains align with the direction of the applied field as good as their domain orientations allow. For manufacturing one *wing* of the so called *butterfly* curve of Fig. 2.8 is run through, starting from point *A* through *B* and ending at *C*. The corresponding dipole orientations within the workpiece are schematically visualised in Fig. 2.8. The dashed contours represent the undeformed state of the workpiece.

The resulting polarisation remains permanent as long as no depolarisation field with higher field strength than the coercive field strength e_c at point *D* is applied. Yet, the polarisation orientation may be flipped, if the butterfly curve is run through the points *D* and *E*, ending at *C*. Consequently depending on the load history of the workpiece, there are two possible permanent polarisations at point *C* in Fig. 2.8, which are addressed by the states *C* and *C'* in Fig. 2.8.

In technical applications the usable range of the electrical field strength in polarisation direction is limited by saturation and the danger of dielectric breakdown. In the opposite direction the field should be restricted to at most 80% of the coercive field strength, cp. [Jen95, Fig. 7.15].

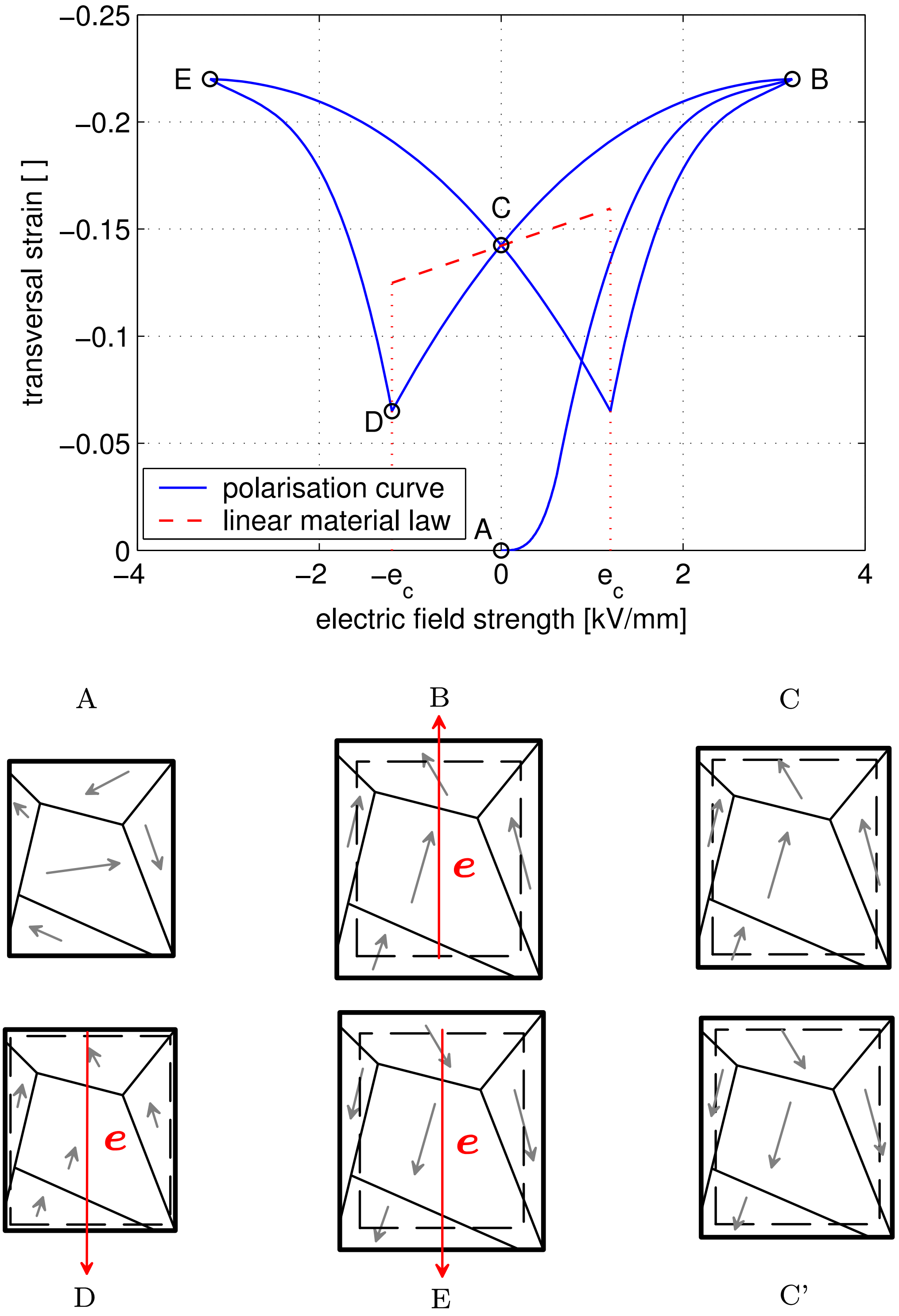

Figure 2.8: The plot above shows the transversal strain versa applied electric field strength for PZT-5A as polarisation curve, i.e. so-called butterfly curve, and linear material law for the small signal range [HH79, p. 450]. The associated strain changes and domain polarisations are schematically visualised below [Pie01, Fig. 1.3].

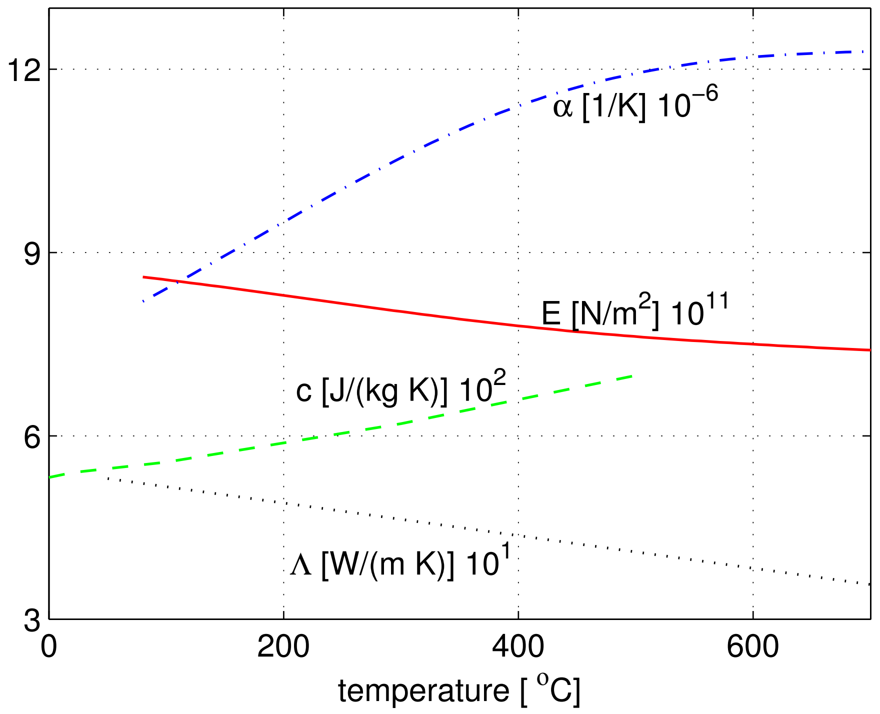

Figure 2.9: E, α, Λ and c of GG20 HC as function of temperature [Bur91, Sec. 9.7].

Temperature Dependence of the Mechanical and Thermal Properties

In order to convey a quantitative idea of the temperature dependence, the linear expansion coefficient α, Young's modulus E, the specific heat coefficient c and the thermal conductivity Λ of cast iron of type GG20HC are given as function of the temperature in Fig. 2.9. GG20HC is a preferred material in the design of brake discs supposed to be subjected to high thermal loads.

In Sec. 3.2.4 the simulation results of a linear thermoelastic analysis of a friction brake are compared with results of a nonlinear finite element analysis, which is set up using these temperature dependencies.

In addition to Fig. 2.9, one has to bear in mind that there are specific temperatures at which the material constitution changes fundamentally. The Curie point, for pure iron at 1033 K, at which a ferromagnetic material becomes paramagnetic is an appropriate example. Since the thermal properties such as the specific heat capacity become highly nonlinear at the Curie point, there is no way to deal with such a fundamental transformation in a linear analysis. Therefore, the upper limit of the physical linearisation is given at this temperature.

2.3 Augmented Field Equations

2.3.1 Generalised Hamilton's Principle

PARKUS [Par70] established a generalised Hamilton's principle for coupled thermoelasticity, which was augmented for piezo-thermoelasticity by NOWACKI [Now78a]. Their formulation uses the thermodynamical functional Π, the summarised work functions of the external mechanical and electrical quantities A and the thermal function Ξ besides the kinetic energy T and states

$$\delta \int_{t_1}^{t_2} (T - \Pi + A)\ \mathrm{d}t = 0\ , \qquad \delta \int_{t_1}^{t_2} \Xi\ \mathrm{d}t = 0\ . \tag{2.36a}$$

The thermal functional Ξ is defined as

$$\Xi = \int_V (H - \eta\Theta\dot{\Theta} - S\Theta)\ \mathrm{d}V + \oint_B \boldsymbol{q}_B^T \boldsymbol{n}_B \Theta\ \mathrm{d}B\ . \tag{2.36b}$$

In (2.36b) the quantity S denotes the heat source density. The scalar potential H, called heat flux potential per volume, is closely related to the fundamental Fourier law of heat conduction:

$$\boldsymbol{q} = -\boldsymbol{\Lambda}(\nabla\Theta)\ , \tag{2.36c}$$

which determines the heat flux $\boldsymbol{q}$ as function of the local temperature gradient and the conductivity matrix $\boldsymbol{\Lambda}$:

$$H = \tfrac{1}{2}(\nabla\Theta)^T\boldsymbol{\Lambda}(\nabla\Theta)\ , \qquad \Longrightarrow \qquad \boldsymbol{q} = -\frac{\partial H}{\partial(\nabla\Theta)^T} = -\boldsymbol{\Lambda}(\nabla\Theta)\ . \tag{2.36d}$$

$\boldsymbol{n}_B$ in (2.36b) is the outer normal vector at the boundary surface element $\mathrm{d}B$.

The thermodynamical functional Π is composed according to

$$\Pi = \int_V (G + \eta\Theta)\ \mathrm{d}V\ , \tag{2.36e}$$

and the external mechanical and electrical work functions get the form

$$A = \int_V \boldsymbol{f}_V^T\boldsymbol{r}\ \mathrm{d}V + \oint_B \left(\boldsymbol{f}_B^T\boldsymbol{r} - \varphi Q_\varphi\right)\ \mathrm{d}B\ . \tag{2.36f}$$

Eq. (2.36) has to be rearranged in a form that only the independent field variables $\boldsymbol{r}$, $\boldsymbol{e}$ and Θ appear as virtual quantities. Therefore, the variations of the dependent variables have to be expressed in terms of the virtual independent quantities. Concerning (2.36) this is possible with one restriction which will be discussed in Sec. 2.3.2.

Separation of variations for the three fields in (2.36), substitution of G in (2.36e) using (2.26) and the Fundamental lemma of the variational approach yield the field equations in weak form:

$$\int_V [-\varrho\delta\boldsymbol{r}^T\ddot{\boldsymbol{r}} - \delta\boldsymbol{\varepsilon}^T\boldsymbol{\sigma} - \delta\bar{\boldsymbol{\varepsilon}}^T\boldsymbol{\sigma}_0 + \delta\boldsymbol{r}^T\boldsymbol{f}_V]\,\mathrm{d}V + \oint_B \delta\boldsymbol{r}^T\boldsymbol{f}_B\,\mathrm{d}B = 0\ , \tag{2.37a}$$

$$\int_V \delta\boldsymbol{e}^T\boldsymbol{d}\,\mathrm{d}V - \oint_B \delta\varphi Q_\varphi\,\mathrm{d}B = 0\ , \tag{2.37b}$$

$$\int_V [-(\nabla\delta\Theta)^T\boldsymbol{q} + \delta\Theta(\Theta\dot{\eta} - S)]\,\mathrm{d}V + \oint_B \delta\Theta\boldsymbol{q}_B^T\boldsymbol{n}_B\,\mathrm{d}B = 0\ . \tag{2.37c}$$

On first sight the equations (2.37) look like three uncoupled field descriptions from mono-disciplinary engineering textbooks. Eq. (2.37a) for instance is identical to (2.14), where no multi-physics is considered at all. But the coupling becomes obvious by eliminating the dependent field variables $\boldsymbol{\sigma}$, $\boldsymbol{e}$ and η using (2.31). On the other hand as long as no specific material law is inserted in (2.37), these variational equations are valid as general, nonlinear field equations.

The Eqs. (2.37a) and (2.37b) could also be derived applying d'Alembert's principle of virtual work. ROSE and SACHAU [RS01] obtained the equivalent formulation on base of Jourdain's principle substituting the variational quantities by their derivatives.

Eq. (2.37c) is also known as the principle of virtual temperature, which is the standard finite element approach concerning the thermal field, see [KW92, Sec. 3.6.2] or [Bat96, Sec. 7.2.1].

BIOT referred to (2.37c) as the complementary variational principle in heat transfer [Bio70, Ch. 8, App. §3]. His corresponding fundamental principle, frequently just called Biot's principle, is formulated in terms of the virtual entropy displacement vector $\delta\boldsymbol{s}$, which is related to (2.36c) by the equation $\Theta\dot{\boldsymbol{s}} = \boldsymbol{q}$. However on contrary to (2.37c), Biot's principle, did not become widely accepted and applied, since the entropy displacement might be a somewhat abstract and inapprehensible quantity.

2.3.2 Strong Thermal and Electrostatic Field Equations

This section relates the weak thermal and electrostatic equations of (2.36) to the corresponding strong formulations.

Variation of the Thermal Functional

Applying the chain rule and Gauss' theorem, the variation δH of the heat flux potential gets a new form:

$$\begin{aligned} \delta H &= \frac{\partial H}{\partial(\nabla\Theta)}\frac{\partial(\nabla\Theta)}{\partial\Theta}\delta\Theta = -(\nabla\delta\Theta)^T\boldsymbol{q} = -\nabla^T(\boldsymbol{q}\delta\Theta) + (\nabla^T\boldsymbol{q})\delta\Theta \ , \\ \Longrightarrow \int_V \delta H \mathrm{d}V &= -\int_V \nabla^T(\boldsymbol{q}\delta\Theta)\ \mathrm{d}V + \int_V (\nabla^T\boldsymbol{q})\delta\Theta\ \mathrm{d}V \ , \\ &= -\oint_B \delta\Theta\ \boldsymbol{q}^T\boldsymbol{n}_B\ \mathrm{d}B + \int_V (\nabla^T\boldsymbol{q})\delta\Theta\ \mathrm{d}V \ . \end{aligned} \tag{2.38}$$

The variation of the second expression in (2.36b) gives:

$$\int_{t_1}^{t_2} \delta(\eta\Theta\dot{\Theta})\ \mathrm{d}t = -\int_{t_1}^{t_2} \dot{\eta}\Theta\delta\Theta\ \mathrm{d}t \underbrace{-\frac{1}{2}\int_{t_1}^{t_2} \Theta\Theta\delta\dot{\eta}\ \mathrm{d}t}_{:=\Delta\Xi} \ , \tag{2.39}$$

in which integration by parts is applied and the fact is used that the variation vanishes at the limits t_1 and t_2:

$$\begin{aligned} \int_{t_1}^{t_2} (\eta\Theta\delta\Theta)^{\cdot}\ \mathrm{d}t &= \int_{t_1}^{t_2} \left(\dot{\eta}\Theta\delta\Theta + \eta\dot{\Theta}\delta\Theta + \eta\Theta\delta\dot{\Theta}\right)\ \mathrm{d}t = 0 \ , \\ \int_{t_1}^{t_2} \dot{\Theta}\Theta\delta\eta\ \mathrm{d}t &= -\frac{1}{2}\int_{t_1}^{t_2} \Theta\Theta\delta\dot{\eta}\ \mathrm{d}t \ . \end{aligned}$$

Eq. (2.39) reveals an important restriction. It is only possible to develop the principle of virtual temperature (2.37c) out of the generalised Hamilton's principle (2.36), if the term $\Delta\Xi$ in (2.39) is neglected.

That is why PARKUS [Par70] restricted the application of (2.36) to isentropic variations. NOWACKI [Now78a] does not comment on this issue and permits arbitrary variations.

Neglecting $\Delta\Xi$, Eq. (2.36) can be rewritten:

$$\int_{t_1}^{t_2} \left(\int_V [(\nabla^T\boldsymbol{q}) - S + \Theta\dot{\eta}]\delta\Theta\ \mathrm{d}V + \oint_B [\boldsymbol{q}_B^T\boldsymbol{n}_B - \boldsymbol{q}^T\boldsymbol{n}_B]\delta\Theta\ \mathrm{d}B \right) \mathrm{d}t = 0 \ . \tag{2.40}$$

For arbitrary variations $\delta\Theta$, arbitrary times t_1, t_2 this equation corresponds to the following relations:

$$\begin{aligned} \nabla^T \boldsymbol{q} &= -\nabla^T \boldsymbol{\Lambda}(\nabla T) \ , \\ &= S - \Theta\dot{\eta} && \text{within the body volume,} && (2.41a) \\ \boldsymbol{q}_B &= \boldsymbol{q} && \text{on the boundary.} && (2.41b) \end{aligned}$$

Eq. (2.41a) is known as the coupled partial differential equation of heat conduction, first derived by DUHAMEL [BW97, Sec. 1.12], who considered the coupled thermoelastic problem. Since it incorporates the entropy change $\dot{\eta}$, it is a very general statement and can easily be augmented for piezo-thermoelasticity applying appropriate material laws like (2.31). Eq. (2.41a) involves second partial derivatives while only first partial derivatives appear in (2.37b). This leads to weaker conditions to define solutions of the problem in (2.37b) and thus the notion of a *weak form* is established.

Furthermore, it has to be emphasised that although the validity of the generalised Hamilton's principle is restricted, the weak equations (2.37) are not, since they could be derived directly out of the corresponding strong forms.

The Electrostatic Field Equation

The second Maxwell equation relates the curl of the electric field strength $\boldsymbol{e}$ to the change of the magnetic induction $\boldsymbol{m}$ [FLS64, Ch. 15]. However, the frequency range in focus here is determined by the mechanical eigenfrequencies and therefore very much lower than the electromagnetic eigenfrequencies. That is why the rate of the magnetic induction may be disregarded, electrostatic conditions are presumed. Furthermore, the electric field strength can be interpreted as gradient field associated to the scalar electric potential field φ:

$$\widetilde{\nabla}\boldsymbol{e} = -\frac{\partial \boldsymbol{m}}{\partial t} \approx \boldsymbol{0} \qquad \Longrightarrow \qquad \boldsymbol{e} = -\nabla\varphi \ . \tag{2.42}$$

Eq. (2.42) is inserted in (2.37b) and again Gauss' theorem is applied:

$$\begin{aligned} \int_V \delta(\nabla\varphi)^T \boldsymbol{d} \, \mathrm{d}V + \oint_B \delta\varphi Q_\varphi \, \mathrm{d}B &= 0 \ , \\ \int_V [\nabla^T(\boldsymbol{d}\delta\varphi) - \delta\varphi\nabla^T\boldsymbol{d}] \, \mathrm{d}V + \oint_B \delta\varphi Q_\varphi \, \mathrm{d}B &= 0 \ , \\ \oint_B \delta\varphi \, \boldsymbol{d}_B^T \boldsymbol{n}_B \, \mathrm{d}B - \int_V \delta\varphi \, \nabla^T \boldsymbol{d} \, \mathrm{d}V + \oint_B \delta\varphi Q_\varphi \, \mathrm{d}B &= 0 \ . \end{aligned} \tag{2.43}$$

For arbitrary variations $\delta\varphi$ Eq. (2.43) is satisfied, if the following conditions hold:

$$\nabla^T \boldsymbol{d} = 0 \qquad \text{within the body volume,} \tag{2.44a}$$

$$\boldsymbol{d}_B^T \boldsymbol{n}_B = -Q_\varphi \qquad \text{on the boundary.} \tag{2.44b}$$

Eq. (2.44a) is equivalent to the statement that there are no free charges within the volume [Now78a, (3)]. On the boundary, i.e. on the electrodes of a piezoelectric device, the charges Q_φ constitute the electric displacement vector, which is aligned normal to the boundary surface but points inwards.

2.3.3 Modal Multifield Approach

The semi–discretisation of the scalar temperature is performed completely analogously to the displacement field in (2.7). The thermal Rayleigh-Ritz approach is defined with time–independent mode functions $\boldsymbol{\Phi}_\vartheta(\boldsymbol{c})$ and modal amplitudes $\boldsymbol{z}_\vartheta(t)$ as functions of time. Subsequently the gradient operation gives the heat flux vector $\boldsymbol{q}$:

$$\vartheta(\boldsymbol{c},t) = \boldsymbol{\Phi}_\vartheta(\boldsymbol{c})\ \boldsymbol{z}_\vartheta(t)\ , \qquad \boldsymbol{\Phi}_\vartheta \in \mathbb{R}^{1,n},\ \boldsymbol{z}_\vartheta \in \mathbb{R}^n\ , \tag{2.45}$$

$$\nabla\vartheta = \nabla\boldsymbol{\Phi}_\vartheta\ \boldsymbol{z}_\vartheta = \boldsymbol{B}_\vartheta\ \boldsymbol{z}_\vartheta \quad \Longrightarrow \quad \boldsymbol{q} = -\boldsymbol{\Lambda}\boldsymbol{B}_\vartheta\ \boldsymbol{z}_\vartheta\ , \tag{2.46}$$

$$\text{with} \qquad \boldsymbol{B}_\vartheta(\boldsymbol{c}) := \nabla\boldsymbol{\Phi}_\vartheta\ .$$

Regarding the electrostatics the modal functions $\boldsymbol{\Phi}_\varphi(\boldsymbol{c})$ describe the spatial distribution of the scalar electrical potential field. The transient behaviour is expressed by the modal coefficients $\boldsymbol{z}_\varphi(t)$. The electrical field strength $\boldsymbol{e}$ follows from a negative gradient operation:

$$\varphi(\boldsymbol{c},t) = \boldsymbol{\Phi}_\varphi(\boldsymbol{c})\ \boldsymbol{z}_\varphi(t)\ , \qquad \boldsymbol{\Phi}_\varphi \in \mathbb{R}^{1,n},\ \boldsymbol{z}_\varphi \in \mathbb{R}^n\ , \tag{2.47}$$

$$\boldsymbol{e} = -\nabla\varphi = -\nabla\boldsymbol{\Phi}_\varphi\ \boldsymbol{z}_\varphi = \boldsymbol{B}_\varphi\ \boldsymbol{z}_\varphi\ , \tag{2.48}$$

$$\text{with} \qquad \boldsymbol{B}_\varphi(\boldsymbol{c}) := -\nabla\boldsymbol{\Phi}_\varphi\ .$$

The extension of the modal approach from the pure mechanical problem in Sec. 2.1.2 to the multifield equations (2.37) is straightforward from the mathematical point of view. However this fact says nothing about the accuracy of the chosen semi-discretisation regarding the applications of interest. This and further topics like data-preparation and comparison to the finite element method will be discussed extensively in the third chapter.

2.3.4 The Equations of Motion of a Piezo-Thermoelastic Body

The presentation is continued substituting the dependent field variable $\boldsymbol{\sigma}$ in (2.37a) referring to (2.31):

$$\begin{aligned}\int_V [\varrho \delta \boldsymbol{r}^T \boldsymbol{a} + \delta \boldsymbol{\varepsilon}^T (\boldsymbol{H}_c\, \boldsymbol{\varepsilon} - \boldsymbol{H}_e^T \boldsymbol{e} - \boldsymbol{H}_\lambda^T \vartheta) + \\ + \delta \bar{\boldsymbol{\varepsilon}}^T \boldsymbol{\sigma}_0 - \delta \boldsymbol{r}^T \boldsymbol{f}_V]\, \mathrm{d}V - \oint_B \delta \boldsymbol{r}^T \boldsymbol{f}_B\, \mathrm{d}B = 0\ . \end{aligned} \tag{2.49}$$

Eq. (2.49) defines the linearised mechanical field equation in weak form. In view of (2.19), it turns out that the additional considered electrostatic and thermal fields only influence the vector of the internal forces, which therefore has to be extended in order to obtain the equations of motion of a piezo-thermoelastic body.

Some new abbreviations in addition to Tab. 2.1 are listed in Tab. 2.4 and allow to transform (2.49) into the following convenient representation:

$$\boldsymbol{M} \begin{pmatrix} \boldsymbol{a}_R \\ \boldsymbol{\alpha}_R \\ \ddot{\boldsymbol{z}}_u \end{pmatrix} = \boldsymbol{h}_{gcc} + \boldsymbol{h}_f + \boldsymbol{h}_{im}\ . \tag{2.50}$$

From the mechanical point of view, it may be concluded that the non-mechanical fields generate distributed mechanical loads. These loads can be expressed as linear functions of the modal amplitudes of the electrostatic field $\boldsymbol{z}_\varphi = \boldsymbol{z}_\varphi(t)$ and of the thermal field $\boldsymbol{z}_\vartheta = \boldsymbol{z}_\vartheta(t)$, respectively. The purely geometric part of the field descriptions is considered by the coupling matrices $\boldsymbol{K}_{u\varphi}$ and $\boldsymbol{K}_{u\vartheta}$. These terms result from inner products of the time-independent mode functions or their partial derivatives according to (2.8), (2.47) and (2.45) and involve the material coefficients in the volume integrals of Tab. 2.4.

2.3.5 The Electrostatic Equation

In (2.37b), the electric displacement vector $\boldsymbol{d}$ is a dependent field variable. If $\boldsymbol{d}$ is eliminated using the linear material law (2.31), the electrostatic field equation is given by

$$\int_V \delta \boldsymbol{e}^T (\boldsymbol{H}_e \boldsymbol{\varepsilon} + \boldsymbol{H}_\epsilon \boldsymbol{e} + \boldsymbol{H}_p \vartheta)\, \mathrm{d}V = \oint_B \delta \varphi Q_\varphi\, \mathrm{d}B\ . \tag{2.51}$$

Using the modal approach from Sec. 2.3.3, this description can be transformed to

$$\int_V \boldsymbol{B}_\varphi^T \left(\boldsymbol{H}_e \boldsymbol{B}_u \boldsymbol{z}_u + \boldsymbol{H}_\epsilon \boldsymbol{B}_\varphi \boldsymbol{z}_\varphi + \boldsymbol{H}_p \boldsymbol{\Phi}_\vartheta \boldsymbol{z}_\vartheta \right) \mathrm{d}V = \oint_B \boldsymbol{\Phi}_\varphi^T Q_\varphi\, \mathrm{d}B\ . \tag{2.52}$$

$\boldsymbol{K}_{u\varphi}$	$\boldsymbol{K}_{u\vartheta}$
The mechanical-electrostatic coupling matrix $\boldsymbol{K}_{u\varphi} := \int_V \boldsymbol{B}_u^T \boldsymbol{H}_e^T \boldsymbol{B}_\varphi \, \mathrm{d}V$	The mechanical-thermal coupling matrix $\boldsymbol{K}_{u\vartheta} := \int_V \boldsymbol{B}_u^T \boldsymbol{H}_\lambda^T \boldsymbol{\Phi}_\vartheta \, \mathrm{d}V$

$\boldsymbol{h}_{im}$
The extended vector of the internal forces $\boldsymbol{h}_{im} = \begin{pmatrix} \boldsymbol{0} \\ \boldsymbol{0} \\ -\boldsymbol{D}_{uu}\dot{\boldsymbol{z}}_u - \boldsymbol{K}_{uu}\boldsymbol{z}_u - \boldsymbol{K}_\sigma \boldsymbol{z}_u + \boldsymbol{K}_{u\varphi}\boldsymbol{z}_\varphi + \boldsymbol{K}_{u\vartheta}\boldsymbol{z}_\vartheta \end{pmatrix}$

$\boldsymbol{K}_{\varphi u}$	$\boldsymbol{K}_{\varphi\varphi}$
The electrostatic-mechanical coupling matrix $\boldsymbol{K}_{\varphi u} := \int_V \boldsymbol{B}_\varphi^T \boldsymbol{H}_e \boldsymbol{B}_u \, \mathrm{d}V = \boldsymbol{K}_{u\varphi}^T$	The electric capacity matrix $\boldsymbol{K}_{\varphi\varphi} := \int_V \boldsymbol{B}_\varphi^T \boldsymbol{H}_\epsilon \boldsymbol{B}_\varphi \, \mathrm{d}V = \boldsymbol{K}_{\varphi\varphi}^T$

$\boldsymbol{K}_{\varphi\vartheta}$	$\boldsymbol{h}_\varphi$
The electrostatic-thermal coupling matrix $\boldsymbol{K}_{\varphi\vartheta} := \int_V \boldsymbol{B}_\varphi^T \boldsymbol{H}_p \boldsymbol{\Phi}_\vartheta \, \mathrm{d}V$	The electric charge load vector $\boldsymbol{h}_\varphi := \oint_B \boldsymbol{\Phi}_\varphi^T Q_\varphi \, \mathrm{d}B$

Table 2.4: Definition of additional volume integrals and abbreviations for terms of the equations of motion and the electrostatic equation of a piezo-thermoelastic body.

With the volume integrals, which are summarised in Tab. 2.4, Eq. (2.52) can be rewritten as

$$\boldsymbol{h}_\varphi = \boldsymbol{K}_{\varphi\varphi}\boldsymbol{z}_\varphi + \boldsymbol{K}_{\varphi u}\boldsymbol{z}_u + \boldsymbol{K}_{\varphi\vartheta}\boldsymbol{z}_\vartheta \ . \tag{2.53}$$

The algebraic equation (2.53) is called the sensor equation. It is needed to calculate the electric quantities, e.g. the electric charges $\boldsymbol{h}_\varphi$, if the piezo-ceramic components are used as sensors or, more generally, if they are part of arbitrary electric circuits, see [Pre02, Ch. 3] and [RS01].

2.3.6 The Thermal Equation

In order to remain within the realm of a linear theory it has to be assumed that the increment of temperature ϑ according to (2.27) is small, or at least moderate, compared to the reference temperature Θ_0:

$$\frac{|\vartheta|}{\Theta} = \frac{|\Theta - \Theta_0|}{\Theta} \ll 1 \ . \tag{2.54}$$

As a rule of thumb NOWINSKI recommends in [Now78b, Ch. 6] not to exceed a temperature increment of approx. 200 K. This range is motivated by the idea that the maximum thermal strain (2.32) should be of the same order of magnitude as the strain resulting from mechanical stress. Consider for instance the material GG20HC of Fig. 2.9. The maximum elastic strain is reached for $\varepsilon_p \approx 0.0025$. The maximum permitted temperature increase then follows from $\alpha\,\vartheta_p \approx \varepsilon_p$ and is $\vartheta_p \approx 240$ K, which is in accordance with Nowinski's rule of thumb.

It should be noted that besides the material law (2.31), which enables the elimination of the entropy density in (2.37c), the thermal equation itself has to be linearised. Consider the linearised weak thermal field equation that is deduced from (2.37c):

$$\int_V [-(\nabla\delta\Theta)^T\boldsymbol{q} + \delta\Theta\Theta_0(\boldsymbol{H}_\lambda\dot{\boldsymbol{\varepsilon}} + \boldsymbol{H}_p^T\dot{\boldsymbol{e}} + \boldsymbol{H}_a\dot{\vartheta}) - \delta\Theta S]\ \mathrm{d}V + \oint_B \delta\Theta\boldsymbol{q}_B^T\boldsymbol{n}_B\ \mathrm{d}B = 0\ . \quad (2.55)$$

The substitution of Θ by Θ_0 in (2.55) may be interpreted as an additional physical linearisation effecting the already linearised material coefficients $\boldsymbol{H}_\lambda$, $\boldsymbol{H}_p$ and $\boldsymbol{H}_a$. However, the definition of $\boldsymbol{H}_a = \varrho c/\Theta_0$ from (2.31f) makes obvious that the linearisation of the field equation exclusively applies to the influences of the displacement and the electrostatic field on the temperatures and not to the generic thermal description, cp. [CJ59, Ch. 1].

The comparison of a nonlinear and a linear thermoelastic analysis of a brake disc in Sec. 3.2.4 illustrates the influences of nonlinearities by example.

In (2.55) the natural boundary conditions are represented by the heat flux through the boundary. It depends on the physical circumstances how this term has to be introduced into the thermal equation. For Neumann conditions the boundary heat flux q_B is given explicitly. If convection occurs on the boundary surface a Robin or mixed boundary condition is imposed, specified by the film coefficient h_f and the bulk temperature ϑ_∞ of the fluid [LL01, Sec. 4.1]. Although this list is not complete, we confine ourselves to these two cases:

$$\boldsymbol{q}_B^T\boldsymbol{n}_B = -q_B - h_f(\vartheta_B - \vartheta_\infty)\ . \quad (2.56)$$

The partial differential equation in weak form (2.55) is reduced to a set of ordinary differential equations by the Rayleigh-Ritz approach of Sec. 2.3.3:

$$\begin{aligned}\int\limits_V \big[&\boldsymbol{B}_\vartheta^T\boldsymbol{\Lambda}\boldsymbol{B}_\vartheta\boldsymbol{z}_\vartheta - \boldsymbol{\Phi}_\vartheta^T S + \Theta_0\boldsymbol{\Phi}_\vartheta^T\left(\boldsymbol{H}_\lambda\boldsymbol{B}_u\dot{\boldsymbol{z}}_u + \boldsymbol{H}_p^T\boldsymbol{B}_\varphi\dot{\boldsymbol{z}}_\varphi + \right.\\ &\left. + \boldsymbol{H}_a\boldsymbol{\Phi}_\vartheta\dot{\boldsymbol{z}}_\vartheta\right)\big]\ \mathrm{d}V - \oint_B \boldsymbol{\Phi}_\vartheta^T(\bar{q} - h_f\boldsymbol{\Phi}_\vartheta\boldsymbol{z}_\vartheta + h_f\vartheta_\infty)\ \mathrm{d}B = 0 \quad (2.57)\end{aligned}$$

The geometric linearisation again enables the decomposition of volume and time integration and leads to the volume integrals and abbreviations, which are summarised by Tab. 2.5.

$\boldsymbol{C}_{\vartheta\vartheta}$	$\boldsymbol{C}_{\vartheta\varphi}$
The heat capacity matrix $\boldsymbol{C}_{\vartheta\vartheta} := \int_V \Theta_0 \boldsymbol{\Phi}_\vartheta^T \boldsymbol{H}_a \boldsymbol{\Phi}_\vartheta \, \mathrm{d}V = \boldsymbol{C}_{\vartheta\vartheta}^T$	The thermal-electrostatic coupling matrix $\boldsymbol{C}_{\vartheta\varphi} := \int_V \Theta_0 \boldsymbol{\Phi}_\vartheta^T \boldsymbol{H}_p^T \boldsymbol{B}_\varphi \, \mathrm{d}V = \Theta_0 \boldsymbol{K}_{\varphi\vartheta}^T$
$\boldsymbol{K}_{\vartheta\vartheta}$	$\boldsymbol{C}_{\vartheta u}$
The conductivity matrix $\boldsymbol{K}_{\vartheta\vartheta} := \int_V \boldsymbol{B}_\vartheta^T \boldsymbol{\Lambda} \boldsymbol{B}_\vartheta \, \mathrm{d}V = \boldsymbol{K}_{\vartheta\vartheta}^T$	The thermal-mechanical coupling matrix $\boldsymbol{C}_{\vartheta u} := \int_V \Theta_0 \boldsymbol{\Phi}_\vartheta^T \boldsymbol{H}_\lambda \boldsymbol{B}_u \, \mathrm{d}V = \Theta_0 \boldsymbol{K}_{\vartheta u}^T$
$\boldsymbol{K}_{\vartheta R}$	$\boldsymbol{h}_{\vartheta R}$
The Robin load matrix $\boldsymbol{K}_{\vartheta R} := \oint_B h_f \boldsymbol{\Phi}_\vartheta^T \boldsymbol{\Phi}_\vartheta \, \mathrm{d}B = \boldsymbol{K}_{\vartheta R}^T$	The Robin load vector $\boldsymbol{h}_{\vartheta R} := \oint_B \boldsymbol{\Phi}_\vartheta^T h_f \, \mathrm{d}B$
$\boldsymbol{h}_{\vartheta N}$	$\boldsymbol{h}_{\vartheta S}$
The Neumann load vector $\boldsymbol{h}_{\vartheta N} := \oint_B \boldsymbol{\Phi}_\vartheta^T \, \mathrm{d}B$	The heat source vector $\boldsymbol{h}_{\vartheta S} := \int_V \boldsymbol{\Phi}_\vartheta^T \, \mathrm{d}V$

Table 2.5: Volume integrals and abbreviations for terms of the thermal equation.

Finally, the coupled linearised thermal field equation can be stated:

$$\boldsymbol{C}_{\vartheta\vartheta}\,\dot{\boldsymbol{z}}_\vartheta + \boldsymbol{C}_{\vartheta\varphi}\,\dot{\boldsymbol{z}}_\varphi + \boldsymbol{C}_{\vartheta u}\,\dot{\boldsymbol{z}}_u + \left(\boldsymbol{K}_{\vartheta\vartheta} + \boldsymbol{K}_{\vartheta R}\right)\boldsymbol{z}_\vartheta = \boldsymbol{h}_{\vartheta S}\,S + \boldsymbol{h}_{\vartheta N}\,q_B + \boldsymbol{h}_{\vartheta R}\,\vartheta_\infty \tag{2.58}$$

The generalised velocities $\dot{\boldsymbol{z}}_u$ in (2.58) indicate that the temperature field depends on the displacements and the strains. Whereas the thermal effect on the displacements is well known and widely accounted for in finite element analysis, the feedback from displacements on temperatures, called the Gough-Joule effect [SW01], is relatively unacquainted and very frequently neglected because of its limited influence on the temperatures compared to the other terms.

If it is intended to identify the well-known uncoupled heat conduction equation of solids in discretised form, (2.58) can be rewritten assuming $\boldsymbol{C}_{\vartheta u} \approx \boldsymbol{0}$ and $\boldsymbol{C}_{\vartheta\varphi} \approx \boldsymbol{0}$, cp. [LMTS96].

2.3.7 Topological Aspects

Eqs. (2.50), (2.58) and (2.53) are to be posted for each body of the articulated mechanism under consideration. For a global representation these equations are rewritten in condensed form for a general elastic body $(\ )^{(i)}$ with electrostatic and thermal properties:

$$\begin{aligned} \boldsymbol{M}^{(i)}\boldsymbol{b}^{(i)} &= \boldsymbol{h}_{gcc}^{(i)} + \boldsymbol{h}_{f}^{(i)} + \boldsymbol{h}_{im}^{(i)}(\boldsymbol{z}_{\varphi}^{(i)}, \boldsymbol{z}_{\vartheta}^{(i)}, \boldsymbol{z}_{u}^{(i)}) \ , && \text{(2.59a)} \\ \dot{\boldsymbol{z}}_{\vartheta}^{(i)} &= \dot{\boldsymbol{z}}_{\vartheta}^{(i)}(\dot{\boldsymbol{z}}_{\varphi}^{(i)}, \boldsymbol{z}_{\vartheta}^{(i)}, \dot{\boldsymbol{z}}_{u}^{(i)}) \ , && \text{(2.59b)} \\ \boldsymbol{h}_{\varphi}^{(i)} &= \boldsymbol{h}_{\varphi}^{(i)}(\boldsymbol{z}_{\varphi}^{(i)}, \boldsymbol{z}_{\vartheta}^{(i)}, \boldsymbol{z}_{u}^{(i)}) \ . && \text{(2.59c)} \end{aligned}$$

Besides the mechanical description (2.59a) the set-up of a piezo-thermoelastic body requires the definition of two additional, uniquely assigned elements. The thermal element reflects (2.59b) and evaluates the thermal state of the body. The electrostatic element stands for the measurement capabilities of the piezo-ceramic devices attached to body $(\ )^{(i)}$ and calculates the electric charges $\boldsymbol{h}_{\varphi}^{(i)}$, i.e. the sensor output of the piezo-patches according to (2.59c).

The actuation capabilities of the piezo-patches are reflected by the input variable $\boldsymbol{z}_{\varphi}^{(i)}$ in (2.59a). From that point of view the elastic body $(\ )^{(i)}$ may be interpreted as a controlled plant, with $\boldsymbol{z}_{\varphi}^{(i)}$ representing its input and $\boldsymbol{h}_{\varphi}^{(i)}$ its output. These quantities are supposed to be used for the set-up of an appropriate control law such as $\boldsymbol{z}_{\varphi}^{(i)} = \boldsymbol{z}_{\varphi}^{(i)}(\boldsymbol{h}_{\varphi}^{(i)})$, see the piezoelectric applications in Sec. 3.1 and Sec. 4.2.

The thermal and electrostatic equations of the complete system can be arranged as follows:

$$\dot{\bar{\boldsymbol{z}}}_{\vartheta} = \Big(\ldots\ \dot{\boldsymbol{z}}_{\vartheta}^{(i)}\ \ldots\Big)^{T} \ , \qquad \bar{\boldsymbol{h}}_{\varphi} = \big(\ldots\ \boldsymbol{h}_{\varphi}^{(i)}\ \ldots\big)^{T} \ . \tag{2.60}$$

Analogously to Sec. 2.1.5, the pure mechanical part of the equations of motion describing the complete multibody system reads:

$$\sum_{(i)} \left[\frac{\partial \boldsymbol{b}^{(i)}}{\partial \ddot{\boldsymbol{y}}}\right]^{T} \left[\boldsymbol{M}^{(i)}\boldsymbol{b}^{(i)} - \boldsymbol{h}_{gcc}^{(i)} - \boldsymbol{h}_{f}^{(i)} - \boldsymbol{h}_{im}^{(i)}\right] \ = \ \bar{\boldsymbol{M}}\ddot{\boldsymbol{y}} - \bar{\bar{\boldsymbol{h}}} = \boldsymbol{0} \ . \tag{2.61}$$

$\bar{\boldsymbol{M}}(\boldsymbol{y}, t)$ represents the symmetric inertia matrix of the complete multibody system. $\bar{\bar{\boldsymbol{h}}}(\dot{\boldsymbol{y}}, \boldsymbol{y}, \bar{\boldsymbol{z}}_{\vartheta}, \bar{\boldsymbol{z}}_{\varphi}, t)$ now includes the generalised Coriolis forces, the generalised applied forces and the generalised loads due to thermal and electrostatic influences.

In its general form the model equations of the complete system are given by:

$$\begin{aligned} \bar{\boldsymbol{M}}(\boldsymbol{y}, t)\ddot{\boldsymbol{y}} &= \bar{\bar{\boldsymbol{h}}}(\dot{\boldsymbol{y}}, \boldsymbol{y}, \bar{\boldsymbol{z}}_{\varphi}, \bar{\boldsymbol{z}}_{\vartheta}, t) \ , && \text{(2.62a)} \\ \dot{\bar{\boldsymbol{z}}}_{\vartheta} &= \dot{\bar{\boldsymbol{z}}}_{\vartheta}(\dot{\boldsymbol{y}}, \dot{\bar{\boldsymbol{z}}}_{\varphi}, \bar{\boldsymbol{z}}_{\vartheta}) \ , && \text{(2.62b)} \\ \bar{\boldsymbol{h}}_{\varphi} &= \bar{\boldsymbol{h}}_{\varphi}(\boldsymbol{y}, \bar{\boldsymbol{z}}_{\varphi}, \bar{\boldsymbol{z}}_{\vartheta}) \ . && \text{(2.62c)} \end{aligned}$$

Eqs. (2.59) presume that the electrostatic and thermal field of body $(\ )^{(i)}$ do not interfere with those of other bodies. Mechanical interactions between separated bodies of a mechanism are to be modelled either as applied forces or by kinematic constraints, see Sec. 2.1.5.

If the thermal field of two bodies interact, the mutual influence has to be modelled explicitly defining appropriate boundary conditions (2.56). Consider e.g. a heat flux $\boldsymbol{q}^{(e)}$ that is emitted over the boundary of body $(\ )^{(e)}$ and is absorbed as $\boldsymbol{q}^{(a)}$ by Body $(\ )^{(a)}$. These terms may depend on the temperature fields of both bodies, which leads to the additional constraint equation $\mathbf{0} = \boldsymbol{q}^{(e)} + \boldsymbol{q}^{(a)}$ that has to be maintained during the time integration.

Interactions of the electrostatic fields of two bodies may be treated analogously, although they are rather unlikely to occur concerning piezo-ceramic patches.

3 Basic Modelling Concepts and Processes

Whenever a concept such as material constitution, field equations or semi-discretisation has been introduced in the previous chapter, it has been presented in a symmetric manner so that the associated terms of all three physical fields have been considered simultaneously. Since the modelling issues that are related to the electromechanical coupling and those related to the thermo-mechanical coupling differ fundamentally, it is not possible to proceed in the same way.

The modelling of adaptive structures with piezo-ceramic patches involves two main tasks:

Data provision: Industrial finite element tools are capable to supply the mechanical data of solid bodies, but do not yet provide data of light-weight structures with distributed piezo-patches. Thus, an appropriate technique to obtain the modal body data describing the electrostatic field and its coupling with the displacement field on the basis of readily available information has to be defined.

Optimisation and Control: Efficient strategies for the optimisation and control set-up of structures with distributed actuators and sensors are a field of active research and far from being state-of-the-art, see e.g. [LLMB00].

Compared to these topics, the geometric description of the electrostatic field by means of appropriate modal functions is straightforward, since the geometric shape of the piezo-patches can be exploited.

Thus, the main difference to the thermoelastic modelling is already given. Although the employment of global modes has stood the test of time in flexible multibody dynamics, experiences regarding the application of the Raleigh-Ritz approach on the numerical analysis of coupled thermal and mechanical fields are rare, see e.g. [BRK02]. Consequently, the modal modelling of the phenomenon thermoelasticity is characterised by two main problems:

Temperature field: The geometric distribution of temperatures has to be described in appropriate manner w.r.t. the objectives and the intention of the physical analysis.

Coupling of thermal and mechanical field: Eq. (2.59) defines a bi-directional coupling of the discretised thermal and mechanical problem. Therefore, a modal approach to deal with this specific multifield interaction in an efficient way is the goal regarding this point.

Since automatic error control is not available so far, the result of the modal semi-discretisation still relies on the intuition of the engineer [Sim01]. This fact reveals an obvious risk, which may be underlined by the following statement of BATHE: "The most important aspect in a Ritz analysis is the selection of appropriate Ritz basis vectors because the results can only be as good as the Ritz basis vectors allow them to be." [Bat96, Sec. 10.3.3].

On the other hand, the modal approach offers the chance to streamline the solution basis incorporating all available information about the system of interest. Modelling assumptions that take into account whether a physical effect or a corresponding material property is of technical relevance concerning the objective of the analysis alleviate the simulation task substantially.

In road vehicle dynamics e.g., the analysis relies on the incorporation of important elasto-kinematic effects. Information about the spatial distribution and frequency content of the loading may be exploited to select appropriate modes directly [Bat96, Sec. 9.3.3] or by frequency response analysis [Die99]. Although errors up to 10 or 15% compared to nonlinear FE results have been observed in specific cases, this modelling achieved a broad acceptance in automotive applications [PFL03].

It should to be noted that the modal approach, and that holds for piezoelectric as well as for thermoelastic applications, is in principle restricted to linear phenomena even though some specific extensions like geometric stiffening exist. However, the linearity allows to calculate all matrices that represent the geometric properties separately from the time integration. That way, it is possible to obtain an efficient, low-dimensional representation of multifield problems, which is feasible for system dynamical analysis.

Another issue that applies to both multifield phenomena concerns the use of finite element data, which are well suited to provide information about the distributed properties of bodies. Nowadays, no stand-alone solutions but conclusive data management and utilisation of already available product information are requested [SK00]. Therefore the methodology to introduce in this chapter uses finite element data as far as they are available.

As a result of the discussion above, this chapter is divided into two sections. The first one exclusively concerns with the modelling and the data evaluation for piezo-ceramic devices which is subsequently demonstrated by means of a moderately complex, single body example. The second section describes the preprocessing for thermoelastic multibody simulations and presents two verification examples.

3.1 Modelling of Electromechanics

The introduction to electrostatics in Ch. 2 provides the physical foundations for the modelling of so-called smart or adaptive structures. One promising design concept among others also addressed by this label is focused on thin piezo-ceramic patches which are attached to a mounting structure.

These patches can be used as actuators and/or sensors within a control loop. The electrodes of these patches constitute the electrical interface to influence and/or detect the electrostatic field within the piezo-ceramic device. In order to demonstrate the basic principle of this design, Sec. 3.1.1 presents an analytical model of a Kirchhoff plate with an attached piezo-ceramic actuator in the usual strength-of-material notation, engineers are familiar with.

For numerical analysis, a straightforward modelling approach would incorporate the multiphysical finite element data to describe the mechanical and the electrostatic properties of the structure under consideration. But an efficient representation of light-weight structures in focus here requires beam and shell elements. Although the finite element modelling of piezo-electric devices on shell elements is a field of current research [Pie01], it is not yet supported by an industrial finite element tool. As a consequence native electromechanical finite element data is not available. The sections 3.1.2 and 3.1.3 describe a technique to enable nevertheless the simulation of light-weight structures with beam and shell elements. These multifield data are obtained accessing purely mechanical finite element data that is readily available.

The design of smart structures requires to determine positions where the piezo-ceramic patches have to be attached on the structure. Furthermore, the control of the structure has to be set up. A case study of a controlled metal sheet is used to introduce these topics in Sec. 3.1.4, see also VACULÍN and HECKMANN in [VH04b] and HECKMANN, ARNOLD and VACULÍN in [HAV05]. The discussion of advantages and limitations of the chosen approach completes the section.

3.1.1 An Analytical Example

Consider a plate with attached piezo-ceramic patch as sketched in Fig. 3.1. $\boldsymbol{\sigma}^+$ denotes the additional stress field, which arises from the presence of the electrostatic field, cp. [Pre02, Sec. 3.8].

From the electrostatic point of view, the piezo-ceramic patch is a flat capacitor. The electric potential φ is assumed to depend linearly on the thickness co-ordinate s and on the voltage $z_{\varphi,i}$ that is applied to the electrodes at s_0 and s_1. The electric field strength $\boldsymbol{e}$ follows from (2.48):

$$\boldsymbol{e} = -\nabla\varphi = -\nabla\left(\frac{s-s_0}{s_1-s_0}\right) z_{\varphi,i} = -\begin{pmatrix} 0 \\ 0 \\ 1 \end{pmatrix} \frac{z_{\varphi,i}}{s_1-s_0}\,, \quad \text{for} \quad s_0 \le s \le s_1\,. \tag{3.1}$$

The actuation capability of a transversely isotropic piezo-patch can be formulated on the basis of the material constitution (2.31g) together with (3.6):

$$\boldsymbol{\sigma}^+ = -\boldsymbol{H}_e^T\,\boldsymbol{e} = \begin{pmatrix} 0 & 0 & 0 & 0 & e_{24} & 0 \\ 0 & 0 & 0 & e_{24} & 0 & 0 \\ e_{31} & e_{31} & e_{33} & 0 & 0 & 0 \end{pmatrix}^T \begin{pmatrix} 0 \\ 0 \\ 1 \end{pmatrix} \frac{z_{\varphi,i}}{s_1-s_0}\,. \tag{3.2}$$

Provided that the plane stress assumption holds, i.e. the stress components normal to the plate's midplane are negligible, Eq. (3.2) can be simplified to

$$\begin{pmatrix} \sigma_{11}^+ \\ \sigma_{22}^+ \\ \sigma_{12}^+ \end{pmatrix} = \begin{pmatrix} e_{31} \\ e_{31} \\ 0 \end{pmatrix} \frac{z_{\varphi,i}}{s_1-s_0}\,. \tag{3.3}$$

These actuation stresses can be integrated over the thickness of the piezo-patch

$$m_x = \int_{s_0}^{s_1} \sigma_{11}^+\, z\,\mathrm{d}z \;= e_{31}\,\underbrace{(s_0 + 0.5(s_1-s_0))}_{s_m}\, z_{\varphi,i} = \int_{s_0}^{s_1} \sigma_{22}^+\, z\,\mathrm{d}z \;= m_y\,, \tag{3.4}$$

where m_x and m_y are the bending moments due to the piezoelectric actuator, defined per unit length as it is usual done in the classical Kirchhoff plate theory [Sza77, Ch.II, §12]. The term s_m represents the distance from the midplane of the sheet to the midplane of the attached piezo-patch and may be interpreted as the moment arm of the inplane piezoelectric actuation force. As

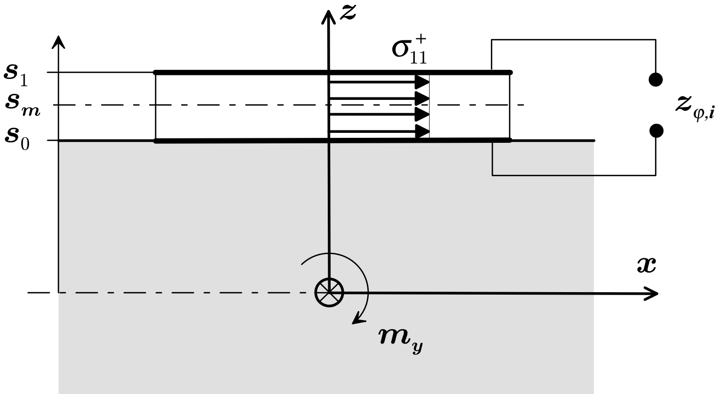

Figure 3.1: Sketch of a piezo-patch attached to the mounting structure.

a consequence of the transversal isotropy of the piezo-ceramic material, the bending moments do not depend on the orientation, i.e. they are hydrostatic.

Although (3.4) will not be used to model the influence of the piezoelectric actuation, the following conclusion may be drawn: For constant bending moments m_x and m_y, the patch thickness may be increased in order to decrease the level of the applied voltages.

The maximum allowable voltage $z_{\varphi,max}$ is restricted because the maximum field strength e_{max}, $e_{max} = z_{\varphi,max}/(s_1 - s_0)$, is restricted due to linearity and the danger of dielectric breakdown, see Sec. 2.2.3. Therefore , Eq. (3.4) may be used to adjust the thickness of the attached patch in order to account for the maximum field strength but retaining the same actuation result.

3.1.2 Piezo-Patches on Beams

In the previous section the modelling basics of structures with piezo-ceramic devices have been demonstrated. Now the presentation is continued analysing structures which are given in finite element representation.

Consider a beam structure as it will be used in Sec. 4.2 in order to appraise the active damping potential for a railway car body. In principle, the kinematics of beams has already been discussed in Sec. 2.1.2. However, if finite element data of beam structures is employed, the displacements are not given for the complete geometry $\boldsymbol{c}$ of the beam, but only at discrete positions, namely at the node positions $\boldsymbol{c}_k$ as $\boldsymbol{u}(\boldsymbol{c}_k, t)$. As a consequence necessary information is missing and has to be regained.

A beam element is geometrically defined by two nodes $k = 1,\ 2$. The aim is to obtain the matrices $\boldsymbol{K}_{u\varphi}$ and $\boldsymbol{K}_{\varphi\varphi}$ of Tab. 2.4 for a piezo-ceramic patch located on a lateral surface of the beam element.

Discrete mode matrices are known for every node k, located at the position $\boldsymbol{c}_k \in \mathbb{R}^3$ which specify the displacements $\boldsymbol{\Phi}_{u,k} \in \mathbb{R}^{3,m}$ and rotations $\boldsymbol{\Psi}_{u,k} \in \mathbb{R}^{3,m}$ as functions of all considered modes j, $1 \leq j \leq m$, see (2.11).

According to the finite element approach the beam element with length l is mapped on a normalised parameter ξ with

$$x_1(\xi) = \frac{l}{2}(\xi + 1) \,, \qquad -1 \leq \xi \leq 1 \,. \tag{3.5a}$$

For interpolation purpose, the following six functions of ξ are to be defined [GHSW95, Sec. 7.6.4]:

$$\begin{aligned} N_1 &= \frac{1}{2}(1-\xi)\,, & N_2 &= \frac{1}{2}(1+\xi)\,, \\ N_3 &= \frac{1}{4}(2-3\,\xi+\xi^3)\,, & N_4 &= \frac{l}{8}(1-\xi-\xi^2+\xi^3)\,, \\ N_5 &= \frac{1}{4}(2+3\,\xi-\xi^3)\,, & N_6 &= \frac{l}{8}(-1-\xi+\xi^2+\xi^3)\,. \end{aligned} \tag{3.5b}$$

These functions are used to organise the matrices $\boldsymbol{N}_1$, $\boldsymbol{N}_2 \in \mathbb{R}^{3,12}$, where $(\ )'$ denotes the partial derivative w.r.t. x_1:

$$\begin{aligned} \boldsymbol{N}_1 &= \begin{bmatrix} N_1 & 0 & 0 & 0 & 0 & 0 & N_2 & 0 & 0 & 0 & 0 & 0 \\ 0 & N_3 & 0 & 0 & 0 & N_4 & 0 & N_5 & 0 & 0 & 0 & N_6 \\ 0 & 0 & N_3 & 0 & N_4 & 0 & 0 & 0 & N_5 & 0 & N_6 & 0 \end{bmatrix}\,, \\ \boldsymbol{N}_2 &= \begin{bmatrix} 0 & 0 & 0 & N_1 & 0 & 0 & 0 & 0 & 0 & N_2 & 0 & 0 \\ 0 & N_3' & 0 & 0 & 0 & N_4' & 0 & N_5' & 0 & 0 & 0 & N_6' \\ 0 & 0 & N_3' & 0 & N_4' & 0 & 0 & 0 & N_5' & 0 & N_6' & 0 \end{bmatrix}\,. \end{aligned} \tag{3.5c}$$

The displacement field of the beam may then be written similarly to (2.10) and Fig. 2.3, but in terms of the finite element method:

$$\boldsymbol{u} = \left[\boldsymbol{N}_1 - \widetilde{\begin{pmatrix} 0 \\ c_2 \\ c_3 \end{pmatrix}} \boldsymbol{N}_2\right] \boldsymbol{u}^e \qquad \text{with} \qquad \boldsymbol{u}^e = \begin{pmatrix} \boldsymbol{u}_1 \\ \boldsymbol{\varphi}_1 \\ \boldsymbol{u}_2 \\ \boldsymbol{\varphi}_2 \end{pmatrix}\,. \tag{3.5d}$$

The vector $\boldsymbol{u}^e$ summarises the finite element degrees of freedom of the beam element, constituted by the displacement $\boldsymbol{u}_k$ and the rotations $\boldsymbol{\varphi}_k$ at both nodes $k = 1,\, 2$. If the translatory and the angular degrees of freedom are in fact independent, the kinematical approach of (3.5d) is equivalent to the Timoshenko beam which considers shear deformation of the beam's cross section [BP92, Sec. 4.5.2]. For the Euler-Bernoulli beam additional constraints within the vector $\boldsymbol{u}^e$ have to mind.

The representation (3.5d) enables to switch from the finite element to the modal approach by the approximation

$$\boldsymbol{u}^e \approx \begin{pmatrix} \boldsymbol{\Phi}_{u,1} \\ \boldsymbol{\Psi}_{u,1} \\ \boldsymbol{\Phi}_{u,2} \\ \boldsymbol{\Psi}_{u,2} \end{pmatrix} \boldsymbol{z}_u\,. \tag{3.5e}$$

This information is sufficient to reevaluate the displacement and strain field of the beam element as function of the modal amplitudes $\boldsymbol{z}_u$ according to (2.8).

Analogously to (3.1), the electric potential $\varphi|_i$ within the volume of one specific patch i is given as a linear function of the thickness co-ordinate s, $s_0 \leq s \leq s_1$:

$$\varphi|_i = \boldsymbol{\Phi}_\varphi \, \boldsymbol{z}_\varphi|_i = \left(\frac{s - s_0}{s_1 - s_0} \right) z_{\varphi,i} \ , \tag{3.6}$$

$$\boldsymbol{e}|_i = -\nabla \varphi|_i = \boldsymbol{B}_{\varphi,i} \, z_{\varphi,i} \ . \tag{3.7}$$

For a single patch i the modal amplitude $\boldsymbol{z}_\varphi$ is a scalar quantity and can be physically identified as the instantaneous voltage applied to the electrodes of the patch. $\boldsymbol{B}_{\varphi,i}$ is a constant vector oriented normal to the electrodes.

In general not only a single but quite a number of piezo patches are attached on a structure in order to set up structural control. Considering this case every component of $\boldsymbol{z}_\varphi$ is related to one specific patch. With the i-th unit vector $\boldsymbol{b}_i$ the formal synthesis of the global vector $\boldsymbol{z}_\varphi$ reads:

$$z_{\varphi,i} = \boldsymbol{b}_i \ \boldsymbol{z}_\varphi \tag{3.8}$$

Thus the complete information is given to perform a simplified volume integration. The terms $\boldsymbol{K}_{u\varphi}$ and $\boldsymbol{K}_{\varphi\varphi}$ of Tab. 2.4 can be rewritten:

$$\boldsymbol{K}_{u\varphi} = \sum_i \int_V \boldsymbol{B}_u^T \boldsymbol{H}_e^T \boldsymbol{B}_{\varphi,i} \, \boldsymbol{b}_i \ \mathrm{d}V_i = \sum_i \int_V \boldsymbol{B}_u^T \ \mathrm{d}V_i \ \boldsymbol{H}_e^T \boldsymbol{B}_{\varphi,i} \, \boldsymbol{b}_i \ , \tag{3.9}$$

$$\boldsymbol{K}_{\varphi\varphi} = \sum_i V_i \, \boldsymbol{b}_i^T \boldsymbol{B}_{\varphi,i}^T \boldsymbol{H}_\epsilon \boldsymbol{B}_{\varphi,i} \, \boldsymbol{b}_i = \mathrm{diag}\left\{C_i\right\} = \begin{pmatrix} \cdots & & \\ & \left. \dfrac{\epsilon_{33} B}{(s_1 - s_0)} \right|_i & \\ & & \cdots \end{pmatrix} . \tag{3.10}$$

The capacity matrix $\boldsymbol{K}_{\varphi\varphi}$ has diagonal form. Each nonzero element assigns the electric capacity C_i to the associated piezo-ceramic patch. B denotes the area of the electrode and ϵ_{33} is the permittivity of the piezoelectric material, introduced in Tab. 2.2.

The stiffness matrix $\boldsymbol{K}_{uu}$ results from the volume integral of the product $\boldsymbol{B}_u^T \boldsymbol{H}_c \boldsymbol{B}_u$ according to Tab. 2.1. The electrostatic-mechanical coupling matrix $\boldsymbol{K}_{u\varphi}$ bases on the integration of the product $\boldsymbol{B}_u^T \boldsymbol{H}_e^T \boldsymbol{B}_\varphi$, see Tab. 2.4 or (3.9). It follows, that both matrices $\boldsymbol{K}_{uu}$ and $\boldsymbol{K}_{u\varphi}$ rely on the term $\boldsymbol{B}_u = \boldsymbol{B}_u(\boldsymbol{c})$, which represents the geometric distribution of the strain field in modal co-ordinates. This similarity offers an easy method for verification.

The evaluation process introduced in this section may be organised in such a way that the strain field is reevaluated, i.e. $\boldsymbol{B}_u^*(\boldsymbol{c})$ and subsequently the matrix $\boldsymbol{K}_{uu}^*$ are obtained. The matrix $\boldsymbol{K}_{uu}^*$ is then compared with the original finite element result $\boldsymbol{K}_{uu}$:

$$\Delta \boldsymbol{K}_{uu} = \boldsymbol{K}_{uu}^* - \boldsymbol{K}_{uu} \tag{3.11}$$

$\Delta\boldsymbol{K}_{uu}$ vanishes identically for the analytical solution. Thus, the verification approach is based on the following assumptions: If $\Delta\boldsymbol{K}_{uu}$ is sufficiently small to be negligible, then $\boldsymbol{B}_u^* \approx \boldsymbol{B}_u$. And if $\boldsymbol{B}_u$ is known, an important precondition for the proper evaluation of the electromechanical coupling matrix $\boldsymbol{K}_{u\varphi}$ is given.

It should be noted that the stiffness matrix is even a quadratic expression of the actual term to verify, namely the strains. Therefore, Eq. (3.11) gives a sensitive information about the proper reevaluation of the strain field. In Sec. 3.1.4, this approach is exemplified.

Besides the material coefficients ϵ_{33} and e_{31} and the geometric patch measures s_0, s_1 and B, the presented process requires the finite element data $\boldsymbol{c}_k$, $\boldsymbol{\Phi}_{u,k}$ and $\boldsymbol{\Psi}_{u,k}$. This information is needed anyway if it is intended to perform multibody simulation of flexible bodies. For this data WALLRAPP [Wal94] proposed a *Standard Input Data* file format that is supported by a number of multibody packages.

3.1.3 Piezo-Patches on Shells

The piezo-ceramic patch is now supposed to be located upon a shell element, defined geometrically by the four nodes $k = 1 \ldots 4$, one at each corner. As before it is supposed that the node positions $\boldsymbol{c}_k \in \mathbb{R}^3$ and the discrete mode matrices $\boldsymbol{\Phi}_{u,k} \in \mathbb{R}^{3,m}$ and $\boldsymbol{\Psi}_{u,k} \in \mathbb{R}^{3,m}$, specifying the displacements and rotations of nodes as functions of all considered modes j, $1 \leq j \leq m$, are given.

For interpolation the shell mid-plane is mapped on a normalised (ξ, ζ)-area using the following functions [ANS03],

$$\begin{array}{llll} N_1 = \frac{1}{4}(1-\xi)(1-\zeta)\,, & N_2 = \frac{1}{4}(1+\xi)(1-\zeta)\,, & & \\ & & -1 \leq \xi, \zeta \leq 1\,, & \\ N_3 = \frac{1}{4}(1-\xi)(1+\zeta)\,, & N_4 = \frac{1}{4}(1+\xi)(1+\zeta)\,, & & \end{array} \tag{3.12a}$$

which be may be organised by defining a matrix $\boldsymbol{N} \in \mathbb{R}^{3,12}$

$$\boldsymbol{N}_1 = \begin{bmatrix} N_1 & 0 & 0 & N_2 & 0 & 0 & N_3 & 0 & 0 & N_4 & 0 & 0 \\ 0 & N_1 & 0 & 0 & N_2 & 0 & 0 & N_3 & 0 & 0 & N_4 & 0 \\ 0 & 0 & N_1 & 0 & 0 & N_2 & 0 & 0 & N_3 & 0 & 0 & N_4 \end{bmatrix} . \tag{3.12b}$$

The position of a shell point $\boldsymbol{c}_s(\boldsymbol{\xi})$ specified by $\boldsymbol{\xi} = (\xi\ \zeta\ s)^T$ and visualised in Fig. 3.2 is approximated by

$$\boldsymbol{c}_s(\boldsymbol{\xi}) = \boldsymbol{N}\boldsymbol{c}^e + s\boldsymbol{N}\boldsymbol{n}^e\,, \tag{3.12c}$$

where the vector $\boldsymbol{c}^e$ organises the positions of the four corner nodes and $\boldsymbol{n}^e$ summarises the unit

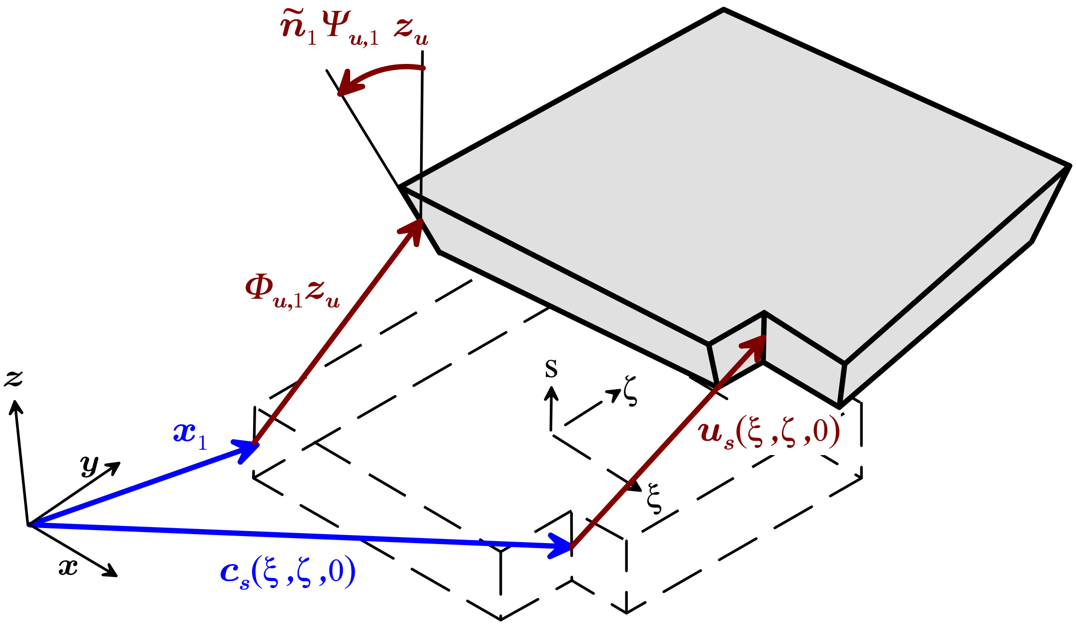

Figure 3.2: Co-ordinates and displacement quantities at one corner and at an arbitrary point on the midplane of the shell element.

normals to the shell mid-plane in the node points:

$$\boldsymbol{c}^e = \left(\boldsymbol{x}_1^T\ \boldsymbol{x}_2^T\ \boldsymbol{x}_3^T\ \boldsymbol{x}_4^T\right)^T , \qquad \boldsymbol{n}^e = \left(\boldsymbol{n}_1^T\ \boldsymbol{n}_2^T\ \boldsymbol{n}_3^T\ \boldsymbol{n}_4^T\right)^T . \tag{3.12d}$$

An iso-parametric approach uses the same interpolation for geometry $\boldsymbol{c}_s$ and displacement $\boldsymbol{u}_s$, which are now given directly as functions of the modal amplitudes

$$\boldsymbol{u}_s(\boldsymbol{\xi}, \boldsymbol{z}_u) = \left(\boldsymbol{N\Phi}^e - s\boldsymbol{N\Psi}^e\right) \boldsymbol{z}_u . \tag{3.12e}$$

Here, the matrices $\boldsymbol{\Phi}^e$ and $\boldsymbol{\Psi}^e$ represent the predescribed node displacements and rotations of the four corner nodes:

$$\boldsymbol{\Phi}^e = \begin{pmatrix} \boldsymbol{\Phi}_{u,1} \\ \boldsymbol{\Phi}_{u,2} \\ \boldsymbol{\Phi}_{u,3} \\ \boldsymbol{\Phi}_{u,4} \end{pmatrix} , \qquad \boldsymbol{\Psi}^e = \begin{pmatrix} \tilde{\boldsymbol{n}}_1\boldsymbol{\Psi}_{u,1} \\ \tilde{\boldsymbol{n}}_2\boldsymbol{\Psi}_{u,2} \\ \tilde{\boldsymbol{n}}_3\boldsymbol{\Psi}_{u,3} \\ \tilde{\boldsymbol{n}}_4\boldsymbol{\Psi}_{u,4} \end{pmatrix} . \tag{3.12f}$$

To be consistent the strain field evaluation on base of these displacements in modal description has to use the same assumptions as the underlying finite element analysis.

If the modal analysis was done with a Kirchhoff shell element neglecting shear deformation normal to the midplane, the differential strain-displacement operator $\nabla_{u,K}$ has to be used:

$$\nabla_{u,K} = \begin{pmatrix} \frac{\partial}{\partial x_1} & 0 & 0 & \frac{\partial}{\partial x_2} & 0 & 0 \\ 0 & \frac{\partial}{\partial x_2} & 0 & \frac{\partial}{\partial x_1} & 0 & 0 \\ 0 & 0 & 0 & 0 & 0 & 0 \end{pmatrix}^T . \tag{3.13}$$

The differential strain-displacement operator $\nabla_{u,RM}$ according to the Reissner-Mindlin assumption looks like [ZT00b, Ch. 8]

$$\nabla_{u,RM} = \begin{pmatrix} \frac{\partial}{\partial x_1} & 0 & 0 & \frac{\partial}{\partial x_2} & 0 & \frac{\partial}{\partial x_3} \\ 0 & \frac{\partial}{\partial x_2} & 0 & \frac{\partial}{\partial x_1} & \frac{\partial}{\partial x_3} & 0 \\ 0 & 0 & 0 & 0 & \frac{\partial}{\partial x_2} & \frac{\partial}{\partial x_1} \end{pmatrix}^T . \tag{3.14}$$

Eqs. (3.13) and (3.14) use partial derivatives to Cartesian co-ordinates, while (3.12e) is formulated in parameter space. The relation between both vector spaces is given by the Jacobian matrix $\boldsymbol{J}_s$:

$$\left(\frac{\partial}{\partial \boldsymbol{c}_s}\right)^T = \boldsymbol{J}_s^{-1} \left(\frac{\partial}{\partial \boldsymbol{\xi}}\right)^T , \qquad \text{with} \qquad \boldsymbol{J}_s = \left(\frac{\partial \boldsymbol{c}_s}{\partial \boldsymbol{\xi}}\right)^T . \tag{3.15}$$

The strain field of the shell element is completely described. The further evaluation process is identical to the one for the beam element, i.e. the eqs. (3.6) to (3.10) hold for a shell element as well.

3.1.4 Control of a Metal Sheet

Model Description and Simulation Scenario

A metal sheet is presented as an example to demonstrate the feasibility of the proposed methodology. The structure of Fig. 3.3 is equipped with piezo-elements in order to control the vibrations, that are excited by a force impact acting on the centre node of the plate while the displacements on the four corners of the sheet are constrained to be zero.

The elastic steel sheet has the dimensions $1\,\text{m} \times 1.3\,\text{m}$ and is $0.9 \cdot 10^{-3}\,\text{m}$ thick. Initially it has been modelled with the industrial finite element tool ANSYS. The structure is discretised by 140 finite elements of type Shell63 [ANS03] with linear shape functions for bending and membrane deformation, which corresponds to the Kirchhoff shell theory introduced in Sec. 3.1.3.

The modal representation of the metal sheet considers 14 eigenfrequencies, which are specified in Tab. 3.1. The structural damping is set to 0.01. The piezo-elements are attached on both sides of

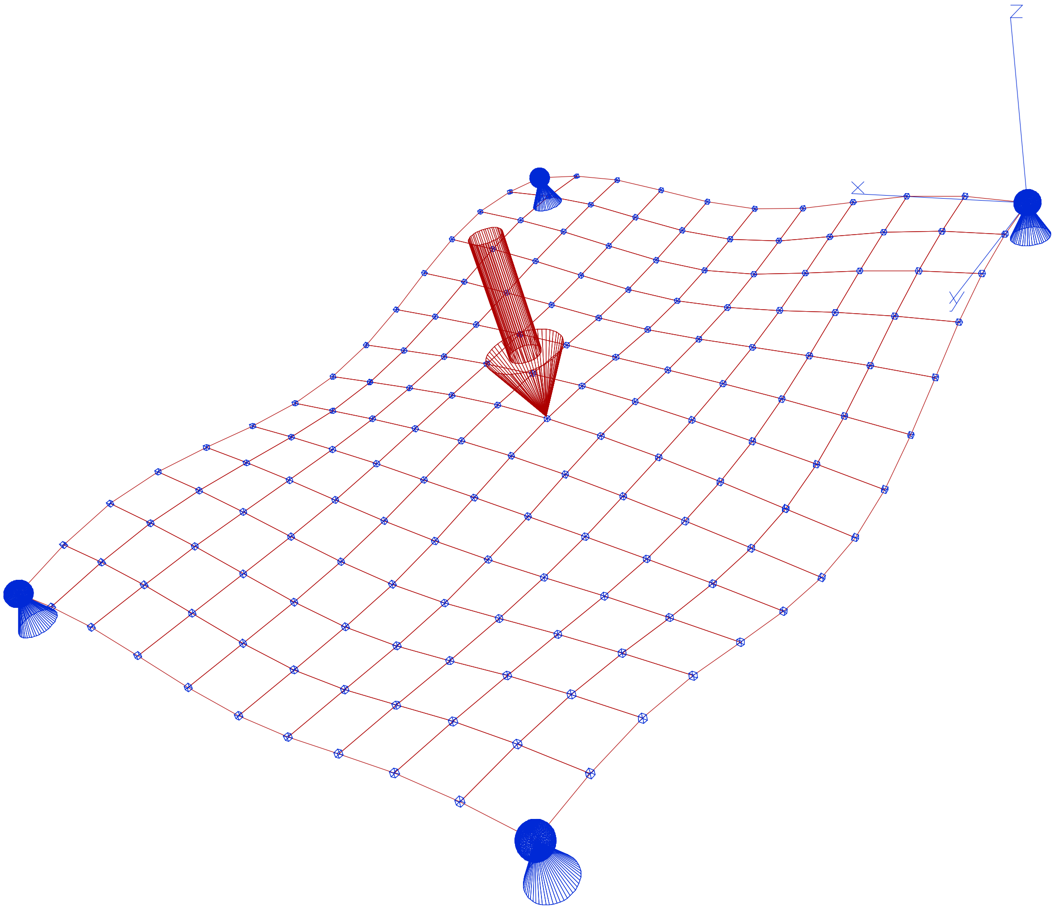

Figure 3.3: Simulation model of the metal sheet with excitation force.

140 finite elements visualised by the mesh in Fig. 3.3. All additional input data of the model is listed in Appendix A.1.

The transient simulation scenario assumes the excitation by a force impact at the time 0.1 s at the centre position, characterised by the amplitude of 20 N over the time period of 0.01 s, see Fig. 3.8. The goal is to minimise the acceleration at the centre of the metal sheet employing not more than 24 patches.

As already noted in Sec. 3.1.2 the comparison of the stiffness matrix offers an easy way to verify

Mode i	1	2	3	4	5	6	7
Frequency [Hz]	1.135	2.557	2.922	3.613	6.412	7.257	7.825

Mode i	8	9	10	11	12	13	14
Frequency [Hz]	10.184	12.735	13.186	14.242	14.905	18.843	19.908

Table 3.1: Eigenfrequencies of the metal sheet model.

	$\boldsymbol{K}_{uu}$(original FE-result)						
1	50.913	0	0	0	0	0	0
2		258.144	0	0	0	0	0
3			337.082	0	0	0	0
4				515.188	0	0	0
5					1623.376	0	0
6						2078.824	0
7	sym.						2417.146
	$\boldsymbol{K}^{*}_{uu}$ (evaluated according to Sec. 3.1.2)						
1	50.351	0	0	-0.803	0	0	-2.757
2		254.573	0	0	0	0	0
3			330.052	0	0	-3.506	0
4				509.770	0	0	6.560
5					1553.771	0	0
6						2030.214	0
7	sym.						2341.896
	$\boldsymbol{K}^{**}_{uu}$ (includes the stiffness of all 280 piezo-elements)						
1	51.099	0	0	0	0	0	0
2		260.005	0	0	0	0	0
3			339.951	0	0	0	0
4				516.081	0	0	0
5					1638.077	0	0
6						2079.905	0
7	sym.						2436.467
	1	2	3	4	5	6	7

Table 3.2: Comparison of the first 7 × 7 elements of the stiffness matrices $\boldsymbol{K}_{uu}$, $\boldsymbol{K}^{*}_{uu}$ and $\boldsymbol{K}^{**}_{uu}$.

the evaluation of the electromechanical data. Tab. 3.2 gives the first 7 × 7 elements of the stiffness matrix $\boldsymbol{K}_{uu}$ as they are received as result of the finite element modal analysis. The second matrix in Tab. 3.2 specifies $\boldsymbol{K}^{*}_{uu}$, i.e. the stiffness values as they are obtained by the reevaluation of the strain field $\boldsymbol{B}^{*}_{u}(\boldsymbol{c})$.

The main diagonal elements of the matrix $\boldsymbol{K}^{*}_{uu}$, which represent the squared mechanical eigenvalues, differ from the corresponding FE-results by about 1.1% to 4.3%. The other, non-vanishing elements of $\boldsymbol{K}^{*}_{uu}$ are negligible, since they hardly alter the stiffness eigenvalues, e.g. by 0.1% for the worst case.

The FE-results are based on the ANSYS finite element type Shell63 that uses an optimised numerical volume integration scheme [ANS03, Sec. 14.63]. For $\boldsymbol{K}_{uu}^{*}$, only the integration over the shell midplane has been performed numerically, the integration normal to the midplane has been formulated analytically according to [ZT00b, Ch. 8]. These circumstances explain that differences are to notice at all. However, in view of the fact that the stiffness values are a quadratic indicator for the accuracy with which the strains could be reevaluated, these differences are negligible.

For the third matrix $\boldsymbol{K}_{uu}^{**}$ in Tab. 3.2, the mechanical stiffness of all 280 piezo-ceramic elements have been added to the original finite element stiffness matrix $\boldsymbol{K}_{uu}$. The extended matrix is then analysed in order to obtain new eigenvalues, which consider as well the stiffness due to the additional attachment of the 280 piezo-ceramic elements. Tab. 3.2 itemises the elements of the diagonalised matrix $\boldsymbol{K}_{uu}^{**}$ with the new, squared eigenvalues on the main diagonal.

An increase of about 0.1% to 0.9% concerning the stiffness values can be observed in Tab. 3.2, when the first and the third matrix are compared. Since the final structure will only include 24 patches, the actual effect of the patch attachment on the stiffness will be even smaller.

Control Design and Optimisation Approach

For controller design the description of the elastic body with piezo-elements is transformed to a state space form:

$$\begin{aligned} \dot{\underline{x}} &= \underline{A}\,\underline{x} + \underline{B}\,\underline{u} \quad , \\ \underline{y} &= \underline{C}\,\underline{x} + \underline{D}\,\underline{u} \quad , \end{aligned} \tag{3.16}$$

Eq. (3.16) defines a multi-input multi-output (MIMO) system, where $\underline{x}$ is the state vector consisting of the modal co-ordinates and their first time derivatives, i.e. $\underline{x}^T = [\,\boldsymbol{z}_u^T \;\; \dot{\boldsymbol{z}}_u^T\,]$. The input vector $\underline{u}$ contains the voltages on the electrodes of the piezo-elements $\boldsymbol{z}_\varphi$, while the corresponding charges $\boldsymbol{h}_\varphi$ are included in the output vector $\underline{y}$. The system matrices $\underline{A}, \underline{B}, \underline{C}, \underline{D}$ are composed of the matrices $\boldsymbol{M}_{uu}$, $\boldsymbol{K}_{uu}$, $\boldsymbol{D}_{uu}$, $\boldsymbol{K}_{u\varphi}$ and $\boldsymbol{K}_{\varphi\varphi}$, which are defined in Tab. 2.1 and Tab. 2.4:

$$\begin{aligned} \underline{A} &= \begin{pmatrix} \boldsymbol{0} & \boldsymbol{I} \\ -\boldsymbol{M}_{uu}^{-1}\boldsymbol{K}_{uu} & -\boldsymbol{M}_{uu}^{-1}\boldsymbol{D}_{uu} \end{pmatrix}, & \underline{B} &= \begin{pmatrix} \boldsymbol{0} \\ -\boldsymbol{M}_{uu}^{-1}\boldsymbol{K}_{u\varphi} \end{pmatrix}, \\ \underline{C} &= \begin{pmatrix} \boldsymbol{K}_{u\varphi}^T & \boldsymbol{0} \end{pmatrix}, & \underline{D} &= \begin{pmatrix} \boldsymbol{K}_{\varphi\varphi} \end{pmatrix}, \end{aligned} \tag{3.17}$$

where $\boldsymbol{I}$ is the identity matrix and $\boldsymbol{0}$ is the zero matrix. The number r of inputs and m of outputs in (3.16) corresponds to the number of piezo-elements and the number of states n is the double of the elastic degrees of freedom, provided that large reference motion is not considered.

Traditional state feedback with linear quadratic regulator (LQR) control design is applied to the

	$[\boldsymbol{\Phi}_u(\boldsymbol{c}_m)]_{i,z}$ [m]				
i	1	4	7	11	14
z	0.446	-0.0056	-0.7134	0.0640	-0.6447

Table 3.3: Normalised modal displacements $\boldsymbol{\Phi}_u(\boldsymbol{c}_m)$ in [m] at the centre node for five modes.

MIMO system (3.16). In the first stage it is supposed that every shell element of the elastic structure is equipped with one piezo-patch on each side. Each piezo-patch serves simultaneously as an actuator and a sensor. The output vector $\underline{y}$ includes output charges of the piezo-patches instead of states, which are needed for the LQR design. However, one can construct a state estimate $\bar{\underline{x}}$ such that the control law retains similar closed-loop properties, [Pre02, Sec. 7.6].

Furthermore, it is presumed that the structural matrices $\boldsymbol{M}_{uu}$, $\boldsymbol{D}_{uu}$ and $\boldsymbol{K}_{uu}$ of the system have been diagonalised and the eigenmodes have been scaled in such a way, that the mass matrix $\boldsymbol{M}_{uu}$ is the identity matrix and the squared eigenvalues are arranged on the main diagonal of the stiffness matrix $\boldsymbol{K}_{uu}$ [GK87, Sec. 8.3].

The control design relies on the selection of the weighting matrix $\underline{Q}$ in the LQR design cost function:

$$J = \int_0^{\infty} \left(\underline{x}^T \underline{Q}\, \underline{x} + \underline{u}^T \underline{R}\, \underline{u} \right) \mathrm{d}t \tag{3.18}$$

with $\underline{R} := \boldsymbol{I}$ and

$$\underline{Q} = k_Q \begin{pmatrix} \underline{Q}_{11} & \boldsymbol{0} \\ \boldsymbol{0} & \underline{Q}_{22} \end{pmatrix} . \tag{3.19}$$

k_Q is a scalar parameter, $\underline{Q}_{11}$ and $\underline{Q}_{22}$ are diagonal matrices, which have to be defined in order to meet the optimisation objectives, namely to minimise the vertical acceleration on the centre node.

The term V represents the sum of the kinetic and deformation energy, if defined as follows:

$$V = \frac{1}{2}\, \underline{x}^T \underline{Q}\, \underline{x} \qquad \text{with} \quad \underline{Q}_{11} = \text{diag}\left\{\omega_i^2\right\} \quad \text{and} \quad \underline{Q}_{22} = \boldsymbol{I} , \tag{3.20a}$$

where ω_i denotes the i-th eigenvalue. Consequently, the cost-function (3.18) can be interpreted physically for this choice of the weighting matrices $\underline{Q}_{11}$ and $\underline{Q}_{22}$, see [HL93].

However, the optimisation objective is defined w.r.t. the motion of the centre node. Therefore, the weighting matrices have been set to

$$\underline{Q}_{11} = \text{diag}\left\{\omega_i \ \cdot \ |[\boldsymbol{\Phi}_u(\boldsymbol{c}_m)]_{i,z}|\right\} \qquad \text{and} \qquad \underline{Q}_{22} = \boldsymbol{0} \tag{3.20b}$$

for the following simulations. $|[\boldsymbol{\Phi}_u(\boldsymbol{c}_m)]_{i,z}|$ denotes the modal displacements concerning the i-th mode in vertical direction at the centre node. Tab. 3.3 lists these displacements omitting the modes which do not affect the central position at all.

The solution of the optimisation problem (3.18) with (3.20b) is a constant gain linear state feedback [HGP98, Sec. 8.2]:

$$\underline{u} = -\underline{K}\,\underline{x}\ . \tag{3.21}$$

An important feature is the efficient selection of the piezoelectric patches, which will be used for the controller of the flexible body. The applied selection criterion is directly based on the feedback gain $\underline{K}$ of the LQR controller. The matrix $\underline{K}$ is a r-by-n matrix, where $r = 280$ is the number of inputs and $n = 28$ is the number of states of the controlled system. Since the inputs represent the voltages applied on the piezo-patches, each column vector $[\underline{K}]_l$ $(1 \leq l \leq r)$ can be assigned to one specific patch and the corresponding vector norm ζ_l can be evaluated:

$$\zeta_l = \sqrt{[\underline{K}]_l^T\ [\underline{K}]_l}\ ,\ 1 \leq l \leq r\ . \tag{3.22}$$

Those 24 patches with the largest norm ζ_l are assumed to be the most important and are selected for control. After the selection of the reduced set of patches, a new LQR design is performed.

Fig. 3.4 depicts the block diagram of the final control set-up. A Luenberger observer is used to estimate the state vector from the output measurements $\underline{y}$. The parameter k_Q from (3.19) is tuned to use the patches as efficiently as possible, i.e. the controller should use the whole linear range of the piezo-element for the expected disturbances.

Simulation Results

Since the considered structure is symmetric w.r.t. two main axes and the patches are located on both sides of the metal sheet, the final number of patches will be a multiple of eight. The importance of

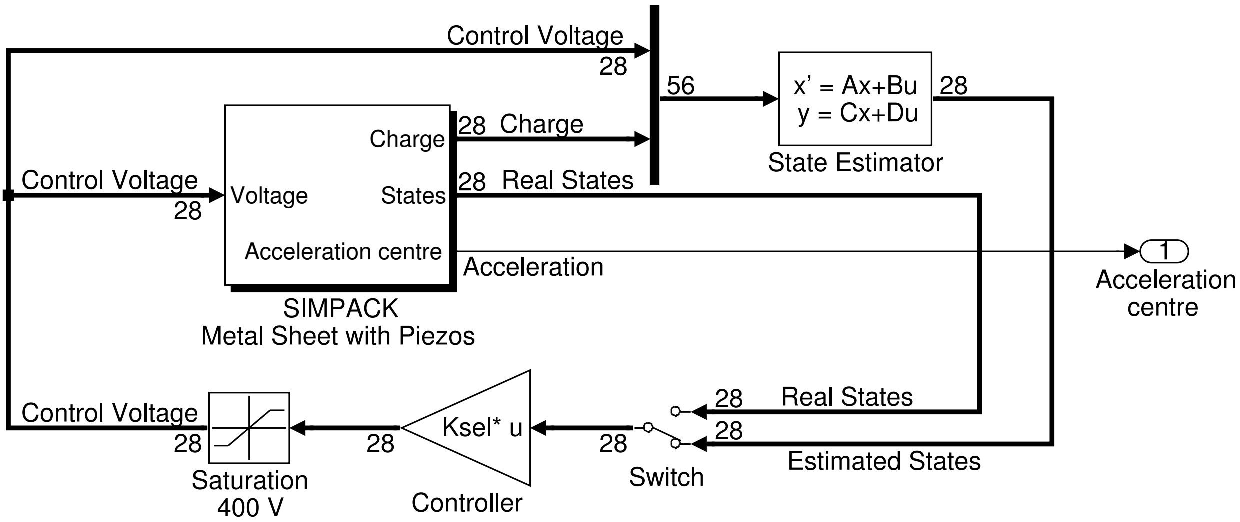

Figure 3.4: Block diagram of the control loop [VH04b].

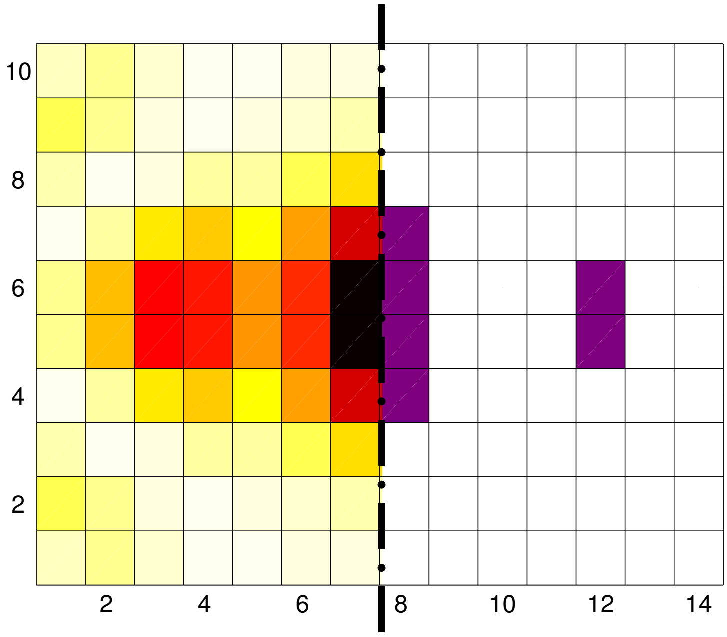

Figure 3.5: Mesh with piezo-patches: The shades of grey on the left half plane reflect the corresponding value ζ_l according to (3.22). The patches that have been selected for control are marked on the right hand side.

the patch positions w.r.t. the control of the motion of the sheet's centre point and the finally selected set of patches are illustrated in Fig. 3.5.

A comparison of the accelerations in the centre of the metal sheet is presented in Figure 3.6. The

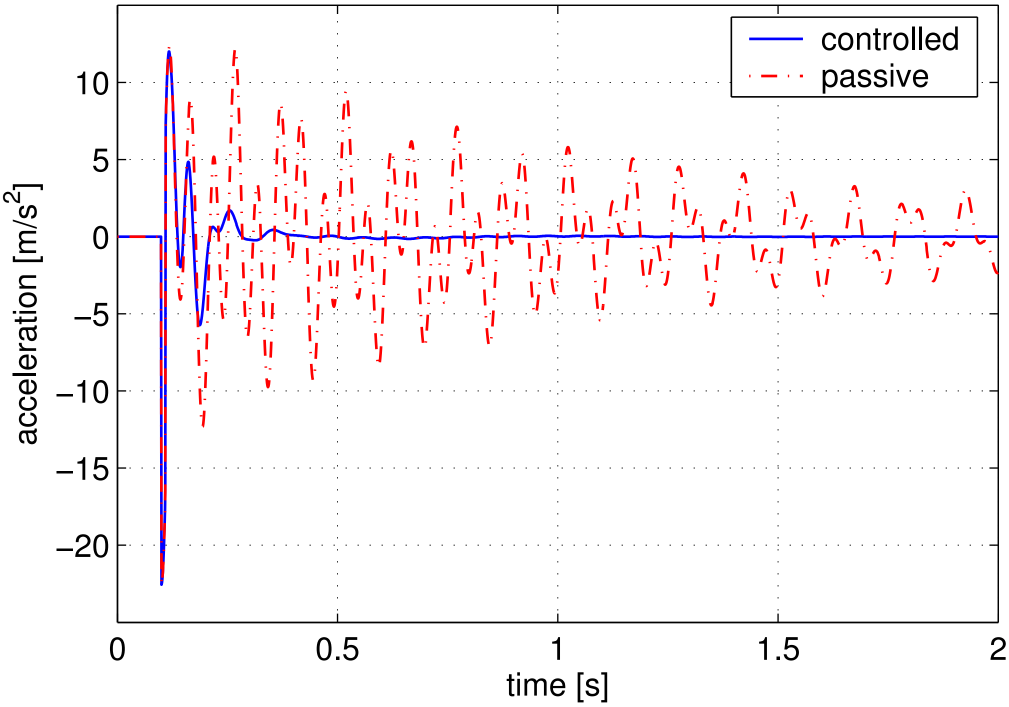

Figure 3.6: Comparison of the acceleration at the centre node.

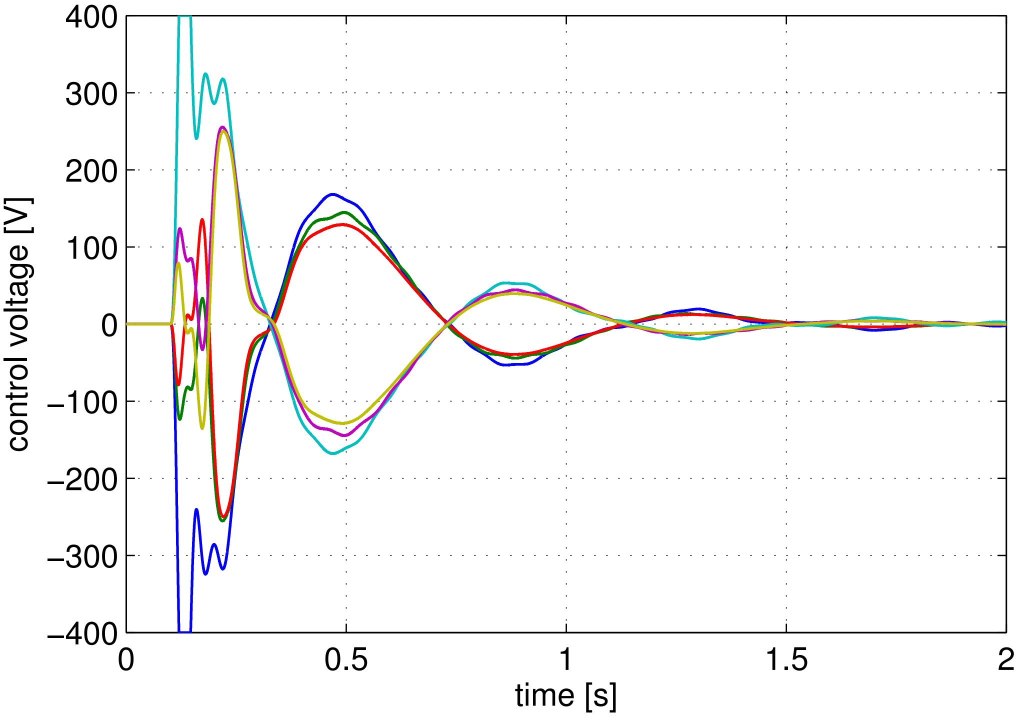

Figure 3.7: Time plot of the applied voltages.

dash-dotted line shows the response of the sheet without any controller. The structure is damped by structural damping only. The solid line represents the controlled system from the Fig. 3.4, which contains a state estimator and LQR feedback controller. The damping behaviour of the structure is significantly enhanced by the active structural control set-up. The optimisation objectives are therefore achieved. The voltages applied to the piezo-patches are presented in Figure 3.7.

A saturation block as part of the controller in Fig. 3.4 limits the voltage to 400 V. This restriction is necessary since unexpected high disturbances may lead to very high voltages and as a consequence to dielectric breakdown of the piezo-elements. The specific cut-off voltage was chosen in such a way that it is reached only in immediate response to the assumed force impact.

Fig. 3.8 analyses the simulation results from the energetic point of view. Surprisingly, the instantaneous mechanical energy of the structure, evaluated by (3.20), does not decrease monotonously. This behaviour is nor caused by the state estimator, neither due to the voltage limitation, but has to be attributed to the LQR design and could also be observed with the pure energy cost function (3.20) in (3.18).

Except for the structural damping, the decrease of the mechanical energy corresponds to the cumulative electric work of the piezo-patches W_e, which may be obtained by one of the following calculations:

$$W_e = \int \underline{u}^T \underline{C}\,\underline{\dot{x}}\;\mathrm{d}t = \int \dot{\boldsymbol{z}}_u^T \boldsymbol{K}_{u\varphi}\,\boldsymbol{z}_\varphi\;\mathrm{d}t = \int \underline{u}^T \underline{\dot{y}}\;\mathrm{d}t = \int P_e\;\mathrm{d}t \tag{3.23}$$

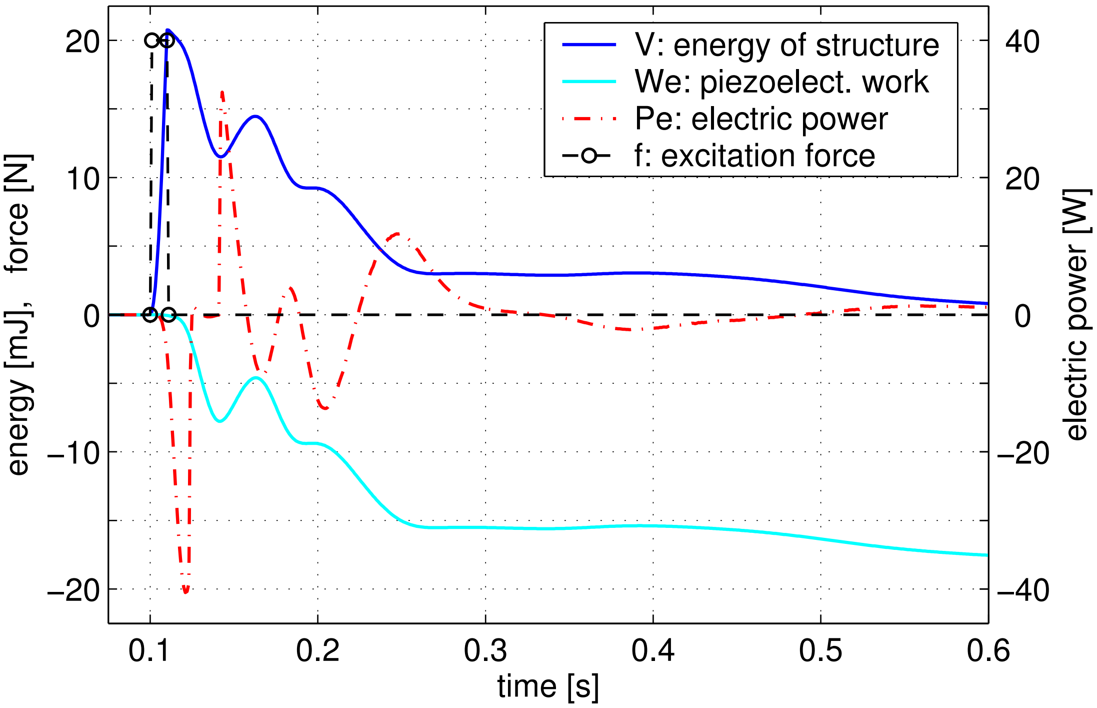

Figure 3.8: Time plot of the instantaneous energy of the mechanical structure V, the cumulative electric work of the piezo-patches W_e, the electric power P_e and the excitation $f(t)$.

3.1.5 Discussion of the Approach

The presented preprocessing method is based on the description of the mechanical structure in finite element representation. The electrical and electromechanical data are generated subsequently. Therefore, the determination of optimal patch locations and control parameters may be set up in a very efficient way. Whatever optimisation methodology might be employed, the costly structural finite element analysis has to be performed only once. The optimisation task is decomposed.

The contrasting concept, namely the simultaneous optimisation of structure, actuator placement and control parameters offers a greater potential to improve the performance of smart structures, see e.g. [LLMB00]. However, the complexity of the optimisation task has then to be ruled which might be difficult for structures with a complex geometrical shape close to realistic design.

The proposed selection of patch locations based on the cost functional from optimal control proved to be very efficient since the advanced solution methods that have been developed for LQR control and the associated RICCATI equation can be applied, see [HGP98, Sec. 8.2.6]. The advantage in comparison with selection criteria based on controllability and observability Gramians [HL93] consists of the possibility to consider specific optimisation objectives by means of an appropriate weighting matrix $\boldsymbol{Q}$.

Special care is necessary if the attachment of piezo-patches changes the structural properties significantly and if piezo-ceramic actuators excite modes that are not considered in the modal description of the structure (*spill over effect*) [Pre02, Sec. 9.13].

The outlined technique is linear w.r.t. the geometrical behaviour and the physical description of materials. The control is based on voltage driven electrodes. Recent publications propose the charge control of the piezo-patches and expect the physical behaviour to be closer to the linear idealisation with less hysteresis [Pre04]. Approaches for the finite element analysis that include geometrical and physical nonlinear effects have also been published [SLHL00].

3.2 Modelling of Thermoelasticity

In this section a novel approach to simulate thermoelastic behaviour in multibody dynamics is introduced. In order to accomplish high efficiency only those effects are considered that have a significant impact on the solution of the thermoelastic problem.

The section starts presenting two classical problems from literature that demonstrate the physical background of the thermoelastic problem and its implications.

On that basis a strategy is developed that exploits reasonable simplifications and introduces a modal reduction scheme. Since the coupled thermal and mechanical analysis is a standard task of industrial finite element tools, the necessary data are readily available.

The section continues with two case studies posting verification examples, in which the results of finite element analysis are compared to the solutions of the proposed modal approach. The limitations, advantages and disadvantages of the modal multifield approach concerning thermoelasticity are discussed with respect to these verification results.

3.2.1 The Effects of Coupling and Inertia

The theoretical framework which has been developed in Ch. 2 has led to (2.59) and (2.57), where a bi-directional coupling of the thermal and mechanical problem is given. Fortunately in most of the usual engineering applications is it possible to omit the mechanical coupling term in the thermal equation, i.e. to neglect the Gough-Joule effect, and the inertia terms associated with thermal induced displacements in the equations of motion, which is called Duhamel's assumption. The following section is supposed to justify these simplifications.

The Coupled Thermoelastic Beam

Lifshitz and Roukes [LR00] discussed the influence of full thermoelastic coupling on a beam structure. They considered a rectangular Euler-Bernoulli beam according to Fig. 3.9 with bending deflection $u(x)$ in the x-z-plane, which leads to a uni-directional strain field in x-direction $\varepsilon_{xx}(x,z)$. I denotes the beam's geometrical moment of inertia, h its height and A its cross section area.

The thermal description is based on (2.41) presuming linear isotropic material and only accounts for thermal gradients in z-direction. Eq. (3.24) summarises the modelling assumptions adapting tensorial index notation, i.e. $(\ )_{,xx}$ denotes the second partial derivative w.r.t. x [LR00]:

$$\vartheta_{,xx} \approx 0 \ , \qquad \vartheta_{,yy} = 0 \ , \qquad \varepsilon_{xx} = -z\,u_{,xx} \ , \qquad \nu \approx 0 \ , \qquad I_\vartheta = \int_A z\vartheta \,\mathrm{d}y\mathrm{d}z \ , \tag{3.24}$$

where the cross section integral I_ϑ represents the thermal load of the beam, see [BW97, (10.11.2)].

The coupled partial differential equations of the beam get the form

$$\frac{\Lambda}{\varrho c}\,\vartheta_{,zz} + z\,E\alpha\Theta_0\,\dot{u}_{,xx} = \dot{\vartheta} \ , \tag{3.25a}$$

$$\varrho A\,\ddot{u} + (EI\,u_{,xx} + E\alpha I_\vartheta)_{,xx} = 0 \ . \tag{3.25b}$$

For the solution of (3.25) harmonic vibrations of the beam are considered with geometrical shape functions $u_o(x)$ and $\vartheta_o(x,z)$, that align with the geometrical boundary conditions:

$$u(x,t) = u_o(x)\,\mathrm{e}^{j\omega t} \ , \qquad \vartheta(x,z,t) = \vartheta_o(x,z)\,\mathrm{e}^{j\omega t} \ , \qquad \omega \in \mathbb{C} \ . \tag{3.26}$$

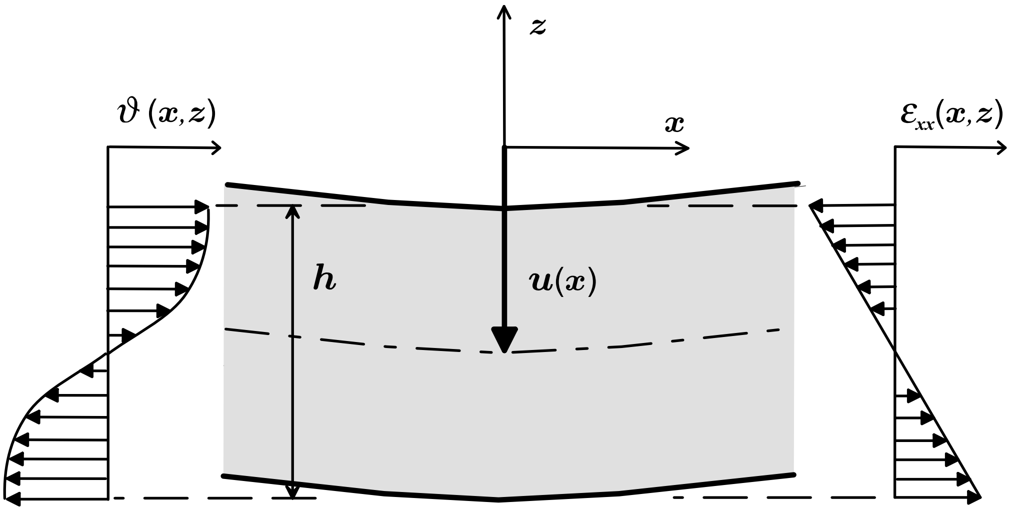

Figure 3.9: Co-ordinate definitions, temperature field $\vartheta(x,z)$, displacement field $u(x)$ and strain field $\varepsilon_{xx}(x,z)$ at a beam section according to [LR00].

If (3.26) is inserted in (3.25a), a particular solution of the thermal field may be obtained that satisfies the boundary condition of vanishing heat fluxes on the lateral surfaces of the beam, $\vartheta_{o,z}(z = \pm h/2) = 0$:

$$\vartheta_o = \frac{E\alpha\Theta_0}{\varrho c}\, u_{o,xx} \left[z - \frac{\sin(kz)}{k\cos(kh/2)} \right] \qquad \text{with} \qquad k = \sqrt{j\omega \frac{\varrho c}{\Lambda}}\;. \tag{3.27}$$

With the temperature solution (3.27), I_ϑ from (3.24) can be integrated and inserted into (3.25b), which yields the following eigenvalue equation:

$$\varrho A u_o\, \omega^2 - \underbrace{E \left[1 + \frac{E\alpha^2\Theta_0}{\varrho c} \left(1 + \frac{24}{h^3 k^3} \Big(\frac{kh}{2} - \tan\big(\frac{kh}{2}\big) \Big) \right) \right]}_{\bar{E}(\omega)} I\, u_{o,xxxx} = 0\;. \tag{3.28}$$

Eq. (3.28) looks similar to the eigenvalue equation of a classical Euler-Bernoulli beam, e.g. [Bre88, (6.120)], in which a frequency-dependent Young's modulus $\bar{E}(\omega)$ is introduced.

In the limit cases $\operatorname{Re}\omega \to 0$ and $\operatorname{Re}\omega \to \infty$, the following expressions are obtained:

$$\lim_{\operatorname{Re}\omega \to 0} \bar{E}(\omega) = E\;, \qquad\qquad \lim_{\operatorname{Re}\omega \to \infty} \bar{E}(\omega) = E \left(1 + \frac{E\alpha^2\Theta_0}{\varrho c} \right)\;. \tag{3.29}$$

For a stiff beam with very high eigenfrequencies, the imaginary part of $\bar{E}(\omega)$ vanishes and the real part can be identified as the adiabatic Young's modulus, the one-dimensional analogue to (2.34). That means, a high frequency vibration occurs as a adiabatic process since the thermal field, which is comparable "slow" with large time constants, cannot follow the fast displacement variations.

On contrary, for weak beams with very low eigenfrequencies, $\bar{E}(\omega)$ recovers the isothermal value of Young's modulus. The displacements change very slowly, the thermal field is balanced almost all the time.

Isothermal and as well adiabatic reversible processes do not alter the entropy of the system, or in short, there is no dissipation. That is also indicated by (3.29) in which both limiting values are purely real. On the other hand, for intermediate frequencies $\bar{E}(\omega)$ and consequently ω are complex quantities. The vibration according to (3.26) is damped although no damping force was defined explicitly in (3.25b).

This phenomenon is called thermoelastic damping or internal friction [Zen60]. Vibrations result in strain changes in the beam. This is accompanied by temperature changes and consequently by a heat flow. Since heat flow is an irreversible process under non-isothermal, i.e. real conditions, vibration energy is finally stored in a mechanically irrecoverable way, see [KM92]. ZENER [Zen60] concludes, that thermoelastic coupling changes a Hooke solid into a standard linear solid with an-elastic properties, cf. [GHSW95, Sec. 6.2.1.3].

The significance of thermoelastic damping for practical engineering problems is demonstrated, if the eigenvalue ω of (3.28) is directly compared to the classical, isothermal eigenvalue of the Euler-Bernoulli beam ω_o:

$$\frac{\omega}{\omega_o} = \sqrt{1 + \frac{E\alpha^2\Theta_0}{\varrho c}\left(1 + \frac{24}{h^3k^3}\left(\frac{kh}{2} - \tan(\frac{kh}{2})\right)\right)}\,, \tag{3.30a}$$

$$\xi := k_o h = h\sqrt{\frac{\omega_o \varrho c}{2\Lambda}}\,, \qquad a(\xi) = \frac{\operatorname{Im}\omega}{\omega_o}\,, \qquad s(\xi) = \frac{\operatorname{Re}\omega - \omega_o}{\omega_o}\,. \tag{3.30b}$$

The parameter ξ combines a number of geometrical and physical parameters. Fig. 3.10 shows frequency shift $s(\xi)$ and attenuation $a(\xi)$ of a steel beam due to thermoelastic coupling.

The attenuation reaches its maximum value $\hat{a} = 5.5 \cdot 10^{-4}$ at $\hat{\xi} = 2.23$. The maximum frequency shift is 0.1 %. The design parameter value $\hat{\xi} = 2.23$ specifies e.g. a steel beam, $h = 2\,$mm high, with the first eigenfrequency $\omega_o/(2\pi) = 4.8$ Hz (1 m long, both ends fixed).

These results clarify that for conventional structures in mechanical engineering the eigenvalues are changed only very slightly due to thermoelastic damping, see also [BW97, Ch. 2] and [Now78b, Ch. 8]. From the system dynamical point of view the mechanical eigenvalue problem may be considered separately from the thermal eigenvalue problem. This is an important conclusion which will be exploited for the modal approach.

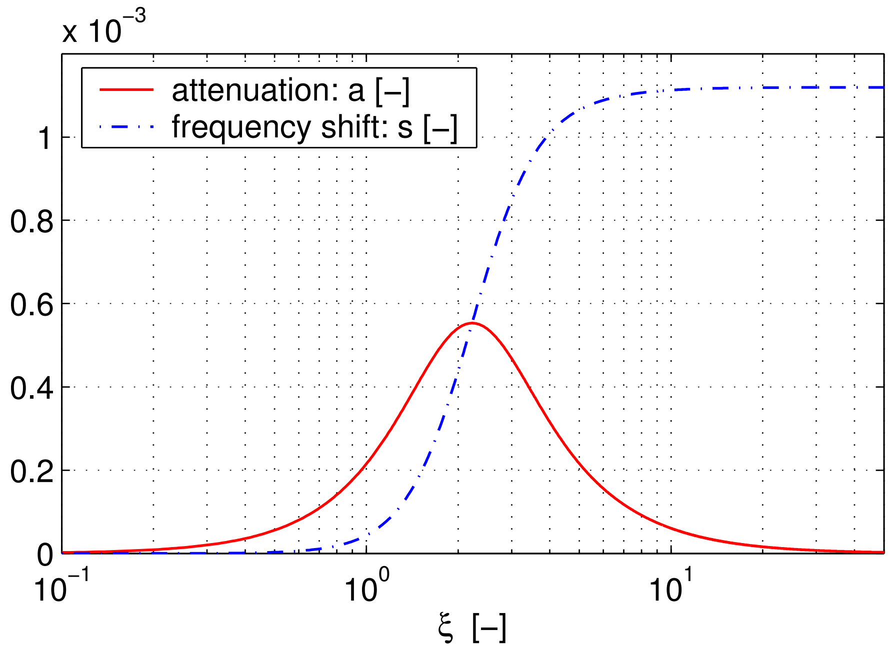

Figure 3.10: Attenuation and frequency shift of a rectangular steel beam due to thermoelastic coupling [LR00, Fig. 1].

Duhamel's Assumption

In 1837, DUHAMEL noted that the mechanical inertia terms are not significant in the equations of thermoelasticity, since the time rate of temperature change is sufficiently slow (Duhamel's assumption). In 1950, this question was examined by DANILOVSKAYA in more detail [BW97, Sec. 2.5]. Her argumentation supports the selection of modes which are capable to describe thermal influences on the displacement field and is therefore presented briefly in what follows.

Consider an elastic half space, $x > 0$, which is constrained in such a way that only displacements in x-direction occur. The plane $x = 0$ is suddenly exposed to a heat flux according to a Robin boundary condition with a finite film coefficient h_f. In the thermal description (3.25a), the mechanical coupling term is neglected. The mechanical equation is formulated in terms of stress components:

$$\frac{\Lambda}{\varrho c}\,\vartheta_{,xx} = \dot{\vartheta}\ , \tag{3.31a}$$

$$\frac{E(1-\nu)}{\varrho(1+\nu)\,(1-2\nu)}\,\sigma_{xx,xx} - \ddot{\sigma}_{xx} = \frac{E\alpha}{1-2\nu}\,\ddot{\vartheta}\ . \tag{3.31b}$$

The initial and boundary conditions are

$$\begin{aligned} \vartheta(x,0) &= 0\ , & \sigma_{xx}(x,0) &= \dot{\sigma}_{xx}(x,0) = 0\ , \\ \Lambda\,\vartheta_{,x}(0,t) &= h_f\left[\vartheta(0,t) - \vartheta_\infty\,\right]\ , & \sigma_{xx}(0,t) &= 0\ , \\ \lim_{x\to\infty}\vartheta(x,t) &= 0\ , & \lim_{x\to\infty}\sigma_{xx}(x,t) &= 0\ . \end{aligned} \tag{3.31c}$$

The analytical solution of (3.31) via Laplace transformation yields an expression that is somewhat cumbersome to interpret. That is why the discussion here is based on the graphical presentation of the analytical solution in Fig. 3.11.

It is interesting to study the behaviour for a film coefficient h_f tending towards infinity. An infinite boundary conductance means, that the boundary temperature at $x = 0\,,\ t = 0$ discontinuously jumps to the environmental temperature ϑ_∞ (*thermal shock load*). The structural response consists of a compressive wave propagating with sonic speed through the elastic body. Fig. 3.11 visualises the pressure as function of time at an exemplary point. For the assumed material the maximum pressure reaches values beyond its strength.

From a practical viewpoint it is even more interesting to study the behaviour for smaller film coefficients h_f. The maximum pressure decreases very rapidly for finite boundary conductances. Even in heat exchanger design real film coefficients beyond $10^5\ \mathrm{W/(m^2K)}$ cannot be reached.

As a consequence for real load cases the wave propagation of thermoelastic loads may be disregarded without introducing a substantial error. Since wave propagation is a genuine inertia effect it may be concluded that the inertia terms are negligible in the equations of thermoelasticity. This

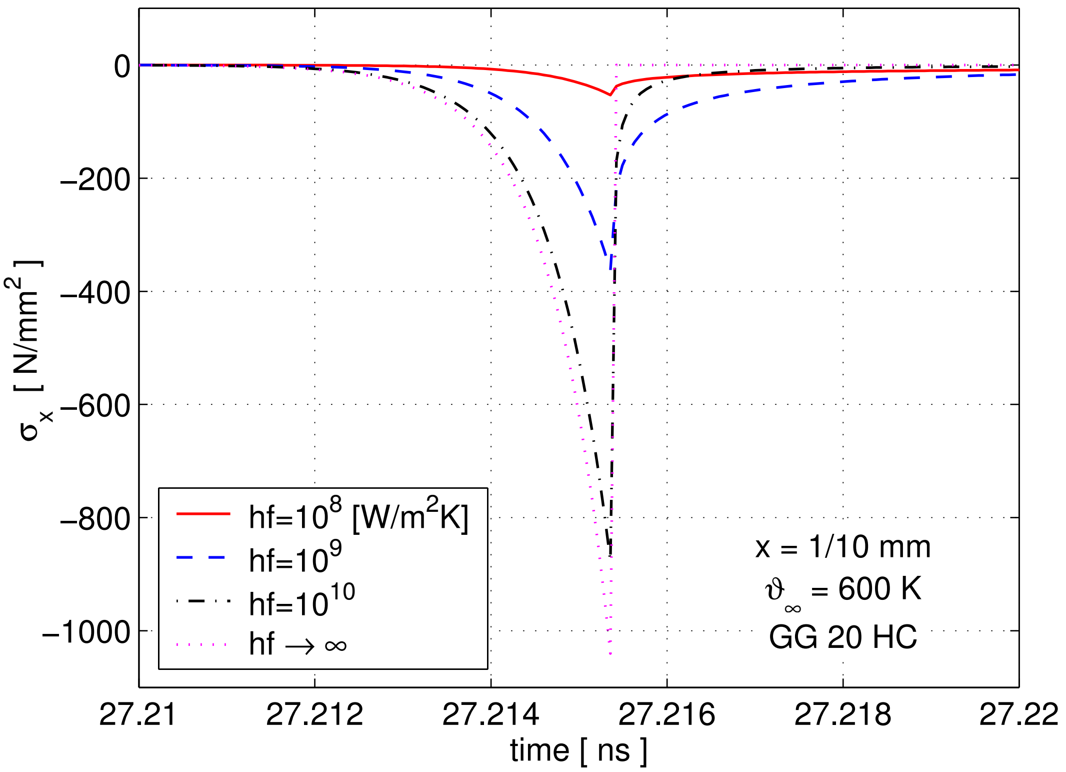

Figure 3.11: Propagating pressure waves due to thermal shock for various film coefficients h_f. The results are based on the analytical solution of (3.31), evaluated for the material GG20HC (physical data see Sec. 3.2.3) at the position $x = 1/10\,\mathrm{mm}$.

conjecture was considered at the very beginning when the theory of thermoelasticity was developed by DUHAMEL in 1837.

3.2.2 Thermal Response Modes

From the mechanical point of view the thermal field may be interpreted as a specific source of distributed mechanical loads. These specific loads may be considered to establish the modal representation of the mechanical structure by a range of corresponding particular solutions of the equations of motion.

Additionally the analytical models introduced in the previous section motivate simplifications. Firstly they allow to deal with the thermal eigenvalue problem and the mechanical eigenvalue problem separately. Secondly they justify to neglect inertia terms regarding deflections due to thermal loads.

These considerations lead to a specific modal reduction scheme that organises the access to existing finite element data and its transfer into the modal representation. Fig. 3.12 delineates the essentials of this scheme, which consists of four steps:

1. Firstly, the thermal finite element description has to be reduced. The modal approach in (2.45) is rewritten in discretised form for the temperature ϑ at a specific node k, located at $\boldsymbol{c}_k$: $\vartheta = \vartheta(\boldsymbol{c}_k)$. The number of thermal degrees of freedom of the finite element system is denoted by n_ϑ and of the modal system by m_ϑ:

   $$\vartheta(\boldsymbol{c}_k) = \boldsymbol{\Phi}_\vartheta(\boldsymbol{c}_k)\, \boldsymbol{z}_\vartheta \;, \qquad 1 \le k \le n_\vartheta \;, \tag{3.32a}$$

   $$\boldsymbol{\Phi}_\vartheta(\boldsymbol{c}_k) = [\; \ldots \; \vartheta_i \; \ldots \;] \;, \qquad 1 \le i \le m_\vartheta \;. \tag{3.32b}$$

   The temperatures of all nodes k, assigned to a specific mode i constitute one modal temperature field $\boldsymbol{\vartheta}_i$ and one column of the thermal modal matrix $\hat{\boldsymbol{\Phi}}_\vartheta$ in the finite element discretisation[1]:

   $$\boldsymbol{\vartheta}_i = (\; \ldots \vartheta_k \ldots \;)^T \;, \qquad \boldsymbol{\vartheta}_i \in \mathbb{R}^{n_\vartheta} \;, \tag{3.32c}$$

   $$\hat{\boldsymbol{\Phi}}_\vartheta = [\; \ldots \; \boldsymbol{\vartheta}_i \; \ldots \;] \qquad \hat{\boldsymbol{\Phi}}_\vartheta \in \mathbb{R}^{n_\vartheta, m_\vartheta} \;. \tag{3.32d}$$

   Hence, each vector $\boldsymbol{\vartheta}_i$ represents a discrete thermal mode, i.e. assigns one temperature to each node or finite element degree of freedom respectively. A mode may be a solution of the thermal eigenvalue problem $[\hat{\boldsymbol{C}}_{\vartheta\vartheta}\kappa_i + \hat{\boldsymbol{K}}_{\vartheta\vartheta}]\boldsymbol{\vartheta}_i = 0$ as it is presented in Fig. 3.14 on p. 77, or a solution of a steady state problem. The selection of specific modes may also be motivated by given spatial or time load distributions, as it is demonstrated in Fig. 3.18 on p. 84.

   The following modal reduction of the finite element equations is a standard reduction approach and yields the matrices of the thermal system according to Tab. 2.5:

   $$\boldsymbol{C}_{\vartheta\vartheta} = \hat{\boldsymbol{\Phi}}_\vartheta^T \hat{\boldsymbol{C}}_{\vartheta\vartheta}\, \hat{\boldsymbol{\Phi}}_\vartheta \;, \qquad \boldsymbol{K}_{\vartheta\vartheta} = \hat{\boldsymbol{\Phi}}_\vartheta^T \hat{\boldsymbol{K}}_{\vartheta\vartheta}\, \hat{\boldsymbol{\Phi}}_\vartheta \;. \tag{3.32e}$$

2. The second step consists of a static analysis of the mechanical system. Each thermal mode $\boldsymbol{\vartheta}_i$ constitutes one mechanical load vector $\hat{\boldsymbol{h}}_i$ and results in one corresponding static displacement solution $\boldsymbol{u}_i$, further on called a *thermal response mode*:

   $$\hat{\boldsymbol{h}}_i = \boldsymbol{f}(\boldsymbol{\vartheta}_i) \;, \qquad \hat{\boldsymbol{K}}_{uu}\boldsymbol{u}_i = \hat{\boldsymbol{h}}_i \;, \qquad \boldsymbol{u}_i \in \mathbb{R}^{n_u} \;. \tag{3.33}$$

3. In the third step additional displacement modes have to be evaluated and selected that represent the native mechanical behaviour of the system, see [SWD99] and [Die99] for appropriate mode selection techniques.

   These purely mechanical modes $\boldsymbol{u}_l$ together with the thermal response modes constitute the mechanical modal matrix $\hat{\boldsymbol{\Phi}}_u$ in finite element discretised form:

   $$\hat{\boldsymbol{\Phi}}_u = [\; \ldots \; \boldsymbol{u}_i \; \ldots \; \boldsymbol{u}_l \; \ldots] \;, \qquad m_\vartheta < l \le m_u \;, \qquad \hat{\boldsymbol{\Phi}}_u \in \mathbb{R}^{n_u, m_u} \;. \tag{3.34a}$$

   If the column vectors of $\hat{\boldsymbol{\Phi}}_u$ are linearly dependent, a maximum subset of linearly independent column vectors is selected to meet the demands of the Ritz approach. But the verification

---

[1] The accent ($\hat{\ }$) indicates finite element quantities if they might be mixed up with the corresponding modal terms.

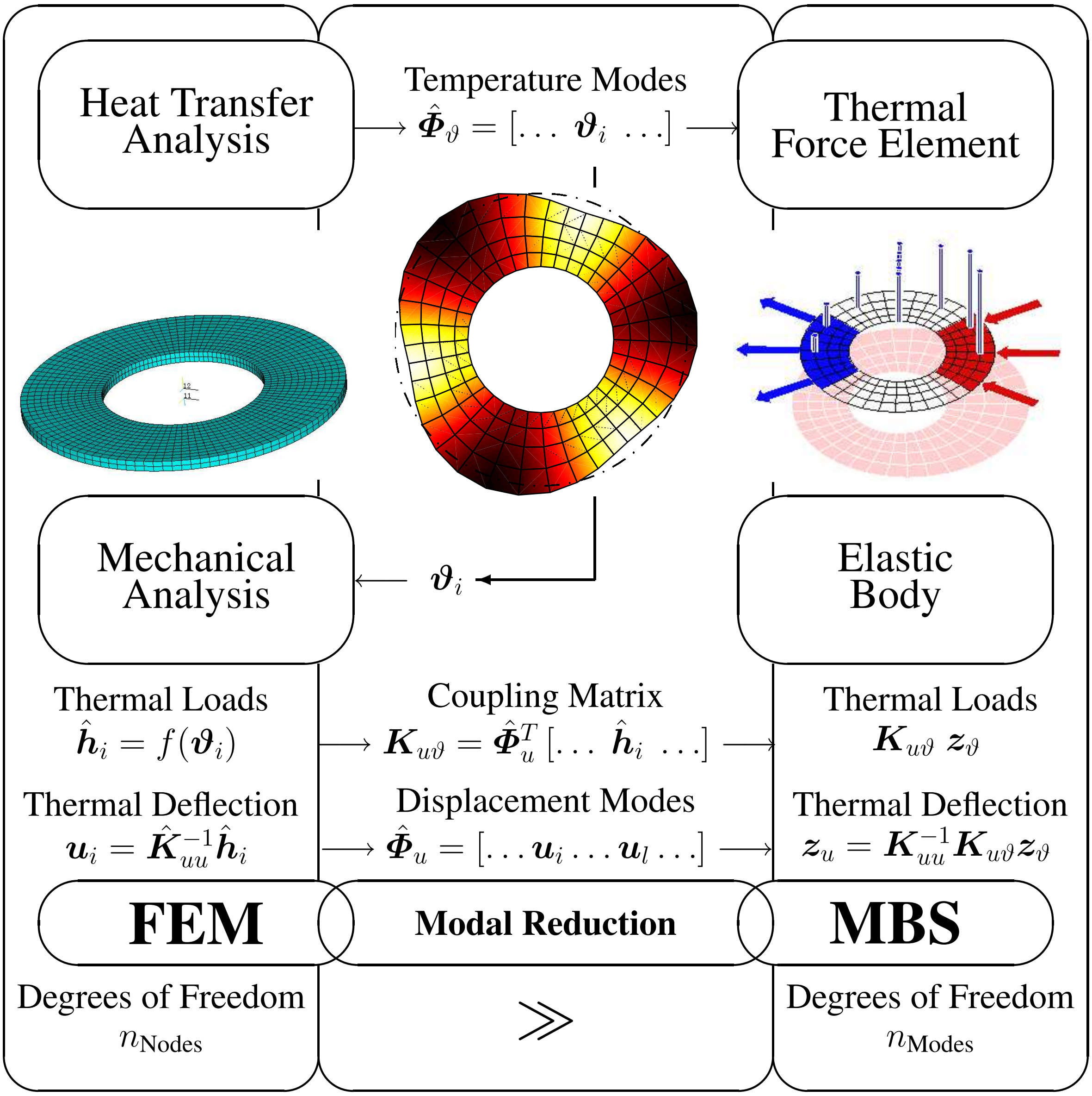

Figure 3.12: Reduction from finite element to modal description with thermal modes $\boldsymbol{\vartheta}_i$, thermal response modes $\boldsymbol{u}_i$ and purely mechanical modes $\boldsymbol{u}_l$.

examples will show that this situation is not likely to occur since both kinds of displacement solutions are of completely different nature.

4. The definition (3.34a) enables the transformation of the mechanical system from the finite element to the multibody description that is based on the modal approach in (2.7). That way, the volume integrals of Tab. 2.1 are obtained by accessing the finite element data. The modal reduction of the finite element mass and stiffness matrix, $\hat{\boldsymbol{M}}_{uu}$ and $\hat{\boldsymbol{K}}_{uu}$, exemplifies this transformation, which is presented in detail in [SW99, Ch. 6]

$$\boldsymbol{M}_{uu} = \hat{\boldsymbol{\Phi}}_u^T \hat{\boldsymbol{M}}_{uu} \hat{\boldsymbol{\Phi}}_u \ , \qquad \boldsymbol{K}_{uu} = \hat{\boldsymbol{\Phi}}_u^T \hat{\boldsymbol{K}}_{uu} \hat{\boldsymbol{\Phi}}_u \ . \tag{3.34b}$$

The load vectors $\hat{\boldsymbol{h}}_i$ describe the influence of the thermal modes on the displacement field. Therefore the thermal-mechanical coupling matrix $\boldsymbol{K}_{\vartheta u}$ of Tab. 2.4 can be provided as the reorganisation of the thermal load vectors:

$$\boldsymbol{K}_{\vartheta u} = \hat{\boldsymbol{\Phi}}_u^T [\ \dots\ \hat{\boldsymbol{h}}_i\ \dots\ ]\ . \tag{3.34c}$$

The columns $\boldsymbol{u}_i$ or $\boldsymbol{u}_l$ respectively of the finite element modal matrix $\hat{\boldsymbol{\Phi}}_u$ in (3.34a) are assembled according to the FE-internal numbers of the nodal DoF. The matrix of the modal shape functions $\boldsymbol{\Phi}_u(\boldsymbol{c}_k)$ in (2.7) is a rearrangement of $\hat{\boldsymbol{\Phi}}_u$ so that the displacements are explicitly given as modal vectorial displacements of the node k at its position $\boldsymbol{c}_k$:

$$\hat{\boldsymbol{\Phi}}_u \Longrightarrow \quad \boldsymbol{\Phi}_u(\boldsymbol{c}_k) \qquad\qquad\qquad \boldsymbol{\Phi}_u(\boldsymbol{c}_k) \in \mathbb{R}^{3,m_u}\ . \tag{3.34d}$$

For each node k, one local modal matrix $\boldsymbol{\Phi}_u(\boldsymbol{c}_k)$ exits in the modal description compared to one global modal matrix $\hat{\boldsymbol{\Phi}}_u$ for the complete body in the finite element description.
In practise, the matrices $\boldsymbol{\Phi}_u(\boldsymbol{c}_k)$ only of those nodes of a body have to be on hand in multibody simulations, where joints, force elements or constraints are attached to or the kinematic information is requested explicitly. After the modal transformations in (3.34) have been performed, the modal data of other nodes can be omitted without any truncation error.

The crucial step of this scheme is the first one, i.e. the modal reduction of the temperature field. The approach used for this step has to be tailored to the modelling task. If this is accomplished the further steps two to four concerning the definition of thermal response modes and the corresponding modal reduction of the mechanical field are straightforward and may even be organised as an automated process. The accuracy or the convergence properties respectively of the modal multifield representation rely on an appropriate thermal field description. On the other hand, a substantial reduction of the number of degrees of freedom may be achieved that way.

Since inertia terms may be neglected, there is no need to define differential system variables for the simulation of the mechanical field as long as only thermal loads are involved. It is sufficient to evaluate the deflection response to the instantaneous temperature distribution as a driven equilibrium solution in a quasi-static manner. The transient temperature field drives the deformation behaviour of the flexible structure. More precisely, if only thermal loads are considered, the thermal state $\boldsymbol{z}_\vartheta$ is evaluated by means of (2.58), whereas the deformation state $\boldsymbol{z}_u$ follows from the static equation

$$\boldsymbol{z}_u = \boldsymbol{K}_{uu}^{-1} \boldsymbol{K}_{u\vartheta} \boldsymbol{z}_\vartheta\ . \tag{3.35}$$

This modal approach clearly distinguishes deflection due to thermal and due to mechanical influence. This fact may also be exploited in those cases in which thermal and mechanical loads are simultaneously present. The time derivatives of those components of $\boldsymbol{z}_u$ that correspond to thermal response modes may be neglected according to Duhamel's assumption. The discretised equations of motion are then treated as differential algebraic equations (DAE) in a way which was already proposed by SACHAU [Sac96] in order to process modes related to very high stiffness values.

The verification examples in the following two sections demonstrate the significance and the limitations of these theoretical considerations and the proposed reduction scheme. Hence, different approaches to represent the thermal field are applied according to Step 1 of the reduction scheme. The thermally induced deflections are reproduced by the corresponding thermal response modes.

3.2.3 Verification Example 1: Disc with Thermal Loads

Simulation Scenario

The first thermoelastic verification example simulates a two-dimensional temperature and displacement field of a circular disc (thickness $s = 7\,\mathrm{mm}$, outer radius $r_a = 0.15\,\mathrm{m}$). Two thermal boundary conditions are defined and illustrated in Figure 3.13. On one sector of the circular disc at $-40° \leq \beta \leq 40°$, a constant heat flux $q_B = 3000\,\mathrm{W/m^2}$ is applied, the opposite sector at $140° \leq \beta \leq 220°$ is cooled by a fluid with a bulk temperature of 200 K below reference Θ_0, see Appendix A.2 for the complete list of model parameters.

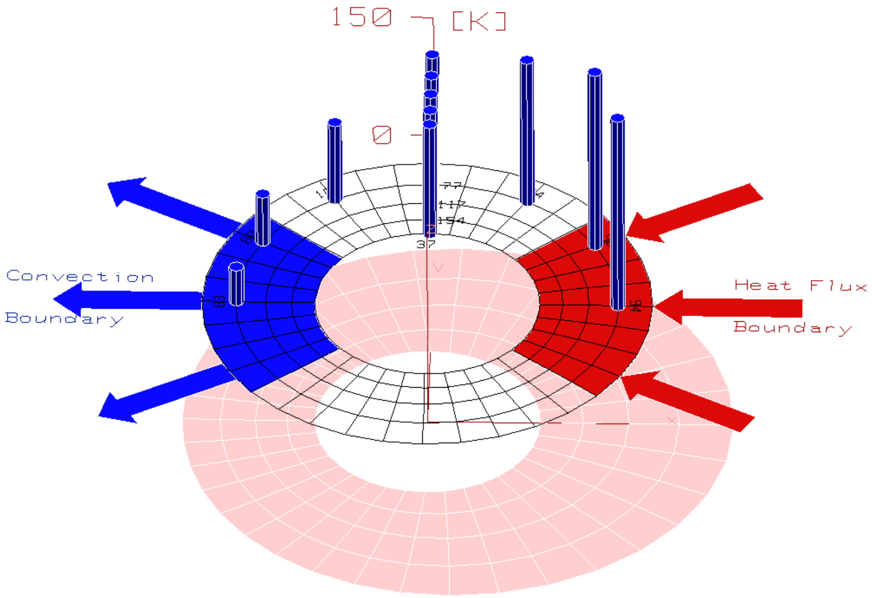

Figure 3.13: Definition, temperature and displacement results of the model *Disc with Thermal Loads*.

The only mechanical boundary condition predetermines the displacements at the inner circle of the disc at radius $r_i = 0.075\,\mathrm{m}$, which are set to zero. Since the thickness of the disc is small compared to its radial dimensions, the stress component perpendicular to the disc is assumed to be zero, i.e. the plane stress concept is applied.

For verification this scenario is evaluated in three different set-ups. The finite element model uses a mesh with 180 nodes which gives 360 mechanical and 180 thermal DoF. The transient finite element results serve as a reference solution.

Both the thermal and mechanical field are analysed dynamically, i.e. in particular the mechanical inertia terms are considered in all three simulation set-ups. Only the Gough-Joule effect, i.e. the influence of the mechanical field on the temperature field, is neglected, which may be justified by the arguments given in Sec. 3.2.1.

Modal Modelling of the Temperature Field

Two modal models are defined which both represent the temperature field by seven thermal eigenmodes. For this purpose, the thermal eigenvalue problem $[\hat{\boldsymbol{C}}_{\vartheta\vartheta}\kappa_i + \hat{\boldsymbol{K}}_{\vartheta\vartheta}]\boldsymbol{\vartheta}_i = 0$ of dimension 180 is solved and the first seven eigenvalues κ_i and the corresponding eigenvectors $\boldsymbol{\vartheta}_i$ are evaluated.

Fig. 3.14 visualises six of the seven selected thermal eigenvectors, i.e. seven temperature fields, by shades of grey. Except for the first one, each eigenvalue κ_i occurs twice. For reasons of symmetry

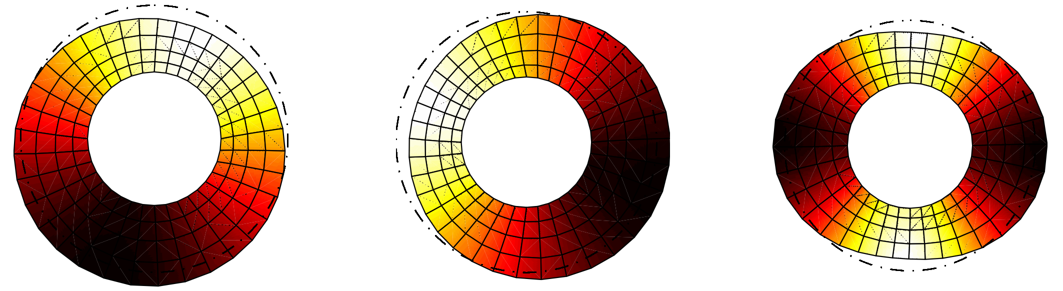

Mode 2
$\kappa_2 = -0.0010\ 1/\mathrm{s}$
$\bar{\omega}_2 = 18740$ Hz

Mode 3
$\kappa_3 = -0.0010\ 1/\mathrm{s}$
$\bar{\omega}_3 = 18740$ Hz

Mode 4
$\kappa_4 = -0.0038\ 1/\mathrm{s}$
$\bar{\omega}_4 = 21340$ Hz

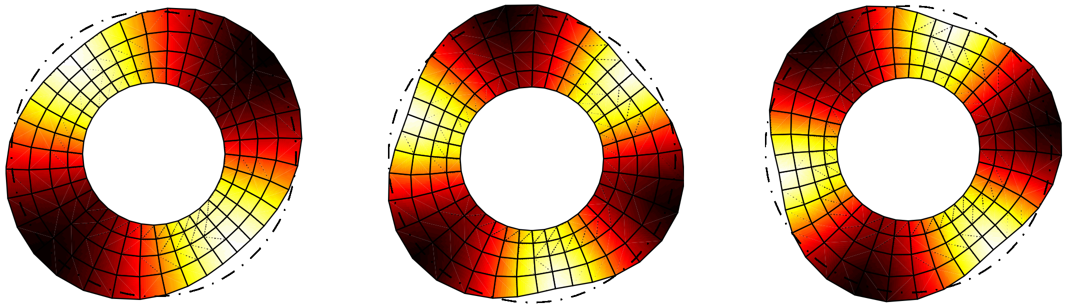

Mode 5
$\kappa_5 = -0.0038\ 1/\mathrm{s}$
$\bar{\omega}_5 = 21340$ Hz

Mode 6
$\kappa_6 = -0.0081\ 1/\mathrm{s}$
$\bar{\omega}_6 = 25230$ Hz

Mode 7
$\kappa_7 = -0.0081\ 1/\mathrm{s}$
$\bar{\omega}_7 = 25230$ Hz

Figure 3.14: Thermal modes and thermal eigenvalues κ_i, the corresponding thermal response modes and mechanical frequencies $\bar{\omega}_i$.

there are for each eigenvalue κ_i two similar eigenvectors that could be transformed into each other by a rotation around the disc's centre. Additionally the eigenvectors can be told by their number of temperature maxima and minima. The Modes 2 and 3 possess one maximum and one minimum, the Modes 4 and 5 are characterised by two maxima and two minima and the Modes 6 and 7 by three maxima and minima.

The first thermal eigenvalue $\kappa_1 = 0$ arises from the fact that no homogeneous or Dirichlet boundary condition is imposed for the thermal problem. The corresponding eigenvector describes a spatially uniform temperature field which is not shown in Fig. 3.14.

Modal Modelling of the Displacement Field

The two modal models differ in their displacement field description. The first one uses 18 purely mechanical eigenmodes, i.e. 18 eigenvectors of the mechanical eigenvalue problem, which has the initial dimension 240. However, according to Fig. 3.13, the problem has an additional symmetry plane, which has been exploited to halve the dimension of the mechanical problem.

For the second modal model, the reduction scheme from Sec. 3.2.2 is applied which yields seven thermal response modes supposed to represent the displacement field. The essentials of the modal models compared to the FEM reference model are summarised in Tab. 3.4.

	Thermal DoF	Mechanical DoF
FEM	180	360
reference model	nodal temperatures	nodal displacements in x and y
BMM	7	18
basic modal model	thermal eigenmodes	purely mechanical eigenmodes
MMA	7	7
modal multifield approach	thermal eigenmodes	thermal response modes

Table 3.4: Summary of the three different model set-ups.

Fig. 3.14 depicts six thermal response modes by the deformed mesh compared with the dash-dotted undeformed outer circle contour. Since the thermal response modes turned out to be orthogonal, a mechanical eigenvalue ω_i and frequency $\bar{\omega}_i$ ($\bar{\omega}_i = \omega_i/(2\pi)$) can be assigned to each of them.

The first thermal response mode with $\bar{\omega}_1 = 20032$ Hz related to $\kappa_1 = 0$ represents a purely radial displacement field. This can be given analytically adopting a solution from literature in cylindrical co-ordinates for the radial displacement u_r as function of a uniform temperature ϑ [BW97, (9.10.3)]:

$$u_r(r,\vartheta) = \frac{\alpha\,\vartheta}{2}\,\left[(1+\nu+2C_1)\,r + \left(2C_2-(1+\nu)r_i^2\right)\,r^{-1}\right]\;, \tag{3.36}$$
$$\text{with}\quad C_2 = -C_1\,r_i^2\;,\quad C_1 = \frac{(1-f)(1-\nu^2)}{2(1+f+\nu(1-f))}\quad\text{and}\quad f := \frac{r_i^2}{r_a^2}\;.$$

Exploiting the disc's simple geometry mass and stiffness properties that correspond to the first thermal response mode (M_{11}, K_{11}) may be computed analytically, if (3.36) is interpreted as shape function of a Ritz-approach:

$$u = u_r\,q\;, \qquad\qquad M_{11}\,\omega_1^2 + K_{11} = 0 \tag{3.37}$$
$$T = \frac{1}{2}\,\dot q^T M_{11}\,\dot q \quad\text{with}\quad M_{11} = \varrho\int_{r_i}^{r_a}\int_0^{2\pi}\int_0^{s} u_r^2\;\mathrm{d}z\,r\mathrm{d}\beta\,\mathrm{d}r\;,$$
$$V = \frac{1}{2}\,q^T K_{11}\,q\;\text{ with }\;K_{11} = \frac{E}{1-\nu^2}\int_{r_i}^{r_a}\int_0^{2\pi}\int_0^{s}\left[\left(\frac{\partial u_r}{\partial r}\right)^2 + 2\nu\frac{\partial u_r}{\partial r}\frac{u_r}{r} + \left(\frac{u_r}{r}\right)^2\right]\mathrm{d}z\,r\mathrm{d}\beta\,\mathrm{d}r\;.$$

With the geometrical and physical parameters from Appendix A.2, the eigenfrequency $\bar\omega_1 = 20211\,\mathrm{Hz}$ is obtained, which is less than 1% different from the eigenvalue result of the FE-model. Whereas the FEM approximates the displacements as piecewise linear functions in this case, a linear and a rational function of the radius are superimposed by the analytical approach in (3.36). This fact may explain that both methods yield different results at all.

Comparison of the Simulation Results

The light-grey areas at the bottom of Fig. 3.13 give an impression of the induced displacement field at $t_e = 18000\,\mathrm{s}$. The bars visualise the temperatures at a few selected nodes and give an idea of the temperature distribution.

Fig. 3.15 compares the transient temperatures and displacements at Node 101. The finite element and the modal results of the thermal field coincide. The results indicate that the seven thermal eigenmodes are well suited to represent the thermal behaviour.

The modal simulation of the displacement field with seven thermal response modes (MMA) again yields the same results as the finite element method. But the modal description of the displacements with 18 purely mechanical eigenmodes (BMM) does not represent the deflection caused by the inhomogeneous temperature field properly although a larger number of modal DoF are involved.

Obviously the modal reduction scheme from Sec. 3.2.2 is an efficient approach for the problem

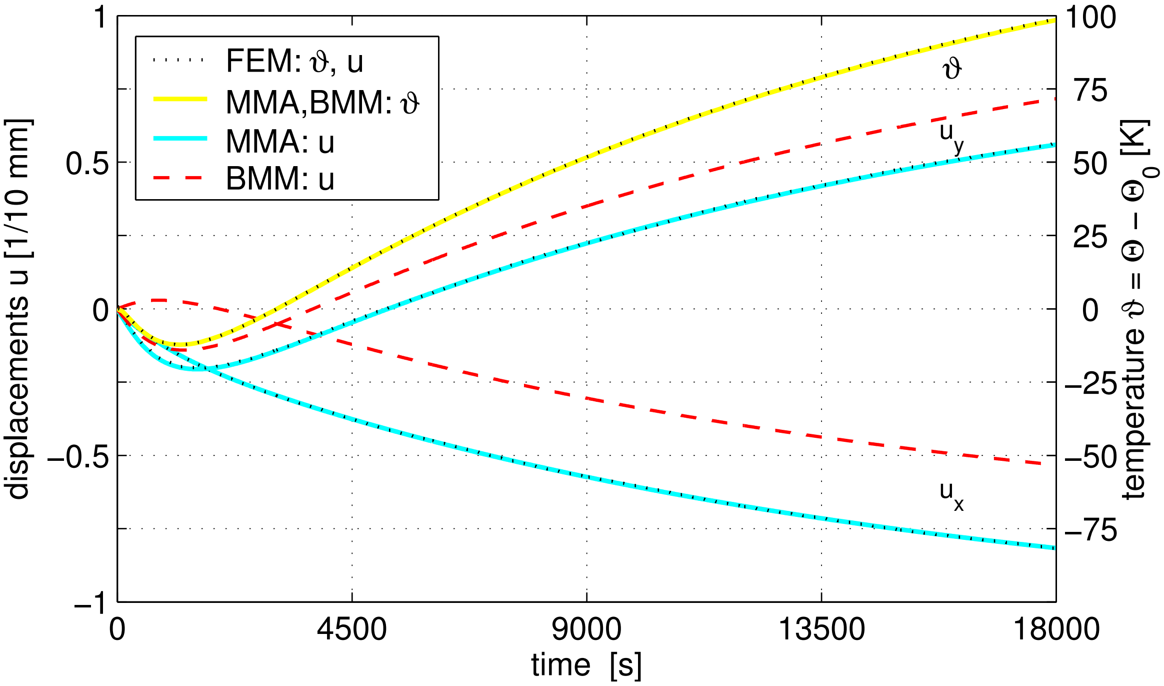

Figure 3.15: Transient temperatures $\vartheta(t)$ and displacements $u_x(t)$ and $u_y(t)$ at Node 101 ($r_{101} = 0.1262$ m, $\beta_{101} = 120°$). Identification of the models according to Tab. 3.4.

given above. This conclusion may be supported by the mechanical frequencies of the thermal response modes given in Fig. 3.14. In multibody dynamics, the frequency range around $20\,000$ Hz would certainly be omitted, if a traditional mode selection approach based on purely mechanical eigenfrequencies is performed. As a result the corresponding eigenvectors with those displacement components would be missing that are obviously necessary to reflect deformations caused by thermal loads. On the other hand the consideration of modes with frequencies around $20\,000$ Hz constitutes a very stiff system of differential equations which may lead to serious numerical problems, see [Sim01].

However, a view on the time axis of Fig. 3.15 makes clear that the deformations caused by the given thermal loads proceed very slowly in comparison with the usually observed mechanical frequencies in multibody dynamics. This is another argument to justify the truncation of the inertia terms associated to thermal deflections, i.e. to thermal response modes.

3.2.4 Verification Example 2: Hot Spot

Following the Verification Example 1 of Sec. 3.2.3 another benchmark problem is considered in the present section to study the capability of thermal response modes. This benchmark shall involve high thermal loads leading to large temperature gradients. In particular the neglect of inertia terms concerning thermally induced displacements according to Sec. 3.2.1 shall be justified this way.

Additionally it should be figured out to which extent and with which costs the modal approach is suitable to describe a more uneven, localised temperature distribution.

Therefore, *disc brake hot spotting* was selected in order to develop a benchmark scenario with all the above mentioned properties. In [KRD98] KAO et al. report on localised temperature distributions called hot spots which were found in automotive brake systems. These were often regularly spaced around the rotating brake disc and exceed temperatures up to $800°$C. They result in thermally induced judder with frequencies of typically 6 to 20 cycles per revolution of the wheel, i.e. approximately 10-100 Hz. The excitation mechanism is not yet completely understood, but it seems to involve the excitation by the wheel suspension and the susceptibility of the brake disc for structural vibrations.

Although this phenomenon is frequently addressed in the literature, see e.g. [Ste98] and [Jac03] and their list of references, it is difficult to adopt a simulation scenario from literature. Most related articles were written by authors who investigated the problem in industrial cooperation. However, the applied scenario incorporates as much published information as possible.

The main purpose of the scenario is to serve as a benchmark for the modal multifield approach. The comparison of the modal results with a reference solution obtained by finite element analysis shall reveal the capabilities and limitations of the scheme proposed in Sec. 3.2.2.

The set-up of an entire brake model for identification involves a big deal of additional modelling issues like hydraulics, contact, friction or wear, see [WHSM99]. Such a project is beyond the scope of the present thesis.

Definition of Loads

Consider a typical middle class car, which initially runs at velocity of $25\,\mathrm{m/s}$. This vehicle is stopped with constant deceleration of $5\,\mathrm{m/s^2}$ until it comes to halt. The braking conditions are assumed to perform in such a way that nine hot spots, equally spaced on the disc, occur. All load conditions, see Fig. 3.16, may be deduced as functions of time just on base of this specification.

In view of the presumed symmetric braking conditions, it is sufficient to observe only a $60°$ sector on one brake disc. The transient heat flux to impose follows from the change of the kinetic energy of the vehicle which is assumed to be completely transformed into heat energy.

The time window for which the heat flux acts upon the observed sector of the disc corresponds to the time span, the brake pad is in contact with the hot spot area. Consequently the load time span is a function of the instantaneous angular velocity of disc and the load history consists of 34 discrete contact events. The transient values of heat flux and corresponding load time span are shown in

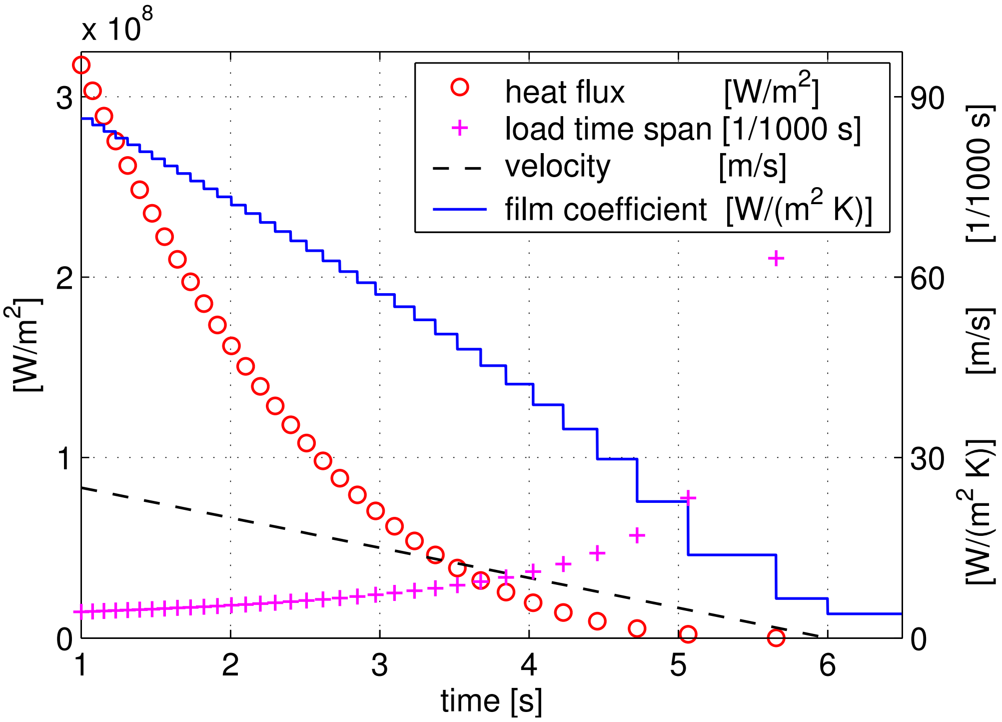

Figure 3.16: Hot spot scenario: definition of transient loads

Fig. 3.16.

The full model specifications are listed in Appendix A.3. This applies as well for the spatial distribution of the heat flux, which has the shape of a geometrically continuous B-spline hump on the $60°$ sector. The heat flux values given in Fig. 3.16 apply to the centre of the hump at $r_h = 0.1\,\text{m}$, $\beta_h = 0°$ and $z_h = 0.01\,\text{m}$.

The film coefficient, which specifies the cooling of the disc by air stream, depends on the instantaneous velocity of the car and is defined according to [GM01, Tab. 2.3-1]. In order to simplify the load definition, the film coefficient is approximated by a step function, see Fig. 3.16.

In between two contact events, the convective boundary condition is defined on the complete surface of the disc. During the contact event, the surface except for the observed $60°$ sector is cooled. In order to prevent load impacts all loads are applied continuously imposing a ramp-up and ramp-down time, see Appendix A.3.

Finite Element Model

The brake disc ($r_i = 0.075\,\text{m}$, $r_a = 0.150\,\text{m}$ and $s = 10\,\text{mm}$) is modelled with the industrial finite element tool ANSYS. The disc volume is discretised by $2\,592$ hexahedron elements with quadratic shape functions of type Solid90 for the thermal FE-model and of type Solid95 for the mechanical FE-model [ANS03]. Since a mesh with $15\,120$ nodes is created, $15\,120$ thermal DoF and $45\,360$

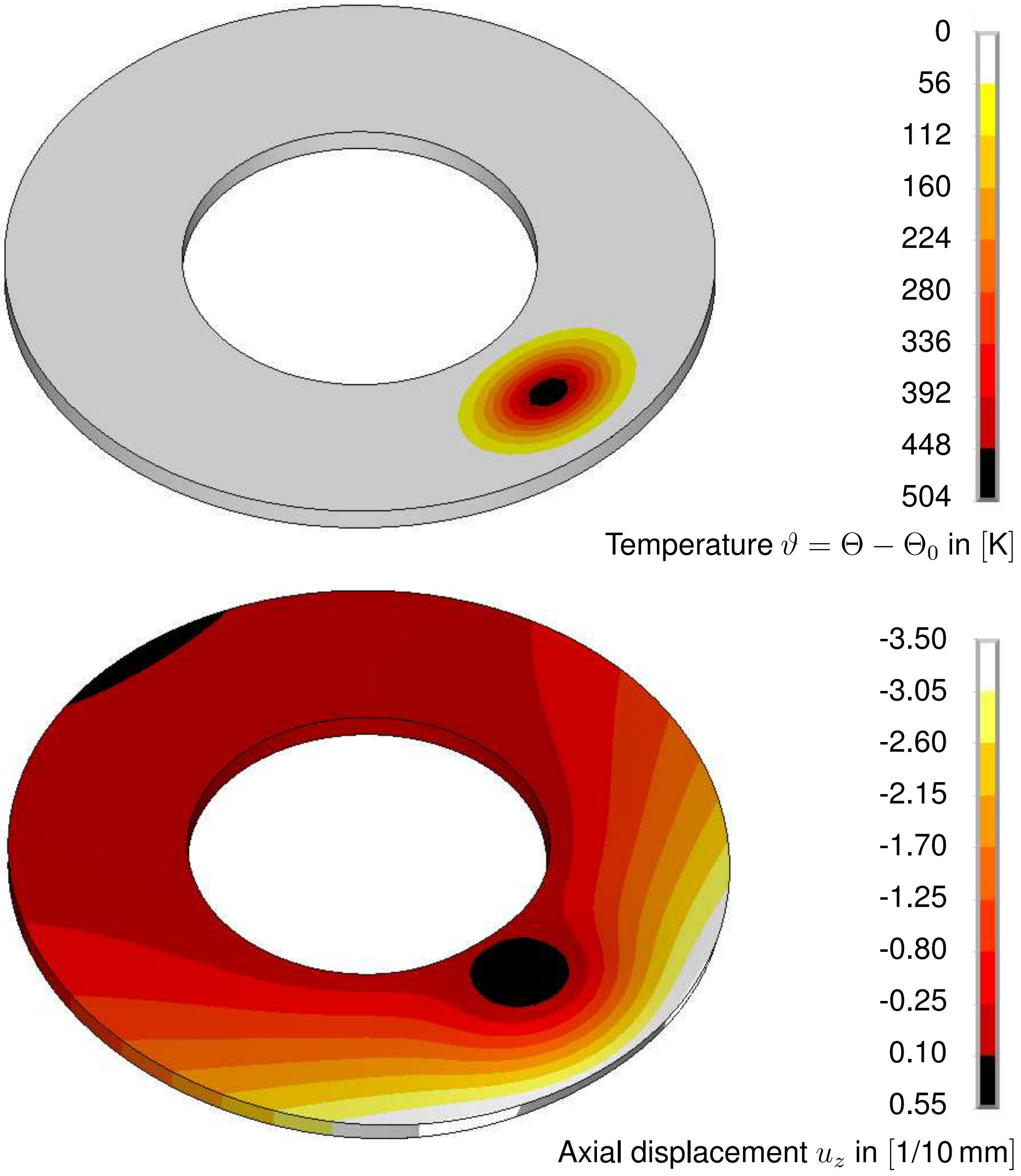

Figure 3.17: Finite element results of the thermal and the displacement field at $t = 2.199\,\mathrm{s}$.

mechanical DoF are involved.

Unless otherwise noted the simulations are set up with constant material parameters. The material is cast iron GG20HC, which is a frequently used material for brake discs [Bur91, Sec. 9.7].

All transient FE-simulations are performed completely dynamically. The Gough-Joule effect is not considered, since there are no appropriate finite elements in ANSYS.

Fig. 3.17 shows the temperature and the displacement field in axial direction at $t = 2.199\,\mathrm{s}$.

Modal Approach

The time-independent mode functions $\boldsymbol{\Phi}_\vartheta$ are analytically defined and chosen according to the assumed spatial load distribution. They are based on a separation of variables for the three scalar elements of the Lagrange position co-ordinate $\boldsymbol{c} = (r, \beta, z)^T$ in a cylindrical system:

$$\boldsymbol{\Phi}_\vartheta(\boldsymbol{c}) = \begin{pmatrix} \Phi_{r,1}(r) \cdot \Phi_{\beta,1}(\beta) \cdot \Phi_{z,1}(z) \\ \Phi_{r,1}(r) \cdot \Phi_{\beta,1}(\beta) \cdot \Phi_{z,2}(z) \\ \vdots \\ \Phi_{r,i}(r) \cdot \Phi_{\beta,j}(\beta) \cdot \Phi_{z,k}(z) \\ \vdots \end{pmatrix} \quad \text{with} \quad \begin{array}{rcl} i & \in & [1,\, 2]\,, \\ j & \in & [1,\, \ldots\, ,18]\,, \\ k & \in & [1,\, \ldots\, ,5]\,. \end{array} \tag{3.38}$$

The two radial shape function $\Phi_{r,i}(r)$, six of the eighteen used angular shape function $\Phi_{\beta,j}(\beta)$ and all five axial shape function $\Phi_{z,k}(z)$ are shown in Fig. 3.18.

This selection of shape functions establishes a system with 180 modal DoF for the thermal field, that expose the following properties:

1. The 180 modal shape functions are linearly independent.

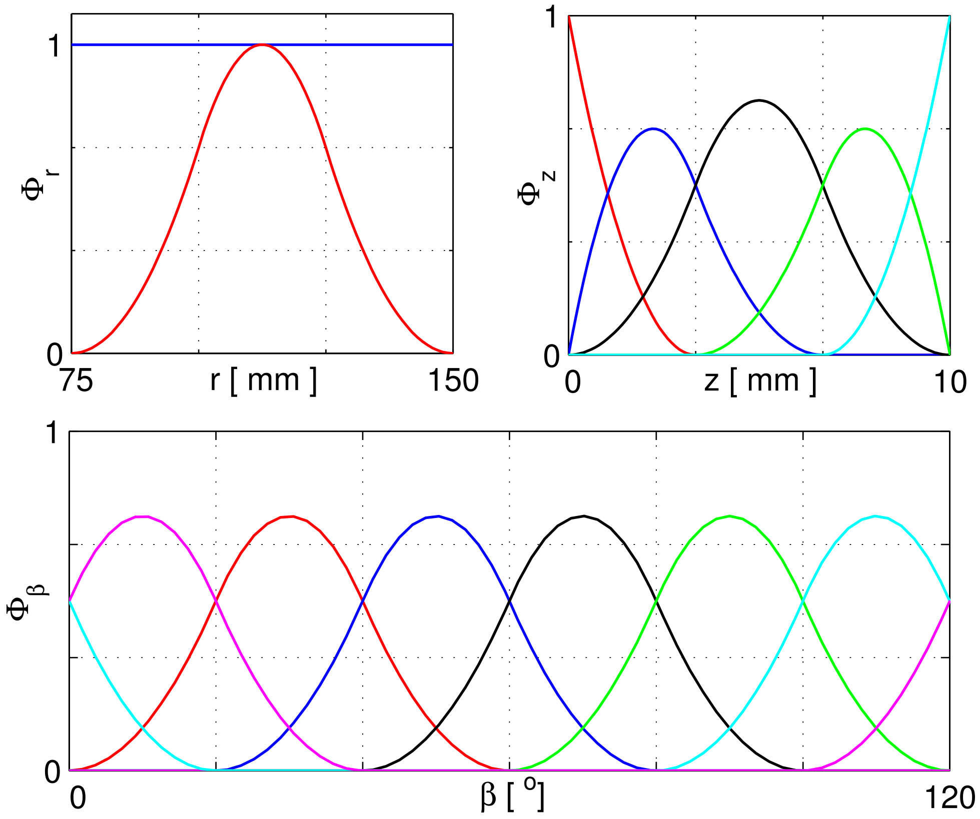

Figure 3.18: Quadratic B-spline shape functions of the modal approach for the thermal field.

2. They are at least once continuously differentiable.
3. They allow as well the description of a homogeneous temperature field with $\vartheta \neq 0$.
4. If required the discretisation may be easily refined or coarsened and therefore be adapted to the given simulation task. Here, the choice is aligned with the assumption that nine hot spots occur regularly spaced.

Since a specific brake design configuration typically displays a characteristic number of hot spots [Ste98], the last assumption has to be verified in each application in praxis. As reported by KAO et al. in [KRD98], such identification of the modal approach is possible by experiment but may result in a system with a higher number of modal DoF than presented above.

With the given shape functions the system of ordinary differential equations of the temperature field (2.58) can be established. The solution of the thermal eigenvalue problem gives 180 eigenvalues κ_i within the range of $-21.9 \leq \kappa_i \leq 0$ [1/s]. Since the approach is characterised by 36 symmetry planes, the eigenvalues are grouped closely around five distinct points on the real axis.

The representation of the mechanical field is obtained according to the modal reduction scheme of Sec. 3.2.2, whereby only thermal response modes are selected .

If the mechanical inertia terms are neglected and only thermal loads are considered, the evaluation of the mechanical deformation state is very simple, since it may be argued based on (3.33) and (3.34):

$$\hat{\boldsymbol{K}}_{uu} \left[\boldsymbol{u}_1, \; \ldots \; , \boldsymbol{u}_{180}\right] = \left[\hat{\boldsymbol{h}}_1, \; \ldots \; , \hat{\boldsymbol{h}}_{180}\right] \; , \tag{3.39a}$$

$$\hat{\boldsymbol{\Phi}}_u = \left[\boldsymbol{u}_1, \; \ldots \; , \boldsymbol{u}_{180}\right] \; , \tag{3.39b}$$

$$\boldsymbol{K}_{uu} = \boldsymbol{K}_{u\vartheta} \; . \tag{3.39c}$$

However according to (2.50) or Tab. 2.4 respectively, employing the assumption above, it can be stated:

$$\boldsymbol{K}_{uu} \, \boldsymbol{z}_u = \boldsymbol{K}_{u\vartheta} \, \boldsymbol{z}_\vartheta \; , \tag{3.39d}$$

which leads to the identity $\boldsymbol{z}_u = \boldsymbol{z}_\vartheta$ that of course only holds for this specific example.

Referring to (2.58), the final set of equations for this problem are then given with:

$$\boldsymbol{C}_{\vartheta\vartheta} \, \dot{\boldsymbol{z}}_\vartheta + \left(\boldsymbol{K}_{\vartheta\vartheta} + \boldsymbol{K}_{\vartheta R}\right) \boldsymbol{z}_\vartheta = \boldsymbol{h}_{\vartheta N} \, q_B + \boldsymbol{h}_{\vartheta R} \, \vartheta_\infty \; , \tag{3.40a}$$

$$\boldsymbol{z}_u = \boldsymbol{z}_\vartheta \; , \tag{3.40b}$$

which is additionally simplified by the setting $\vartheta_\infty = 0$, i.e. the temperature of the air stream and the reference temperature Θ_0 coincide.

For the sake of demonstration the mass $\hat{\boldsymbol{M}}_{uu}$ and the stiffness matrix $\hat{\boldsymbol{K}}_{uu}$ of the mechanical FE-system were transformed into their corresponding modal representation and an eigenvalue analysis of the reduced mechanical system has been performed. The 180 eigenfrequencies range from $1\,231$ Hz up to $624\,230$ Hz. A dynamic multibody simulation with frequencies up to $600\,000$ Hz is unthinkable and therefore another strong argument for the truncation of inertia terms related to thermoelastic displacements is given.

Simulation Results: Temperature

Fig. 3.19 shows the temperature curves at two sample nodes for the thermal finite element and the modal simulation. Node 415 coincides with the centre of the heat flux load. Node 4519 has the same radial and angular co-ordinate but is located on the lower surface of the disc ($\boldsymbol{c}_{4519} = (0.1\,\mathrm{m},\ 0°,\ 0\,\mathrm{m})^T$). Furthermore, the plot shows the relative error

$$\Delta(t) = \frac{\vartheta_{\text{FEM}} - \vartheta_{\text{MMA}}}{\vartheta_{\text{FEM}}}$$

for Node 415 at the beginning of each contact event.

As long as the time gradients of the temperature are large, the differences between the modal and

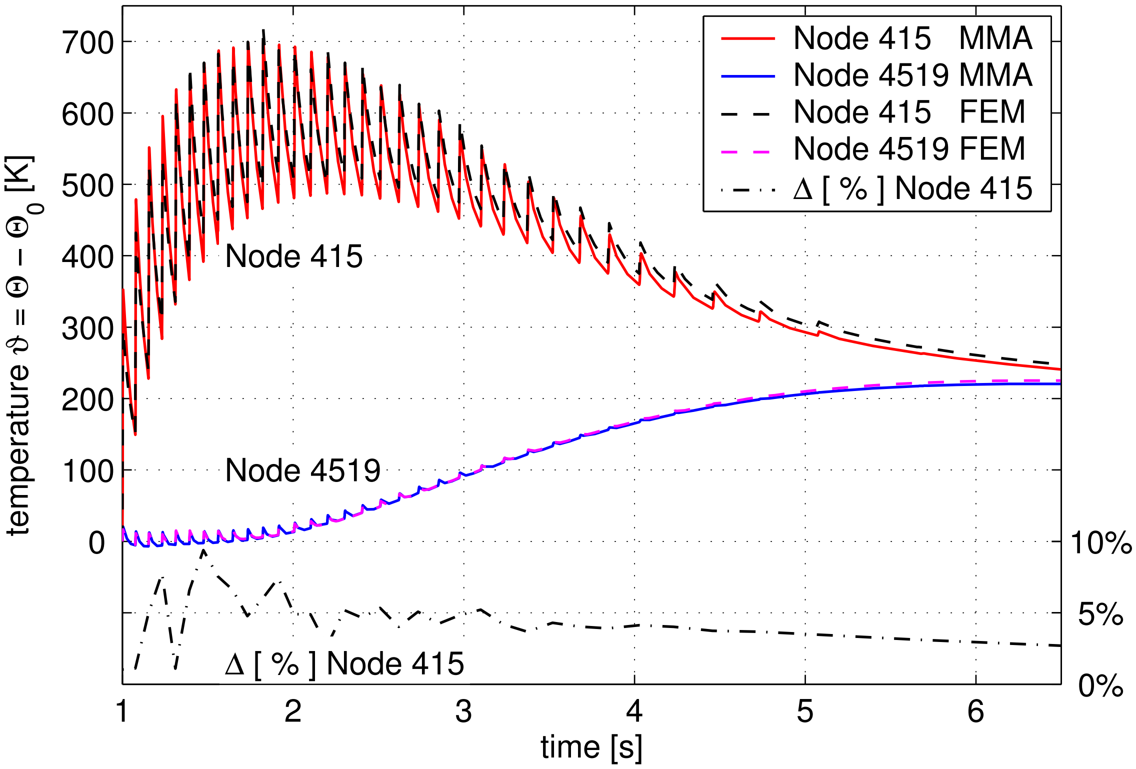

Figure 3.19: Transient temperature results at two nodes: finite element method (FEM) vs. modal multifield approach (MMA).

the FE-results oscillate with values between 0 and 9%. The relative error Δ oscillates even stronger during or immediately after each contact event (not shown in Fig. 3.19). The phase between two contact events has a smoothing effect on the temperature differences. When the time gradients of the temperature get smaller, the relative error is smoother and its absolute value is less than 5%.

On the other hand the time gradients at the beginning of the simulation surely are extremely large and might not be reached or even exceeded in practical applications.

An interesting detail may be observed in the temperature plot of Node 4519 in Fig. 3.19. The temperature at Node 4519 is in phase with the contact events, although Node 4519 is at least 10 mm away from the hot spot load. This immediate response requires an infinite thermal wave speed and cannot be justified by physical understanding. This behaviour may be attributed to the parabolic differential equation of heat conduction which does not consider thermal inertia, see [Now78b, Ch. 7].

In numerical tests it has been found that the errors were larger if less than five functions $\Phi_z(z)$ of Fig. 3.18 were used for the modal approximation of the temperature field.

Simulation Results: Displacement

The mechanical displacements in all three directions obtained with the FE- and the modal model at Node 20 ($\boldsymbol{c}_{20} = (0.15\,\mathrm{m},\ 0°,\ 0.01\,\mathrm{m})^T$) on the outer contour edge of the disc are shown in Fig. 3.20. For a brake disc the axial deformation is much more relevant than the in-plane displacements. Therefore, the relative error Δ is only given for the u_z-component.

On the contrary to the in-plane displacements the axial deformation is additionally determined by bending and not only influenced by direct thermal expansion. This may be shown from two formulas of the analytical plate theory, in which the axial temperature distribution is used to express equivalent membrane loads N_ϑ and bending moments M_ϑ in terms of the strength-of-material representation [BW97, (12.2.6b)]:

$$N_\vartheta = \alpha\, E \int\limits_{-s/2}^{s/2} \vartheta \,\mathrm{d}z\ , \qquad\qquad M_\vartheta = \alpha\, E \int\limits_{-s/2}^{s/2} \vartheta\, z \,\mathrm{d}z\ .$$

According to these equations large axial temperature gradients cause bending moments which result in comparable large displacements at the outer contour of the disc.

Compared to the results of Fig. 3.19 the time plot of relative errors for the axial displacement in Fig. 3.20 is smoother but the errors themselves are slightly larger than for the temperature analysis. It is frequently observed that a Rayleigh-Ritz approximation provides upper bounds for the stiffness

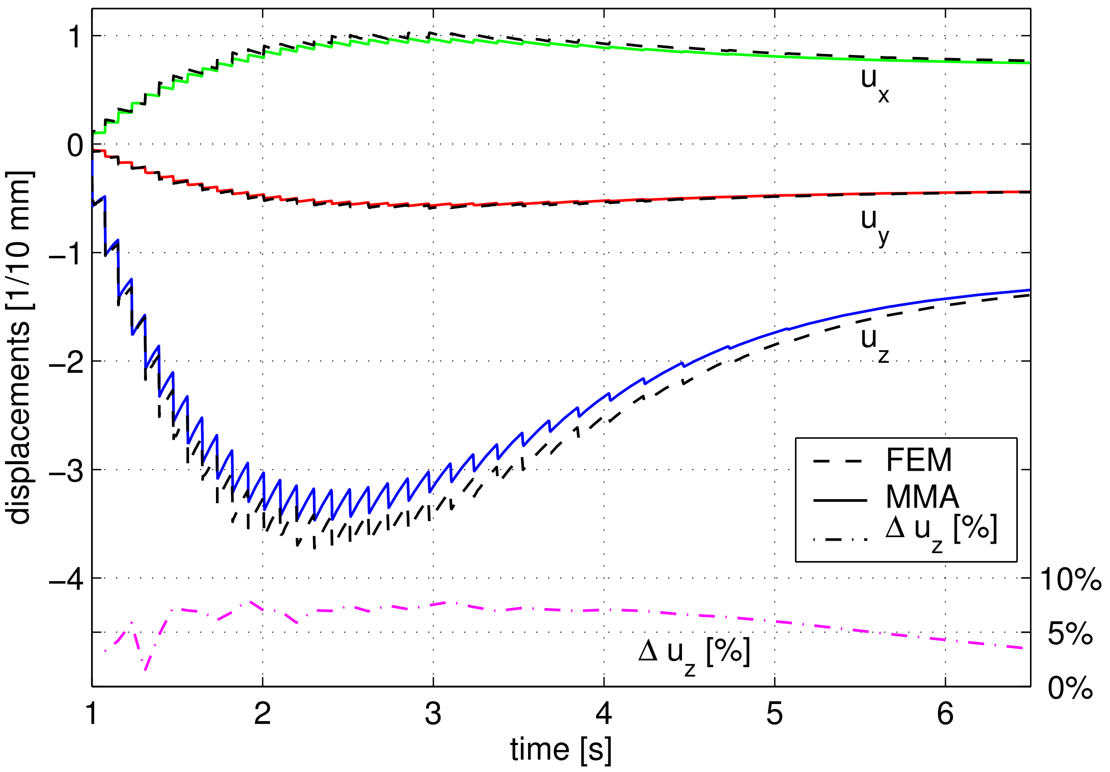

Figure 3.20: Transient displacement results at Node 20: finite element method (FEM) vs. modal multifield approach (MMA).

values compared to the original system [GK89, Sec. 6.2.3]. Therefore, in Fig. 3.20 the absolute values of the displacements in the modal analysis are smaller than the ones of the FE results.

The results in Fig. 3.20 give another justification to neglect the inertia terms associated to the thermal deflections in the equations of motions following Duhamel's assumption (Sec. 3.2.1). The temperature gradients are extremely large at the beginning of the simulation, but nevertheless the modal multifield approach reproduces the displacements of the finite element analysis qualitatively correct.

Comparison of Linear and Nonlinear Analysis

This section is continued by a physically nonlinear finite element analysis to study the influence of temperature dependent material parameters. For this purpose the material coefficients given in Fig. 2.9 on p. 36 are approximated as linear functions of the temperature, which is again documented in Appendix A.3.

All other conditions and loads are the same as for the linear FE-simulation. Fig. 3.21 presents the comparison of the nonlinear analysis with the linear one.

The relative difference of the temperature results $\Delta\vartheta(t)$ at Node 415 ranges between +7% and

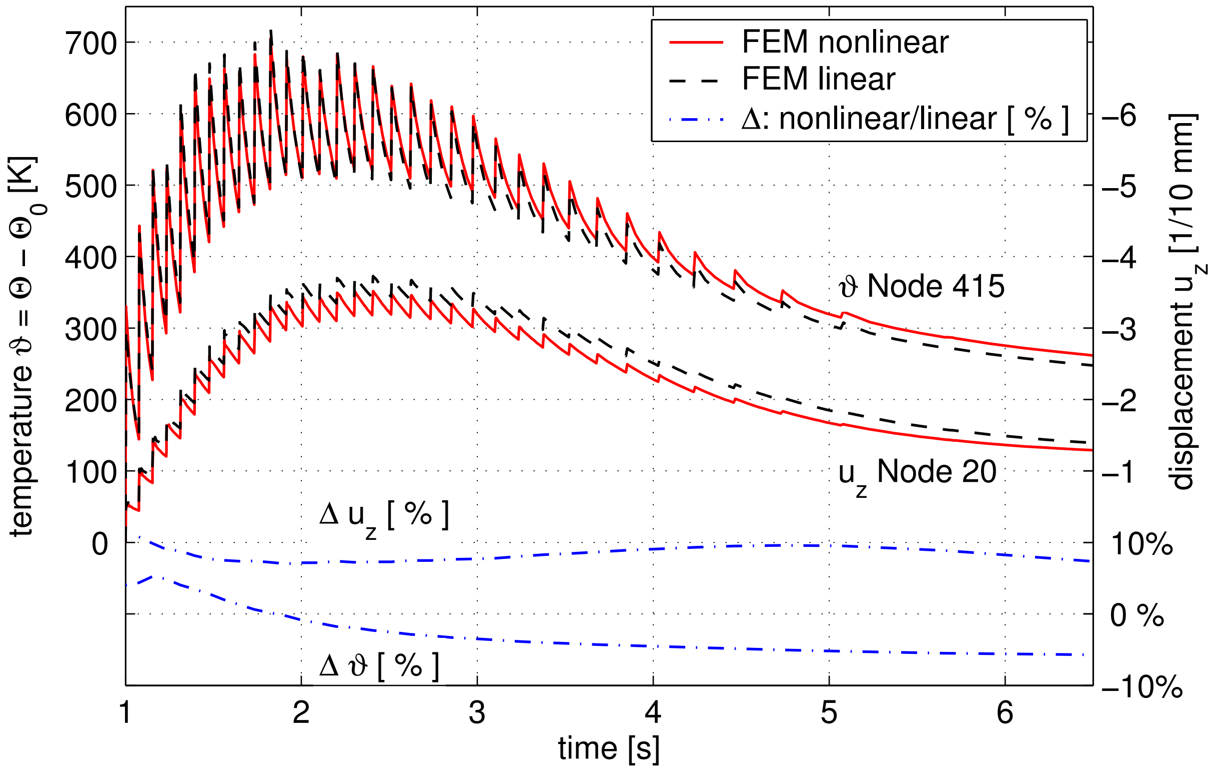

Figure 3.21: Comparison of nonlinear finite element analysis vs. linear finite element analysis: transient displacement (u_z) and temperature (ϑ) results.

-7%. The relative difference of the axial displacements $\Delta u_z(t)$ at Node 20 remains slightly below 10% during the whole simulation. The linear analysis tends to overestimate the displacement results.

Résumé

The modal simulation results of the hot-spot-scenario correspond quite well with the FE results. The differences in the linear evaluations of the thermal field are in the range of 5%, the linear evaluations of the displacement field differ approximately by 8%, whereby the modal multifield approach tends to underestimate the finite element results.

Additionally, significant differences in the numerical effort of the methods have been observed. Tab. 3.5 lists the CPU time, which has been spent for each simulation set-up. All simulations has been performed on the same hardware (workstation HP 9000/785, operating system HP-UX B.11.0, 3 GB memory).

The modal multifield simulation has been performed in MATLAB with the standard Dormand-Prince time integrator Ode45 with the absolute and relative error tolerance of 10^{-3}. Adjusting both error tolerances to 10^{-6} results in $47.8\,$s spent CPU-time, but did not significantly change the

Set-up	Time [s]	Time [normalised]
simulation time	5.5	1.0
modal multifield simulation	26.6	4.8
linear thermal FE-analysis	19377.0	3523.0
linear mechanical FE-analysis	110087.0	20016.0
nonlinear thermal FE-analysis	28639.0	5207.0
nonlinear mechanical FE-analysis	250426.0	45532.0

Table 3.5: Comparison of computational costs (CPU time).

simulation results.

The finite element simulations are performed applying the implicit Euler method with automatic time step control, which is the standard ANSYS time integration scheme. In the comparison of CPU time it has to be taken into account that the finite element simulations are set up completely dynamically, whereas the modal evaluation of the displacement field is a purely static one. As well the nonlinear FE-simulations cannot be compared directly to the modal evaluations. It is nevertheless interesting that the nonlinear FE-analysis has taken about 50% up to 130% more CPU time than the linear one.

With the benchmark *hot spot* chances and limits of the thermoelastic modal multifield approach are illustrated by means of a challenging application. The results reveal in particular a high numerical efficiency combined with an acceptable loss of accuracy.

4 Tools and Applications

Based on the theoretical framework of Chapter 2 and the modelling issues in Chapter 3, the now following elaboration is devoted to advanced applications of the concept in multibody dynamics. Compared to Ch. 3, the discussion is widened from moderately complex single body models, which exemplify specific modelling assumptions, to assembled multibody systems to demonstrate the broad capabilities of the approach and the chances for system dynamical engineering.

Since the mechanical influence of the nonmechanical field quantities is independent from the body's reference frame motion, see the definition of $\boldsymbol{h}_{im}$ in Tab. 2.4, the proposed methods for multifield representation in Ch. 3 can be carried over completely to applications with nonlinear reference motion of the flexible body under consideration.

The first section of the present chapter briefly introduces the software components of the simulation environment for multifield analysis in multibody dynamics. The structural control methodology from Sec. 3.1 is then applied to a railway car body. The exposition covers the modelling, the control synthesis for active damping and its evaluation by simulation, see also [HV02] and [VH04a]. A feasibility study which is supposed to present an approach how the thermoelastic behaviour of a high accuracy machine tool may be modelled by means of multibody dynamics, exemplifies the thermoelastic capabilities of the modal multifield approach from Sec. 3.2.

4.1 Software Components and Interfaces

Each step of a development process has different requirements. That is why specialised software tools are available, each tailored to meet the needs of a particular design task [SK00]. In this thesis the commercial finite element tool ANSYS has been used to analyse the structural properties of flexible bodies, the industrial tool SIMPACK is employed as multibody dynamics software and the control system synthesis is performed with the widespread MATLAB Simulink toolbox. Following the idea of *concurrent engineering* the different software tools are interconnected by interfaces.

Due to the floating frame of reference formulation in multibody dynamics, the data exchange from FEM to MBS relies on additional mechanical considerations and an appropriate preprocessing, which have been published by WALLRAPP [Wal94]. Tab. 4.1 summarises input, output and intermediate data of this standard interface further on called *MechFembs*. It has been necessary to extend the standard functionality of MechFembs in order to account for the thermomechanical coupling, since the consideration of thermal response modes and of mechanical loads caused by temperature fields are new issues of the modal reduction.

The preprocessing of heat transfer finite element data and their transfer into the modal description as proposed in Sec. 3.2.2 requires a new interface called *ThermFembs*. The main problem here is to define thermal modes that are appropriate to the given analysis objective. Since ANSYS does not support the modal reduction of thermal fields, this task is completely performed by ThermFembs.

The third interface *PiezoFembs* evaluates the data of piezo-ceramic patches and their electromechanical coupling according to the calculation processes in Sec. 3.1.2 and Sec. 3.1.3.

Besides these offline interfaces the online simulation environment of SIMPACK has also been extended. Two new types of software components are necessary to enable the simulation of multibody systems with flexible bodies that are additionally influenced by multiphysical field quantities: distributed force elements and modal sensors.

A distributed force element

- is uniquely assigned to a specific flexible body $(\ )^{(i)}$.
- provides a load vector $\boldsymbol{h}_{i+}^{(i)}$ for the right-hand side of the equations of motion of this body (2.59a). This load vector is added vectorially to the vector of the internal forces $\boldsymbol{h}_{i}^{(i)}$ (defined in Tab. 2.1) so that the sum corresponds to $\boldsymbol{h}_{im}^{(i)}$ (see Tab. 2.4).
- may or may not have own state variables such as $\boldsymbol{z}_{\vartheta}$ in (2.59b).
- allocates memory and assigns data of matrices and vectors to establish equations of type (2.59b) or (2.59c) on p. 46, which are interpreted as specific force laws from the point of view of the multibody system.
- may accept external input quantities like the voltage vector $\boldsymbol{z}_{\varphi}$, which may be provided via so called SIMPACK-MATLAB *interprocess communication*, see below.

A modal sensor

- returns the instantaneous modal state $\boldsymbol{z}_{u}^{(i)}$ and its derivatives $\dot{\boldsymbol{z}}_{u}^{(i)}$ of the body $(\ )^{(i)}$ when invoked.
- is accessible for the SIMPACK-MATLAB interprocess communication.

The physical background of the distributed force is not specified by the distributed force element. That way the specification is open for future developments which may consider other field quanti-

Mechanical Preprocessing Interface FEM to MBS: *MechFEMBS*

	Input	Intermediate	Output	Comment and Reference
Geometry	$\boldsymbol{c}_k$	$\hat{\boldsymbol{\Phi}}_u$	$\boldsymbol{c}_I$	Important nodes only†.
Mechanical eigenmodes	$\boldsymbol{u}_l$		$\boldsymbol{\Phi}_u(\boldsymbol{c}_I)$	Step 4 of the modal reduction scheme in Sec. 3.2.2 on p. 74.
Thermal response modes	$\boldsymbol{u}_i$			
Other modes	$\boldsymbol{u}_{\dots}$			
Inertia data	$\hat{\boldsymbol{M}}_{uu}$		$\boldsymbol{M}^\star$, $\boldsymbol{h}^\star_{gcc}$	Definitions in Tab. 2.1, p. 21.
Stiffness data	$\hat{\boldsymbol{K}}_{uu}$		$\boldsymbol{K}_{uu}$	
Thermal loads	$\boldsymbol{h}_i$		$\boldsymbol{K}_{u\vartheta}$	Step 2, Sec. 3.2.2, p. 73.

Thermal Preprocessing Interface FEM to MBS: *ThermFEMBS*

	Input	Intermediate	Output	Comment and Reference
Geometry	$\boldsymbol{c}_k$	$\boldsymbol{\vartheta}_i$, $\hat{\boldsymbol{\Phi}}_\vartheta$	$\boldsymbol{c}_I$	Important nodes only†.
Thermal modes	‡		$\boldsymbol{\Phi}_\vartheta(\boldsymbol{c}_I)$	Step 1, Sec. 3.2.2, p. 73.
Heat capacity matrix	$\hat{\boldsymbol{C}}_{\vartheta\vartheta}$		$\boldsymbol{C}_{\vartheta\vartheta}$	Definitions in Tab. 2.5 on p. 45. Modal reduction according to Step 1, Sec. 3.2.2, p. 73.
Conductivity matrix	$\hat{\boldsymbol{K}}_{\vartheta\vartheta}$		$\boldsymbol{K}_{\vartheta\vartheta}$	
Robin load matrix	$\hat{\boldsymbol{K}}_{\vartheta R}$		$\boldsymbol{K}_{\vartheta R}$	
Robin load vector	$\hat{\boldsymbol{h}}_{\vartheta R}$		$\boldsymbol{h}_{\vartheta R}$	
Neumann load vector	$\hat{\boldsymbol{h}}_{\vartheta N}$		$\boldsymbol{h}_{\vartheta N}$	
Heat source vector	$\hat{\boldsymbol{h}}_{\vartheta S}$		$\boldsymbol{h}_{\vartheta S}$	

Electrostatic Preprocessing Interface FEM to MBS: *PiezoFEMBS*

	Input	Intermediate	Output	Comment and Reference
Geometry	$\boldsymbol{c}_k$	$\boldsymbol{c}^e$, $\boldsymbol{n}^e$	$\boldsymbol{c}_I$	Important nodes only†.
Element specification	$k_{1\dots4}{}^\natural$		$\boldsymbol{K}_{\varphi\varphi}$ $\boldsymbol{K}_{u\varphi}$	Evaluation for beams Sec. 3.1.2 on p. 53. Evaluation for shells Sec. 3.1.3 on p. 56.
Modal displacements	$\boldsymbol{\Phi}_u(\boldsymbol{c}_k)$	$\boldsymbol{u}^e$, $\boldsymbol{\Phi}^e$, $\boldsymbol{\Psi}^e$		
Modal rotations	$\boldsymbol{\Psi}_u(\boldsymbol{c}_k)$			
Patch position	s_0, s_1			
Material data	e_{31}, ϵ_{33}			

†: Important nodes are in particular nodes at which joints, force elements or constraints are attached.

⋆: Only constant, state independent terms of the multibody inertia data are stored, see [Wal94].

‡: The evaluation of thermal (eigen-)modes is no standard capability of industrial finite element tools.

♮: Each finite element is specified by the numbers of the nodes at the element corners or ends.

Table 4.1: Overview on preprocessing interfaces and their input, output and intermediate results.

ties as the presented electrostatic and thermal terms. Concerning thermally induced displacements this developer version of SIMPACK does not realise the full potential of thermal response modes, since the associated inertia terms are still present in (2.50). Duhamel's assumption is only exploited to define thermal response modes based on a static finite element analysis.

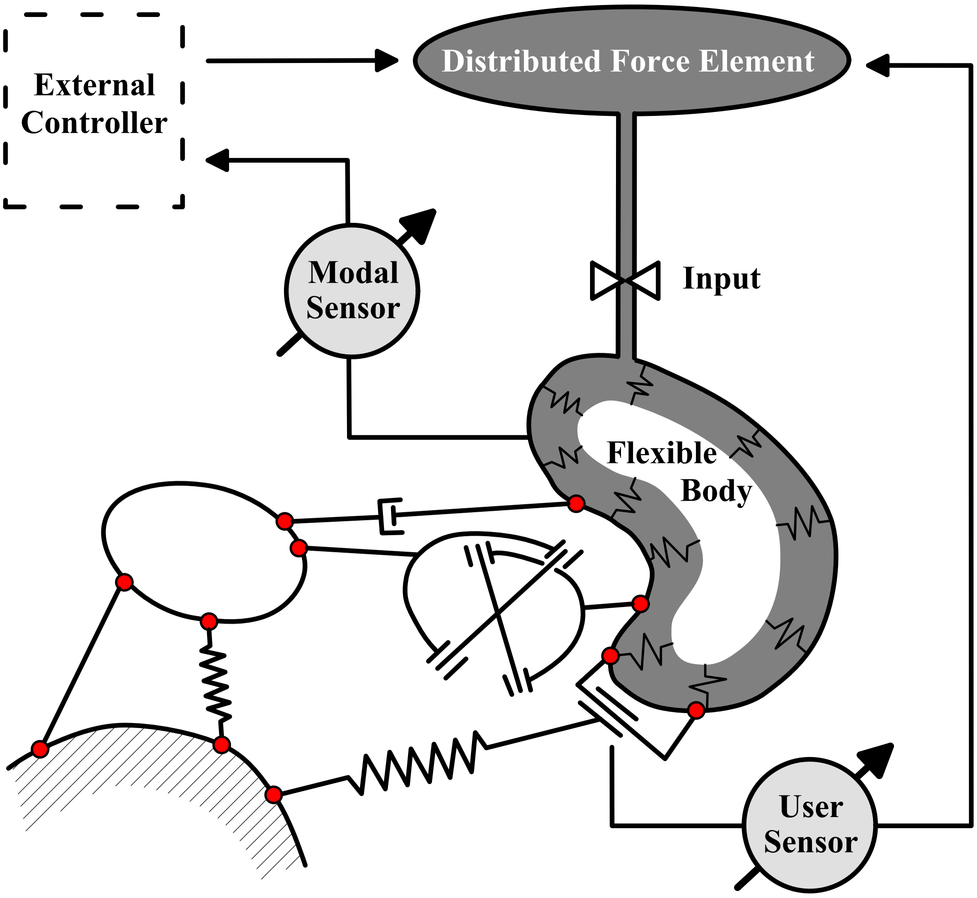

Figure 4.1: Assembly of a multibody system with flexible body, distributed force element, modal sensor and an exemplary user sensor.

Additional boundary conditions may require the definition of additional software components. If e.g. it is intended to define a heat flux due to mechanical friction on the surface of a flexible body, a specific routine has to be specified that evaluates the instantaneous friction performance. This routine accesses mechanical information like friction force and relative velocity of the friction partners and returns the heat flux if invoked by the distributed force element. Since such routines are software components which are tailored for specific applications by the user, they may be called *user sensors*. The definition of such a user element is a standard SIMPACK functionality. Fig. 4.1 shows an exemplary multibody system in a schematic way.

The standard interface between SIMPACK and the *computer aided control engineering* (CACE) tool MATLAB Simulink has two main features, see [VKS01]. On one hand, SIMPACK models can be linearised and exported to MATLAB in the form of linear system matrices. On the other hand, co-simulation via *interprocess communication* (IPC) may be performed.

Consider e.g. a multibody system with a controller that is modelled in MATLAB Simulink. The dynamics of the multibody system is numerically integrated w.r.t. time by SIMPACK, the dynamics of the controller is handled by MATLAB Simulink. Both time integration processes proceed in parallel, but exchange data in discrete time steps. This scheme is therefore designed according to the structure of a digital controller and enables the testing of the control set-up concerning sampling and stability problems.

The collaboration of all introduced components and interfaces, which constitute the simulation environment, is demonstrated in the next two sections.

4.2 Active Damping of Railway Car Body Vibrations

4.2.1 Motivation

New generations of ground and air vehicles will more and more profit from light-weight design because of economic and environmental reasons. However, light-weight structures are more susceptible to structural vibrations. This drawback is aggravated by increasing operational speeds and demands on passenger comfort. Additionally, there are conceptual design studies that propose to replace classical bogie vehicles by blueprints with only one or two axles per vehicle, [Gre03]. Such future vehicles will not profit from the mechanical prefiltration and damping characteristics of the railway bogies.

These facts give reason to think about the concept of smart or adaptive structures. First computational and experimental proposals for the application of piezo-patches on railway vehicles to suppress car body vibrations have already been studied, [HTTT03]. However, the design, optimisation and evaluation of a structural control concept concerning a complex railway vehicle is still a challenging task and far away from being state-of-the-art.

4.2.2 Development Process and Environment

Multibody simulation tools are widely accepted for the analysis of railway vehicle dynamics and there is a great deal of experiences in this field, see e.g. [Gan04]. Even elaborate problems such as two railway vehicles simultaneously crossing an elastic bridge have already been solved with reasonable effort of about $580\,\mathrm{s}$ computational time for $10\,\mathrm{s}$ simulation time [DHS01]. The extended MBS environment that have been introduced in Sec. 4.1 makes use of these proven capabilities in railway vehicle dynamics and allows additionally to evaluate structural control concepts and to examine their feasibility and efficiency.

The background of the assumed development process is the question whether and to which extent the comfort characteristics of a classical railway car body design can be improved by structural control with distributed piezo-ceramic actuators and sensors.

It is presumed that a verified multibody model of the railway vehicle is available which has been used to evaluate its driving dynamics. This model has to be extended in order to enable the comfort analysis. That is why the originally rigid car body model is to be replaced by a flexible one with piezoelectric patches on appropriate positions. The excitation by the rail irregularities transmitted via wheel-rail contact and the bogie to the car body is identified be the most important one w.r.t. the comfort properties.

Fig. 4.2 shows an overview on the specific tasks the entire design job is compost of and gives the corresponding tools. The first step of the development process consists of the finite element modelling of the car body. Since the vehicle component car body has to be dimensioned concerning mechanical strength and fatigue, a FE model of the car body is created anyway.

The FE data of the mechanical structure and the results of the FE eigenvalue analysis are the input data of the interface MechFembs that provides the multibody data of the flexible car body. For all technically possible patch locations the electrostatic and electromechanical coupling data are then generated by the interface PiezoFembs, see Tab. 4.1.

The existing multibody model of the railway vehicle is upgraded with the flexible car body description and a distributed force element and a modal sensor are initialised. Furthermore, the excitation by rail irregularities is defined.

The system equations of the vehicle model are linearised and exported to the computer aided control engineering (CACE) tool, which is used to select appropriate patches w.r.t. the given design objective. The information about the reduced set of patches that have been selected for control is returned to the multibody model. Using the CACE capabilities the controller parameters are optimised according to the approach that has been the presented in Sec. 3.1.4 and a state estimator is designed.

The system is finally simulated in parallel: the vehicle system including the piezoelectric actuators and sensors is numerically integrated by the MBS tool, while the transient controller and estimator dynamics is integrated by the CACE tool. The processes communicate at discrete time events exchanging the actuator and sensor signals. In order to shorten the calculation time the processes may be performed in parallel on different computers, even on different platforms.

The detailed simulation scenario assumes the railway vehicle to run at the velocity of 162 km/h on a straight track with pseudo-stochastic rail irregularities based on the measurements of the real track Göttingen to Hannover [EG99]. The simulation time is set to 10 seconds. The acceleration at the centre of the car body's floor is defined as criterion to assess the comfort improvements of the structural control set-up.

Since industrial multibody simulation tools are tailored for problems in vehicle dynamics this spe-

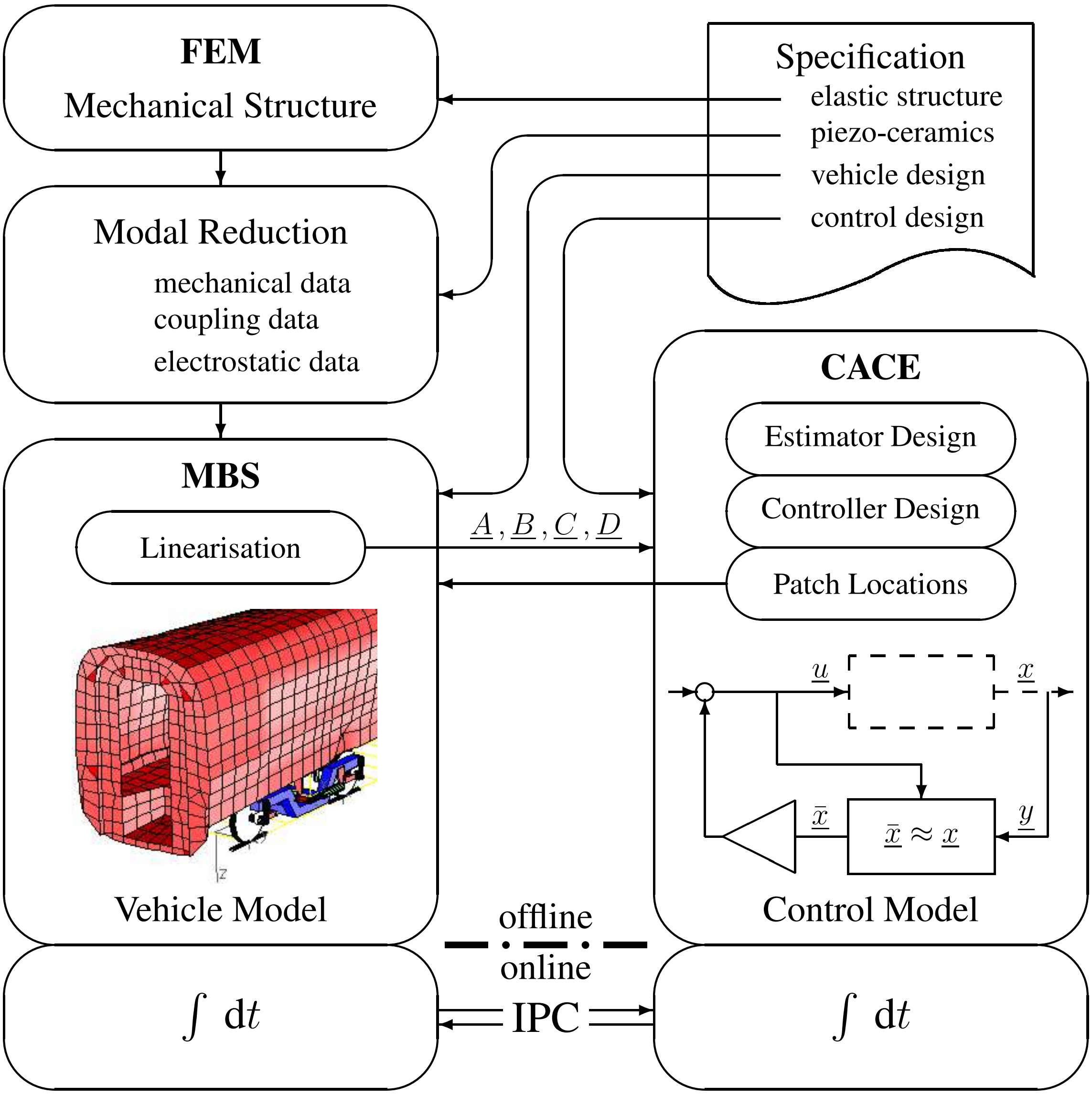

Figure 4.2: Simulation environment including finite element (FEM), multibody simulation (MBS) and computer aided control engineering (CACE) tools and inter-process communication interface (IPC).

cific scenario may easily be adapted to modified problem definitions. The variation of parameters such as the speed of the vehicle or the curvature of the track is a standard functionality as well, see e.g. [Rul98, Sec. 3.7].

The development process is at first performed and tested with a simplified beam model, which provides more insight in particular regarding the control and optimisation set-up. The experiences that have been gained that way are carried over to a second simulation with the detailed bogie railway vehicle.

4.2.3 Simplified Beam Model

The simplified structure consists of a beam model of the half railway car body with a mass of 17 500 kg, see Fig. 4.3. The car body is supported by two linear spring-damper elements each characterised by the stiffness coefficient $c = 358\,830$ N/m and the damping coefficient $d = 20\,000$ Ns/m, which reflect the compliance of the secondary suspensions of the railway vehicle. The elasticity of the primary suspension is neglected since the stiffness of the primary suspension exceeds the one of the secondary suspension by several orders of magnitude.

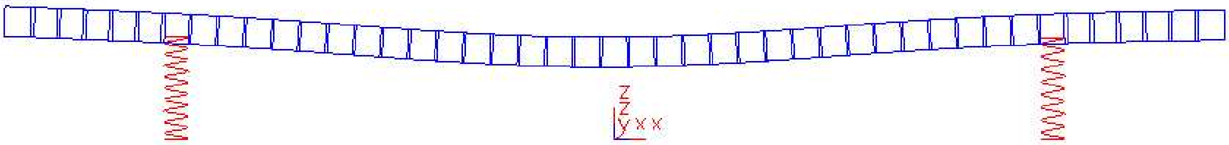

Figure 4.3: Simplified beam model of the railway car body with suspensions.

The FE model for this simplified structure is built up with 45 nodes and 44 beam elements of type Beam4 [ANS03]. For the finite element eigenvalue analysis the FE structure is supported by springs at those nodes at which the secondary suspension is supposed to be attached in the multibody model. That way the obtained eigenmodes reflect the conditions that arise from the assembly of the multibody vehicle model.

The modal model considers the first three bending eigenmodes, see Fig. 4.4, with frequencies of

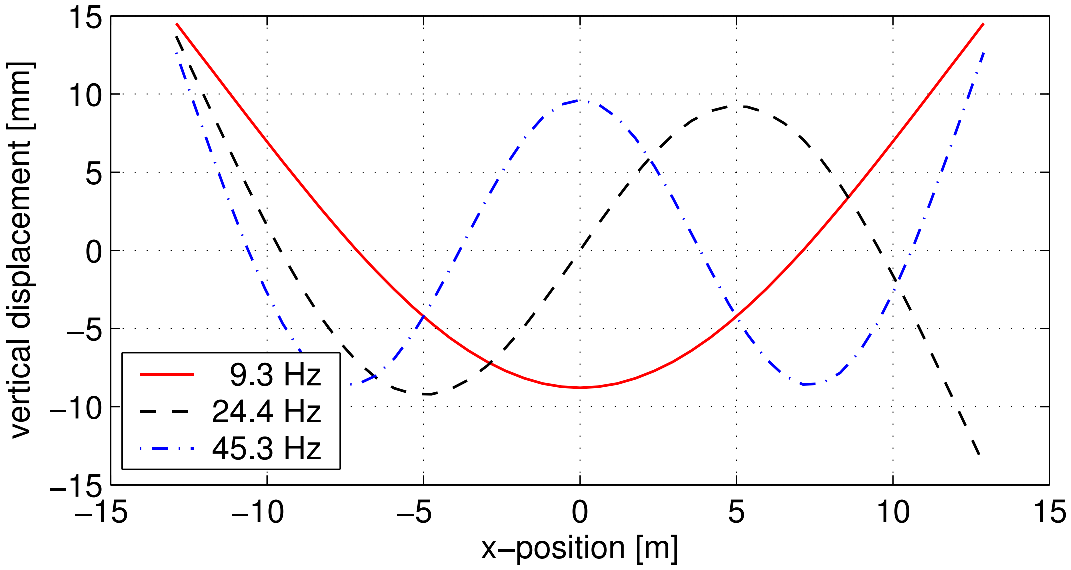

Figure 4.4: Eigenmodes of the the simplified beam model.

$9.3\,\mathrm{Hz}$, $24.4\,\mathrm{Hz}$ and $45.3\,\mathrm{Hz}$. The geometrical parameters of the beam are chosen in a way that the first eigenfrequency of the simplified beam model coincides with the first eigenfrequency of the detailed car body model. The length of the beam structure is $25.8\,\mathrm{m}$ and the distance of the spring-damper elements is $19\,\mathrm{m}$, which corresponds to the detailed car body model.

Fig. 4.5 presents the optimal location of piezo-patches for different numbers of patches.The first configuration in Fig. 4.5 uses four patches, i.e. two patches located on each side of the beam (collocated patches). The last configuration has 32 patches. The second configuration with eight patches has been selected for the simulation experiments.

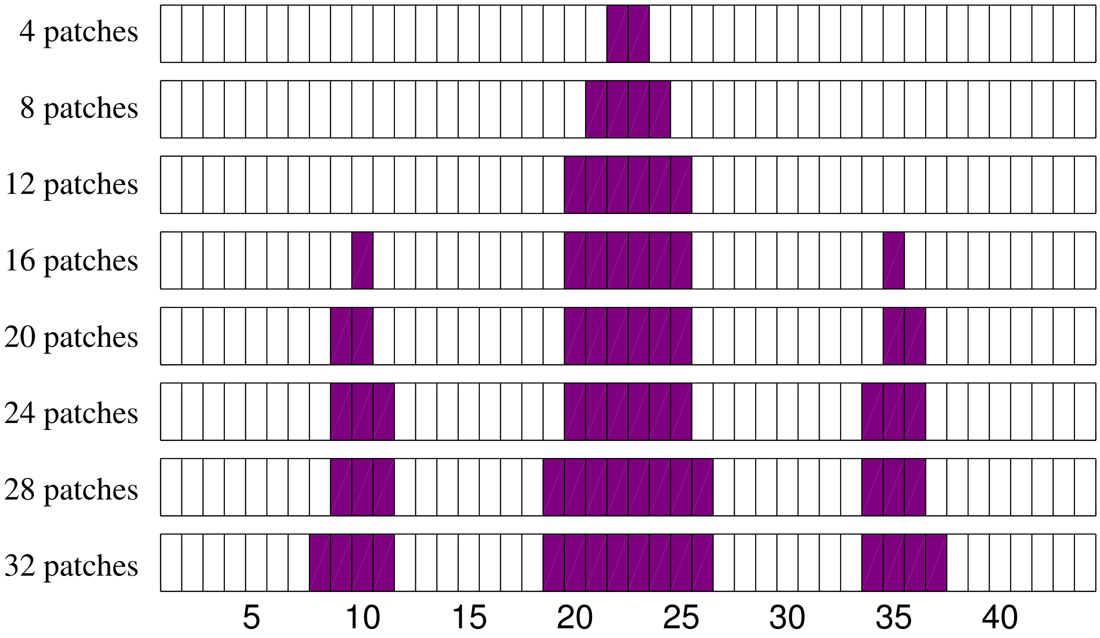

Figure 4.5: Optimal locations of the beam model for a different number of patches.

A comparison of Fig. 4.5 with Fig. 4.4 demonstrates that the positions of the first and the third eigenmode with maximum curvature of the modal displacements are preferred locations to attach structural actuators and sensors. This is well-known and was already proven by experiments, see e.g. [Lau97]. The modal displacement of the second eigenmode at the central position, where the comfort improvements shall be assessed, is zero. Therefore this eigenfrequency is not considered in the weighting matrix $\underline{Q}_{11}$ in (3.20b) and the corresponding eigenmode does not affect the selection of appropriate patches.

The simulation results in Fig. 4.6 indicate a reduction of the vertical acceleration at the centre of the beam. Since the patch selection procedure as well yields reasonable results, the development process chain is now applied to a more realistic vehicle model, an authentic *multi*body model.

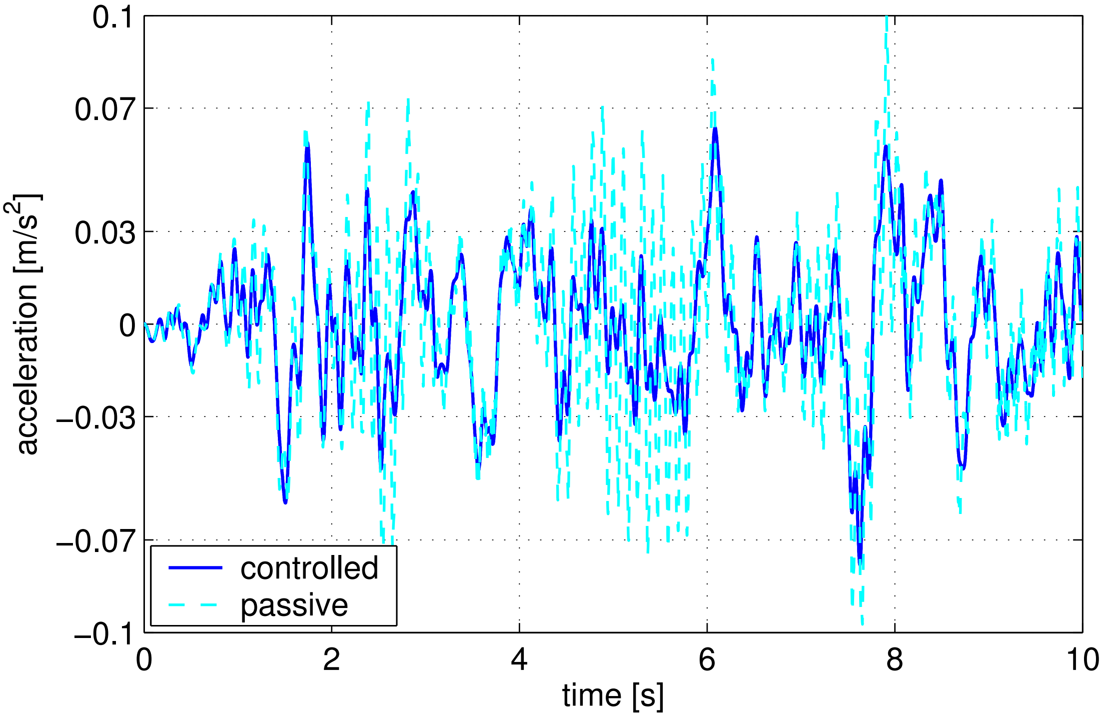

Figure 4.6: Comparison of the acceleration on the centre of the simplified beam model.

4.2.4 Detailed Car Body Model

The generic model of a bogie railway vehicle in Fig. 4.7 originates from the Mechatronic Train project, funded by the European Community, and was used to evaluate different mechatronical concepts [EG99].

The model consists of two identical bogies with the elastic car body mounted on top. Each bogie has two wheel-sets that are guided by a right-hand and a left-hand trailing arm each. This assembly is spring-mounted and damped by a set of three-dimensional and rotatory force elements that defines the primary suspension and mainly deals with the running stability.

The secondary suspension from the bogie to the car body is mainly a set of soft air-springs which are supposed to improve the passengers' ride comfort. Nonlinear bump-stops restrict the lateral motion of the car body relative to the bogie frame. Additional spring and damper elements influence the yaw and the roll motion of the bogies and the car body. All together a total number of 79 partly nonlinear force elements including four air-springs with eigendynamics are installed, see [MeT01] for detailed input parameter sets.

As profiles for rails and wheels the German norm combination UIC60/S1002 is used. To avoid discontinuous contact point locations that would lead to serious numerical complications each wheel-rail contact is modelled by a specific kinematic constraint with a smoothing algorithm called *quasi-elastic contact model.* Its basic principle is to account for the elastic deformation of wheel and rail qualitatively in the whole contact region and thus ensure the necessary smoothness of the system equations [Net98].

The FE model of vehicle car body is built up with $3\,632$ nodes and $3\,796$ elements of type Shell63 [ANS03] with bilinear shape functions for bending and membrane deflection which leads to $21\,792$ mechanical DoF.

$1\,170$ of the total $3\,796$ elements have been preselected as potential positions of piezo-patches. Less suitable positions like the neighbourhood of the suspension mounting parts on the car body and the entry areas have been rejected this way. The optimal patch locations have been determined as a subset of these 1170 positions applying the method from Sec. 3.1.4.

The final, optimised configuration considers 16 patches of the approximate size $800 \times 400\,\mathrm{mm}^2$ and $0.4\,\mathrm{mm}$ thick. The actual size of the patches varies somewhat, since the discretisation, i.e. the element geometry, of the mounting structure depends on constructive issues. In general it is difficult to manufacture piezo-elements of this large size, but an arbitrary number of smaller patches can be connected electrically in parallel to the same circuit and then behave identically to one large piezo-element. The maximum electric field is assumed to be $1\,$kV/mm, which limits the maximum voltage to 400 V.

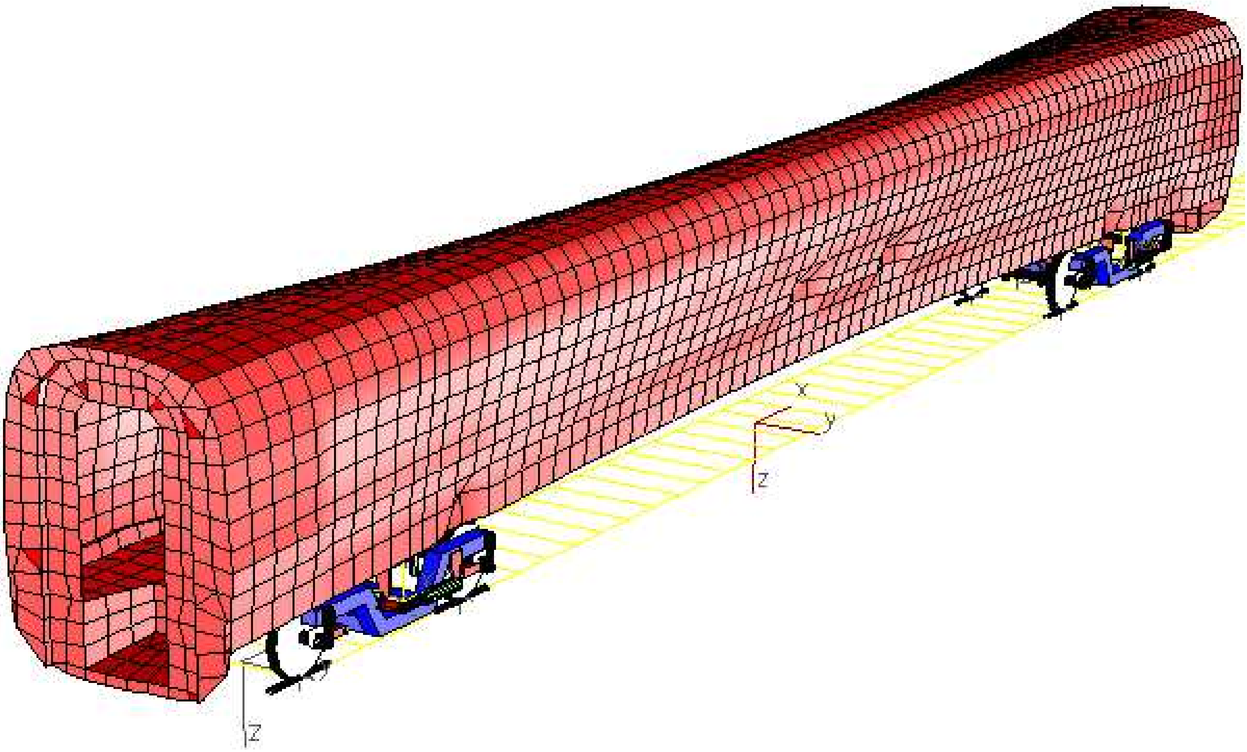

Figure 4.7: SIMPACK model of the railway car body with suspensions on a track.

i-th Mode	1	2	3	4	5	6	7
Frequency [Hz]	9.6	9.7	12.7	16.8	18.6	18.7	19.8
$[\boldsymbol{\Phi}_u(\boldsymbol{c}_m)]_{i,z}$ [mm]	0	14.0	-0.011	28.9	-1.74	-0.013	0

Table 4.2: Frequencies and modal displacements at the central node in vertical direction for the first seven car body eigenmodes.

The modal representation of the car body includes the first seven eigenmodes that are between 9 and 20 Hz. They are given in Tab. 4.2 together with the corresponding modal displacements at the central node.

All together the vehicle model has 124 states of first order. The 14 states of the state estimator as part of the control model have to be counted additionally. The control loop looks very similar to Fig. 3.4, whereas 14 instead of 28 states are involved here. The state estimator is designed six times faster than the closed loop system which leads to estimator eigenvalues with a real part of about $\mathrm{Re}\,\omega_e = -806$ 1/s, cp. [Pre02, Sec. 7.6].

The sampling rate, with which both time integration processes exchange data, has been set to 1 ms. An adapted version of the BDF-code DASSL, see Sec. 2.1.5, is used to integrate the multibody model, the Dormand-Prince integrator Ode45 deals with the control model.

The results of the transient simulation are presented in Fig. 4.8. The root mean square (RMS) value of the controlled structure is about 16% smaller than in the passive case. Fig. 4.8 reveals

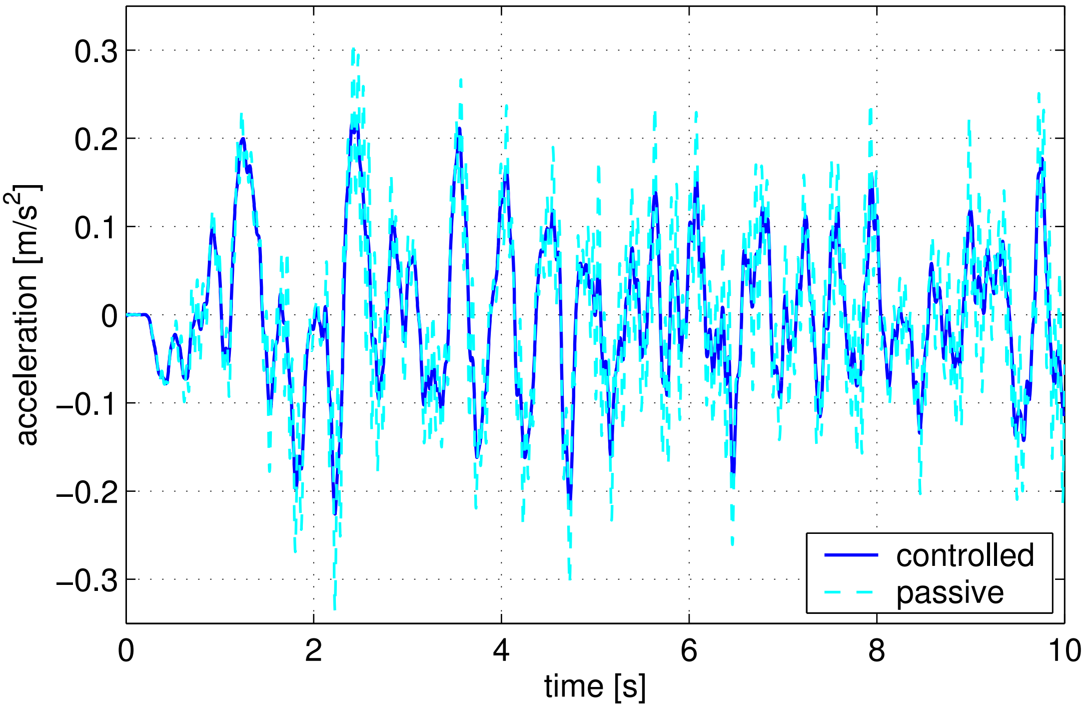

Figure 4.8: Comparison of the acceleration in vertical direction at the centre of the car body

significant differences compared to the results of the simplified beam model in Fig. 4.6, which justifies the efforts of detailing. Although the simplified model overestimates the improvements of the control set-up, it gives a first insight nevertheless.

The time integration of the multibody model has spent 448 CPU-s on the hardware specified together with Tab. 3.5 on p. 90. However, due to dynamics of the state estimator the time integration of the control model runs about 90 times slower than the one of the vehicle model and determines the over-all performance of the coupled system. Thus, the control model has been moved to an X86-based PC with 4 GB memory and two Intel $3\,199$ MHz Xeon processors with the operating system WindowsXP. With this distributed simulation set-up the entire time integration of the coupled system lasted $15\,362$ s.

4.3 A Machine Tool with Thermoelastic Deformations

4.3.1 Motivation

Modern machine tool drives show excellent dynamical properties and allow high accelerations of slides and tool heads. However, for point-to-point working tasks the accumulation of high power inputs near frequently used start and stop positions cannot be avoided for physical reasons. Due to performance losses localised thermal loads may be generated and result in an inhomogeneous temperature field of the machine base or other machine components.

The corresponding inhomogeneous thermal expansion causes tool centre point displacements that are difficult to be measured and which are widely accepted to be unavoidable. However, since technical demands on the accuracy tend to increase, this acceptance does not apply for future generations of high accuracy machine tools.

In the industrial practice the MBS model of the machine tool is not only used to simulate the working task. As outlined in Fig. 4.2 the SIMPACK environment is as well capable to provide the linear system matrices of the model. This data is already used to design the controller for all three drives of the machine tool. In this section an extension of this simulation environment is presented for new measurement and control strategies in order to deal with the thermoelastic deformation of machine tools.

4.3.2 Simulation Scenario

The feasibility study was defined in cooperation with an industrial partner who also provided a finite element model of the machine base. The welded construction of the machine is sketched in the SIMPACK model in Fig. 4.9.

The machine is symmetric w.r.t. a vertical plane and is assembled with two cantilever arms, one at each side. Each cantilever arm is driven by a linear induction device and moves along a magnet liner which is parallel to the y-axis of the machine. The cantilever carries x- and z-drives and the tool head with the tool centre point (TCP) at its tip. The flat workpiece on the machine table in Fig. 4.9 demonstrates the position of the work-plane.

As a starting point of the feasibility study it is assumed that the working task of the machine is repeated very often and varies only slightly. The objective of the study is to reproduce a constant thermal operating state of the machine that is reached after a sufficiently large time span. This is a frequently observed operating condition in the industrial use of machine tools. Fig. 4.10 shows the predefined positioning loop of the cantilever arm along the y-axis which is assumed to be repeated periodically.

In order to model the thermal behaviour a heat source of intensity $\bar{q}$ at the position $\bar{y} = \bar{y}(t)$ is

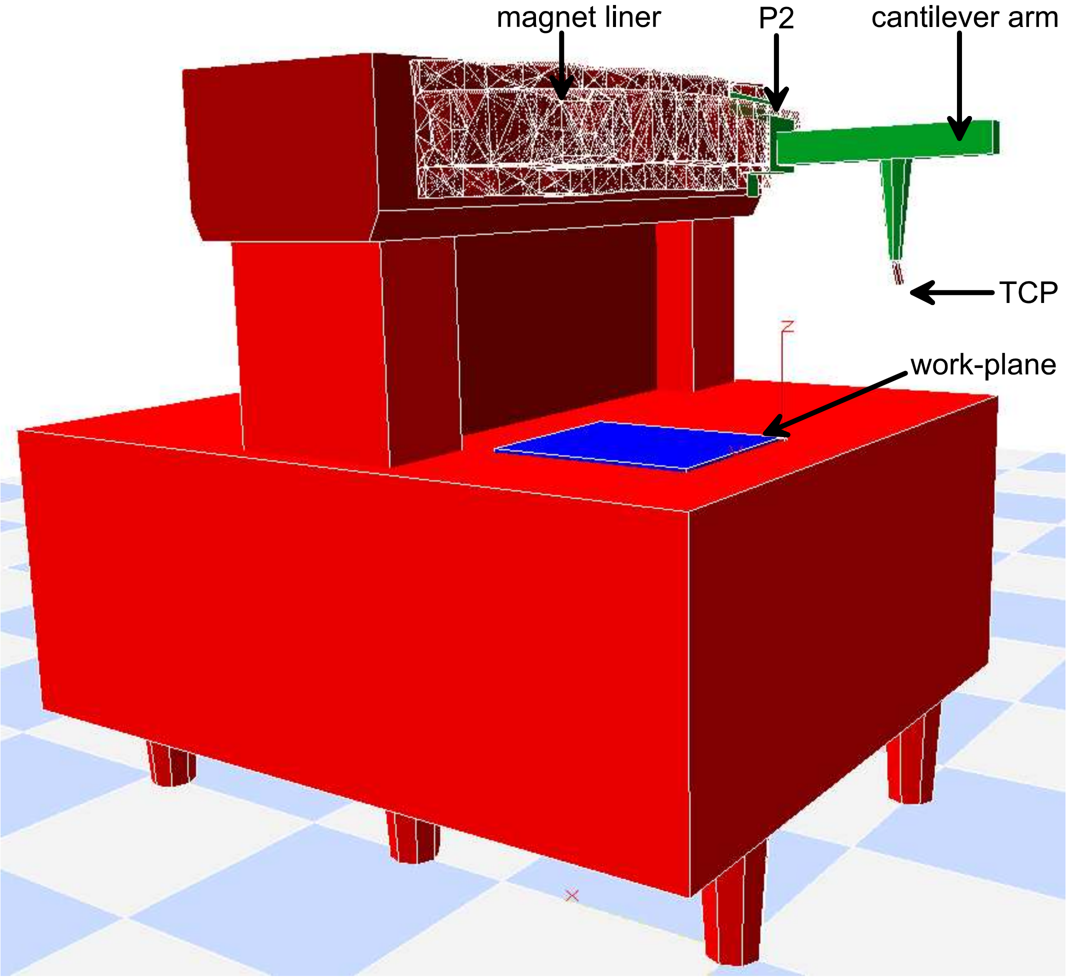

Figure 4.9: Principle lay-out of the machine tool in SIMPACK.

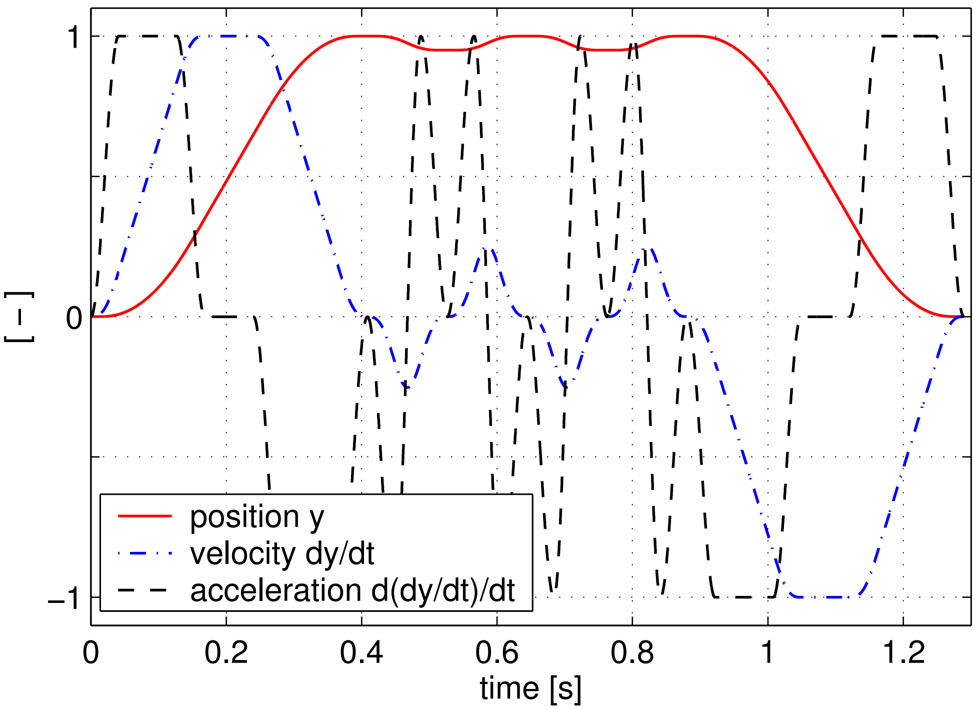

Figure 4.10: Predefined positioning loop $\bar{y} = \bar{y}(t)$ and its time derivatives in normalised representation.

considered to move along an isotropic one-dimensional continuum, described by the co-ordinate y. For mathematical representation, the formulation of a point source by means of the Dirac function $\mathfrak{d}(y-\bar{y})$, see [Now78b, (19.28)], is extended by a term that accounts for the geometrical dimensions of the heat source, i.e. the drive head on the cantilever arm. The heat flux is assumed to be distributed as a Gaussian bell-shaped curve with a parameter a that reflects the length of the drive head:

$$-\Lambda\vartheta_{,yy} + \varrho c\dot{\vartheta} = Q(t,y,\bar{y}) = \begin{cases} \bar{q}\;\mathfrak{d}(y-\bar{y}) & \text{point source} \\ \bar{q}\,\sqrt{\frac{a}{\pi}}\,\exp(-a(y-\bar{y})^2) & \text{distributed source} \end{cases} \tag{4.1}$$

For constant hot running conditions the time dependent terms in (4.1) have to vanish. The localised heat supply $q = q(y)$ is obtained as time average over one positioning loop with period T:

$$\left.\begin{array}{rcl} \bar{q}(t) & = & \bar{q}(t+nT) \\ \bar{y}(t) & = & \bar{y}(t+nT) \\ n & \to & \infty \end{array}\right\} \Longrightarrow -\Lambda\vartheta_{,yy} \approx \frac{1}{T}\int\limits_0^T Q(t,y,\bar{y})\;\mathrm{d}t = q(y) \tag{4.2}$$

Since the specific design of the cantilever suspension involves only very small frictional forces, the mechanical power is almost completely invested into the kinetic energy of the cantilever arm and may be easily described based on the predefined kinematic scenario in Fig. 4.10. If it is assumed, that a constant share of the consumed electrical power is transformed into heat energy

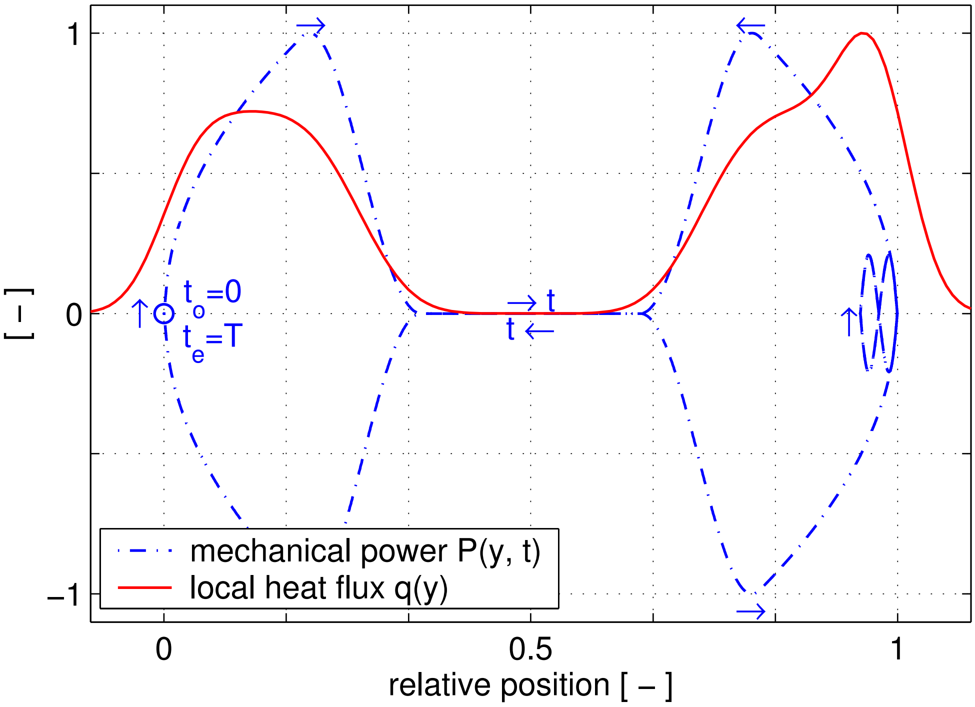

Figure 4.11: Mechanical power consumption and quasi-stationary heat flux.

and conducted to the surface of the machine base, the complete information to evaluate the localised heat supply $q = q(y)$ according to (4.2) is given.

Fig. 4.11 presents the results of this numerical evaluation. The mechanical power consumption is plotted versus the relative position of the cantilever arm on the magnet liner with the time as curve parameter. The start and stop positions are denoted by the relative position 0 and 1 respectively.

The power consumption, specified by the instantaneous product of mass m, velocity $\dot{y}$ and acceleration $\ddot{y}$ from Fig. 4.10, has distinct maxima in the neighbourhood of start and stop positions. Therefore, the quasi-stationary heat flux accumulates at specific positions on the magnet liner. On the other hand, those parts of the magnet liner at which the cantilever arm moves with constant velocity, are not subjected to heat loads.

4.3.3 Finite Element Analysis

The thermal finite element model of the machine base consists of $20\,641$ tetrahedral shaped elements of type Solid90 [ANS03] with $40\,471$ nodes or thermal DoF respectively.

A steady state heat transfer FE analysis has been performed using the analytical heat source introduced above as quasi-stationary load. The solid curve in Fig. 4.11 is taken as heat flux distribution in y-direction along the upper surface of the magnet liner, which is visualised in Fig. 4.12. In the

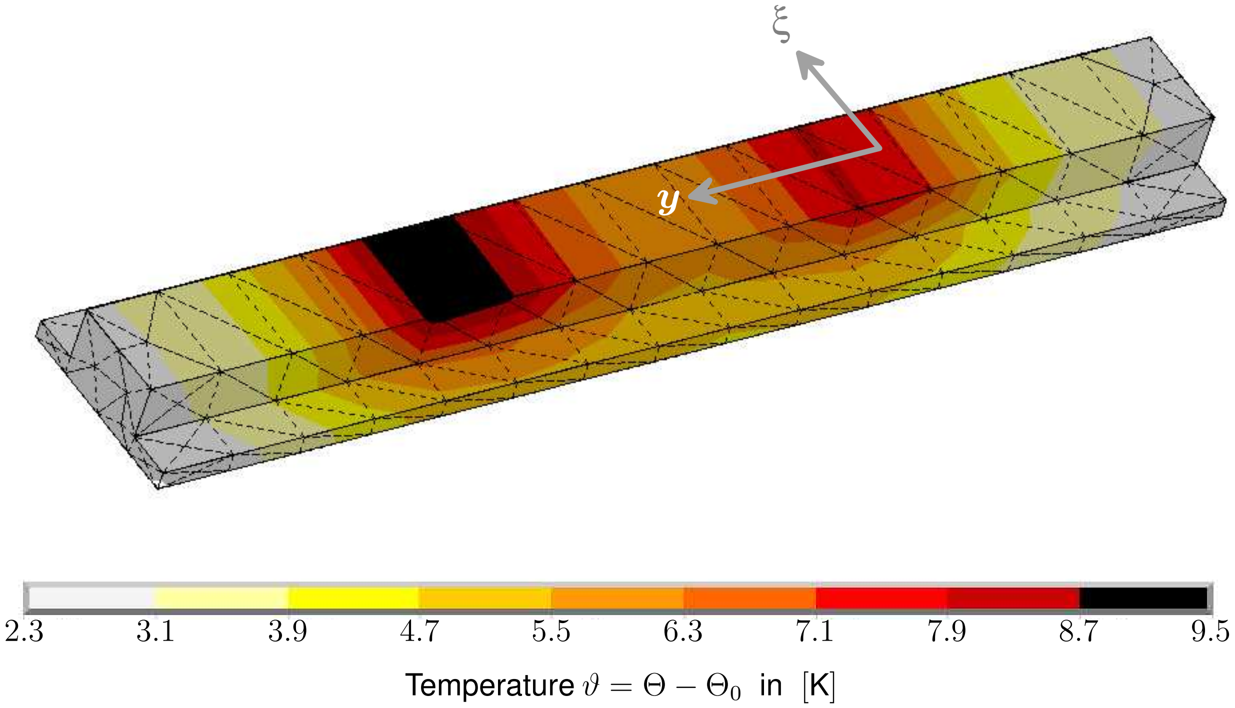

Figure 4.12: Temperature field at the magnet liner, obtained by FE analysis.

ξ-direction on the upper surface, the heat flux is modelled to be constant. Robin boundary conditions are defined on the complete surface of the machine base with two different film coefficients to reflect different cooling conditions due to the air-stream forced by the moving of the cantilever.

The heat transfer analysis is performed twice, separated for each cantilever drive. Since all structural analysis, the thermal as well as the following mechanical, are linear, the solutions may be superimposed.

Fig. 4.12 presents the results of one heat transfer FE analysis. Since the temperatures mainly vary on the magnet liner while the other elements of the machine base show only small temperature differences, Fig. 4.12 only visualises the temperature field of the magnet liner. Two distinct temperature maxima on the magnet liner are clearly visible.

The two FE temperature field solutions of the complete machine base have been applied as separate thermal loads on the mechanical finite element model of the base structure, which uses the same mesh as the thermal FE-model. However, the mesh now specifies 20 641 elements of type Solid95 [ANS03] with 121 413 mechanical DoF. The solutions of these steady state FE analysis yield the displacement fields of the machine base caused by the temperature fields and are interpreted as thermal response modes according to Sec. 3.2.2.

Fig. 4.13 plots the thermal displacements of a reference point on the deformed surface of the magnet liner, which moves along the motion path of the cantilever arm with constant velocity from its start

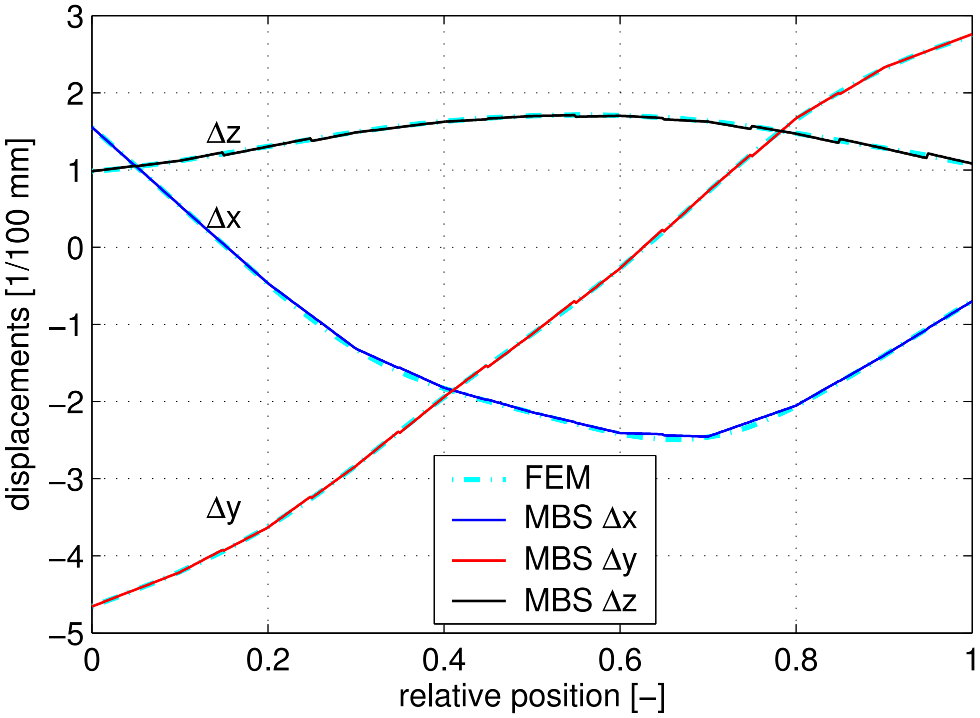

Figure 4.13: Comparison of the thermal displacements as evaluated by FEM and the corresponding thermal response mode.

to its stop position. The backside of the machine is not subjected to thermal loads, i.e. the second cantilever drive is assumed to be out of use. Fig. 4.13 compares the FE results along the motion path with the corresponding multibody deformations modelled by thermal response modes.

Besides the steady state analysis, a finite element eigenvalue analysis is performed and 27 eigenmodes of the machine base are obtained. That way, the dynamical properties of the mechanical structure up to the frequency of 400 Hz are described. Tab. 4.3 gives an overview of the evaluated eigenfrequencies of the machine base.

A unified set of modes consisting of 27 mechanical eigenmodes in the frequency range according to Tab. 4.3 and two thermal response modes has been used to reduce the finite element description of the machine base and get a modal multifield representation according to Fig. 3.12. The coupling between the eigenmodes and the thermal response modes is comparable weak, but the unified set

No.	Frequencies [Hz]									
1-10	90.1	104.5	114.4	116.6	119.4	138.7	157.5	187.9	188.5	209.1
11-20	269.1	285.7	290.5	295.8	311.2	321.7	326.5	332.7	335.8	337.0
21-27	354.2	360.8	371.0	380.0	383.5	386.5	390.9			

Table 4.3: Eigenfrequencies of the machine base obtained from a FE eigenvalue analysis.

of modes is not orthogonal with respect to the mass and the stiffness matrix. In view of the fact that both groups of modes contain a different physical information which is worth to be retained, the unified set of modes has not been orthogonalised for the multibody simulation.

On a trial basis a supplementary orthogonalisation of the 29 modes has been performed yielding $1\,694$ Hz and $2\,368$ Hz as additional frequencies due to the thermal response modes, while the eigenfrequencies of Tab. 4.3 remain unchanged.

4.3.4 Multibody Simulation

Fig. 4.9 shows the principle structure of the multibody model and the FE mesh of the magnet liner. Also the complete machine base originates from the FE model and is mechanically represented as flexible body in modal representation.

Since the machine base rests on six feet, which are not fixed to the foundation, its reference frame has three degrees of freedom that allow a plane motion of the machine base frame w.r.t the inertial frame. Six stick-slip force elements reflect the dry friction conditions between machine base and ground.

The suspension of the cantilever arm is modelled by spring-damper elements, which connect the deformed magnet liner and the base of the cantilever arm. The cantilever arm itself is assumed to be rigid. Since the arm moves along the liner, so called *moved markers* have be defined that represent the working points of the suspension forces at the machine base.

The current position of a moved marker does in general not coincide with the position $\boldsymbol{c}_k$ of a known node k with the known modal matrix $\boldsymbol{\Phi}_u(\boldsymbol{c}_k)$. Since the modal representation does not include any topological information about the flexible body, neither the position of the moved marker nor its displacement due to the deformation of the machine base is given explicitly. Therefore, this information has to be evaluated by interpolation from four known positions in the neighbourhood, which is the actual capability of a moved marker. The reference point for Fig. 4.13 has been modelled with such a moved marker. Thus, it is also verified that the interpolation of positions and displacements works satisfactory.

In order to simulate the working task of the machine tool a controller for the y-drive is modelled. The kinematic scenario from Fig. 4.10 serves as target specification of the control loop, which is adjusted in such a way that the positioning error induced by the drive control is at least one order of magnitude smaller than the other displacements and cannot falsify the results.

Three different measurements are compared in Fig. 4.14, where all results concern the displacements w.r.t. the workpiece on the table of the machine tool. Again, it is assumed that the second

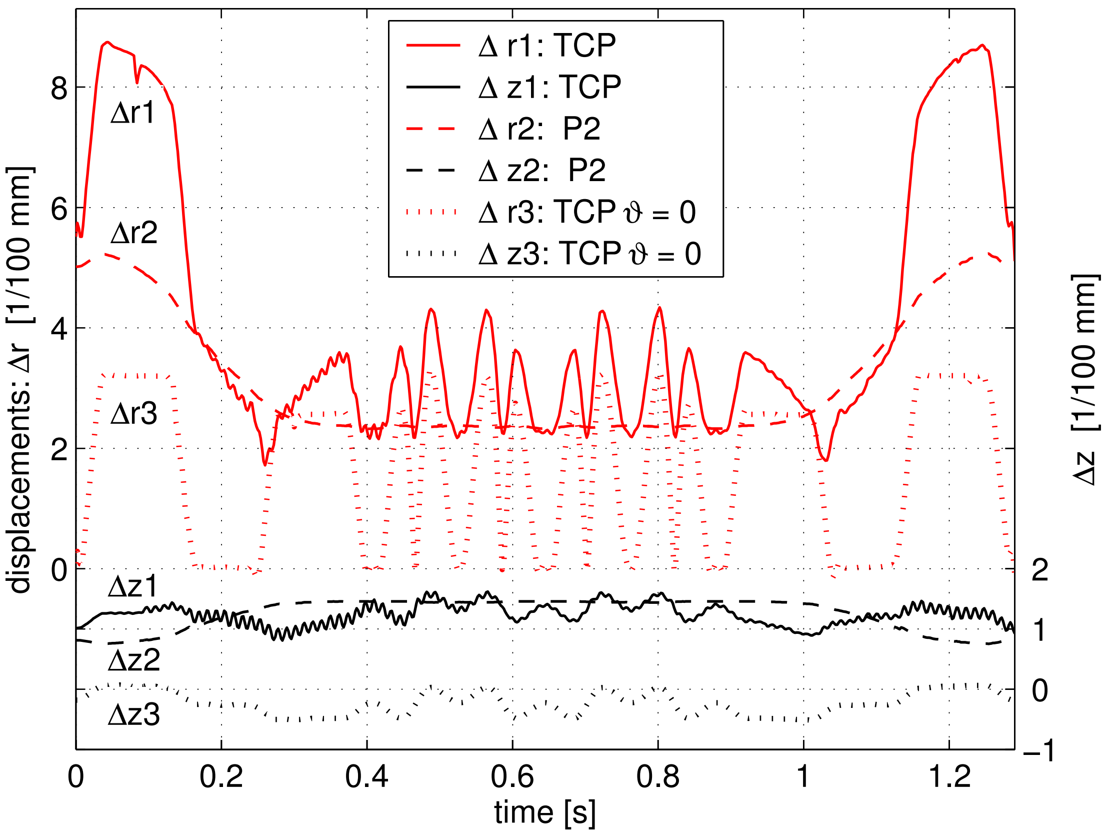

Figure 4.14: MBS displacement results at the tool center point (TCP) in solid lines and at the reference point P2 on the magnet liner in dashed lines. $\Delta r_{\dots}$ denotes the absolute displacement parallel to the work plane, while $\Delta z_{\dots}$ is measured normal to the work-plane. The third couple of curves in dotted lines visualises the TCP-displacements in a simulation without any thermal load ($\vartheta = 0$).

cantilever drive is out of use.

The dotted curves give the tool centre point (TCP) displacements of a multibody simulation without any thermal loads and serve as a reference. These displacements are only caused by the response of the machine base structure and the cantilever suspension to the dynamical loads given by the predefined kinematic scenario.

The other two measurement types in Fig. 4.14 additionally involve the displacements which are induced by the temperature field of the machine base.

The dashed curves plot the displacements of the reference point P2 on the magnet liner, which moves with the cantilever arm. The solid curves again give the displacements of the TCP at the tip of the cantilever arm. The difference between the P2- and TCP-displacements are caused by the kinematic amplification of the cantilever arm.

The thermally induced displacements influence the motion of the TCP mostly in the neighbourhood of the start position at the beginning and at the end of the simulation. However, since the working task consists of a point-to-point job, these deviations are not crucial in this case. More important are the deflections at the stop position, which is reached several times within $0.4\,s$ and 0.9 s. The dotted and the solid curves differ here by about $10\,\mu$m to $20\,\mu$m, which is a relevant error concerning the demanded accuracy of machine tools. It could be confirmed that thermal displacements of this order of magnitude have already been observed in the industrial use of machine tools.

Besides the thermal deflection, the response of the machine base structure corresponds mainly to the acceleration curve in Fig. 4.10 and is of static nature. The vibrations in Fig. 4.14 primarily originate from the compliance of the cantilever suspension. This statement could be verified by an accompanying simulation, for which the compliance of the cantilever suspension is neglected. The structural damping of the machine base has also no significant influence (Lehr's damping coefficient $d = 0.004$). These facts together with the lowest eigenfrequency of 90.1 Hz from Tab.4.3 leads to the conclusion that the machine base is a well designed, stiff structure.

The time integration has spent $3\,580$ CPU-s. This high computational effort is caused by the high frequency band width of the MBS model. Since the inertia terms that correspond to the thermal response modes have not been neglected for this simulation, frequencies up to 2.400 Hz are present, which leads to a very stiff system, cf. [Sim01].

With the results presented above the controller design of the machine may be extended to additionally consider thermal displacements modelled by a few thermal response modes. Temperature sensors may be used to observe the thermal state of the real machine base. This thermal state drives the thermal displacement state. With a discretisation by appropriate thermal response modes, it is possible to compensate the thermal displacements by the control law. Thus, the feasibility of the approach which enables to account for thermal influences on the quality of working task of the machine is demonstrated.

5 Summary and Outlook

Outline of the Presentation

The multifield description of the present work extends the classical flexible body representation in multibody dynamics. Therefore a review of the state-of-the-art in dealing with flexible multibody systems commences the exposition.

The kinematics are based on the floating frame of reference formulation to separate large reference motion from linear elastic deformation, which is described by global modes. This approach is inserted into the Hamilton's principle in order to obtain the equations of motion. The exploitation of the topology of multibody systems enables a very efficient recursive evaluation of these equations for chain- or tree-structured systems as well as for structures with closed kinematic loops.

In order to obtain a linear material law that describes the influence of mechanical, electrical and thermal field quantities on a material particle, a thermodynamical potential, namely the electric Gibbs potential, is approximated by a quadratic form. Analogously to the displacement field of the flexible body, the temperature field and the electrical potential field are spatially semi-discretised by global modes. The coupled set of field equations in weak form is obtained by means of a generalised Hamilton's principle and compared to the strong formulation of the thermal and the electrostatic field.

Since native electromechanical finite element data of beam and shell structures is not yet available in industrial finite element tools, a technique to evaluate the electromechanical data of piezoceramic devices based on purely mechanical finite element data is introduced. Further modelling issues such as verification are exemplified by the simulation of a metal sheet, which is excited by a force impact. A strategy to control the structural vibrations and determine the optimal device locations is given.

In view of some fundamental arguments from literature, so-called thermal response modes are proposed in order to model thermoelastic problems. This scheme, which reduces the mechanical and thermal finite element description into a modal representation, neglects the influence of the inertia terms regarding deflections caused by thermal loads. The Gough-Joule effect, i.e. the influence of the mechanical deformation on the temperature field, also turned out to be small enough to be neglected. The feasibility of the approach is shown by means of the simulation of a circular disc with constant thermal loads and the simulation of hot spots on a brake disc. Evaluations with the finite element method are taken as a reference in order to justify the statements about the properties of the modal multifield approach. Thus, an extraordinary efficiency with only small losses of accuracy could be demonstrated.

An extended development environment for the design of smart structures consisting of finite element, multibody simulation and computer aided control engineering tool with appropriate interfaces and software components is realised. The development of an active damping regime of a railway car body exemplifies the application of this environment. Since multibody tools are tailored for vehicle applications, a large number of options and capabilities, which e.g. allow quasi-stochastic excitations based on railway track measurements to be defined, support the assessment of smart structures in specific design configurations.

In order to simulate the working task of a machine tool, the approximately 160 000 degrees of freedom that are defined by the finite element model of the machine base are reduced to the essential information of interest. The modal multifield representation of the structure employs only 29 degrees of freedom and is therefore suited for control design as well. By analysing the simulation results it can be shown that the thermally induced tool centre point displacements take on remarkable values, which are difficult to gauge with conventional measurement devices of machine tools.

Outlook and Open Problems

It is a characteristic of smart structures that the physical modelling is only one part of the actual task. The design optimisation problem and the set-up of appropriate control concepts are important as well. The presented methodology is supposed to support this process. However, additional parameter studies and comparisons in order to streamline the weighting within the LQR control of the piezo-ceramic devices in Sec. 3.1.4 are necessary.

The implementation of active structural control devices in practice still has to deal with major pitfalls such as the handling of multi-channel-signal-processing for the simultaneous use of distributed patches for actuation and sensor purposes.

Although realisations like tennis rackets and snow-boards exist, passive damping applications have to deal with a crucial lack of robustness against parameter variations. That is why semi-active strategies gain more and more importance, see e.g. [CC02]. Of course, the proposed environment is suitable for the simulation of passive or semi-active vibration damping scenarios as well, in particular if large reference motion is involved as demonstrated in [Hec03].

Neglecting the inertia terms that correspond to the thermal induced deflections is not only useful to justify the definition of thermal response modes but also improves the numerical properties of a thermoelastic multibody system. Therefore, the consistent transfer of the modal multifield approach into an industrial multibody simulation environment has to exploit this fact and neglect specific mass terms, which requires a modification of the multibody formalism of Sec. 2.1.5.

The upgrade of the specific machine tool model from Sec. 4.3 will include the development of an appropriate approach to discretise the temperature distribution on the magnet liner in space in order to deal with continuously varying working tasks. The transient temperature behaviour of the machine base during the warm-up phase is another point of interest.

The presented hot-spot-scenario in Sec. 3.2.4 only delineates the beginning of a development that may lead to a consistent thermal and mechanical brake model. Possible subjects of research are numerous and include effects such as temperature dependent friction, dynamical interaction of brakes and vehicle suspensions or aircraft landing gears, wear prediction, electromechanical brake actuation, anti-skid system set-up, brake noise generation and so on.

If all three considered fields - the thermal, the electrostatic and the mechanical - are simultaneously present, the application of the modal multifield approach constitutes a still outstanding modelling challenge. The simulation of a micro-electromechanical device here comes to mind. A comparison of the publication by CHIAO and LIN, *Self-Buckling of Micromachined Beams under Resistive Heating* [CL00], with the thermal buckling simulation in [HAV05] reveals that the problem specification in micro-scale systems are frequently quite similar to the macro-scaled systems which are mainly addressed by the present thesis.

As a final conclusion it may be stated that the presented low-dimensional representation of distributed phenomena opens new chances for system dynamical engineering issues. Complex applications, which could be analysed so far either in detail using the finite element method or only roughly neglecting important influences, may now be modelled more comprehensively from a system dynamical point of view.

A Specification of Input Data

In this chapter, the input data of all simulations presented in Ch. 3 is summarised. The reader should therefore be enabled to reproduce all results and to assess the reasonability of the chosen modelling approaches.

The appended ANSYS scripts were performed with the versions ANSYS Release 7.1 and ANSYS Release 8.0, while the MATLAB scripts run with the Version 6.5.1.199709 Release 13 (Service Pack 1). Both simulation tools are installed on a HP-UX 11.0 operating platform.

A.1 Control of a Metal Sheet

Tab. A.1 outlines the physical and geometrical information of the mechanical structure on which the simulations in Sec. 3.1.4 are based.

Entity	Symbol	Unit	Value
mounting structure			
Young's modulus	E	N/m^2	$2.1 \cdot 10^{11}$
Poisson constant	ν	-	$0.3 \cdot 10^{0}$
Density	ϱ	kg/m^3	$7.85 \cdot 10^{3}$
Length		m	$1.3 \cdot 10^{0}$
Width		m	$1.0 \cdot 10^{0}$
Thickness	$2\|s_0\|$	m	$0.9 \cdot 10^{-3}$

Table A.1: Geometrical, physical and control set-up data of the simulations in Sec. 3.1.4.

The ANSYS script in Fig. A.1 refers to the data set in Tab. A.1 and may be executed in order to obtain the finite element model of the simulated structure. The corresponding physical, geometrical and control set-up data for the piezo-ceramic patches is given in Tab. A.2.

```
/filname,metsheet,1
/PREP7
!*** geometry ************
BLC4, , ,1,1.3
!*
!*** element *************
ET,1,SHELL63
!*
R,1,.0009,.0009,.0009,.0009,,,
!*** material ***
MP,EX,1,2.1e11
MP,NUXY,.3
MP,DENS,1,7800
!*
!*** meshing *************
TYPE,1
REAL,1
MAT,1
LSEL,S,Length,,.9,1.1
LESIZE,all,,,10
LSEL,S,Length,,1.2,1.4
LESIZE,all,,,14
alls
MSHAPE,0,2D
MSHKEY,0
AMESH,all
!*
!*** boundary conditions ***
NSEL,S,NODE,,1,2
NSEL,A,NODE,,12,
NSEL,A,NODE,,26,
D,all,UX,,,,,UY,UZ
alls
!*
!*** end ******************
finish
save
```

Figure A.1: ANSYS script defining the FE-model of the simulations in Sec. 3.1.4.

Entity	Symbol	Unit	Value
piezo-ceramic patch			
Elasticity	$c_{11} = c_{22}$	N/m^2	$1.26 \cdot 10^{11}$
	c_{12}	N/m^2	$7.95 \cdot 10^{10}$
	c_{44}	N/m^2	$2.33 \cdot 10^{10}$
Permittivity	ϵ_{33}	F/m	$1.3 \cdot 10^{-8}$
Piezoelectric coefficients	$e_{31} = e_{32}$	C/m^2	$-6.5 \cdot 10^{0}$
Length		m	$9.29 \cdot 10^{-1}$
Width		m	$0.1 \cdot 10^{0}$
Thickness	$s_1 - s_0$	m	$0.2 \cdot 10^{-3}$
control set-up			
Weighting factor	k_Q	-	$1.0 \cdot 10^{10}$
Estimator eigenvalues	ι	1/s	$\leq -5.81 \cdot 10^{1}$
$\iota \pm \mathrm{j}\upsilon$	υ		$\leq 2.96 \cdot 10^{0}$

Table A.2: Geometrical, physical and control set-up data of the simulations in Sec. 3.1.4.

As a result of the modal reduction process which includes the generation of the electrostatical-mechanical coupling data, the set of equations in (A.1) are yielded:

$$\begin{aligned} \boldsymbol{M}_{uu}\ddot{\boldsymbol{z}}_{uu} + \boldsymbol{D}_{uu}\dot{\boldsymbol{z}}_{u} + \boldsymbol{K}_{uu}\boldsymbol{z}_{u} &= \boldsymbol{h}_{f} + \boldsymbol{K}_{u\varphi}\,\boldsymbol{z}_{\varphi}\ , \\ \boldsymbol{K}_{u\varphi}^{T}\boldsymbol{z}_{u} + \boldsymbol{K}_{\varphi\varphi}\,\boldsymbol{z}_{\varphi} &= \boldsymbol{h}_{\varphi}\ . \end{aligned} \tag{A.1}$$

The terms of (A.1) are detailed in Table A.3.

Term	Specification	Reference		
$\boldsymbol{M}_{uu}$	$\boldsymbol{I}_{14}$			
$\boldsymbol{K}_{uu}$	$\mathrm{diag}\{2\pi\bar{\omega}_i\}^2$	$\bar{\omega}_i$	see	Tab. 3.1
$\boldsymbol{D}_{uu}$	$\mathrm{diag}\{4\,\pi\,\bar{\omega}_i \cdot 0.01\,\}$	$\bar{\omega}_i$	see	Tab. 3.1
$\boldsymbol{h}_f$	$\boldsymbol{\Phi}_u^T(\boldsymbol{c}_m)\cdot(\,0\;\;0\;\;f(t)\,)^T$	$\boldsymbol{\Phi}_u(\boldsymbol{c}_m)$	see	Tab. 3.3
		$f(t)$	see	Fig. A.2
$\boldsymbol{K}_{\varphi\varphi}$	$6.035714\cdot 10^{-5}\cdot\boldsymbol{I}_{140}$			
$\boldsymbol{K}_{u\varphi}$			see	Tab. A.4

Table A.3: Specification of the matrices and vectors in (A.1).

The time plot of the force impact $f(t)$, which acts on the central node and is represented by the external force $\boldsymbol{h}_f(t)$ in (A.1) is visualised in Fig. A.2.

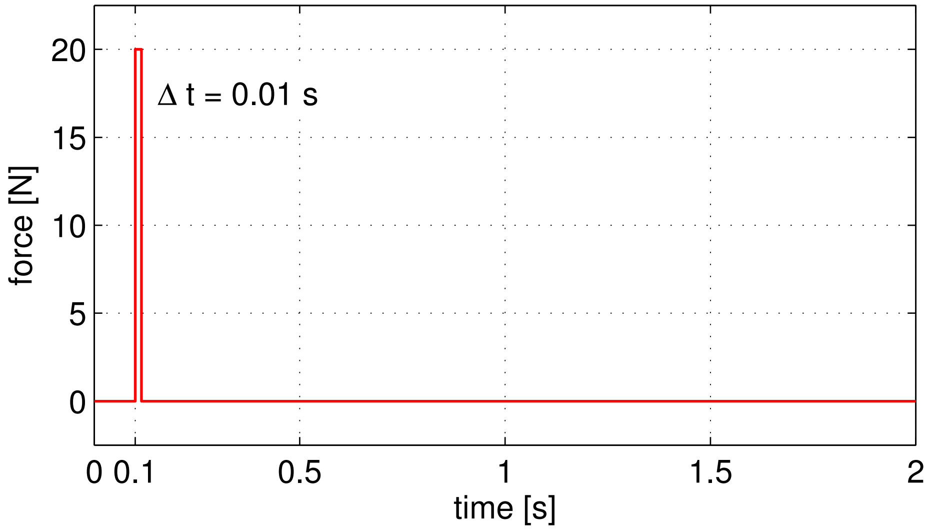

Figure A.2: Excitation force $f = f(t)$ of the simulations in Sec. 3.1.4.

The mechanical-electrostatic coupling matrix $\boldsymbol{K}_{u\varphi}$ for the 24 patches, which have been selected for control may be reproduced according to Tab. A.4.

	$\boldsymbol{K}^o_{u\varphi} \times 10^3$					
	Patch location according to the “rows/columns” in Fig. 3.5					
	5/3	6/3	4/7	5/7	6/7	7/7
	Column					
Row	1	2	3	4	5	6
1	-0.05271	-0.05271	-0.06994	-0.07128	-0.07128	-0.06994
2	-0.01336	0.01336	-0.06078	-0.02109	0.02109	0.06078
3	0.17383	0.17383	0.02452	0.02575	0.02575	0.02452
4	-0.16151	-0.16151	-0.00201	-0.02244	-0.02244	-0.00201
5	0.08756	-0.08756	0.04678	0.01631	-0.01631	-0.04678
6	0.04499	0.04499	0.07603	0.06706	0.06706	0.07603
7	0.14890	0.14890	0.69639	0.84684	0.84684	0.69639
8	0.19791	-0.19791	-0.04510	-0.00597	0.00597	0.04510
9	-0.20089	0.20089	0.02545	0.00501	-0.00501	-0.02545
10	0.88852	0.88852	0.29247	0.36419	0.36419	0.29247
11	0.36838	0.36838	-0.29860	-0.12046	-0.12046	-0.29860
12	-0.16931	0.16931	-1.29737	-0.51188	0.51188	1.29737
13	0.08835	-0.08835	0.87111	0.39817	-0.39817	-0.87111
14	-2.03473	-2.03473	1.34832	1.61667	1.61667	1.34832
	Patch location according to the “rows/columns” in Fig. 3.5					
	4/8	5/8	6/8	7/8	5/12	6/12
	Column					
Row	7	8	9	10	11	12
1	-0.06994	-0.07128	-0.07128	-0.06994	-0.04525	-0.04525
2	-0.06078	-0.02109	0.02109	0.06078	-0.01057	0.01057
3	-0.02452	-0.02575	-0.02575	-0.02452	-0.18047	-0.18047
4	-0.00201	-0.02244	-0.02244	-0.00201	-0.19656	-0.19656
5	-0.04678	-0.01631	0.01631	0.04678	-0.08225	0.08225
6	-0.07603	-0.06706	-0.06706	-0.07603	0.10919	0.10919
7	0.69639	0.84684	0.84684	0.69639	-0.00829	-0.00829
8	-0.04510	-0.00597	0.00597	0.04510	0.23504	-0.23504
9	-0.02545	-0.00501	0.00501	0.02545	0.29432	-0.29432
10	-0.29247	-0.36419	-0.36419	-0.29247	-0.43043	-0.43043
11	-0.29860	-0.12046	-0.12046	-0.29860	-0.01715	-0.01715
12	-1.29737	-0.51188	0.51188	1.29737	-0.14617	0.14617
13	0.87111	0.39817	-0.39817	-0.87111	-0.15748	0.15748
14	1.34832	1.61667	1.61667	1.34832	-1.51955	-1.51955

Table A.4: The mechanical-electrostatic coupling matrix $\boldsymbol{K}^o_{u\varphi}$ of those 12 patches on the upper side of the sheet that have been selected for control in Sec. 3.1.4. The corresponding matrix for the 12 patches on the lower side is given by the relation $\boldsymbol{K}^u_{u\varphi} = -\boldsymbol{K}^o_{u\varphi}$.

A.2 Verification Example 1: Disc with Thermal Loads

The simulations in Sec. 3.2.3 are based on the data set that is listed in Tab. A.5.

Entity	Symbol	Unit	Value
Young's modulus	E	N/m^2	$2.1 \cdot 10^{11}$
Poisson constant	ν	-	$0.3 \cdot 10^{0}$
Density	ϱ	kg/m^3	$7.8 \cdot 10^{3}$
Thermal conductivity	Λ	W/(mK)	$4.3 \cdot 10^{1}$
Thermal expansion	α	1/K	$1.2 \cdot 10^{-5}$
Specific heat capacity	c	J/(kgK)	$4.65 \cdot 10^{2}$
Inner radius	r_i	m	$0.75 \cdot 10^{-1}$
Outer radius	r_a	m	$1.5 \cdot 10^{-1}$
Thickness	s	m	$0.7 \cdot 10^{-2}$
Heat flux	q_B	$\mathrm{W/m^2}$	$3.0 \cdot 10^{3}$
Film coefficient	h_f	$\mathrm{W/(m^2K)}$	$1.0 \cdot 10^{1}$
Bulk temperature	ϑ_∞	K	$-2.0 \cdot 10^{2}$

Table A.5: Geometrical and physical data for the simulation in Sec. 3.2.3.

The modal temperatures $\boldsymbol{\Phi}_\vartheta(\boldsymbol{c}_{101})$ and displacements $\boldsymbol{\Phi}_u(\boldsymbol{c}_{101})$ in Tab. A.6 are necessary to reproduce the modal results, which have been presented in Fig. 3.15. Tab. A.6 and Tab. A.7 specify the

	i	1	2	3	4	5	6	7
	1	0.87510	0.40688	-1.06108	0.85506	0.10805	-0.26688	-0.41564
$\boldsymbol{K}_{\vartheta R}$	2		0.42070	-0.40853	0.35791	0.46809	0.25855	-0.46681
	3			1.32947	-1.09077	0.02433	0.50825	0.45817
×	4				0.97486	0.02561	-0.47928	-0.54225
	5					0.77536	0.68636	-0.54814
10^4	6						0.94332	-0.14935
	7	symm.						0.80697
$\boldsymbol{h}_{\vartheta N}^T\, q_B$	1	0.96107	-0.44650	1.16539	0.93883	0.11808	0.29321	0.45588
$\boldsymbol{h}_{\vartheta R}^T\, \vartheta_\infty$	1	-0.64045	-0.29777	0.77656	-0.62579	-0.07906	0.19534	0.30419
$\boldsymbol{\Phi}_\vartheta(\boldsymbol{c}_{101})$	1	0.02733	-0.02465	-0.03039	-0.01571	-0.03729	0.02288	0.03553
$\boldsymbol{\Phi}_u(\boldsymbol{c}_{101})$	x	-0.33167	0.59218	0.00874	0.56248	0.15440	-0.55310	-0.05368
	y	0.57078	-0.20656	-0.67374	0.00452	-0.67483	0.10753	0.63471

Table A.6: Verification Example 2: Robin load matrix and load vectors of (A.2), modal temperatures $\boldsymbol{\Phi}_\vartheta$ in [K] and modal displacements $\boldsymbol{\Phi}_u$ in [m] concerning Node 101.

Term	Specification	Reference
$\boldsymbol{M}_{uu}$	$\boldsymbol{I}_7$	
$\boldsymbol{C}_{\vartheta\vartheta}$	$\boldsymbol{I}_7$	
$\boldsymbol{K}_{uu}$	$\mathrm{diag}\{2\pi\bar{\omega}_i\}^2$	$\bar{\omega}_i$ see Fig. 3.14
$\boldsymbol{K}_{\vartheta\vartheta}$	$\mathrm{diag}\{\kappa_i\}$	κ_i see Fig. 3.14
$\boldsymbol{K}_{u\vartheta}$	$\mathrm{diag}\{2\pi\bar{\omega}_i\}^2$	$\bar{\omega}_i$ see Fig. 3.14

Table A.7: Specification of thermal and mechanical system matrices of (A.2).

terms of the thermal and mechanical equations in modal representation:

$$\begin{aligned} \boldsymbol{C}_{\vartheta\vartheta}\,\dot{\boldsymbol{z}}_\vartheta + (\boldsymbol{K}_{\vartheta\vartheta} + \boldsymbol{K}_{\vartheta R})\,\boldsymbol{z}_\vartheta &= \boldsymbol{h}_{\vartheta N}\,q_B + \boldsymbol{h}_{\vartheta R}\,\vartheta_\infty\ , \\ \boldsymbol{M}_{uu}\ddot{\boldsymbol{z}}_{uu} + \boldsymbol{K}_{uu}\boldsymbol{z}_u &= \boldsymbol{K}_{u\vartheta}\,\boldsymbol{z}_\vartheta\ . \end{aligned} \tag{A.2}$$

The FEM reference solutions are evaluated with the models that are documented in Fig. A.3.

```
/filname,thermodisc,1
/PREP7
!*** geometry *************
CYL4,  , ,.15
CYL4,  , ,.075
ASBA, 1, 2
!*** elements2switch ******
ET,1,SHELL57  !  thermal
!ET,1,SHELL63 ! mechanical
R,1,.007,.007,.007,.007,,,
!*** material *************
MP,EX,1,2.1e11
MP,NUXY,.3
MP,DENS,1,7800
MP,C,1,465
MP,ALPX,1,1.2e-5
MP,KXX,1,43
!*** meshing **************
TYPE,1
MAT,1
REAL,1
LESIZE,all,,,9,,,,,0
MSHAPE,0,2D
MSHKEY,0
AMESH,all
!*** boundary conditions ***
CSYS,1
!*** mechanical ***
!NSEL,S,LOC,X,.0749,.0751
!D,all,UX,,,,,UY
!alls,
!D,all,UZ
!*** thermal ***
NSEL,S,LOC,Y,-41,41
ESLN,S,1,all
SFE,all,1,HFLUX,,3000,,,
NSEL,S,LOC,Y,139,221
ESLN,S,1,all
SFE,all,1,CONV, ,10
SFE,all,1,CONV,2,-200
alls
!*** end ******************
finish
save
```

Figure A.3: ANSYS script defining the FE model of the simulations in Sec. 3.2.3.

A.3 Verification Example 2: Hot Spot

Tab. A.8 gives the linear physical parameters, which have been used for the finite element and the modal modelling of the brake disc in Sec. 3.2.4. Consequently these values as well appear in the ANSYS script in Fig. A.4 and again in the MATLAB script in Fig. A.7.

Physical Entity	Symbol	Unit	Value
Young's modulus	E	N/m^2	$8.0 \cdot 10^{10}$
Density	ϱ	kg/m^3	$7.25 \cdot 10^{3}$
Thermal conductivity	Λ	W/(mK)	$4.7 \cdot 10^{1}$
Thermal expansion	α	1/K	$1.04 \cdot 10^{-5}$
Specific heat capacity	c	J/(kgK)	$7.0 \cdot 10^{2}$

Table A.8: Material data for linear analysis.

```
/filenam,StrHotSp
/PREP7
!*** elements2switch *********
ET,1,PLANE77  ! thermal
ET,2,SOLID90  ! thermal
!ET,1,PLANE82 ! mechanical
!ET,2,SOLID95 ! mechanical
!*** material ***************
MP,EX,1,8e10
MP,NUXY,.26
MP,DENS,1,7250
MP,C,1,700
MP,ALPX,1,1.04e-5
MP,KXX,1,47
!*** geometry ****************
CYL4,0,0,.075,0,.15,360,
CYL4,0,0,.075,0,.15,60,
CYL4,0,0,.075,60,.15,90,
CYL4,0,0,.075,90,.15,120,
CYL4,0,0,.075,120,.15,180,
CYL4,0,0,.075,180,.15,240,
CYL4,0,0,.075,240,.15,270,
CYL4,0,0,.075,270,.15,300,
CYL4,0,0,.075,300,.15,360,
APTN,all
!*** meshing *****************
TYPE,1
LSEL,S,RADIUS,,.074,.076
LESize,all,.00437,
LSEL,S,RADIUS,,.14,.15
LESize,all,.00873,
LSEL,S,LENGTH,,.0749,.0751
LESize,all,.00625,
AMESH,all
TYPE,2
MAT,1
ESIZE,,2
EXTOPT,ACLEAR,1,0,
EXTOPT,ATTR,0,0,0
VEXT,all,,,0,0,.01,1,1,1
!*** end *********************
ET,1,0
finish
save
```

Figure A.4: ANSYS script defining the FE model of Verification Example 2 in Sec. 3.2.4.

Three MATLAB scripts are used to set-up the modal model of the brake disc. Fig. A.5 defines a general quadratic B-spline. The script in Fig. A.6 evaluates the modal shape functions $\boldsymbol{\Phi}_\vartheta(\boldsymbol{c}_k)$, which are visualised in Fig. 3.18. The system matrices of (3.40) can be calculated with the script in Fig. A.7.

```
function [y, dy]=myBspline(t,x);
%%%% evaluation of coefficients of quadratic B-spline %%%%%%%%%
%%%% t: knot vector, starts & ends with tripels, row vector %%%
%%%% x: position parameter, scalar                    %%%%%%%%%
%%%% y: values at x,        row vector                %%%%%%%%%
%%%% dy: derivatives at x,  row vector                %%%%%%%%%
y =zeros(length(t)-3,1)'; dy=y;                  %%% initialise
N= zeros(length(t)-1,3);  dN=N; o=N; do=N;       %%% initialise
if x >= t(1) && x <= t(end);            %%% only take if inside
   %%%%% get intervall index %%%%%%%%%%%%%%%%%%%%%%%%%%%%%%%%%%
   i=length(t);                       %%% start at the end of t
   while t(i)~=t(1) && i > 0 && x <= t(i)
      i=i-1;                                %%% count downwards
   end;
   %%%%%% recursively evalute B-splines of order 1, 2 and 3 %%%
   N(i,1)=1;                                      %%% 1st order
   for m=[2 3];                           %%% 2nd and 3rd order
     for j=[i-2 i-1 i];
       if t(j) < t(j+m-1);            %%% prevent division by 0
          do(j,m)= 1/(t(j+m-1)-t(j));
          o(j,m) =(x-t(j))*do(j,m);
       end;
     end;
     for j=[i-2 i-1 i];
       N(j,m) =o(j,m)*N(j,m-1)+(1-o(j+1,m))*N(j+1,m-1);
       dN(j,m)=do(j,m)*N(j,m-1)+o(j,m)*dN(j,m-1); %%% chain rule
       dN(j,m)=dN(j,m)-do(j+1,m)*N(j+1,m-1)       %%% chain rule
       dN(j,m)=dN(j,m)+(1-o(j+1,m))*dN(j+1,m-1);  %%% chain rule
     end;
   end;
   y=N(1:length(t)-3,3)'; dy=dN(1:length(t)-3,3)';    %%% return
end;
```

Figure A.5: MATLAB script to define quadratic B-splines, see [RS99, Sec. 5.1].

```
function [PtvX, gPtvX]=PHItheta(X);
%%%%%%%   evaluation of modal shape functions for     %%%%%%%%%%%%%
%%%%%%%        thermal field of brake disc            %%%%%%%%%%%%%
%%%%%%% X:     cylindrical position on disc;          %%%%%%%%%%%%%
%%%%%%% PtvX:  vector of modal shape functions at X   %%%%%%%%%%%%%
%%%%%%% gPtvX: gradient of modal shape functions at X %%%%%%%%%%%%%

thd= .01                                  %%% thickness of disc [m]
ri = .075                                 %%% inner radius [m]
ra = .15                                  %%% outer radius [m]

%%% coefficients w.r.t.   axial co-ordinate X(3,1) %%%%%%%%%%%%%%%%
trz=[0 0 0 1 2 3 3 3]*thd/3;
[fz fzs]=myBspline(trz, X(3,1));
%%% coefficients w.r.t.  radius co-ordinate X(1,1) %%%%%%%%%%%%%%%%
trr=ri+[0 0 0 1 2 3 3 3]*(ra-ri)/3;
[tmp tmps]=myBspline(trr, X(1,1));
fr(1)=1; frs(1)=0; fr(2)=tmp(3); frs(2)=tmps(3);%%% reduce approach
%%% coefficients w.r.t. angular co-ordinate X(2,1) %%%%%%%%%%%%%%%%
trp=[0 0 0:1:24 24 24]*pi/9;                           %%% easy
[tmp tmps]=myBspline(trp, X(2,1)+pi/3);                %%% way to
tmp(:,22:23) = tmp(:,22:23) + tmp(:,4:5);              %%% make a
tmps(:,22:23)= tmps(:,22:23)+ tmps(:,4:5);             %%% cyclic
fp=tmp(6:23); fps=tmps(6:23);                          %%% B-spline

%%% multiplication according to Eq. (3.38) %%%%%%%%%%%%%%%%%%%%%%%%
i=0;
for iw=1:length(fp);
      for ir=1:length(fr);
            for iz=1:length(fz);
               i=i+1;
               PtvX(i,1) =fp(iw)*fr(ir)*fz(iz);
               gPtvX(i,1)=frs(ir)*fp(iw)*fz(iz);
               gPtvX(i,2)=fps(iw)*fr(ir)*fz(iz)/r;
               gPtvX(i,3)=fzs(iz)*fp(iw)*fr(ir);
            end;
      end;
end;
```

Figure A.6: MATLAB script to define modal shape functions of the hot spot scenario in Sec. 3.2.4.

```
function [Ctt,Ktt,Ktr1,Ktr2,htn]=HotSpotSysMatrices();
%%%    evaluate modal system matrices of the thermal   %%%%%%%%%%%%
%%%    equation of the hot spot scenario, see (3.40)   %%%%%%%%%%%%
%%% Ctt:  heat capacity matrix                         %%%%%%%%%%%%
%%% Ktt:  conductivity matrix                          %%%%%%%%%%%%
%%% Ktr1: Robin load matrix, load area not included    %%%%%%%%%%%%
%%% Ktr2: Robin load matrix, only load area considered %%%%%%%%%%%%
%%% htn:  Neumann load vector, normalised              %%%%%%%%%%%%

%% physical & geometrical parameters in SI-Units
rho   =7250; % density
csp   =700;  % specific heat capacity
lambda=47;   % heat conductivity
hf    =1  ;  % film coefficient
ri    =0.075;% inner radius
ra    =0.15; % outer radius
thd   =0.01; % disc thickness
%% initialise %%%%%%%%%%%%%%%%%%%%%%%%%%%%%%%%%%%%%%%%%%%%%%%%%%%%%
Ctt=zeros(180,180); Ktt=Ctt; Ktr1=Ctt; Ktr2=Ctt; htn=zeros(180,1);
%% knotvectors for spatial load distribution %%%%%%%%%%%%%%%%%%%%%%
qtr=[0 0 0 1 2 3 3 3]*(ra-ri)/3 + ri;
qtp=[0 0 0 1 2 3 3 3]*pi/9;
qa=16/9;    %%% normal. factor => q = 1 for  r=ri+(ra-ri)/2, p=pi/6
%% location of Gauss points & corresponding weights for    %%%%%%%%
%% gaussian quadrature with 3^2 (boundary) or 3^3 (volume) %%%%%%%%
%% points per element, exact for polynomial of 5th order   %%%%%%%%
a= [-sqrt(.6) 0 sqrt(.6)];          b=[5 8 5]/9;
DR=[1+a, 3+a, 5+a]*(ra-ri)/6 + ri; wr=[b b b];
DZ=[1+a, 3+a, 5+a]* thd/6;         wz=[b b b];
DP=[1+a]*pi/18;                    wp=[b];
for i=3:2:35;
   DP=[DP, (i+a)*pi/18];           wp=[wp, b];
end;
%% differential  volume and boundary elements %%%%%%%%%%%%%%%%%%%%%
dpdz=thd/3*pi/9/4;                    %%% cylinder surface element
drdp=(ra-ri)/3*pi/9/4;                %%% circle sector element
drdpdz=(ra-ri)/3*thd/3*pi/9/8;        %%% volume element
```

Figure A.7: Page 1 of the MATLAB script to evaluate the modal system matrices of the Verification Example 2 in Sec. 3.2.4, integration scheme see [ZT00a, Sec. 9.9].

```
%%%% integration %%%%%%%%%%%%%%%%%%%%%%%%%%%%%%%%%%%%%%%%%%%%%%%%%%%
for iz=1:length(wz);
  for ip=1:length(wp);
    for ir=1:length(wr);
       GPV=[DR(ir); DP(ip); DZ(iz)];                %%% Gauss point
       WV=wr(ir)*wz(iz)*wp(ip);                     %%% weight
%%%% volume integration %%%%%%%%%%%%%%%%%%%%%%%%%%%%%%%%%%%%%%%%%%%%
       [PtvX, gPtvX]=PHItheta(GPV);    %%% get values & derivatives
       Ctt=Ctt+PtvX*PtvX’  *GPV(1,1)* WV * drdpdz;
       Ktt=Ktt+gPtvX*gPtvX’*GPV(1,1)* WV * drdpdz;
%%%% integration over both circle surfaces %%%%%%%%%%%%%%%%%%%%%%%%%
       if (iz==1)                                   %%% only once
         WS=wr(ir)*wp(ip);                          %%% weight
         [PtvXo, void]=PHItheta([GPV(1:2,1);0.01]); %%% get values
         [PtvXu, void]=PHItheta([GPV(1:2,1);0]);    %%% get values
         Ktr1=Ktr1+ (PtvXo*PtvXo’+ PtvXu*PtvXu’)*GPV(1,1)*WS*drdp;
%%%% integration over load area %%%%%%%%%%%%%%%%%%%%%%%%%%%%%%%%%%%%
         if (ip <=9)           %%% only for angle p: 0 <= p <= pi/3
           Ktr2=Ktr2+(PtvXo*PtvXo’)*GPV(1,1)*WS*drdp;
           [Qr, void]=myBspline(qtr, GPV(1,1));
           [Qp, void]=myBspline(qtp, GPV(2,1));
           Qrp=qa*Qr(3)*Qp(3);
           htn=htn + PtvXo*Qrp*GPV(1,1)*WS*drdp;
         end;
       end;
     end;
%%%% integration over cylinder surfaces %%%%%%%%%%%%%%%%%%%%%%%%%%%%
    GPi=[ri; DP(ip); DZ(iz)];                       %%% Gauss point
    GPa=[ra; DP(ip); DZ(iz)];                       %%% Gauss point
    [PtvXi, void]=PHItheta(GPi);                    %%% get values
    [PtvXa, void]=PHItheta(GPa);                    %%% get values
    Wia=wz(iz)*wp(ip);                              %%% weight
    Ktr1=Ktr1+(PtvXi*PtvXi’)*Wia*ri*dpdz;
    Ktr1=Ktr1+(PtvXa*PtvXa’)*Wia*ra*dpdz;
   end;
end;
Ktr1=Ktr1 * hf; Ktr2=Ktr2 * hf; Ktr1=Ktr1-Ktr2;      %%% return
Ctt=Ctt*csp*rho; Ktt=lambda*Ktt;                     %%% return
```

Figure A.8: Page 2 of the MATLAB script of Fig. A.7.

Fig. A.9 shows schematically how the thermal loads are applied at each contact event and has to be read together with the transient load values of Tab. A.9.

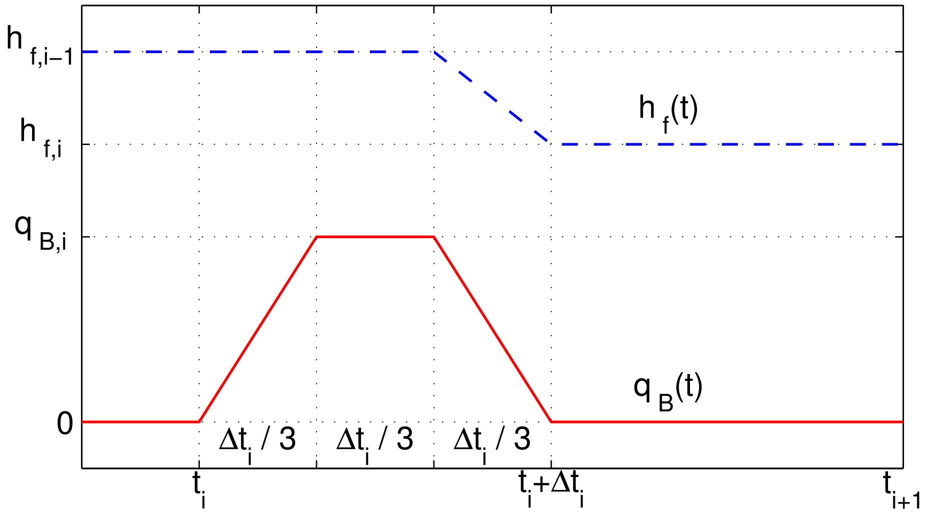

Figure A.9: Transient load scheme of the Verification Example 2 for $1 \leq i \leq 35$, to be read in conjunction with Tab. A.9.

The spatial distribution of the heat flux load follows from the analytical equations (A.3), which define a B-spline hump on basis of the quadratic B-spline curve $b(\xi, \boldsymbol{\tau})$ with knot vector $\boldsymbol{\tau} = (\tau_1 \;\; \tau_2 \;\; \tau_3 \;\; \tau_4)$ and position parameter ξ:

$$b(\xi, \boldsymbol{\tau}) = \begin{cases} 0 & \text{if} \quad \xi < \tau_1 \,, \\ \dfrac{(\xi - \tau_1)^2}{(\tau_3 - \tau_1)(\tau_2 - \tau_1)} & \text{if} \quad \tau_1 \leq \xi < \tau_2 \,, \\ \dfrac{(\xi - \tau_1)(\tau_3 - \xi)}{(\tau_3 - \tau_1)(\tau_3 - \tau_2)} + \dfrac{(\xi - \tau_2)(\tau_4 - \xi)}{(\tau_3 - \tau_2)(\tau_4 - \tau_2)} & \text{if} \quad \tau_2 \leq \xi < \tau_3 \,, \\ \dfrac{(\tau_4 - \xi)^2}{(\tau_4 - \tau_2)(\tau_4 - \tau_3)} & \text{if} \quad \tau_3 \leq \xi \leq \tau_4 \,, \\ 0 & \text{if} \quad \tau_4 < \xi \,. \end{cases} \tag{A.3a}$$

$$\boldsymbol{\tau}_r = (0.075 \;\; 0.1 \;\; 0.125 \;\; 0.15) \;\; [\mathrm{m}] \,, \qquad \boldsymbol{\tau}_\phi = \left(0 \;\; \frac{\pi}{9} \;\; \frac{2\pi}{9} \;\; \frac{\pi}{3}\right) \; [\mathrm{rad}] \,, \tag{A.3b}$$

$$q_B(r, \phi, t) = \frac{16}{9} \cdot q_B(t) \cdot b(r, \boldsymbol{\tau}_r) \cdot b(\phi, \boldsymbol{\tau}_\phi) \,. \tag{A.3c}$$

The equivalent formulation may be taken from Fig. A.8, where the load distribution appears after the comment line *% integration over load area %*.

The matrix $\hat{\boldsymbol{\Phi}}_u(\boldsymbol{c}_k)$, which is necessary to reproduce the displacement results at a specific node k at the position $\boldsymbol{c}_k$ has to be evaluated according to the scheme in Fig. 3.12. The 180 modal temperature fields $\boldsymbol{\vartheta}_i$ are used to define 180 mechanical loads $\hat{\boldsymbol{h}}_i$ and lead to 180 vectorial displacements $\boldsymbol{u}_i(\boldsymbol{c}_k)$, which form the matrix $\hat{\boldsymbol{\Phi}}_u(\boldsymbol{c}_k)$.

	Time	Load Time Span	Heat Flux	Film Coefficient
i	t_i $[s]$	Δt_i [1/100 s]	$q_{B,i}$ $\left[\frac{\mathrm{kW}}{\mathrm{m}^2}\right]$	$h_{f,i}$ $\left[\frac{\mathrm{W}}{\mathrm{m}^2\mathrm{K}}\right]$
0	0.0000	0.000	0	86.9
1	1.0000	0.435	317606	86.9
2	1.0760	0.442	303347	85.9
3	1.1531	0.449	289307	84.8
4	1.2316	0.456	275492	83.7
5	1.3113	0.464	261903	82.6
6	1.3924	0.472	248546	81.5
7	1.4749	0.481	235423	80.3
8	1.5590	0.490	222541	79.1
9	1.6448	0.499	209902	77.9
10	1.7322	0.510	197511	76.6
11	1.8215	0.521	185375	75.4
12	1.9127	0.532	173498	74.0
13	2.0060	0.545	161886	72.7
14	2.1015	0.558	150546	71.3
15	2.1994	0.572	139483	69.9
16	2.3000	0.588	128705	68.4
17	2.4033	0.605	118221	66.8
18	2.5097	0.623	108037	65.2
19	2.6194	0.643	98164	63.6
20	2.7328	0.666	88611	61.9
21	2.8503	0.691	79391	60.0
22	2.9724	0.718	70514	58.1
23	3.0996	0.750	61995	56.1
24	3.2326	0.786	53850	54.0
25	3.3724	0.828	46097	51.8
26	3.5200	0.877	38756	49.3
27	3.6770	0.936	31852	46.7
28	3.8454	1.009	25416	43.8
29	4.0281	1.103	19483	40.6
30	4.2295	1.228	14100	36.9
31	4.4571	1.410	9332	32.6
32	4.7246	1.705	5271	26.9
33	5.0659	2.328	2071	18.5
34	5.6556	6.316	104	9.1
35	6.0000	0.000	0	4.0

Table A.9: Verification Example 2: transient load definitions.

In order to perform a nonlinear finite element analysis and reproduce the results of Fig. 3.21, the material parameters of the ANSYS script from Fig. A.4 have to substituted according to the values that are listed in Tab. A.10. The load definitions remain unchanged, but the parameters of the ANSYS time integration scheme should be adapted.

Physical Entity	Symbol	Unit	a_0	a_ϑ
Young's modulus	E	N/m^2	$8.635 \cdot 10^{10}$	$-2.1 \cdot 10^{7}$
Density	ϱ	kg/m^3	$7.25 \cdot 10^{3}$	0.0
Thermal conductivity	Λ	W/(mK)	$5.5 \cdot 10^{1}$	$-2.67 \cdot 10^{-2}$
Thermal expansion	α	1/K	$8.092 \cdot 10^{-6}$	$7.7 \cdot 10^{-9}$
Specific heat capacity	c	J/(kgK)	$5.998 \cdot 10^{2}$	$3.34 \cdot 10^{-1}$

Table A.10: Material data for the nonlinear finite element analysis as linear functions of the temperature according to: $a(\vartheta) = a_o + a_\vartheta \, \vartheta$.

Bibliography

[ANS03] ANSYS, Inc. ANSYS® *Release 7.1 Theory Reference*, 2003.

[AV04] M. Arnold and O. Vaculín, editors. *Multibody System Simulation in Vehicle System Dynamics. To the memory of Willi Kortüm (1938 – 2002)*, Vol. 41, No. 5:335-429 of *Vehicle System Dynamics*. Taylor & Francis, 2004.

[Bal89] J. Bals. Aktive Schwingungsdämpfung flexibler Strukturen. Forschungsbericht DLR-FB 90-03, DLR, Deutsche Forschungsanstalt für Luft- und Raumfahrt, Institut für Dynamik der Flugsysteme, Oberpfaffenhofen, Germany, 1989.

[Bat96] H.J. Bathe. *Finite Element Procedures*. Prentice Hall, New Jersey, 1996.

[BCP96] K.E. Brenan, S.L. Campbell, and L.R. Petzold. *Numerical solution of initial–value problems in differential–algebraic equations*. SIAM, Philadelphia, 2nd ed., 1996.

[Bio70] M.A. Biot. *Variational Principles in Heat Transfer*. Oxford University Press, Oxford, UK, 1970.

[BJO86] H. Brandl, R. Johanni, and M. Otter. A very efficient algorithm for the simulation of robots and similar multibody systems without inversion of the mass matrix. In *IFAC Theory of Robots*, Vienna, Austria, 1986.

[BP92] H. Bremer and F. Pfeiffer. *Elastische Mehrkörpersysteme*. Teubner–Verlag, Stuttgart, 1992.

[Bre88] H. Bremer. *Dynamik und Regelung mechanischer Systeme*. Teubner–Verlag, Stuttgart, 1988.

[BRK02] T. Bechtold, E.B. Rudnyi, and J.G. Korvink. Automatic order reduction of thermo-electric models for MEMS: Arnoldi vs. Guyan. In *Proc. of The Fourth International Conference on Advanced Semiconductor Devices and Microsystems, ASDAM 2002*, Smolenice Castle, Slovakia, 2002.

[Bur91] M. Burckhardt. *Fahrwerkstechnik: Bremsdynamik und PKW–Bremsanlagen*. Vogel-Fachbuch Kraftfahrzeugtechnik. Vogel–Verlag, Würzburg, 1991.

[BW97] B.A. Boley and J.H. Weiner. *Theory of Thermal Stresses*. Dover Publications, Mineola, New York, 1997.

[CC02] L.R. Corr and W.W. Clark. Comparison of low-frequency piezoelectric switching shunt techniques for structural damping. *Smart Materials and Structures*, 11:370–376, 2002.

[CH94] K.H. Chan and N.W. Hagood. Modeling of nonlinear piezoceramics for structural actuation. *SPIE Proceedings*, Vol. 2190:194–205, 1994.

[CJ59] H.S. Carslaw and J.C. Jaeger. *Conduction of Heat in Solids*. Oxford University Press, Oxford, UK, 2nd ed., 1959.

[CL00] M. Chiao and L. Lin. Self-buckling of micromachined beams under resititive heating. *Journal of Microelectromechanical Systems*, 9(1):146–151, 2000.

[DFP01] P. De Man, A. François, and A. Preumont. Robust feedback control of a baffled plate through vibroacoustic optimization. In *42nd AIAA Structural Dynamics Conference*, Seattle, USA, 2001.

[DHS01] S. Dietz, G. Hippmann, and G. Schupp. Interaction of vehicles and flexible tracks by co–simulation of multibody vehicle systems and finite element track models. In *17th Symposium Dynamics of Vehicles on Roads and Tracks IAVSD 2001*, Copenhagen, August 20–24 2001.

[Die99] S. Dietz. *Vibration and Fatigue Analysis of Vehicle Systems Using Component Modes*. No. 401 in Fortschritts-Berichte VDI Reihe 12. VDI-Verlag, Düsseldorf, 1999.

[dR02] V. d'Alessandro and N. Rinaldi. A critical review of thermal models for electro-thermal simulation. *Solid-State Electronics*, 46:487–496, 2002.

[EG99] B. Ellis and R. Goodall. The mechatronic train: Requirements and concepts. In *Proc. of World Congress on Railway Vehicles*, pp. 1–7, Tokyo, 1999.

[Eic93] A. Eichberger. *Simulation von Mehrkörpersystemen auf parallelen Rechnerarchitekturen*. No. 332 in Fortschritts-Berichte VDI Reihe 8. VDI-Verlag, Düsseldorf, 1993.

[FEN96] C.R. Fuller, S.J. Elliott, and P.A. Nelson. *Active Control of Vibration*. Academic Press Ltd., London, 1996.

[FLS64] R.P. Feynman, R.B. Leighton, and M. Sands, editors. *The Feynman Lectures on Physics*, Vol. II, Mainly Electromagnetism and Matter. Addison-Wesley Publishing Company, Reading, Massachusetts, 1964.

[Gan04] R. Gansekow. Approval of the Siemens Desiro Series Vehicle Dynamics for Use in Great Britain. *SIMPACK News*, Vol. 8 (1), 2004.

[GC01] M. Geradin and A. Cardona. *Flexible Multibody Dynamics: A Finite Element Approach*. J. Wiley and Sons, New York, 2001.

[GHSW95] D. Gross, W. Hauger, W. Schnell, and P. Wriggers. *Technische Mechanik*. Bd. 4. Springer–Verlag, Berlin, 2nd ed., 1995.

[GK87] R. Gasch and K. Knothe. *Strukturdynamik*. Bd. 1. Springer–Verlag, Berlin, 1987.

[GK89] R. Gasch and K. Knothe. *Strukturdynamik*. Bd. 2. Springer–Verlag, Berlin, 1989.

[GKK00] U. Gabbert, W. Kreher, and H. Köppe. Mathematical modeling and numerical simulation of smart structures controlled by piezoelectric wafers and fibers. *Functional Materials (EUROMAT99)*, 13:525–530, 2000.

[GM01] C. Groth and G. Müller. *FEM für Praktiker*. Band 3: Temperaturfelder. expert–Verlag, Renningen, 4th ed., 2001.

[Gre03] M. Gretzschel. *Mechatronische Antriebs- und Lenkkonzepte für Schienenfahrzeuge der nächsten Generation*. No. 541 in Fortschritts-Berichte VDI Reihe 12. VDI-Verlag, Düsseldorf, 2003.

[GSW97] U. Gabbert, I. Schulz, and C.T. Weber. Actuator placement in smart structures by discrete-continous optimization. In U. Gabbert, editor, *Smart Mechanical Systems - Adaptronics*, No. 244 in Fortschrittberichte VDI Reihe 11, pp. 83–91. VDI-Verlag, Düsseldorf, 1997.

[Hau89] E. Haug. *Computer Aided Kinematics and Dynamics of Mechanical Systems: Basic Methods*. Allyn and Bacon, Boston, 1989.

[HAV05] A. Heckmann, M. Arnold, and O. Vaculín. A modal multifield approach for an extended flexible body description in multibody dynamics. *Multibody System Dynamics*, 13:299–322, 2005.

[Hec03] A. Heckmann. Representation and simulation of smart structures in multibody dynamics. *PAMM Proceedings in Applied Mathematics and Mechanics*, 2(1):128–129, 2003.

[HGP98] B. Heimann, W. Gerth, and K. Popp. *Mechatronik: Komponenten - Methoden - Beispiele*. Fachbuchverlag Leipzig im Carl Hanser Verlag, München, 1998.

[HH79] K.-H. Hellwege and A.M. Hellwege, editors. *Landolt-Börnstein, Zahlenwerte und Funktionen aus Naturwissenschaft und Technik*, Vol. 11. Springer–Verlag, Berlin, 1979.

[HL93] A. Hać and L. Liu. Sensor and actuator location in motion control of flexible structures. *Journal of Sound and Vibration*, 167(2):239–261, 1993.

[Hoh99] Ch. Hohmann. *Simulation von Verschleiß an Scheibenbremsen.* Shaker Verlag, Aachen, 1999.

[HTTT03] J. Hansson, M. Takano, T. Takigami, T. Tomioka, and Y. Suzuki. Vibration suppression of railway carbody with piezoelectric elements (a study by using a scale model). In *International Symposium on Speed-up and Service Technology for Railway and Maglev Systems 2003 (STECH'03)*, Tokyo, Japan, 2003.

[HV02] A. Heckmann and O. Vaculín. Multibody simulation of actively controlled carbody flexibility. In P. Sas and P. van Hal, editors, *Proc. of International Conference on Noise and Vibration Engineering (ISMA 2002)*, pp. 1123–1132, Leuven, Belgium, 2002.

[HW96] E. Hairer and G. Wanner. *Solving Ordinary Differential Equations II.* Springer-Verlag, Berlin, 2nd ed., 1996.

[Jac03] H. Jacobsson. Aspects of disc brake judder. In *Proc. of the Institution of Mechanical Engineeers, Part D: Journal of Automobile Engineering*, Vol. 217-6, pp. 419–430, 1 June 2003.

[Jae42] J.C. Jaeger. Moving sources of heat and the temperatures at sliding contacts. *Proc. Roy. Soc. N.S.W.*, 176:203–224, 1942.

[Jen95] D.J. Jendritza, editor. *Technischer Einsatz neuer Aktoren.* expert–Verlag, Renningen, 1995.

[KHS02] W. Krüger, R. Heinrich, and M. Spieck. Fluid-structure coupling using CFD and multibody simulation methods. In *Proceedings of ICAS 2002 Congress*, Toronto, Canada, 2002.

[KL93] W. Kortüm and P. Lugner. *Systemdynamik und Regelung von Fahrzeugen.* Springer-Verlag, Berlin, 1993.

[KL95] K. Knothe and S. Liebelt. Determination of temperatures for sliding contact with applications for wheel-rail systems. *Wear*, 189:91–99, 1995.

[KM92] V.K. Kinra and K.B. Milligan. Irreversible heat transfer as a source of thermoelastic damping. In V.K. Kinra and A. Wolfenden, editors, *M3D: Mechanics and Mechanisms of Material, ASTM STP 1169*, pp. 94–123. American Society for Testing and Materials, Philadelphia, 1992.

[KR03] J.G. Korvink and E.B. Rudnyi. Computer-aided engineering of electro-thermal MST devices: Moving from device to system simulation. In *EUROSIME'03, 4th International Conference on thermal and mechanical simulation and experiments in microelectronics and micro-systems*, Aix-en-Provence, France, 2003.

[KRD98] T.K. Kao, J.W. Richmond, and A. Douarre. Thermo-mechanical instability in braking and brake disc thermal judder: an experimental and finite element study. In *Proc. of 2nd International Seminar on Automotive Braking, Recent Developments and Future Trends, IMechE*, pp. 231–263, Leeds, UK, 1998.

[KW92] K. Knothe and H. Wessels. *Finite Elemente*. Springer-Verlag, Berlin, 2nd ed., 1992.

[Lan70] C. Lanczos. *The Variational Principles of Mechanics*. Dover, New York, 4th ed., 1970.

[Lau97] F. Laugwitz. Experimental results on active damping of beams by piezoelectric linear actuators. In U. Gabbert, editor, *Smart Mechanical Systems – Adaptronics*, No. 244 in Fortschritts-Berichte VDI Reihe 11, pp. 195–204. VDI-Verlag, Düsseldorf, 1997.

[LL01] J.H. Lienhard^{IV} and J.H. Lienhard^{V}. *A Heat Transfer Textbook*. Phlogiston Press, Cambridge, Massachusetts, 2001.

[LLMB00] G. Locatelli, H. Langer, M. Müller, and H. Baier. Simultaneous optimization of actuator placement and structural parameters by mathematical and genetic algorithm. In *Smart Structures and Structronic Systems, IUTAM Symposium 2000*. Kluwer Academic Publishers, 2000.

[LMTS96] R.W. Lewis, K. Morgan, H.R. Thomas, and K.N. Seetharamua. *The Finite Element Method in Heat Transfer Analysis*. John Wiley and Sons, Chichester, UK, 1996.

[Lov44] A.E.H. Love. *A Treatise on the Mathematical Theory of Elasticity*. Dover, New York, 4th ed., 1944.

[LR00] R. Lifshitz and M.L. Roukes. Thermoelastic damping in micro- and nanomechanical systems. *Physical Review B*, 61(8):5600 – 5609, 2000.

[MeT01] Mechatronic Technologies for Trains of the Future (Mechatronic Train), June 2001. Brite-Euram Project BE97-4387: Final Technical Report, Task A1 Technical Report *Selection of Vehicle Configurations* and Task A2.1 Technical Report *Extension and Adaption of Existing Software Tools*.

[Min74] R.D. Mindlin. Equations of high frequency vibrations of thermopiezoelectric crystal plates. *International Journal of Solids and Structures*, 10:625 – 637, 1974.

[Net98] H. Netter. *Rad–Schiene Systeme in differential-algebraischer Darstellung*. No. 352 in VDI–Fortschrittsberichte Reihe 12. VDI-Verlag, Düsseldorf, 1998.

[Now78a] W. Nowacki. Some general theorems of thermopiezoelectricity. *Journal of Thermal Stresses*, 1:171 – 182, 1978.

[Now78b] J.L.H. Nowinski. *Theory of thermoelasticity with applications*. Sijthof & Noordhoff International Publishers B.V., Alphen aan den Rijn, Netherlands, 1978.

[Now86] W. Nowacki. *Thermoelasticity*. Pergamon Press, Oxford, UK., 2nd ed., 1986.

[OCC77] N. Orlandea, M.A. Chace, and D.A. Calahan. A sparsity-oriented approach to the dynamic analysis and design of mechanical systems–part1 and part 2. *Journal of Engineering for Industry, Transactions of the ASME*, 1977.

[OG00] D. Ostergaard and M. Gyimesi. Finite element based reduced order modeling of micro electro mechanical systems (MEMS). In *Proc. of International Conference on Modeling and Simulation of Microsystems, MSM 2000*, San Diego, USA, 2000.

[Par70] H. Parkus. *Variational Principles in Thermo- and Magneto-Elasticity*. Springer–Verlag, Wien, 1970.

[PFL03] F. Petrone, G. Fichera, and M. Lacagnina. Modelling of torsion beam rear suspension by using multibody method. In J.A.C. Ambrósio, editor, *Proc. of International Conference on Advances in Computational Multibody Dynamics (Multibody Dynamics 2003)*, IDMEC/IST Lisbon, Portugal, July 1–4, 2003.

[Pie01] V. Piefort. *Finite Element Modelling of Piezoelectric Active Structures*. PhD thesis, Université Libre de Bruxelles, 2001.

[Pre02] A. Preumont. *Vibration Control of Active Structures*. Academic Publishers, Dordrecht, 2nd ed., 2002.

[Pre04] A. Preumont. Active vibration suppression in spacecrafts. In *3rd International Congress on Mechatronics 2004*, Czech Technical University, Prague, July 7-9, 2004.

[PS03] C.C. Painter and A.M. Shkel. Structural and thermal modeling of a z-axis rate integrating gyroscope. *Journal of Micromechanics and Microengineering*, 13, 2003.

[Rin96] A. Rinsdorf. *Theoretische und experimentelle Untersuchungen zur Komfortoptimierung von Scheibenbremsen*. Höppner und Göttert, Siegen, 1996.

[RPH03] M. Rudolph, K. Popp, and W. Hogenkamp. Computation of the temperature between brake disk and pad. *PAMM, Proceedings in Applied Mathematics and Mechanics*, 3(1):124–125, 2003.

[RS99] H.G. Roos and H. Schwetlick. *Numerische Mathematik*. Teubner Verlag, Stuttgart, 1999.

[RS01] M. Rose and D. Sachau. Multibody simulation of mechanism with distributed actuators on lightweight components. In *Proceedings of the SPIE's 8th Annual International Symposium on Smart Structures and Materials*, Newport Beach, USA, 2001.

[Rul98] W. Rulka. *Effiziente Simulation mechatronischer Systeme für industrielle Anwendungen*. PhD thesis, Technische Universität Wien, 1998.

[RWW93] M. Riemer, J. Wauer, and W. Wedig. *Mathematische Methoden der Technischen Mechanik*. Springer–Verlag, Berlin, 1993.

[Sac96] D. Sachau. *Berücksichtigung von flexiblen Körpern und Fügestellen in Mehrkörpersystemen zur Simulation aktiver Raumfahrtstrukturen*. Bericht aus dem Institut A für Mechanik der Universität Stuttgart, Stuttgart, 1996. PhD thesis.

[Sal01] J. Salençon. *Handbook of Continuum Mechanics*. Springer-Verlag, Berlin, 2001.

[Sch97] W. Schiehlen. Multibody dynamics: Roots and perspectives. *Multibody System Dynamics*, 1:149–188, 1997.

[Sha97] A.A. Shabana. Flexible multibody dynamics: Review of past and recent developments. *Multibody System Dynamics*, 1:189–222, 1997.

[Sha98] A.A. Shabana. *Dynamics of Multibody Systems*. Cambridge University Press, Cambridge, 2nd ed., 1998.

[Sim01] B. Simeon. Numerical analysis of flexible multibody systems. *Multibody System Dynamics*, 6:305–325, 2001.

[SK00] A. Stensson and W. Kortüm. State-of-the-art of CAE for mechatronic systems and industry requirements. In R. Isermann, editor, *Proc. of 1st IFAC Conference on Mechatronic Systems, 18.-20.9.2000*, pp. 717–722, Darmstadt, Germany, 2000.

[SLHL00] R. Simkovics, H. Landes, M. Kaltenbacher J. Hoffelner, and R. Lerch. Finite element analysis of hysteresis effects in piezoelectric transducers. In *Smart Structures and Materials 2000: Mathematics and Control in Smart Structures*, Vol. 3984, pp. 33–44, Newport Beach, USA, 2000.

[SS01] P. Schwarz and P. Schneider. Model library and tool support for MEMS simulation. In *Conference on MICROELECTRONIC AND MEMS TECHNOLOGY, 30.5.-1.6.2001*, Vol. 4407 of *SPIE Proceedings Series*, Edinburgh, Scotland, 2001.

[Ste98] T. Steffen. *Untersuchung der Hotspotbildung bei Pkw-Bremsscheiben*. No. 345 in VDI–Fortschrittsberichte Reihe 12. VDI-Verlag, Düsseldorf, 1998.

[SV96] V. Stejskal and M. Valášek. *Kinematics and Dynamics of Machinery*. Marcel Dekker, Inc., New York, 1996.

[SW99] R. Schwertassek and O. Wallrapp. *Dynamik flexibler Mehrkörpersysteme*. Vieweg Verlag, Braunschweig, 1999.

[SW01] B. Schweizer and J. Wauer. Atomistic explanation of the Gough-Joule-effect. *The European Physical Journal, B23*, pp. 383–390, 2001.

[SWD99] R. Schwertassek, O. Wallrapp, and S. v. Dombrowski. Modal representation of stress in flexible multibody simulation. *Nonlinear Dynamics*, 20:381–390, 1999.

[Sza77] I. Szabó. *Höhere Technische Mechanik.* Springer-Verlag, Berlin, 1977.

[Tay03] R.L. Taylor. *FEAP - A Finite Element Analysis Program, Version 7.5 Theory Manual.* University of Berkeley, Dept. of Civil Engineering, Berkeley, 2003.

[TG80] J. Tichý and G. Gautschi. *Piezoelektrische Messtechnik.* Springer–Verlag, Berlin, 1980.

[TMGE00] S. Taschini, J. Müller, A. Greiner, M. Emmenegger, H. Baltes, and J.G. Korvink. Accurate modelling and simulation of thermomechanical microsystem dynamics. *Computer Modelling and Simulation in Engineering*, 1:31–44, 2000.

[Vei01] A. Veitl. *Integrierter Entwurf innovativer Stromabnehmer.* No. 325 in Fortschritt-Berichte VDI Reihe 20. VDI–Verlag, Düsseldorf, 2001.

[VH04a] O. Vaculín and A. Heckmann. Active damping of railway carbody vibrations with piezoelements. In *7th International Symposium on Advanced Vehicle Control AVEC'04*, Arnhem, Netherlands, August 23-27, 2004.

[VH04b] O. Vaculín and A. Heckmann. Simulation and control of smart structures in multibody systems. In *3rd International Congress on Mechatronics 2004*, Czech Technical University, Prague, July 7-9, 2004.

[VKS01] O. Vaculín, W.-R. Krüger, and M. Spieck. Coupling of multibody and control simulation tools for the design of mechatronic systems. In *ASME 2001 Design Engineering Technical Conferences*, No. DETC2001/VIB-21323, Pittsburgh, 2001.

[Vog97] H. Vogel. *Gerthsen Physik.* Springer-Verlag, Berlin, 19th ed., 1997.

[Wal94] O. Wallrapp. Standardization of flexible body modeling in multibody system codes, Part 1: Definition of standard input data. *Mechanics of Structures and Machines*, 22(3):283–304, 1994.

[Was82] K. Washizu. *Variational Methods in Elasticity and Plasticity.* Pergamon Press, Oxford, 3rd ed., 1982.

[WHSM99] J. Wallaschek, K.H. Hach, U. Stolz, and P. Mody. A survey of the present state of friction modelling in the analytical and numerical investigation of brake noise generation. In *Proc. of the ASME Vibration Conference*, Las Vegas, USA, 1999.

[WS91] O. Wallrapp and R. Schwertassek. Representation of geometric stiffening in multibody system simulation. *International Journal for Numerical Methods in Engineering*, 32:1833–1850, 1991.

[YT00] R. Ye and H.S. Tzou. Control of adaptive shells with thermal and mechanical excitations. *Journal of Sound and Vibration*, 231(5):1321–1338, 2000.

[Zen60] C. Zener. *Elasticity and Anelasticity of Metals*. The University of Chicago Press, Chicago, 1960.

[ZT00a] O.C. Zienkiewicz and R.L. Taylor. *The Finite Element Method*, Vol. 1. Butterworth Heinemann, Oxford, 5th ed., 2000.

[ZT00b] O.C. Zienkiewicz and R.L. Taylor. *The Finite Element Method*, Vol. 2. Butterworth Heinemann, Oxford, 5th ed., 2000.

Lebenslauf

07.06.1962		geboren in Worms am Rhein
1968	1972	Westend-Grundschule in Worms
1972	1981	Eleonorengymnasium in Worms bestandene Abiturprüfung am 26.05.1981
1984	1987	Schreinerlehre in der Holzwerkstätte Koch in Bechtheim bei Worms bestandene Gesellenprüfung am 18.07.1987
1987	1991	Holztechnik-Studium an der Fachhochschule Rosenheim Abschluß: Dipl.-Ing. (FH) am 09.09.1991
1991	1996	Konstruktionsingenieur bei der Werkzeug- und Maschinenfabrik Stehle GmbH & Co. in Memmingen
1996	1999	Maschinenbau-Studium an der Technischen Universität München Abschluß: Dipl.-Ing. Univ. am 31.05.1999
1999	2000	CAD-Applikationsingenieur bei der Firma TESIS Wamware CAE Consulting GmbH in München
2000	...	wissenschaftlicher Mitarbeiter im Deutschen Zentrum für Luft- und Raumfahrt, DLR, in Oberpfaffenhofen, davon
2000	2003	im Institut für Aeroelastik, Fahrzeug-Systemdynamik
2004	...	im Institut für Robotik und Mechatronik, Fahrzeug-Systemdynamik

Oberpfaffenhofen, 15. April 2004

Andreas Heckmann